SEISMIC PERFORMANCE OF OFFSHORE CONCRETE GRAVITY PLATFORMS

A Thesis

submitted in partial fulfilment

of the requirements for the degree of

Doctor of Philosophy in Civil Engineering

at the

University of Canterbury

Christchurch

New Zealand.

by

D. Whittaker

October 1987

ABSTRACT

The seismic performance of concrete offshore gravity platforms is investigated. Aspects of dynamic structural analysis are discussed with particular reference to offshore gravity platforms, including soil-structure and water-structure interaction. Results of a seismic hazard analysis using currently available information are presented, and appropriate acceleration response spectra for design purposes are suggested. Site response effects are examined to investigate whether seismic hazard analysis results could be adjusted in a rational manner to account for the response of flexible nonlinear foundation materials. Artificial earthquake records are discussed and a suite of artificial accelerograms are generated to match the suggested design acceleration response spectra for offshore platforms in New Zealand. An experimental testing programme was undertaken to examine the strength and ductility characteristics of circular hollow reinforced and partially prestressed concrete members. Six columns were tested, representing scale models of members which could be used in the critical regions of possible offshore concrete platform configurations. A companion theoretical study was carried out to examine the strength and ductility of circular hollow sections. Results are presented in a design chart form suitable for use by designers. Finally, preliminary design studies were carried out for two different concrete gravity platform types to assess their likely feasibility. Of particular interest was the required distribution of strength to resist moderate earthquake effects and the ductility demands during severe earthquakes.

ACKNOWLEDGEMENTS

The research described in this thesis was carried out in the Department of Civil Engineering, University of Canterbury, under the overall guidance of its Head, Professor R. Park.

This project was supervised by Professor R. Park and Dr A. J. Carr. I wish to sincerely thank Professor Park, as he was initially responsible for organizing this project. Without his commitment and encouragement this work would not have been possible. The extensive guidance provided by Dr Carr on the analytical aspects of this work is also gratefully acknowledged. Dr J. B. Berrill is thanked for his assistance and advice on the seismic hazard analysis aspects of this work.

Acknowledgement is also made of the guidance of the Advisory Committee for the project, which consisted of members from the New Zealand Concrete Society, Ministry of Works and Development, New Zealand Concrete Research Association, Pacific Steel Limited and Shell BP and Todd Oil Services Limited.

Thanks are extended to technical staff of the Department of Civil Engineering, whose considerable efforts and expertise made the experimental work possible. In particular thanks are due to Messrs N. W. Prebble, G. H. Clarke, G. E. Hill, T. V. Scott, F. R. Greenslade and V. A. Scott. Mrs V. J. Grey is thanked for her draughting assistance.

The financial assistance of the following organisations is gratefully acknowledged:

Ministry of Works and Development, Head Office, Wellington.
New Zealand Concrete Research Association, Porirua.
Wilkins and Davies Limited, Auckland.
New Zealand Concrete Society Inc., Wellington.
Pacific Steel Limited, Auckland.
New Zealand Portland Cement Association, Wellington.
BBR New Zealand Limited, Auckland.
New Zealand Wire Limited, Auckland.
Worley Consultants Limited, Auckland.
W. R. Grace (NZ) Limited, Auckland.
University of Canterbury.

TABLE OF CONTENTS

NOTATION

a	=	Acceleration
	or	Total number of earthquakes per unit area per unit time
	or	$\varepsilon_{cc}/(\varepsilon_{cc} + \varepsilon_{un})$ in confined concrete stress-strain model
	or	Horizontal acceleration of water particle due to linear wave
$a(T)$	=	Coefficients in Okubo and Trifunac attenuation relations
a_m	=	Number of earthquakes per unit area per unit time with magnitudes greater than m
$a_g(t)$	=	Ground acceleration time history
a_o	=	Dimensionless frequency parameter
A	=	Area of member
	or	Matrix in complex modal analysis
	or	Coefficient of parabolic transition curve in confined concrete model
A_c	=	Area of confined core of concrete section
A_e	=	Effective area of footing with eccentric vertical load
A_i	=	Amplitude of Fourier component
A_g	=	Gross area of concrete section
A_o	=	Coefficient in Trifunac attenuation relation giving epicentral distance dependence
A_s	=	Total area of nonprestressed longitudinal reinforcement
A_{sh}	=	Area of hoop bars and supplementary cross-tie confining reinforcement
A_{sp}	=	Area of circular spiral bar
A_v	=	Area of hoop legs effective at resisting shear in each layer
A^*	=	Generalised matrix in complex modal analysis
b	=	Earthquake recurrence parameter
	or	f_{un}/f_c' in confined concrete stress-strain model
b_w	=	Width of web of concrete section
$b(T)$	=	Coefficients in Okubo and Trifunac attenuation relations
B	=	Matrix in complex modal analysis
	or	Width of footing
B_e	=	Effective width of footing with eccentric vertical load
B^*	=	Generalised matrix in complex modal analysis
c	=	Cover concrete thickness
	or	$(\varepsilon_{cc}/\varepsilon_{un})^{0.5}$ in confined concrete stress-strain model
	or	Cohesion of soil
c_b	=	Shear wave propagation speed in basement material
c_j	=	Foundation compliance damping coefficient
c_m	=	Added mass coefficient
c_s	=	Shear wave speed
$c(T)$	=	Coefficients in Okubo and Trifunac attenuation relations
C	=	Damping matrix
$CF(T)$	=	Instrument correction factor used in McVerry attenuation relation
C_d	=	Drag coefficient
C_i	=	Inertia coefficient
C_μ	=	Basic seismic spectral coefficient given by NZS 4203
d	=	Displacement
	or	Thickness of surface layer in site response analysis
	or	Effective depth of concrete section
	or	Still water depth
d_{max}	=	Maximum displacement
d_q	=	Factor in Hansen bearing capacity equation modifying surcharge term for depth of embedment
d_s	=	Diameter of circular spiral windings
d_y	=	Yield displacement
d_γ	=	Factor in Hansen bearing capacity equation modifying gravity term for depth of embedment
$d(T)$	=	Coefficient in Trifunac attenuation relation

D	=	Dynamical matrix
	or	Outside diameter of circular hollow section
D_o	=	Outside diameter of circular hollow column
D_i	=	Amplitude of incident displacement wave at base of layered site
D_r	=	Relative density of sand
D_s	=	Amplitude of surface displacement response
e	=	Base of natural logarithm
	or	Eccentricity of applied vertical load on footing
$e(T)$	=	Coefficient in Trifunac attenuation relation
E_c	=	Young's modulus of concrete
E_m	=	Modified initial modulus of elasticity of reinforcing steel
E_p	=	Initial Young's modulus of prestressing tendon
E_s	=	Young's modulus of reinforcing steel
E_{sh}	=	Strain hardening modulus of reinforcing steel
E_{re}	=	Tangent modulus at return coordinate in confined concrete stress-strain model
E_{sec}	=	Secant modulus in confined concrete stress-strain model
E_u	=	Tangent modulus of concrete at beginning of unloading
f_b	=	Steel stress at junction where softened branch merges with skeleton curve
f_c	=	Concrete stress
f_{ch}	=	Characteristic steel stress
	or	Characteristic tendon stress
f_c'	=	Unconfined concrete compressive cylinder strength
f_{cc}'	=	Confined concrete compressive cylinder strength
f_{gc}	=	Term in Katayama and McVerry attenuation relations giving ground condition dependence
f_l	=	Equivalent equal transverse confining stress
f_{lc}	=	Transverse confining stress effective in circumferential direction
f_{lr}	=	Transverse confining stress effective in radial direction
f_{l1}	=	Smaller transverse confining stress
f_{l2}	=	Larger transverse confining stress
f_m	=	Term in Katayama and McVerry attenuation relations giving magnitude dependence
f_{max}	=	Maximum steel stress
f_{new}	=	New concrete stress on reloading to strain ε_{un}
f_o	=	Steel stress at strain reversal
	or	Tendon stress at strain reversal
f_p	=	Stress in prestressing tendon
f_{pa}	=	Tendon stress at limit of proportionality on monotonic stress-strain curve
f_{pb}	=	Tendon stress at beginning of upper straight branch of monotonic stress-strain curve
f_{pi}	=	Initial tendon stress after losses
f_{pu}	=	Ultimate tendon stress
f_{re}	=	Stress at return point to concrete monotonic stress-strain curve
f_{ro}	=	Concrete stress at reloading reversal
f_s	=	Stress in reinforcing steel
f_{su}	=	Ultimate steel stress
f_t	=	Concrete tension stress
f_t'	=	Concrete tensile strength
f_{un}	=	Concrete stress at unloading point
f_y	=	Yield stress of reinforcement
f_{yh}	=	Yield stress of transverse hoop reinforcement
f_Δ	=	Term in Katayama and McVerry attenuation relations giving epicentral distance dependence
$f(T)$	=	Coefficient in Trifunac attenuation relation
F	=	Force
F_D	=	Damping force
F_{Dmax}	=	Maximum damping force
F_{max}	=	Maximum elastic force
F_y	=	Yield force
$F(t)$	=	Periodic Function

$F(x)$	=	Force per unit length induced by wave on submerged cylindrical member
g	=	Acceleration of gravity
$g(T)$	=	Coefficient in Trifunac attenuation relation
G	=	Shear modulus
G_i	=	Initial (small strain) shear modulus
$G(\omega)$	=	Power spectral density function
h	=	Height of large submerged cylindrical body
h''	=	Dimension of concrete core of section measured perpendicular to direction of hoop bars to outside of peripheral hoop
H	=	Horizontal component of applied load to footing
	or	Wave height (trough to crest)
H_{max}	=	Horizontal load to cause footing to slide
i	=	$\sqrt{(-1)}$
i_c	=	Factor in Hansen bearing capacity equation modifying cohesion term for inclination of applied load from vertical
i_q	=	Factor in Hansen bearing capacity equation modifying surcharge term for inclination of applied load from vertical
i_γ	=	Factor in Hansen bearing capacity equation modifying gravity term for inclination of applied load from vertical
I	=	Identity matrix
I_{cr}	=	Second moment of area of cracked concrete section
I_e	=	Effective second moment of area of section
I_g	=	Second moment of area of gross uncracked concrete section
k	=	Wave number
k_e	=	Efficiency factor to allow for reduction in effectiveness of transverse confinement layout
k_j	=	Foundation compliance stiffness coefficient
$k(\gamma)$	=	Stiffness reduction factor (shear strain dependent)
K	=	Stiffness coefficient or matrix
	or	Factor relating the mean effective normal stress and equivalent cohesion of soil
K_{cr}	=	Adjustment factor to yield curvature or ideal moment capacity to allow for variations in cover thickness ratio
$K_{fc'}$	=	Adjustment factor to yield curvature or ideal moment capacity to allow for variations in unconfined concrete compressive cylinder strength
K_h	=	Horizontal foundation stiffness
K_j	=	Foundation stiffness
	or	Initial shear stiffness
K_o	=	Initial stiffness of Ramberg-Osgood stress-strain curve with $r=\infty$
K_{ri}	=	Adjustment factor to yield curvature or ideal moment capacity to allow for variations in longitudinal reinforcement index
K_s	=	Shear stiffness
K_{tc}	=	Adjustment factor to yield curvature or ideal moment capacity to allow for variations in transverse confining stress ratio
K_v	=	Vertical foundation stiffness
K_2	=	Shear modulus multiplying factor
K_θ	=	Rotational foundation stiffness
l_p	=	Equivalent plastic hinge length
L	=	Length of cantilever member from critical section to free end
	or	Length of isolated footing
	or	Wavelength
m	=	Reference earthquake magnitude
M	=	Mass matrix
	or	Earthquake magnitude (local or Richter magnitude)
	or	Moment
M_b	=	Flexural strength from interaction diagram with applied axial load of P_b
M_{ACI}	=	Ideal flexural strength based on the ACI 318 flexural strength method
M_i	=	Ideal moment of resistance
M_o	=	Flexural strength from interaction diagram with zero axial load
M_y	=	First-yield moment of section

M_{1b}	=	Flexural strength from interaction diagram with applied axial load of $2P_b/3$
M_{2b}	=	Flexural strength from interaction diagram with applied axial load of $P_b/3$
N	=	Number of earthquakes greater than particular magnitude per unit time per unit area
N_c	=	Cohesion coefficient for bearing capacity equation (Prandtl bearing capacity factor)
N_q	=	Surcharge coefficient for bearing capacity equation
N_γ	=	Gravity coefficient for bearing capacity equation
n	=	Order of matrix
p	=	Scalar
	or	Probability that given amplitude will not be exceeded
ps	=	Axial prestress stress
P	=	Axial load
	or	Strain hardening exponent in stress-strain model for reinforcing steel
P_b	=	Axial load at balanced failure point
P_e	=	Externally applied axial load
P_{ps}	=	Axial prestress force
P_u	=	Factored axial load on section
P_{yc}	=	Ultimate axial force in compression
P_{yt}	=	Ultimate axial force in tension
P(t)	=	Loading as function of time
q	=	Displacement response vector
	or	Surcharge force per unit length
	or	Surcharge pressure
Q	=	Dimensionless frequency parameter
	or	Ratio of final tangent slope at large steel strains to initial tangent slope
	or	Ultimate bearing capacity of foundation material per unit length
Q_a	=	Overburden load on potential failure plane with platform in place
Q_i	=	Foundation impedance function
Q_o	=	Overburden load on potential failure plane with no platform in place
Q_u	=	Ultimate bearing capacity of isolated footing
Q^*	=	Generalised load vector in complex modal analysis
r	=	Vector associating degrees of freedom with ground motion
	or	Radius of equivalent circular footing
	or	Acoustic impedance ratio
	or	Ramberg-Osgood parameter
	or	$E_c/(E_c - E_{sec})$ in confined concrete stress-strain model
	or	Equivalent radius of large submerged body
R	=	Return period factor
	or	Parameter relating the confined strain ratio $\varepsilon_{cc}/\varepsilon_{co}$ to the confined strength ratio f_{cc}'/f_c' of confined concrete stress-strain model
	or	Ramberg-Osgood curvature parameter in steel stress-strain model
R_e	=	Real part of ...
s	=	Site condition factor in Trifunac attenuation relation
	or	Pitch of circular spiral windings
s_h	=	Spacing of transverse hoops
s_q	=	Factor in Hansen bearing capacity equation modifying surcharge term for shape of footing
s_γ	=	Factor in Hansen bearing capacity equation modifying gravity term for shape of footing
S	=	Spectral quantity
S_a	=	Response spectral acceleration
t	=	Time
	or	Hollow member wall thickness
t_c	=	Thickness of concrete core through wall to outside of hoops
T	=	Natural period of vibration
U	=	Slope of upper straight branch of tendon monotonic stress-strain curve
v	=	Velocity

	or	Parameter in Trifunac attenuation relation for vertical or horizontal earthquake
	or	Equivalent angle of inclination of applied footing load from vertical
	or	Horizontal velocity of water particle due to linear wave
v_b	=	Basic shear stress carried by concrete
v_c	=	Ideal shear stress carried by concrete
v_d	=	Shear stress associated with design shear force on section
v_{max}	=	Maximum velocity
V	=	Shear force
	or	Vertical component of applied load to footing
V_c	=	Shear resistance of concrete member provided by concrete mechanisms
V_i	=	Shear force associated with ideal flexural capacity of member
V_o	=	Shear force associated with flexural overstrength of member
V_s	=	Shear resistance of concrete member provided by steel mechanisms
V_t	=	Ideal shear resistance of concrete member
V_{max}	=	Maximum shear force sustained by member during testing
W_D	=	Work done by viscous damping forces per cycle of response
W_t	=	Total seismic weight of structure
x	=	Vector of acceleration and velocity components in complex modal analysis
	or	Ratio $\varepsilon/\varepsilon_{cc}$ in confined concrete stress-strain behaviour
	or	$(\varepsilon - \varepsilon_{un})/(\varepsilon_{pl} - \varepsilon_{un})$ in confined concrete stress-strain model
	or	$\varepsilon - \varepsilon_{re}$ in confined concrete stress-strain model
	or	Horizontal displacement of water particle due to linear wave
	or	Depth vertically downwards from undisturbed water level
y	=	Vector of velocity and displacement components in complex modal analysis
y_o	=	Vector of scalars
z	=	Vector of modal coordinates
	or	depth measured positive upwards from still water level
z'	=	Vector of conjugate modal coordinates
Z	=	Zone factor
β	=	Bilinear factor
γ	=	Soil shear strain
γ'	=	Effective unit weight of foundation material
Δ	=	Matrix of eigenvectors
	or	Lateral displacement at top of cantilever column member
Δ_f	=	Lateral displacement at top of cantilever column due to flexural deformations only
Δ_y	=	Lateral displacement at top of cantilever column at yield
Δ_p	=	Lateral displacement at top of cantilever column due to plastic deformations along the member
Δ_{max}	=	Maximum experimentally imposed lateral displacement
ε	=	Strain
ε_a	=	Common strain in confined concrete stress-strain model
ε_b	=	Steel strain at junction where softened branch merges with skeleton curve
ε_c	=	Concrete compression strain
ε_{cc}	=	Strain at peak of confined concrete stress-strain curve
ε_{co}	=	Strain at peak of unconfined concrete stress-strain curve
ε_{cu}	=	Ultimate sustainable concrete compression strain
ε_m	=	Current value of maximum imposed tendon strain
ε_{mo}	=	Steel strain at origin of monotonic stress-strain curve
ε_o	=	Steel strain at reversal point
	or	Tendon strain at reversal point
ε_p	=	Strain in prestressing tendon
ε_{pa}	=	Tendon strain at limit of proportionality on monotonic stress-strain curve

ε_{pb}	=	Tendon strain at beginning of upper straight branch of monotonic stress-strain curve
ε_{pl}	=	Plastic strain in confined concrete stress-strain model
	or	Plastic strain on previous cycle in tendon stress-strain model
ε_{pu}	=	Ultimate tendon strain
ε_{re}	=	Strain at return point to concrete monotonic stress-strain curve
ε_{ro}	=	Concrete strain at reloading reversal
ε_s	=	Strain in reinforcing steel
ε_{sh}	=	Strain in reinforcement at commencement of strain hardening
ε_{shift}	=	Amount by which skeleton branch of steel stress-strain curve is moved along strain axis
ε_{ss}	=	Skeleton branch steel strain
ε_{su}	=	Ultimate strain in reinforcement
ε_{spall}	=	Strain at which unconfined cover concrete spalls
ε_{un}	=	Strain at unloading point
ε_y	=	Yield strain in reinforcing steel
ε_{zmx}	=	Maximum tensile value of ε_{zero}
ε_{zmn}	=	Maximum compressive value of ε_{zero}
ε_{zero}	=	Strain at zero stress if tendon unloaded with modulus equal to Young's modulus
λ	=	Eigenvalue
	or	Fraction of critical damping
μ	=	Displacement ductility factor
μ_Δ	=	Displacement ductility factor
μ_ϕ	=	Curvature ductility factor
ν	=	Poisson's ratio
π	=	3.1415926
ρ	=	Mass density
	or	Total volumetric content of nonprestressed longitudinal reinforcement
ρ_b	=	Mass density of basement material in site response analysis
ρ_p	=	Total volumetric content of prestressed reinforcement
ρ_s	=	Mass density of surface layer in site response analysis
	or	Volumetric ratio of spiral confining reinforcement
ρ_w	=	Volumetric ratio of tension reinforcement
σ	=	Normal stress
σ_1'	=	Effective normal vertical stress
σ_m'	=	Mean effective normal stress
τ	=	Shear stress
ϕ	=	Strength reduction factor
	or	Curvature
	or	Reduction factor for Young's modulus of tendon
	or	Angle of internal soil friction
ϕ_y	=	Yield curvature
ϕ_{yb}	=	Basic yield curvature - Theoretical first-yield curvature multiplied by ratio of M_{ACI} to M_y
ϕ_y'	=	First-yield curvature
ϕ_{max}	=	Maximum curvature at critical section
ϕ_u	=	Ultimate curvature sustainable for four reversed load cycles
ϕ_i	=	Phase angle of ith Fourier component
ω	=	Circular frequency

Chapter 1

INTRODUCTION

Offshore concrete gravity platforms have been in use for the past fifteen years for the recovery of oil and gas reserves in the North Sea. Concrete has proved to be an extremely well suited material for offshore applications, mainly because of its excellent durability. Design of the North Sea structures has been governed by loading associated with severe storm waves. Because of the relatively low seismicity of the area design for earthquake effects has been of only minor importance.

With the continuing search for hydrocarbon reserves in other parts of the world, increasing interest has been focussed on the possible use of fixed platform structures in areas with high seismicity. Development of a large natural gas field off the coast of New Zealand is at present underway. This has identified a need for research to determine how possible offshore concrete gravity platform structures should be designed to withstand the effects of earthquake shaking.

This report documents a study undertaken to investigate some of the important aspects related to the seismic performance of offshore concrete gravity platforms. The emphasis in this research is on aspects related to the structural performance of platforms. Geotechnical problems are not considered in any detail.

The following gives a brief outline of the topics covered in this report.

In Chapter 2 fundamental concepts of dynamic analysis of structures are reviewed. Two problems which have particular importance in the analysis of offshore concrete gravity platforms, namely water-structure interaction and soil-structure interaction, are considered.

In Chapter 3 current seismic hazard analysis techniques are reviewed and up to date hazard analysis results are presented. Recommendations are made regarding appropriate acceleration response spectra which could be used for the design of platform structures in New Zealand.

Site response effects are investigated in Chapter 4. The relatively flexible materials often found at offshore sites could significantly amplify the ground motions expected on more competent materials. The site response effects of some well defined example sites are investigated using dynamic time-history computer analyses to examine the influence of flexible nonlinear soil deposits on seabed surface motions.

Methods are examined in Chapter 5 by which artificial earthquake accelerograms can be generated. A suite of artificial records is produced to match the acceleration response spectra estimated from Chapter 3 to be appropriate for the design of New Zealand offshore concrete gravity platforms.

Chapter 6 gives details of an experimental testing programme in which the strength and ductility characteristics of circular hollow concrete members were investigated. Offshore concrete platform designs have often incorporated such members and the six column members tested represented scale models of members which could be used in concrete platform configurations.

Details of a companion theoretical study of the flexural strength and ductility of hollow circular members are reported in Chapter 7. Cyclic moment-curvature analyses of sections were carried out using refined stress-strain models for confined concrete and reinforcing steels. Ranges of variables appropriate to members in offshore concrete platform structures were considered. Results are presented in chart form which would be convenient for use by designers.

In Chapter 8 possible philosophies for the seismic design of offshore concrete platform structures are advanced. Preliminary design studies are carried out for two possible platform configurations at a New Zealand offshore site, and their expected seismic performance is discussed.

Major conclusions from the research are given in Chapter 9, together with recommendations for future research.

Chapter 2

DYNAMIC ANALYSIS FOR SEISMIC RESPONSE OF OFFSHORE CONCRETE GRAVITY PLATFORMS

2.1 INTRODUCTION

Many structural design codes, for example the New Zealand loadings Code for the design of buildings NZS 4203 [2.1], require structures to be designed to resist earthquakes. Although earthquake shaking induces dynamic loading, structures are often designed using equivalent static loading patterns which are simple representations of the expected maximum dynamic effects. For many structures this approach is convenient and considered adequate. However, because of the extreme importance of very large offshore platforms it is appropriate that detailed dynamic analysis should be carried out. This will ensure that adequate protection is provided against earthquake induced damage and that reasonable predictions of the post-elastic behaviour can be made.

Offshore concrete gravity platform structures are among the largest engineered structures built by mankind. Dynamic analysis of these structures can be carried out using the same methods applied to other structural systems. An obvious complication arises because platforms are partly submerged in water and the interaction between the structure and water must be considered. Although many less important structures are analysed as if they were rigidly attached to the ground, it is expected that soil-structure interaction effects will also have a major effect on the dynamic response of concrete gravity platforms.

In this chapter fundamental concepts of dynamic analysis are reviewed, and various dynamic analysis methods which are available are discussed. Two problems which have particular importance for offshore concrete gravity platforms, namely, water-structure interaction and soil-structure interaction, are also considered.

2.2 DYNAMIC ANALYSIS FUNDAMENTALS

The aim of dynamic analysis is to predict the response of a structure to the dynamic loading. All such techniques involve modelling of the real structure by simple analytical models which can be represented mathematically. Dynamic analysis methods involve formulation and solution of the equations of motion of the mathematical model. Where the dynamic loading is prescribed a deterministic method of solution of the equations of motion can be sought. Normally the results required would be the displacement, velocity and acceleration response at various locations in the structure and the actions induced in the structural members. There are a number of important issues which must be considered in order to establish a reasonable structural model and in choosing a suitable method of analysis.

Choice of dynamic structural models necessarily involves simplification of the real structure being examined. Dynamic analysis methods discretise the structure into a finite number of degrees of freedom. The Finite Element Method is often used to model the structure as an assemblage of members, or elements between joints, or nodes. The degrees of freedom are normally the unknown displacements at the nodes and the equations of motion are set up to solve for the unknown displacement responses. The equations of motion for a multi-degree of freedom system can be written in matrix form as in Eqn. 2.1. They represent the equations of dynamic force equilibrium, with the resisting forces on the left hand side and the driving forces on the right hand side.

$$Ma + Cv + Kd = P(t) \qquad (2.1)$$

M, C and K are the mass, damping and stiffness matrices respectively. P(t) is the vector of loads associated with the chosen degrees of freedom and varying with time t. The time

dependent vectors a, v and d are the acceleration, velocity and displacement responses of the degrees of freedom.

The mass of structures is most often considered to be lumped at the nodes as translational and rotational inertia, and in that case the mass matrix M is diagonal. In most civil engineering structures the mass remains constant with time but in general it could be considered to vary. Consistent mass matrices [2.2] allow for the distributed nature of masses along members and are normally derived by considering the energies associated with the masses for each degree of freedom. These matrices are more fully populated than lumped mass matrices.

The global stiffness matrix K can be assembled from the stiffness matrices of the individual members. This is normally done using the Direct Stiffness Assembly Method [2.3]. For structures which remain linearly elastic during response to dynamic loading, the stiffness matrix remains constant. However, if structures undergo large displacements, or are excited into inelastic activity, the changes of the stiffness matrix during the dynamic response must be considered. Structures responding to large earthquakes will often be strained into the inelastic range and nonlinear analysis methods are required to accurately predict their response.

It is clear that the motion in dynamically responding structures is damped but the actual mechanisms of damping are not well understood. The second term in Eqn. 2.1 define linear viscous damping forces proportional to the velocity of the degree of freedom. This assumption is normally made as the equations of motion remain linear, and a suitable choice of damping matrix allows the equations of motion to be solved more easily. Equivalent viscous damping levels have been estimated from forced vibration studies of typical civil engineering structures [2.4].

The equations of motion can be solved for the displacement response by various methods, either in the time domain or the frequency domain. In general the equations are coupled and must be solved simultaneously. Analysis in the time domain involves step by step integration of the equations. In the frequency domain analysis the arbitrary load function is considered as the superposition of many harmonic components by taking its discrete Fourier transform. The steady-state response of the structure to each of the Fourier components is derived and superposed. With the use of Fast Fourier Transforms the frequency domain analysis can be computationally very efficient. It also has advantages when analyses of soil structure interaction problems are being dealt with. Complex valued compliance functions can be incorporated in the analysis to represent soil flexibility and damping effects. For nonlinear structures the frequency domain solution is not possible and time domain solution methods must be used.

2.2.1 Base Excitation Loading

In the case of earthquake excitation there are no applied loads to the structure. Rather, the structure responds to the excitation motion of the ground. The total motion of the structure can be considered as the motion of the ground plus the motion of the structure relative to the ground. The inertia force depends on the total acceleration of the degrees of freedom but the damping and elastic forces are assumed to be dependent only on the relative velocity and displacement. The equation of motion for a "rigid-base" structure can be written as is Eqn. 2.2 and rearranged to give Eqn. 2.3.

$$M\{r\,a_g + a\} + Cv + Kd = 0 \qquad (2.2)$$

$$Ma + Cv + Kd = -Mr\,a_g(t) \qquad (2.3)$$

The quantity $a_g(t)$ represents the known ground translation acceleration time history and r is the vector of displacements associated with unit displacements of the base of the structure. Where rotation of the base can take place the r vector terms would be linear functions of the horizontal and vertical distances of the nodes from the centre of rotation. Normally the ground motion would be a recorded horizontal or vertical accelerogram component. Eqn. 2.3 is

then in the same form as Eqn. 2.1 except the quantities a, v and d are then relative motion responses to be solved for. The term on the right hand side of the equation is the effective load vector.

2.2.2 Dynamic Modal Superposition Analysis

The equations of motion are in general a set of linear coupled equations with the number of unknowns and number of equations equal to the chosen number of degrees of freedom. It can be shown that with a suitable choice of the damping matrix the equations of motion can be uncoupled by transformation to the normal coordinates of the elastic structural system. The normal modes are the eigenvectors derived from the equations of undamped free vibration and the natural frequencies are functions of the associated eigenvalues. The normal modes are a linearly independent set of vectors and so form a basis for the displacement field. Any deformed shape in the real coordinate system can be represented as a linear combination of the normal modes. The scalar quantities by which the normal modes are multiplied are referred to as the modal amplitudes.

The equations of motion can be solved with much less computational effort in the modal coordinates, as the equations are uncoupled and can be solved independently, and often not all modes of response need to be considered. Once the modal responses have been found the responses in the actual coordinate system can be determined by inverting the coordinate transformation. The principle of superposition, applicable to linear elastic structures, is then used to add the responses from all of the normal modes to determine the total dynamic response.

The steps involved in carrying out a modal superposition analysis are :

1. Formulation of the structure mass and stiffness matrices
2. Calculation of the normal modes and frequencies
3. Formation of the generalised mass, damping and stiffness matrices, and the generalised load vector
4. Solution of the uncoupled equations of motion in the modal coordinates
5. Transformation of the modal responses back to structural coordinates
6. Superposition of the responses from each normal mode

The equations of motion will only uncouple if the damping matrix has a suitable form. Rayleigh showed that the equations will uncouple if the damping matrix is a linear combination of the mass and stiffness matrices. In this case the damping matrix exhibits properties of orthogonality with respect to the mode shapes, as do the mass and stiffness matrices. It can be shown that Rayleigh damping results in a hyperbolic variation of the proportion of critical damping with modal frequency. Because little is known about the mechanisms of structural damping, the Rayleigh damping model is often used in modal superposition analyses as it is convenient to apply .

In analyses including soil-structure interaction effects it is often required to model the radiation damping effects with the use of dashpot members incorporated at the foundation of a structural model. The introduction of the additional damping terms into the global damping matrix invariably results in the damping becoming non-proportional, that is, the damping matrix is no longer a linear combination of the mass and stiffness matrices. In that case the equations of motion do not uncouple using the undamped free vibration mode-shapes. This problem is discussed in detail in Section 2.4.

Modal superposition analyses can really only be used for the response analysis of linearly elastic structures. For non-linear elastic or inelastic structures modal analyses are not strictly valid although approximate response predictions for such structures can be obtained by estimating equivalent linear properties.

2.2.3 Response Spectrum Analysis

In the modal superposition analysis method an actual accelerogram record is input and used to determine the effective loading function. The modal responses are calculated separately and combined. The maximum response in each mode will in general occur at different times through the dynamic response. Response spectrum techniques allow the maximum response to be predicted directly from the modal properties of the system and the calculated response spectrum [2.3] of the earthquake accelerogram. It is thus possible to predict the maximum response in each mode and to estimate the maximum response which would be obtained from the superposition of modal responses. This can be done by various simple combination schemes. Probably the most common of these is the so-called Square Root of Sum of Squares (SRSS) method. Any maximum response quantity (displacement, velocity, member force, base shear etc) of interest is calculated for each mode based on the required response spectrum. The likely maximum from the combined modal responses is then estimated by summing the squares of the modal maxima and taking the square root. The method attempts to recognise that it is unlikely that all modal maxima will occur simultaneously but some modes could combine unfavourably. The SRSS combination method has been found to give reasonable estimates of the maximum response obtained by including all normal modes. Other modal combination methods are also available. It should be noted that it is often not necessary to consider responses of all modes of vibration of the structural model. Normally satisfactory predictions of overall response can be obtained by considering only a few dominant modes.

The steps involved in carrying out a response spectrum analysis are:

1. Formulation of the structure mass and stiffness matrices
2. Calculation of the normal modes and frequencies
3. Formation of the generalised mass and stiffness matrices
4. Computation of the maximum modal response quantities using the response spectrum
5. Transformation of the maximum modal responses back to structural coordinates
6. Combination of the maximum responses from each normal mode

A response spectrum analysis will in general require less computational effort than a full modal superposition analysis. Damping is allowed for in the analysis method in the response spectrum itself. For example, it is common to specify approximately 5 percent of critical damping in building structures. The acceleration (or velocity or displacement) response spectrum for 5 percent damped structures responding to the required earthquake accelerogram would be calculated and used as the input response spectrum to the analysis.

The limitations of the response spectrum analysis method are as for the modal superposition method except that the maximum results predicted are only estimates of the combined modal responses.

2.2.4 Analysis of Nonlinear Structures

Accurate response analysis of nonlinear structures can only be obtained using nonlinear analysis techniques. Because the stiffness matrix changes with time in the nonlinear structure, the normal modes and frequencies also change and modal analysis techniques are no longer suitable for the response analysis. In addition, the principle of superposition can only be applied to linear structures, so solution of the equations of motion for nonlinear structures is not possible in the frequency domain.

Approximate dynamic analyses are often carried out on nonlinear structures by assuming some equivalent linear properties to be appropriate. For example, in reinforced concrete structures cracking can reduce the flexural stiffness of the members significantly. When carrying out dynamic analysis of reinforced concrete structures it is common to specify the estimated cracked flexural stiffnesses. A dynamic modal analysis is then carried out assuming linear elastic response. This is the so-called Equivalent Linear Method.

Dynamic analysis of structures which dissipate energy by hysteretic effects, such as inelastic yielding, can also be achieved approximately using the Equivalent Linear Method. Although hysteretic damping cannot be incorporated in a linear analysis it is possible to include additional viscous damping in the dynamic model. Appropriate secant stiffnesses and damping levels may be difficult to estimate though, and the accuracy of the equivalent linear method is likely to deteriorate as the degree of nonlinearity increases. An example of this method is presented in Chapter 4 in which it is attempted to predict the nonlinear response of soil deposits over bedrock during earthquake shaking.

Many structures will display strongly nonlinear behaviour during response to earthquake excitation. The only way to accurately predict response is by nonlinear dynamic analysis using step by step solution methods in the time domain. The incremental form of the equations of motion is set up and the solution procedes in a series of small time increments using the tangent stiffness matrix. At each time step the actions in the members are determined. If a change in the stiffness of any member is found then the global tangent stiffness matrix is updated. It is possible to follow the nonlinear response of structures very accurately using this approach. Detailed nonlinear load-deformation behaviour of members can easily be incorporated.

Nonlinear dynamic analysis is computationally expensive compared with modal analysis and response spectrum methods. There are also numerical difficulties which arise, such as the load overshoot problem, which is due to sudden stiffness changes in a structure. These can generally be overcome by choosing a suitably small time step for the analysis.

In any dynamic analysis in the time domain the time step chosen should be small enough so that the response of the structure can be accurately followed. One criteria which has been suggested is that the time step should be no greater than about one quarter of the shortest significant natural period of the system. If the time step is too large the contribution of high frequency components is filtered out, but often without drastic loss of accuracy. However, for some structural systems the contributions of higher mode effects may be important. It has been suggested [2.5] that higher modes may be excited more in inelastically responding structures.

When developing finite element models for the dynamic analysis of structures it is necessary to decide how the real structure should be represented by a simple mesh of nodes and elements. In general, a larger the number of members will give a more accurate solution, though requiring more computational effort. A finer mesh will result in a larger number of high frequency modes of response being modelled. The mesh size can be related to the maximum frequency of motion for which accurate response will be obtained and the elastic wave propagation speeds in the structure. Consider, for example, modelling the dynamic response of a continuous shear beam of finite length. A dynamic analysis model can be chosen with several shear beam members placed end to end. If accurate predictions of the motion of a particular frequency are required, then the length of the shear beams would have to be chosen small enough so that the length multiplied by the required frequency is less than the shear wave velocity in the material. It would also be necessary to select a time step for the analysis which is a suitably small fraction, say one quarter or less, of the period of vibration corresponding to the required frequency. In structures which respond inelastically the problems of choosing suitable mesh size and time step are compounded. Sensitivity studies can be carried out but the choice is often made on the basis of experience and engineering judgement.

A computer program developed by Sharpe and Carr [2.6], for the dynamic analysis of inelastic plane frame structures subject to earthquake excitation, was used extensively in this research.

2.3 WATER - STRUCTURE INTERACTION EFFECTS IN OFFSHORE CONCRETE GRAVITY PLATFORMS

Water-structure interaction effects are extensively reported in the literature, mainly with regard to wave loading on offshore platform structures. Many of the principles are the same in considering the earthquake response of submerged structures but there is a fundamental difference. In the wave loading case the structure is essentially stationary and the water is in

motion whereas, in the earthquake response case, the structure is moving and the surrounding water is essentially still.

Wave forces on submerged objects can be calculated using the Morison equation [2.7]. The application of the Morison equation to wave loading is discussed more fully in Chapter 8 and only a brief description is given here. The force per unit length F exerted on a stationary submerged cylindrical body with cross-sectional area A and diameter D by a fluid with mass density ρ is given in Eqn. 2.4. The quantities a and v are the instantaneous fluid acceleration and velocity.

$$F = C_i \rho A a + 0.5 C_d \rho D v^2 \qquad (2.4)$$

The first term is a linear inertia force and C_i is the inertia coefficient. The inertia force can be thought of as having two components. The quantity $C_i \rho A$ represents the virtual or effective mass of fluid displaced by the cylinder and can be divided into the actual displaced fluid mass and an added fluid mass which is entrained to the stationary cylinder. The second term in the Morison equation is the nonlinear drag force and C_d is the drag coefficient. Because the fluid velocity and acceleration are out of phase with each other the maximum inertia and drag force components are also out of phase.

Inertia and drag coefficients have been obtained for various shapes of submerged object from experimental and theoretical research. The values have varied considerably but it seems that for wave loading on cylindrical shaped members they may conservatively be taken as the values given in Eqns. 2.5 and 2.6 [2.7].

$$C_i = 2.0 \qquad (2.5)$$

$$C_d = 1.0 \qquad (2.6)$$

For large members, such as those used in concrete offshore platforms, the inertia forces dominate and it is reasonable to ignore the drag terms [2.8].

Various wave theories are available for determining the spatial and temporal variations of water particle acceleration and velocity. These can be used in conjunction with the Morison equation to determine the distribution of forces induced on submerged members.

For the earthquake response of submerged structures it is also found that the viscous drag terms are small and the inertia terms dominate the water interaction effects. Because the water surrounding towers is assumed to be still, the inertia term in the Morison equation includes only the added mass component. The so-called Froude Krylov force obtained from the displaced mass of water multiplied by the acceleration of the surrounding water reduces to zero. Thus the simplest method for dealing with water-structure interaction effects is to combine the added water mass with the structural mass.

The earthquake response of axisymmetric tower structures surrounded by water was investigated in detail by Liaw and Chopra [2.9]. A computer analysis program EATSW was developed as part of that research for calculating the elastic time history response of partly submerged axisymmetric towers to an input earthquake accelerogram. For general non-cylindrical structures the water interaction problem was solved using a finite element representation of the surrounding water. For uniform cylindrical towers analytic solutions are available and are incorporated in the program.

In the theoretical treatment of fluid around a submerged moving structure potential theory is used in which the water is assumed to be incompressible and inviscid, and flow around the moving tower is assumed to be irrotational. In the fluid domain the Navier Stokes Equations of fluid motion reduce to the Laplace Equation with boundary conditions of zero pressure at the free surface and no flow across the physical boundaries at the seabed and tower surfaces. There is good agreement between the potential theory predictions and experimental data which has led to the conclusion that potential theory adequately describes the water

structure interaction effect [2.10]. The analysis of non-cylindrical tower structures by the computer program EATSW requires that an axisymmetric finite element mesh is set up around the tower to represent the water. The program uses a substructuring approach in which the tower and surrounding water are considered as separate substructures. The contributions of water mass to the structure are found using potential theory. The response of the tower is calculated in modal coordinates, with only the first few modes being considered to contribute to the overall response.

From the analytic solutions obtained for cylindrical towers Liaw and Chopra derived distributions of added mass. Similar distributions were derived by Liaw and Reimer [2.11] and are shown in Fig. 2.1. $m_a(z)$ is the added mass per unit length of cylinder, z is the distance measured vertically upwards from the seabed, ρ is the mass density of the the surrounding water, r is the radius of the cylinder and d is the undisturbed depth of water. For the case where the radius of the cylinder is less than about one tenth of the water depth, the added mass is very close to displaced mass of water over most of the submerged height of the tower. Close to the free surface the added mass reduces rapidly to zero. For cylindrical members with a large radius relative to the water depth, the added mass coefficients are significantly less than unity and also reduce to zero at the free surface, but more gradually.

The research on hydrodynamic added mass effects by Liaw and Chopra was applied by Liaw and Reimer [2.11] to the legs of deepwater offshore platforms. That work examined three different approaches to the problem of hydrodynamic interaction to determine the limitations of simple added mass methods. Three shapes of platform leg and dynamic loadings ranging from low frequency wave loadings to high frequency earthquake loadings were considered. In the simplest approach the added mass was taken as simply the displaced mass of water per unit length. In the second approach the free surface effects were considered and added mass corresponding to the analytic distributions for cylinders derived by Liaw and Chopra, given in Fig. 2.1, were used. For the third approach interaction considering the deformability of the tower, such as done in the computer program EATSW, was considered. It was concluded that for slender legs subject to low frequency loading even the simplest approach gave satisfactory results. However, for less slender legs subject to high frequency excitation it was found that the more detailed approaches were necessary.

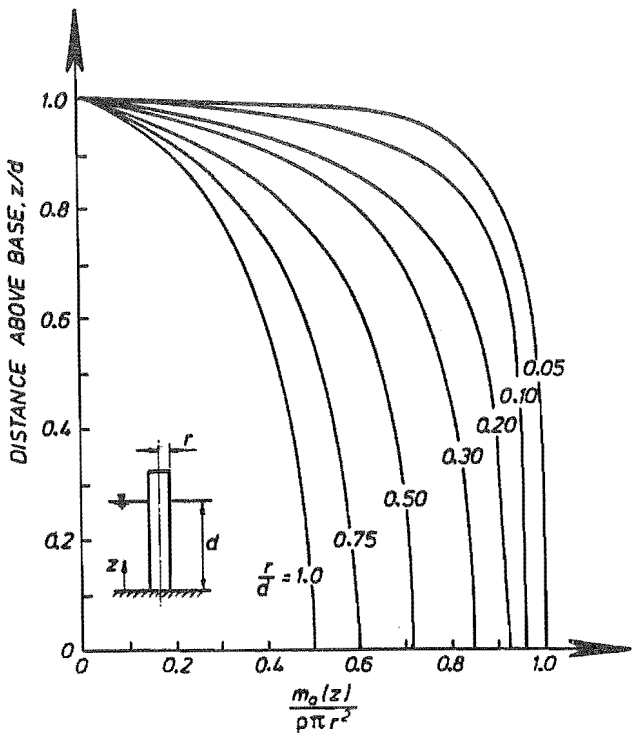

Fig. 2.1 Distributions of Added Water Mass for Cylindrical Members

The deepwater platform legs considered in the work by Liaw and Reimer were combinations of cylindrical and tapered sections and were similar to the shapes of legs used in many of the North Sea platform structures. However, the effect of the massive bases, typical on these platforms, was not considered. It was therefore decided to undertake further work as part of this study to investigate the hydrodynamic interaction of a complete base and leg combination. The aim of this study was to check whether the simple added mass approaches were still appropriate.

Simple test analyses were set up to compare the results of the analysis using the program EATSW with another dynamic analysis program not set up specifically to allow for water-structure interaction effects. The other program was a time history analysis program RUAUMOKO developed at the University of Canterbury [2.6] for the analysis of plane frame structures. Water-structure interaction was allowed for by using the added mass curves in Fig. 2.1.

For the first test analysis a 100 m high cylindrical concrete tower was chosen with an outside diameter of 10 m and a wall thickness of 2 m. The tower was considered to be standing in 100 m of water and rigidly attached at the base. This could be thought of as being a simplified model of a single leg of an offshore concrete platform structure. An analysis was carried out using each of the programs EATSW and RUAUMOKO for the first 10 seconds of the North-south component of the El Centro record of the 18 May 1940 Imperial Valley, California earthquake. The dynamic analysis models used for each of the programs are shown in Fig. 2.2. For the program EATSW the members were axisymmetric finite elements whereas for the program RUAUMOKO simple flexural members were used. The lateral displacement predicted at the top of the tower by the two programs is shown in Fig. 2.3. Theoretically both analyses should have given almost exactly the same response but the agreement obtained is considered excellent.

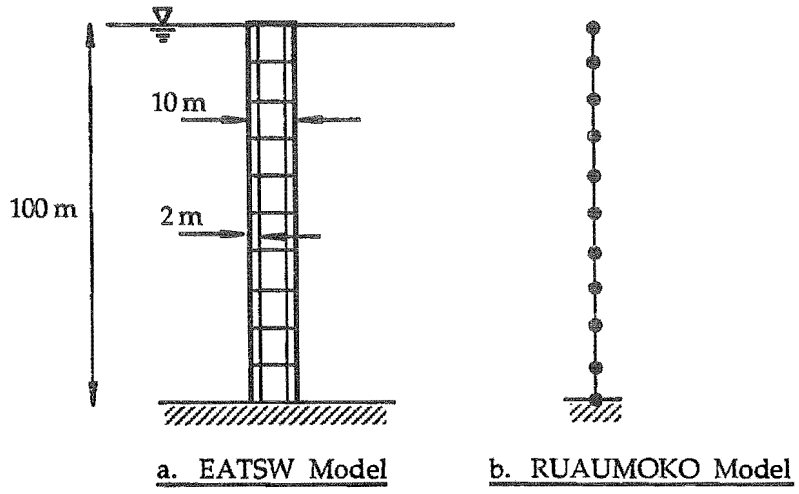

Fig. 2.2 Simple Cylindrical Tower - Dynamic Analysis Models

A second test analysis was conducted on the structure depicted in Fig. 2.4. The shape of this structure is similar to the submerged portion of a North Sea type concrete gravity platform. The base was chosen to be 40 m high and 50 m in diameter. The leg portion had a 10 m outside diameter with a wall thickness of 2 m and extended 60 m above the base to the water surface. Because this was a non-cylindrical tower, the mesh of fluid finite elements shown in Fig. 2.4a was set up for the analysis using the water-structure interaction program, EATSW. The added water mass effects were evaluated in the analysis using the finite element method.

The structural model used for the other program, RUAUMOKO, is shown in Fig. 2.4b and is a stack of ten simple flexural members. The properties of the lower members were chosen to represent the base, and those of the upper members to represent the slender tower. The added

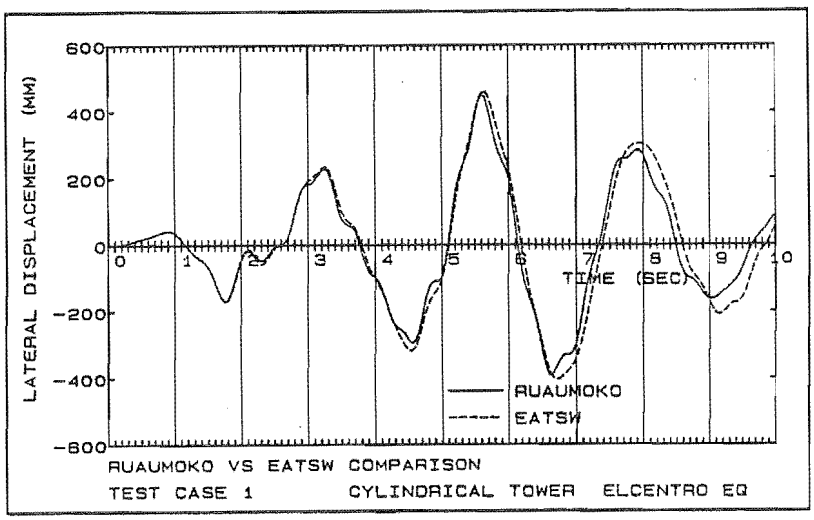

Fig. 2.3 Response of Cylindrical Tower Surrounded by Water

water masses at each of the nodes were determined from Fig. 2.1 by considering the curve appropriate to the radius of the tower at the position of each nodal point. Thus over the lower 40 m base height the curve for r/d = 0.25 was used and for the upper 60 m the curve for r/d = 0.05 was used.

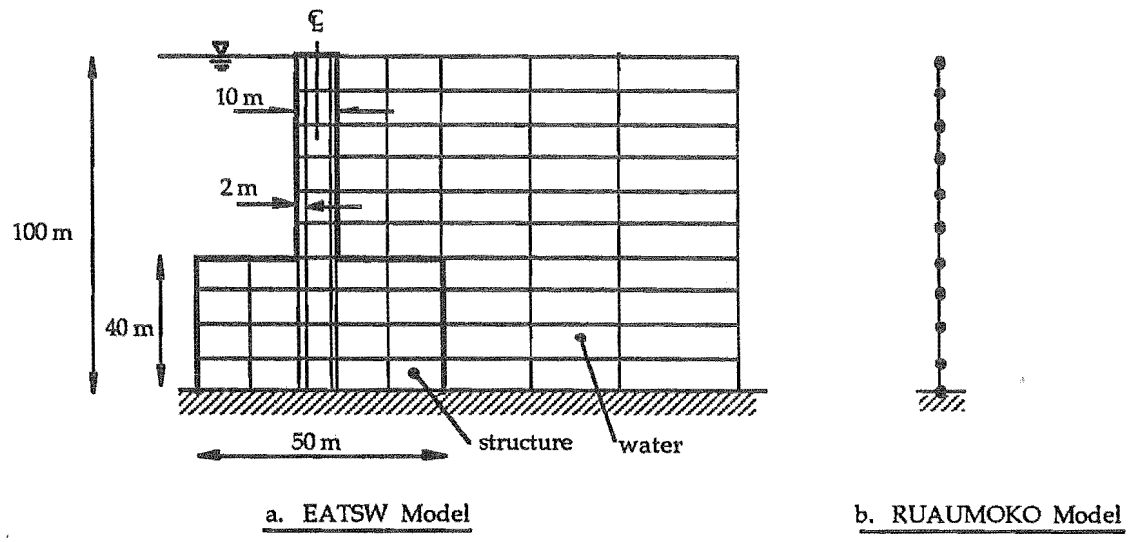

Fig. 2.4 Non-Prismatic Tower - Dynamic Analysis Models

An analysis was carried out using each of the programs for the first 10 seconds of the El Centro earthquake record. A comparison of the displacement responses predicted by each analysis at the top of the tower is shown in Fig. 2.5. The results are quite close with less than 10 percent difference in maximum displacement, bending moment at the base, and base shear.

From this analysis it appears that quite accurate estimates of water-structure interaction effects can be made using the simple cylindrical tower added mass curves by Liaw et al, even for submerged structures with discontinuous profiles such as those encountered in the North Sea type of offshore concrete gravity platform. It is recommended that these curves be used where the member diameters are larger than about 10 percent of the water depth, rather than simply adding the displaced mass of water.

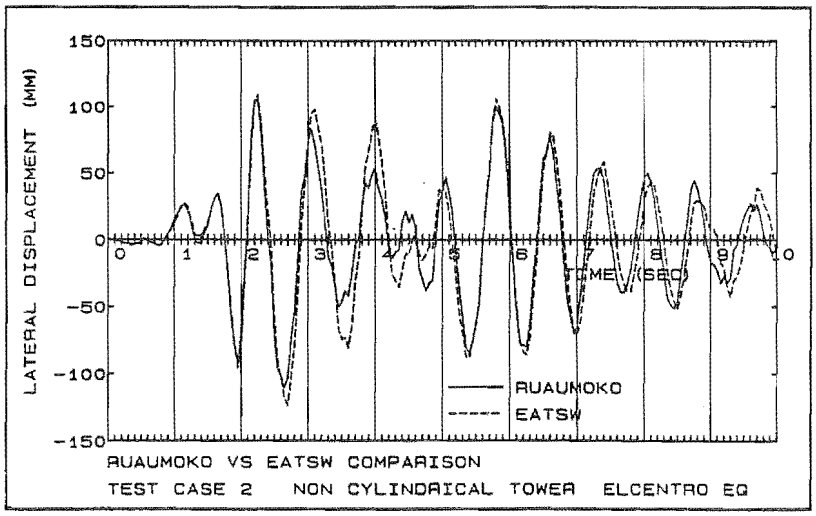

Fig. 2.5 Response of Non-Prismatic Tower Surrounded by Water

2.4 SOIL - STRUCTURE INTERACTION EFFECTS IN OFFSHORE CONCRETE GRAVITY PLATFORMS

2.4.1 General Effects of Soil-Structure Interaction

It is expected that soil structure interaction effects could significantly modify the response of offshore concrete gravity platforms during earthquake excitation. The principal effects of this interaction are the compliance of the the foundation and the loss of kinetic energy from the structure into the surrounding soil. Foundation compliance will lengthen the periods of vibration of the structure which will often lead to a reduction in the level of the response accelerations. The effects of this compliance can be modelled in a dynamic structural analysis by including foundation spring members with appropriate flexibilities.

Kinetic energy which is transmitted back into the surrounding soil may be radiated away to the far-field by propagating stress waves and will eventually be dissipated by the effects of internal soil friction and nonlinear hysteresis. The radiation and dissipation losses can be considered as a single effect called "radiation damping". This can be conveniently modelled in a dynamic structural analysis by the inclusion of viscous dashpots at the structure-soil interface. Appropriate damping coefficients can be chosen to model the energy loss.

2.4.2 Frequency Dependent Compliance Functions

A number of researchers [2.4, 2.12-2.14] have examined theoretically the steady-state response of a harmonically loaded massless rigid disk supported on the surface of a homogeneous linearly elastic half-space. Complex valued, frequency dependent impedance functions have been derived assuming the rigid body displacement modes of the disk are independent. The present study was based on work presented by Veletsos and Verbic [2.14] which gives very similar results to those given by others.

The complex valued impedance functions consist of a stiffness component, being the real part, and a viscous damping component, which is the imaginary part. The impedance functions given by Veletsos and Verbic are of the form given by Eqn. 2.7.

$$Q_j = K_j \, (k_j + i a_o \, c_j) \, d_j \qquad (2.7)$$

where $i = \sqrt{(-1)}$ (2.8)

and $a_o = \omega r/c_s$ (2.9)

Q represents the harmonic force magnitude and d is the steady-state harmonic displacement amplitude. The subscript $_j$ represents any of the possible translational or rotational degrees of freedom. $K_j k_j$ is the real stiffness and $K_j i a_o c_j$ is the complex stiffness, or damping, term. a_o is a dimensionless frequency parameter given by Eqn. 2.9 as a function of the circular frequency ω, the radius of the equivalent circular footing r, and the shear wave speed in the soil c_s. The impedance function given by Eqn. 2.7 is frequency dependent with the coefficients k_j and c_j being functions of the dimensionless frequency parameter a_o. K_j represents the static (zero frequency) stiffness value and thus k_j is equal to unity for a_o equal to zero.

It is appropriate to recall the equations of motion for a single degree of freedom system as in Eqn. 2.10.

$$Ma + Cv + Kd = P(t) \tag{2.10}$$

It is noted that the velocity v and the acceleration a are the first and second derivatives of the displacement d, and the general solution to this second order ordinary differential equation is of the form given in Eqn. 2.11. The velocity can be written in terms of the displacement as in Eqn. 2.12 and the left hand side of the equation of motion can be rewritten as in Eqn. 2.13.

$$d(t) = A\, e^{i\omega t} \tag{2.11}$$

$$v(t) = Ai\omega\, e^{i\omega t}$$

$$= i\omega\, d(t) \tag{2.12}$$

$$Ma + Cv + Kd = Ma + iC\omega\, d + K\, d$$

$$= Ma + [K + iC\omega]\, d \tag{2.13}$$

Equating the real and imaginary stiffness terms in Eqns. 2.7 and 2.13 the stiffness and damping coefficients given in Eqns. 2.14 and 2.15 are obtained.

$$K = K_j k_j \tag{2.14}$$

$$C = c_j\, r/c_s K_j \tag{2.15}$$

The static stiffness values for horizontal translation K_h, vertical translation K_v and rocking about a horizontal axis K_θ are given by the expressions in Eqns. 2.16, 2.17 and 2.18.

$$K_h = 8\rho r c_s^2/(2\text{-}\nu) \tag{2.16}$$

$$K_v = 4\rho r c_s^2/(1\text{-}\nu) \tag{2.17}$$

$$K_\theta = 8\rho r c_s^3/3(1\text{-}\nu) \tag{2.18}$$

ρ, c_s and ν are the mass density, shear wave speed and Poisson's ratio of the half-space material respectively and r is the radius of the equivalent circular footing.

Values of the stiffness coefficients k_j and the damping coefficients c_j given by Veletsos and Verbic for horizontal translation, vertical translation and rocking modes are shown in Fig. 2.6. The dashed lines shown in the figure represent approximate relationships for which Veletsos and Verbic have derived analytic expressions. It should be noted that the horizontal

stiffness coefficient k_h is insensitive to frequency and Poisson's ratio and is taken as a constant. The horizontal damping term c_h is insensitive to frequency and is given as a constant depending on the value of Poisson's ratio. For the vertical translation and rocking modes the coefficients for both stiffness and damping are dependent on frequency and Poisson's ratio.

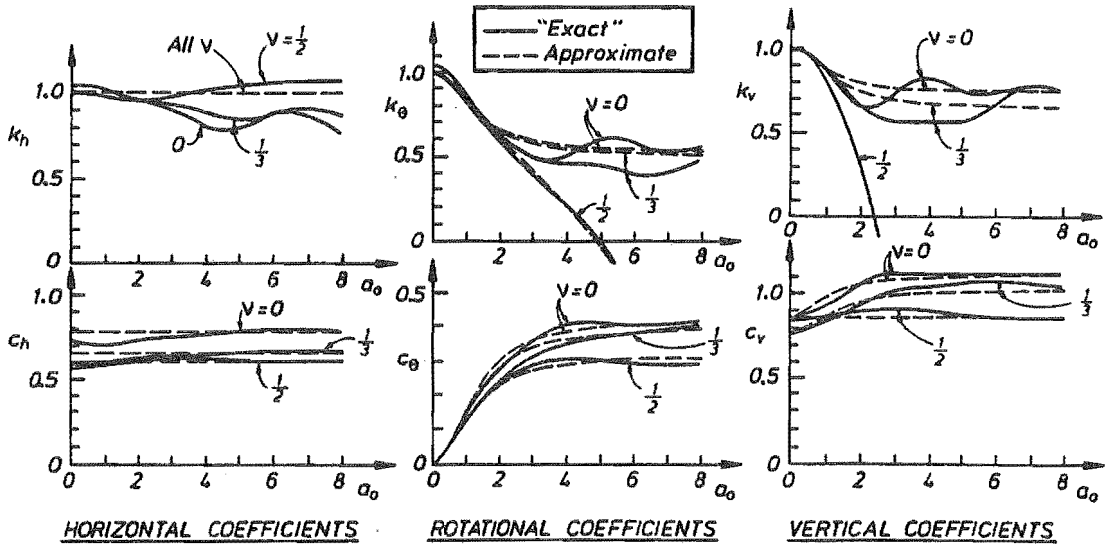

Fig. 2.6 Coefficients for Frequency Dependent Compliance Functions

As the foundation properties are frequency dependent, analysis of soil-structure interaction effects is particularly well suited to solution in the frequency domain. However, only elastic analyses can be performed in the frequency domain. Structures which are subjected to severe earthquake excitation will generally behave inelastically and dynamic analysis must be performed in the time domain. It is therefore desirable that the frequency dependent soil properties could be modelled in a time domain analysis using some constant valued properties.

It is possible that at each time step of a time domain analysis an instantaneous frequency could be estimated in each of the foundation compliance degrees of freedom from the calculated acceleration, velocity and displacement responses. From this frequency the foundation compliances could be reevaluated at each time step. However, this approach was not investigated in this study.

The following section describes a short study to investigate the use of constant, frequency independent soil spring and dashpot members to model the frequency dependent behaviour.

2.4.3 Analysis of Frequency Dependent Foundation Properties

To investigate the effect of the frequency dependence of the foundation behaviour on the response of typical offshore concrete gravity platform structures, a modal analysis procedure was used. A simple model of a North Sea type cantilever platform was studied, and foundation compliance was incorporated in the form of translational and rotational spring and dashpot members. The properties of the rotational spring and dashpot members were different in each of the normal modes, depending on the frequency of the particular mode.

In a conventional modal analysis procedure the equations of motion are uncoupled by a transformation to modal coordinates. For a system with n degrees of freedom this transformation is effected by a transformation matrix with its n columns being the normal modes of the structure. The mass and stiffness matrices reduce to diagonal matrices containing the generalised mass and stiffness terms for each mode. For a proportionally damped system, where the damping matrix is a combination of the mass and stiffness matrices satisfying the

Caughy Series [2.15], the transformation will also reduce that matrix to diagonal form. The n equations of motion are then uncoupled second order ordinary differential equations which may be solved independently for the response of each generalised displacement coordinate.

For the case where the damping is non-proportional, that is where the damping matrix is not a member of the Caughy series, the usual modal transformation will not uncouple the equations of motion, because in general the transformed damping matrix will not be diagonal. When additional dashpot members are incorporated in dynamic structural models to allow for radiation damping effects, then the damping is non-proportional and the conventional modal analysis method is not appropriate.

It is possible to arrange the equations of free vibration of a system with non-proportional damping to give a real symmetric dynamical matrix but the eigenvalues and associated eigenvectors are complex-valued.

2.4.4 Complex Modal Analysis Method

A procedure for the modal analysis of structural systems with non-proportional damping was presented by Hurty and Rubinstein [2.16]. In this method the equations of motion of the multi-degree of freedom system, Eqn. 2.19, are augmented by a second set of equations, shown as Eqn. 2.20.

$$Ma + Cv + Kd = P(t) \tag{2.19}$$

$$Mv - Mv = 0 \tag{2.20}$$

M, C and K are the mass, damping and stiffness matrices, a, v and d are the time dependent acceleration, velocity and displacement responses, and P(t) is the vector of time dependent applied forces. Although Eqn. 2.20 is apparently trivial it can be combined with Eqn. 2.19 in matrix form to give Eqns. 2.21 and 2.22.

$$\begin{bmatrix} 0 & M \\ M & C \end{bmatrix} \begin{Bmatrix} a \\ v \end{Bmatrix} + \begin{bmatrix} -M & 0 \\ 0 & K \end{bmatrix} \begin{Bmatrix} v \\ d \end{Bmatrix} = \begin{Bmatrix} 0 \\ P \end{Bmatrix} \tag{2.21}$$

$$[A]\{x\} + [B]\{y\} = \{Q\} \tag{2.22}$$

where $$\{x\} = \begin{Bmatrix} a \\ v \end{Bmatrix} \tag{2.23}$$

and $$\{y\} = \begin{Bmatrix} v \\ d \end{Bmatrix} \tag{2.24}$$

Eqn. 2.22 is known as the "reduced form" of the equations of motion and contains 2n equations, where n was the number of degrees of freedom of the original system. A and B are real symmetric matrices of order 2n. It should be noted that vector x is the time derivative of the vector y. The homogeneous equations obtained by setting the load vector Q, on the right hand side of the equations, to zero, are first order ordinary differential equations and have solutions of the type given by Eqn. 2.25.

$$\{y\} = \{y_o\} e^{pt} \tag{2.25}$$

hence $$\{x\} = p\{y\} \tag{2.26}$$

$\{y_o\}$ is a vector of scalars, p is a scalar, t is time and e denotes the exponential function. The homogeneous form of Eqn. 2.22 can be written as in Eqn. 2.27 and manipulated to give Eqns. 2.28 and 2.29.

$$p[A]\{y\} = -[B]\{y\} \tag{2.27}$$

thus $p\,[B^{-1}]\,[A]\,\{y\} = -[I]\,\{y\}$ (2.28)

and $[D]\,\{y\} = \lambda\,[I]\,\{y\}$ (2.29)

where $[D] = -[B^{-1}]\,[A]$ (2.30)

and $\lambda = 1/p$ (2.31)

This is an eigen-problem where D is the dynamical matrix of order 2n and is real but in general non-symmetric. I is the identity matrix of order 2n and λ is a scalar quantity. Solution vectors satisfying Eqn. 2.29 can be found using normal eigen-theory. The vectors y will be the eigenvectors and the corresponding scalar quantities λ will be the eigenvalues. The 2n eigenvectors and eigenvalues of the real non-symmetric matrix D will in general be complex-valued and occur in conjugate pairs. From the complex eigenvalues the damped frequencies of vibration of each mode can be calculated.

The eigenvectors are the linearly independent vibration mode shapes of the damped structure, and the eigenvalues are related to the frequency of vibration of each mode. The mode shapes can be shown to be orthogonal, just as for the eigenvectors of a real symmetric dynamical matrix obtained from a proportionally damped system. It should be noted from Eqn. 2.24 that the eigenvectors y contain n complex velocity components and n complex displacement components. Actual displacements of the degrees of freedom can be obtained by considering only the real part of the displacement components. The eigenvector components are not absolute quantities as the eigenvectors can be scaled arbitrarily.

The nonhomogeneous equations of motion (Eqn. 2.22) can be uncoupled by transforming to the complex modal coordinates using the transformation matrix Δ containing the eigenvectors in its columns. The transformation is shown in Eqn. 2.32.

$$\{y\} = [\Delta]\,\{z\} \tag{2.32}$$

Substituting this into Eqn. 2.22 and premultiplying by the transpose of Δ, Eqns 2.33 and 2.34 are obtained, where the vector w is the time derivative of the vector z.

$$[\Delta]^T[A]\,[\Delta]\,\{w\} + [\Delta]^T[B]\,[\Delta]\,\{z\} = [\Delta]^T\{Q\} \tag{2.33}$$

or $$[A^*]\,\{w\} + [B^*]\,\{z\} = \{Q^*\} \tag{2.34}$$

The matrices A^* and B^* are diagonal because of the orthogonality of the eigenvectors and the reduced equations of motion become 2n uncoupled first order ordinary differential equations in the modal coordinates. Each generalised equation of motion can be solved using normal solution procedures, such as evaluation of the convolution integral for the rth mode, as in Eqn. 2.35.

$$z_r(t) = 1/A^*_r \int_a^b e^{p_r(t-\tau)}\, Q^*_r(\tau)\, d\tau \tag{2.35}$$

The evaluation of these integral expressions is complicated slightly because the quantities z_r, A^*_r, p_r and Q^*_r are all complex-valued. Where the eigenvectors appear in conjugate pairs there are companion equations giving the conjugate responses $z_r'(t)$. For linearly elastic structures the principle of superposition can be used to combine the modal responses. Transformation back to the reduced form coordinates can be accomplished as in Eqn. 2.36.

$$\{y(t)\} = \sum_{r=1}^{n} [\{y^r\}\, z_r(t) + \{y^{r'}\}\, z_r'(t)]$$

$$= 2 \sum_{r=1}^{n} R_e\, \{y^r\}\, z_r(t) \tag{2.36}$$

where R_e represents the real part of the complex quantity and $_{r=1}\Sigma^{n}$ indicates summation on r from 1 to n.

As the eigenvectors {y} contain both velocity and displacement components, the velocity components can be ignored and only the displacement components need to be calculated. Thus the displacement response q(t) can be determined from superposition of only the displacement degrees of freedom in the lower half of the eigenvectors as indicated in Eqn. 2.37.

$$\{q(t)\} = 2\ _{r=1}\Sigma^{n}\ R_e\ \{q^r\}\ z_r(t) \qquad (2.37)$$

Substituting for z_r from Eqn. 2.35 we obtain Eqn. 2.38 which gives the time dependent displacement response vector.

$$\{q(t)\} = 2\ _{r=1}\Sigma^{n}\ R_e\ [\{q^r\}/A^*_r\ {}_a\int^b e^{P_r(t-\tau)}Q^*_r(\tau)\ d\tau] \qquad (2.38)$$

2.4.5 Computer Program For Complex Modal Analysis

A computer program CMODAN was written to carry out elastic dynamic response analyses of two-dimensional structures subject to earthquake excitation using the complex modal analysis procedure outlined in the section 2.4.4. The program was set up to analyse simple structures with foundation compliance modelled at the soil-structure interface in the form of horizontal and rotational springs and dashpots. The analytic expressions for the soil compliance functions given by Veletsos and Verbic [2.14] were incorporated in the program. Initially the program was arranged to perform analyses using constant valued foundation member properties based on a chosen value of the dimensionless frequency parameter a_0 (given by Eqn. 2.9). It was thus possible to compare the results with those predicted by an existing time domain dynamic analysis program.

The program used for comparison of the results was RUAUMOKO, described earlier in this chapter. This program incorporates viscous dashpot members with constant damping coefficients but cannot model frequency dependent behaviour. Only elastic analyses were required for this comparison.

A test structure was chosen in order to compare the predicted responses of the complex modal analysis program, CMODAN, with the existing time history program, RUAUMOKO. A simplified model of the Frigg TP1 platform, one of the North Sea concrete gravity platform structures, was used in these analyses. Fig. 2.7 shows the very simple structural model used. Only two nodes were used to represent the platform, with one node representing the deck and the other representing the massive base. Horizontal translational and rotational inertias were included at each node. The platform legs were modelled as a single prismatic member with properties which approximately matched the average properties of the actual leg system. Water-structure interaction was accounted for using the added mass approach outlined in section 2.3.

Soil-structure interaction was modelled using horizontal and rotational springs and dashpots at the base. The parameters chosen to model the foundation were: radius of footing r = 50 m, bulk density of soil ρ = 1600 kg/m^3, propagation speed of shear waves c_s = 300 m/s, and soil Poisson's ratio ν = 0.25. These figures were thought to be of the correct order of magnitude for typical seabed conditions which might be found off the coast of New Zealand.

Response to the north-south component of the 18 May 1940 Imperial Valley earthquake recorded at El Centro was predicted using the two computer programs. Foundation properties for both analyses were based on a dimensionless frequency value of a_0 = 1.0 corresponding to a natural frequency of about 1 Hertz. Fig. 2.8 shows the excellent agreement obtained for the horizontal displacement response. The small amplitude traces represent the response of the platform base and the large amplitude traces represent the displacement response of the deck. The solid curves were obtained from the program RUAUMOKO and the dashed curves were

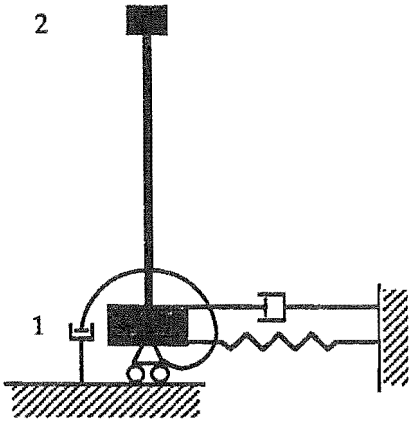

Masses: $M1 = 541 \times 10^6$ kg $MI1 = 337 \times 10^9$ kgm^2
$M2 = 17.9 \times 10^9$ kg $MI2 = 337 \times 10^9$ kgm^2

Shaft: $A = 40$ m^2 $I = 600$ m^4 $E = 30$ GPa
Height = 80 m

Foundation: $\rho = 1600$ kg/m^3 $c_s = 300$ m/s
$r = 50$ m $\nu = 0.25$

Fig. 2.7 Simple Model of Cantilever Type Offshore Concrete Gravity Platform and Foundation

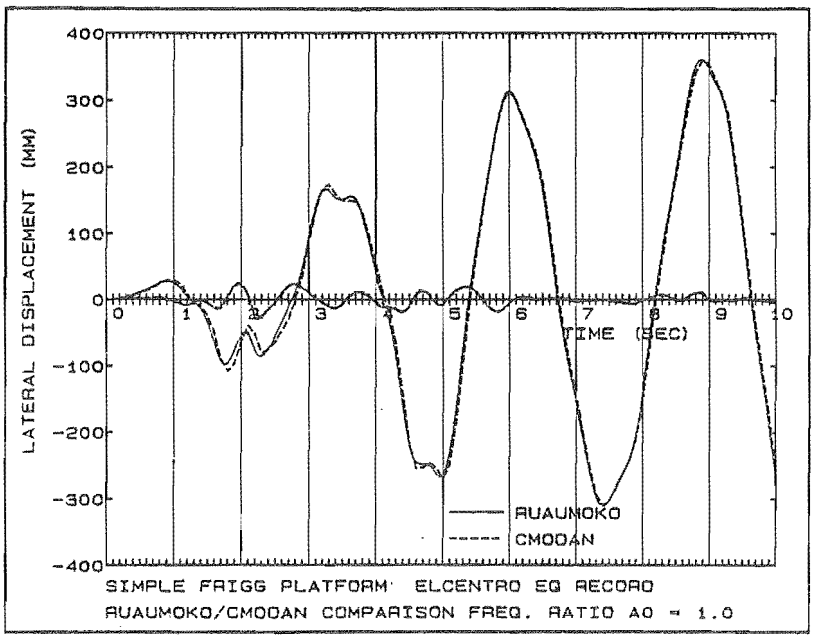

Fig. 2.8 Frequency Independent Soil/Structure Interaction Response

predicted by the program CMODAN. Comparison of the rotational responses indicated very close agreement also.

Member force response histories were not calculated as part of the complex modal analysis. However, as the displacement responses were so close, and the mass and stiffness distributions were identical, then the member force response histories must also have been very similar. It was possible to calculate the overturning moment and horizontal lateral load induced on the foundation by multiplying the rotational and translational displacements by the appropriate stiffness factors. The foundation loadings calculated in this way were in very close agreement with the results predicted by the existing time history analysis program.

The complex modal analysis program was extended to include the effects of frequency dependence of the rotational spring and dashpot foundation members. An iterative procedure was necessary to determine the rotational spring stiffness and dashpot coefficient appropriate for each mode of vibration. This procedure converged quickly, usually within three cycles, as most of the modal frequencies were not significantly affected by the variations in spring and dashpot properties. The complex frequency dependent modal

analysis computer program, CFMODAN, was used to determine the response of the same simple platform model and earthquake record as had been used for the earlier frequency independent analysis.

Comparison analyses were carried out between CFMODAN and the conventional dynamic time history program RUAUMOKO. Foundation member properties were based on a range of values of the dimensionless frequency ratio parameter from a_0 = 0.0, the static value, up to a_0 = 5.0, the effective high frequency limit. It was found that the translational displacement response of the the deck and base remained almost unchanged for the whole range of frequency values used. Fig. 2.9 shows a typical plot of horizontal displacement response of the simplified platform predicted by the two analysis programs. For the results shown, the conventional time history program analysis was based on a frequency parameter having a value of a_0 = 1.0. The small displacement traces, with amplitude up to about 25 mm represent the response of the platform base and the large displacement traces give the response at the deck level. Horizontal displacement response was evidently insensitive to the frequency dependence of the foundation stiffness and damping properties. This was apparent from the constant values of the horizontal stiffness and damping coefficients shown in Fig. 2.6.

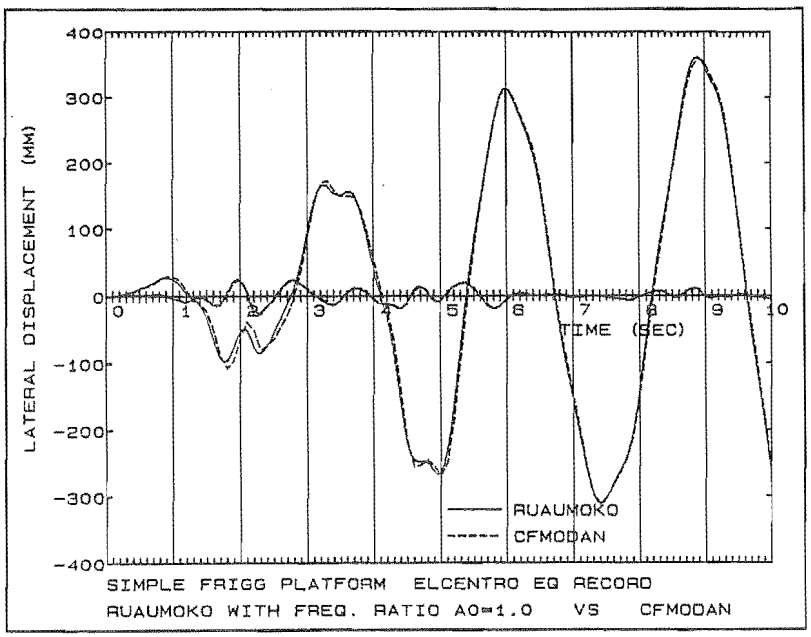

Fig. 2.9 Frequency Dependent Soil/Structure Interaction Response

Rotational displacements of the platform base were found to be quite sensitive to the frequency dependence of the foundation properties. This follows from the large variation in the rotational compliance coefficients, which were shown in Fig. 2.6. The rotational spring stiffness varies by a factor of about two and the rotational dashpot coefficient varies from zero for a_0 = 0. to a maximum at about a_0 = 4.0. Results of the analyses using constant foundation member properties based on various values of the dimensionless frequency ratio parameter a_0 indicated that the base rotations followed a very similar trend but varied in amplitude. Maximum base rotations were predicted for the analysis based on low frequency (a_0= zero) foundation properties. Amplitudes of the base rotations decreased with increasing values of a_0 and were only about 70 percent of the maximum when the high frequency (a_0 = 5.0) foundation properties were used.

The influence of the frequency dependence of the the soil properties on the damped modal periods of vibration of the simple soil-platform system can be seen in Table 2.1. There were four periods of vibration as there were four degrees of freedom considered in the system. Mode

4 displayed the greatest rotational response at the base and the period of this mode was affected the most by the foundation frequency dependence.

Table 2.1 Influence of Frequency Dependence of Soil Properties on Damped Modal Periods of Vibration of Simple Platform Model

$a_o = \omega r/c_s$	Damped Modal Periods (seconds)			
	Mode 1	Mode 2	Mode 3	Mode 4
0.0	2.819	0.904	0.561	0.451
1.0	2.822	0.904	0.560	0.515
3.0	2.829	0.904	0.557	0.701
5.0	2.830	0.904	0.557	0.786

The rotational displacement response of the base predicted by the complex frequency dependent modal analysis program CFMODAN was smaller than responses predicted by the programs CMODAN and RUAUMOKO which both used constant foundation properties based on the particular frequency ratios between $a_o = 0.0$ and $a_o = 5.0$. The maximum base rotations using the frequency dependent analysis were generally only about half of those predicted using the low frequency (a_o = zero) foundation properties.

It should be noted that the apparent large variation in base rotation response had little effect on the translational response of the platform deck. Over the assumed 80 m height of the legs maximum base rotations contributed only about 10 mm horizontal displacement at the deck level. This was quite small compared with the maximum lateral deck displacements of approximately 350 mm.

For the complex frequency dependent modal analysis program CFMODAN the force responses in the foundation springs were calculated in a similar manner as they had been for the frequency independent analysis. However, as the rotational spring stiffness varied with frequency, and was thus different in each mode, it was necessary to compute the force response in each mode before combining to give the total. Fig. 2.10 shows the response histories of foundation overturning moment predicted by the program CFMODAN and also by the conventional time history analysis program RUAUMOKO with foundation properties corresponding to low frequency ($a_o = 1.0$) and high frequency ($a_o = 5.0$) values. Clearly the results from the constant frequency RUAUMOKO analyses bracket the frequency dependent response. This indicated that the frequency dependent response could be matched more closely by choosing properties based on a constant frequency ratio somewhere between the values already tried.

Inspection of the base rotation or foundation overturning moment (Fig. 2.10) traces showed two dominant response frequencies. The first corresponded to the lateral motion of the deck, with large deck displacements resulting in significant base rotation. The second was a higher frequency motion corresponding to the rocking motion of the base itself. A further analysis was carried out using the program RUAUMOKO with foundation properties based on this rocking motion frequency which gave $a_o = 1.87$. The resulting foundation overturning moment response is shown in Fig. 2.11 together with the response predicted by the complex frequency dependent modal analysis program CFMODAN. There is very close agreement between the two responses with most of the peak response values being within a few percent of each other.

It appears that the frequency dependent analysis can be very well approximated by using suitably chosen constant valued foundation properties in a time domain analysis procedure. This is similar to the "tuning procedure" described by Watt et al [2.17].

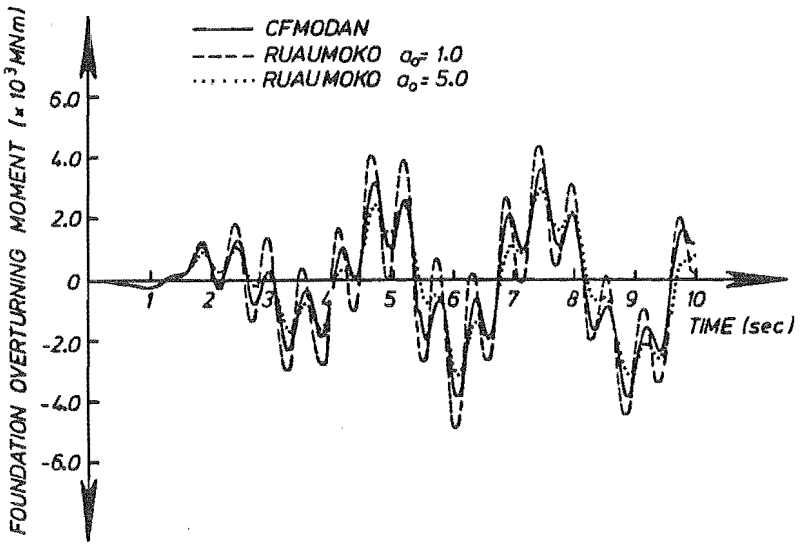

Fig. 2.10 Comparison of Induced Moment on Foundation from Complex Frequency Dependent Modal Analysis and Time Domain Analyses

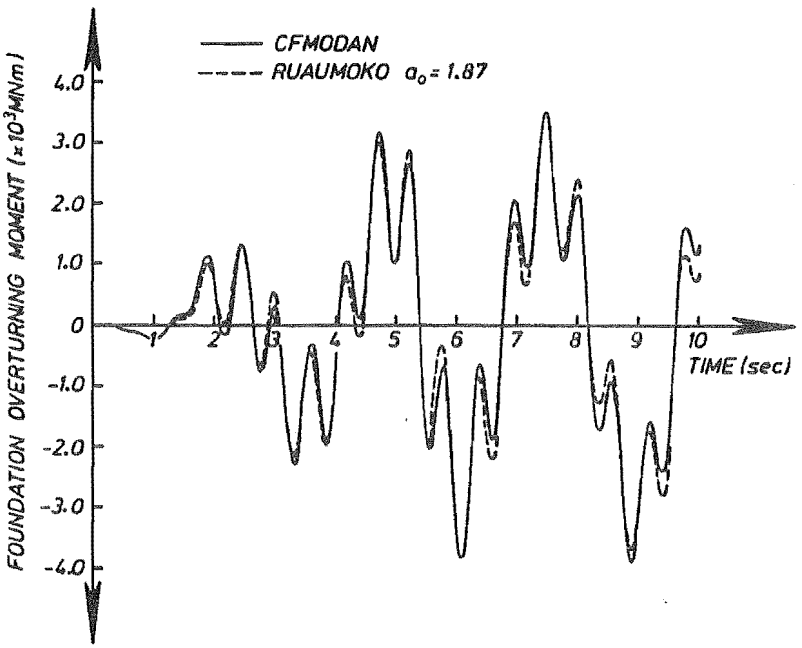

Fig. 2.11 Comparison of Induced Moment on Foundation from Complex Frequency Dependent Modal Analysis and Tuned Dynamic Time History Analysis

Although the time domain analysis could be tuned to give excellent agreement with the frequency dependent analysis for foundation overturning moments, no such agreement could be obtained for base rotations. Fig. 2.12 shows the base rotation responses predicted by the two analysis programs CFMODAN and RUAUMOKO. The latter used foundation properties based on a_0 = 1.87 which had been found to tune the frequency independent analysis for overturning moment. Approximately 25 percent difference in the peak rotations was predicted by the two analyses. There does not appear to be a simple explanation as to why the analysis could be tuned to give good agreement for overturning moment response but not for base rotations.

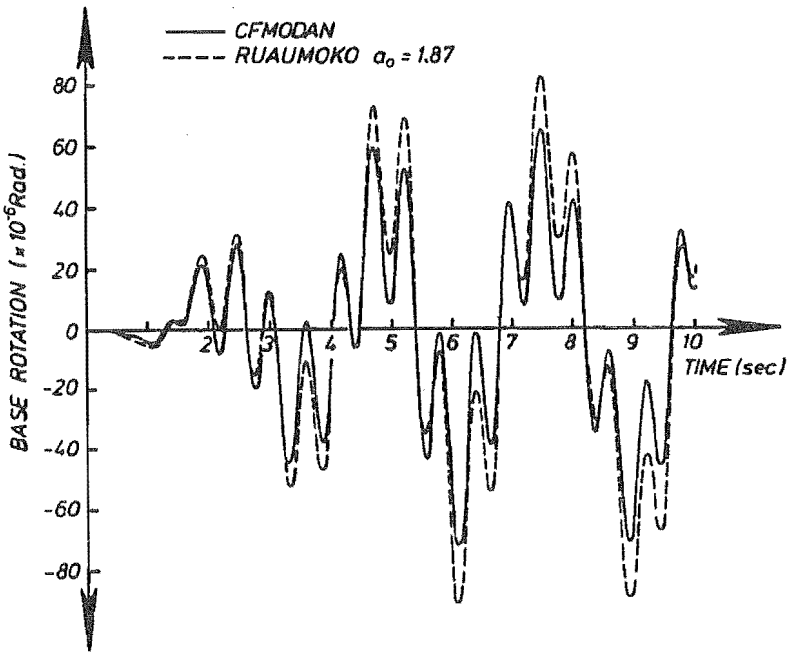

Fig. 2.12 Comparison of Base Rotation Response from Complex Frequency Dependent Modal Analysis and Tuned Dynamic Time History Analysis

2.4.6 Summary of Soil-Structure Interaction Study

Soil-structure interaction effects on offshore concrete gravity platforms of the type installed in the North Sea have been studied briefly using a very simple computer model of a typical platform structure. Foundation interaction was modelled using translational and rotational springs and dashpots, with properties based on the soil compliance functions given by Veletsos and Verbic [2.14]. Particular attention was directed toward determining how the frequency dependent soil behaviour could be satisfactorily modelled using constant valued properties in a time domain analysis procedure.

For the type of structure investigated, comprising a massive base structure, from which rather slender legs extend to support a deck, the soil-structure interaction effects did not have a substantial effect on the lateral response of the the deck. Moments and shears induced in the leg members were also rather insensitive to the soil-structure interaction effects. This suggested that for very severe earthquake excitation, where inelastic behaviour may occur, particularly at the junction between the legs and base, the prediction of overall displacement ductility demands and curvature demands at the critical sections may not be greatly affected by soil-structure interaction effects.

For the prediction of the rotational displacement response of the massive base structures, and loadings induced on the foundations, soil-structure interaction effects were important and the frequency dependence of the soil properties had to be considered. Induced foundation loadings could be predicted using time domain analysis procedures with the foundation modelled as translational and rotational spring and dashpot members. It was found that the rotational spring and dashpot member properties, being strongly frequency dependent, should be based on frequencies corresponding to the dominant rotational displacement response of the base of the structure.

It appeared that the rotational displacement response amplitudes of the large platform bases could not be predicted accurately using a time history analysis with constant valued

foundation member properties. The analysis overestimated the base rotations by about 25 percent compared with the response predicted using a more complete frequency dependent analysis. However, it should be noted that base rotations in the structure investigated contributed little to the displacements of the upper part of the structure. Also, for foundation analysis purposes, it may be more important to predict loadings rather than deformations induced on the foundation by the platform structure.

The scope of the study reported in this section was very limited. Only one type of gravity platform was considered and the dynamic analysis model used to represent this structure was very simple. The foundation properties chosen were only crude estimates of values which could be appropriate. The foundation material was idealised as a homogeneous elastic half-space. In practice soil deposits normally stiffen with depth and during large earthquakes soil behaviour is likely to be nonlinear. The soil properties used in this work were probably appropriate only to elastic behaviour of the foundation material. Based on results presented later in this thesis, the nonlinear behaviour of the soil may also be very important.

2.5 REFERENCES - CHAPTER 2

2.1 NZS 4203: 1984, "Code of Practice for General Structural Design and Design Loadings for Buildings", Standards Association of New Zealand, Wellington, 100 pp.

2.2 Archer, J. S., "Consistent Mass Matrix for Distributed Mass Systems", Journal of the Structural Division, ASCE, Vol. 89, No. ST4, August 1963, pp 161-178.

2.3 Clough, R. W. and Penzien, J. , "Dynamics of Structures", McGraw-Hill, 1975, 634 pp.

2.4 Newmark, N. M. and Rosenblueth, E. , "Fundamentals of Earthquake Engineering", Prentice-Hall, Englewood Cliffs, N.J., 1971, 640 pp.

2.5 Sharpe, R. D. , "The Seismic Response of Inelastic Structures", Ph.D. Thesis, Department of Civil Engineering, University of Canterbury, November 1974.

2.6 Carr, A. J. , "RUAUMOKO", Computer Program Library, Department of Civil Engineering, University of Canterbury, 1986.

2.7 Morison, J. R., O'Brien, M. P., Johnson, J. W. and Schaaf, S. A., "The Force Exerted by Surface Waves on Piles", Petroleum Transactions, AIME, Vol. 189, 1950, pp 149-154.

2.8 Brebbia, C. A. and Walker, S., " Dynamic Analysis of Offshore Structures", Newnes-Butterworths, 1979, 323 pp.

2.9 Liaw, C.-Y. and Chopra, A. K., "Earthquake Response of Axisymmetric Tower Structures Surrounded by Water", Earthquake Engineering Research Center, Report No. UBC/EERC-80/13, University of California, Berkeley, May 1973. 161 pp.

2.10 "Fluid/Structure Interaction During Seismic Excitation", A report by the ASCE Committee on Seismic Analysis of the Committee on Nuclear Structures and Materials of the Structural Division, American Society of Civil Engineers, 1984, 74 pp.

2.11 Liaw, C.-Y. and Reimer, R. B., "Hydrodynamic Interaction Effects on the Cylindrical Legs of Deepwater Platforms", Paper 2324, Proc. Offshore Technology Conference, Houston Texas, 1975.

2.12 Veletsos, A. S. and Wei, Y. T., "Lateral and Rocking Vibration of Footings", Journal of the Soil Mechanics and Foundations Division, ASCE, Vol. 97, No. SM9, Sept. 1971, pp 1227-1248.

2.13 Luco, J. E. and Westmann, R. A., "Dynamic Response of Circular Footings", Journal of the Engineering Mechanics Division, ASCE, Vol. 97, No. EM5, Oct 1971, pp 1381-1395.

2.14 Veletsos, A. S. and Verbic, B., "Basic Response Functions for Elastic Foundations", Journal of the Engineering Mechanics Division, ASCE, Vol. 100, No. EM2, April 1974, pp 189-202.

2.15 Caughy, T. K., "Classical Normal Modes in Damped Linear Systems", Journal of Applied Mechanics, No. 27, 1960, pp 269-271.

2.16 Hurty, W. C. and Rubinstein, M. F., "Dynamics of Structures", Prentice-Hall, Englewood Cliffs, N.J., 1964.

2.17 Watt, B. J., Boaz, I. B., Ruhl, J. A., Shipley, S. A., Dowrick, D. J. and Ghose, A., "Earthquake Survivability of Concrete Platforms", Paper 3159, Proc. Offshore Technology Conference, Houston Texas, 1978.

Chapter 3

ESTIMATION OF ACCELERATION RESPONSE SPECTRA FOR DESIGN OF OFFSHORE CONCRETE GRAVITY PLATFORMS IN NEW ZEALAND

3.1 INTRODUCTION

The purpose of the study reported in this chapter was to estimate reasonable levels of earthquake shaking which offshore concrete gravity platforms should be designed for in New Zealand. It is generally considered uneconomic to provide structures with sufficient strength to remain undamaged during very large earthquakes. A philosophy has evolved for the seismic design of structures on a two-tier basis. Firstly, it is required that during moderate seismic disturbances there should be an acceptably low risk of damage to the structure. A design level of equivalent earthquake loading is chosen to provide sufficient strength throughout the structure to meet this requirement. Secondly, it is required that during very severe shaking there should be an acceptably low risk of collapse of the structure. A similar approach is appropriate for the design of fixed offshore structures in New Zealand. Because of the extreme importance of these structures the acceptable levels of risk may be lower than for many other facilities.

Seismic hazard analyses can be used to estimate likely acceleration response spectra corresponding to various return periods. Such methods are currently being used to determine design spectra for onshore structures in New Zealand and can also be applied to the design of fixed offshore platforms. However, there are additional factors which need consideration when applying these methods to offshore structures. The fundamental period of vibration of typical gravity-based offshore platforms is longer than for most land based structures. Many have periods of 2 to 3 seconds which is at the upper end of the range of periods for which seismic hazard results are currently applicable. Foundation materials at offshore sites may be more flexible than at most onshore sites. This could have a significant influence on the character of ground motions which could be expected at those sites.

A seismic hazard analysis combines a seismicity model with an attenuation relation, using probabilistic methods, to give the probability distribution of some measure of the strength of ground shaking. One particularly useful measure is the uniform risk acceleration response spectrum which may be used directly for design purposes. Attenuation relations are available for predicting the acceleration response spectral amplitudes based on strong motion earthquake recordings. Comparison of attenuation relations based on Japanese and western United States data show considerable difference and result in markedly different uniform risk spectra.

Risk spectra obtained for ground shaking with very long return periods are compared with response spectra calculated from some of the strong motion records available in the world at present. In some cases seismic hazard analyses predict spectral ordinates which are somewhat less than those derived from these records. It is thought prudent to ensure that design spectra corresponding to very long return periods should not fall too far below the spectra from any existing strong-motion record. It is reasonable that design spectra derived from hazard analysis results should be adjusted as necessary to ensure this.

Recommendations are made regarding appropriate acceleration response spectra which could be used for design of offshore concrete gravity platforms in New Zealand. It is suggested that a recently published draft proposal for the New Zealand Loadings Code NZS 4203 code be used. The proposed design spectra in that document are based on the results of recent seismic hazard analysis studies and are adjusted to allow for the uncertainties in the attenuation for long period structures and to ensure that existing strong motion recordings of large earthquakes are adequately accounted for.

3.2 DETAILS OF SEISMIC HAZARD ANALYSIS METHODS

Seismic hazard analysis methods are now being used in New Zealand to generate design acceleration response spectra for the seismic design of structures. For any site, uniform risk acceleration response spectra can be estimated. The risk is quantified by the probability that the response accelerations will be greater than the ordinate of the spectrum. A return period equal to the reciprocal of the exceedance probability can be associated with the predicted spectrum. Thus for a response spectrum estimated for a 100 year return period it is expected that there would be a 1 percent probability of greater response accelerations being experienced in any single year.

The method used for seismic hazard analysis was originally devised by Cornell [3.1] and McGuire [3.2] but has been recently applied to analysis of New Zealand seismicity by Peek [3.3] and Mulholland [3.4] in developing suitable response spectra for use by structural designers.

Seismic hazard analyses are based on a probabilistic combination of a seismicity model, giving the spatial and temporal distribution of earthquake magnitudes and epicentres, with an attenuation relation; a function relating the strength of shaking expected at a site to earthquake magnitude, epicentral distance and ground conditions at the site.

Seismicity models of New Zealand divide the country and surrounding area into a number of regions within which it is expected there will be a uniform rate of occurrence of earthquake magnitudes and epicentres in time and position. Such divisions are made based on the analysis of historical earthquake frequency data, geological information and the known tectonic setting of the country.

Gutenberg and Richter found that the recurrence formula given by Eqn. 3.1 could be used to very closely describe the seismicity over any particular area.

$$\log_{10} N = a - bM \qquad (3.1)$$

N is the number of earthquakes of magnitude M or larger occurring in a given time period per unit area. A plot of $\log_{10} N$ versus M gives a straight line with a slope of -b. The constant a gives the total number of earthquakes occurring. In practice the expression given in Eqn. 3.2 is often used in place of Eqn. 3.1.

$$\log_{10} N = a_m - b(M-m) \qquad (3.2)$$

The parameter m is an arbitrary reference magnitude and 10^{a_m} is the number of earthquakes with magnitude greater than m in the specified time per unit area. In New Zealand the parameter a_4 is often used and for the most active areas the value corresponds to approximately 7 earthquakes greater than magnitude 4 per year per 1000 km^2. The parameter b gives the rate of decay of numbers of earthquakes per unit area and time, with magnitude. This is equal to approximately 1.0 for most areas of the world, including New Zealand.

A maximum magnitude M_{max} can be specified above which it is expected no earthquakes would occur. Currently available New Zealand seismicity models have maximum magnitude values between about 6.5 and 8.5, depending on the region.

Seismicity models can be updated as a better understanding of the variations in seismicity are obtained. At present historical frequency data is available for only a few decades for small to moderate sized earthquakes and perhaps 100 years for large earthquakes. Details of a recent New Zealand seismicity model proposed by Smith and Berryman (1983) [3.5] are given in Fig. 3.1 and Table 3.1.

Attenuation relations describe how the strength of shaking at a particular site can be related to the earthquake magnitude, epicentral distance and ground condition at the site. There are many ways in which the strength of ground shaking can be characterised. Maximum ground

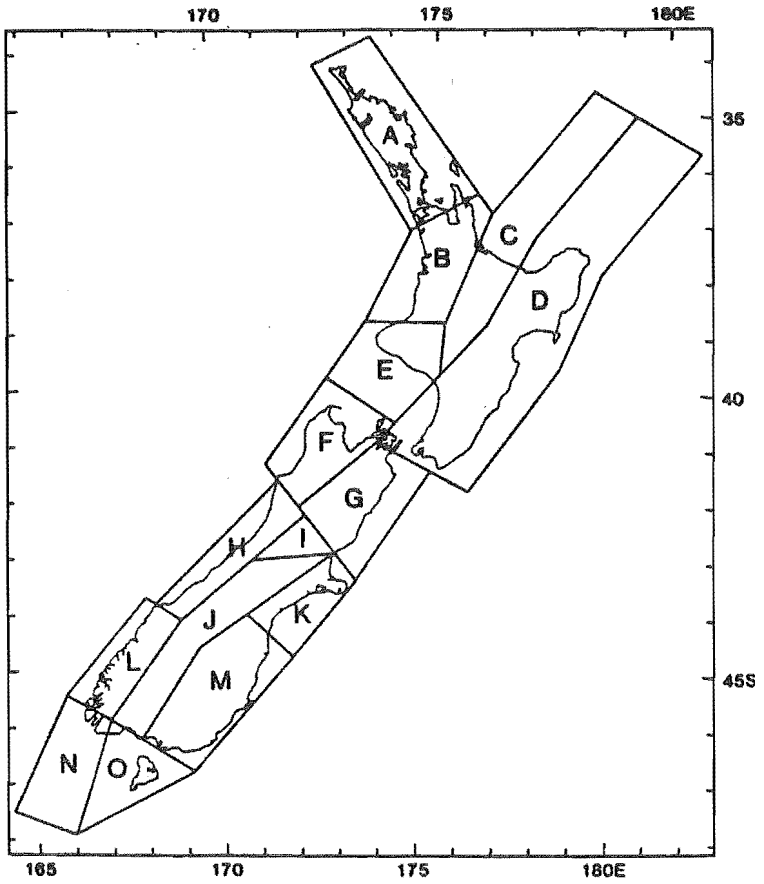

Fig. 3.1 New Zealand Zoning for Smith and Berryman Seismicity Model

Table 3.1 Smith and Berryman Seismicity Model Parameters

Region	a4	b	Mmax
A	0.03	1.20	7.5
B	0.10	1.20	8.0
C	0.45	1.20	7.5
D	0.85	1.13	8.5
E	0.80	1.15	8.5
F	0.70	1.13	8.5
G	0.60	1.10	8.5
H	0.20	1.05	8.5
I	0.40	1.10	8.5
J	0.11	1.10	8.0
K	0.03	1.10	8.0
L	0.70	0.95	8.5
M	0.08	1.10	8.0
N	0.60	1.00	8.5
O	0.08	1.10	8.0

acceleration is perhaps the most obvious, but duration of strong shaking is also important. Peak ground velocity is sometimes considered to be more important than maximum ground acceleration as it measures the pulse with the largest area in the acceleration time history. Of most interest to structural designers are the maximum response accelerations their structures will be subject to. Therefore attenuation relations which deal with acceleration response ordinates directly, rather than any other measure of strength of shaking, are most

useful. Acceleration response spectra give the maximum response acceleration experienced by single degree of freedom oscillators. The level of response depends on the natural period of vibration and the fraction of critical damping. Attenuation relations give predictions of the acceleration response as functions of the natural period.

Because of the complex random processes involved in the energy release and rupture propagation mechanisms, and in the radiation of seismic energy during earthquakes, there is a large amount of scatter in the available data on which attenuation relations are based. Only limited data is available with most having been collected over the last few decades from areas with high levels of seismicity. The largest data sets have been obtained from Japanese and Californian sources and contain only a few hundred strong-motion recordings. Characteristics of earthquakes in these two areas are quite different and it is thought that this is due to the different tectonic behaviour in each area. In California the Pacific Plate is at present undergoing predominantly transcurrent movement past the American Plate. This has resulted in very shallow earthquakes, generally at depths of less than 20 km, which tend to be felt over a relatively small area.

In Japan the thin oceanic crust at the edge of the Pacific Plate is subducting westward beneath the thicker continental crust of the Eurasian Plate. The oceanic trench to the east of the Japan islands and the chain of volcanoes along the length of the country are typical features of subduction zones [3.6]. Earthquake hypocentres tend to be located close to the interface between the subducting plate and the stationary crust or underlying mantle. Most hypocentres are shallow (less than 40 km) but there are also many deep focus earthquakes at depths down to several hundred kilometres.

In New Zealand the tectonic setting is similar to that in Japan. North of the Southern Alps the Pacific Plate is known to be subducting beneath the Indian Plate. South of the Southern Alps it is known that the reverse is happening. This suggests a rather complex state existing in the Southern Alps region itself. The well defined Alpine Fault which runs through the area for hundreds of kilometres is at present very quiet but has obviously been subject to considerable transcurrent movement in the past, and may again in the future. Geological evidence has shown that landsliding in the area, which could have been triggered by earthquakes, has occurred at regular intervals in recent history [3.7].

Because of the similarity in tectonic settings it is generally thought that Japanese attenuation predictions should be more appropriate to New Zealand than western United States results. The limited number of strong-motion records at present available in New Zealand tend to support this theory [3.4, 3.8]. However, it should be noted that the Japanese data is very sparse at distances less than 20 km. Californian seismologists have been rather more fortunate and have obtained several records from the epicentral region of moderate sized earthquakes with magnitudes between 6 and 7. Examination of the hazard analysis results (discussed in section 3.6) indicates that most of the risk at a site is contributed by moderate sized earthquakes within about 20 km. For this reason it is important that the attenuation relation used should be as accurate as possible at short distances. Japanese attenuation models could change substantially for small epicentral distances when records are obtained from the epicentral regions of earthquakes.

3.3 COMPARISON OF JAPANESE AND CALIFORNIAN ATTENUATION MODELS

Recent seismicity and attenuation models were applied in this study to determine likely acceleration response spectra which could be used for the design and analysis of fixed offshore platform structures in New Zealand. It was intended to derive acceleration response spectra for two levels of earthquake. Firstly a design level event, corresponding to a return period of approximately 100 years and secondly, an extreme event, corresponding to a return period of 1000 years or more. From these it would be possible to select suitable ground acceleration time histories, either real or artificially generated, for input to dynamic time history analyses. Gravity based concrete platform structures located in 100 m or greater water depths typically have fundamental periods of vibration of around 2 seconds or more. If significant inelastic deformations were imposed on such a structure during an extreme earthquake the structure

would soften and the period would increase further. Japanese attenuation relations currently available, due to Katayama et al [3.9] and Okubo et al [3.10] consider natural periods up to 3 or 4 seconds. The attenuation relation by Trifunac [3.11], based on Californian data, gives spectral acceleration estimates for structures with natural periods up to about 8 seconds. Comparisons were made between the Japanese and Californian attenuation relations for particular magnitude and epicentral distance cases. The influence of the various attenuation relations on the uniform risk acceleration response spectra was also examined.

3.3.1 The Attenuation Relation of Katayama et al (1978)

The Katayama attenuation relation [3.9] was derived from statistical analysis of 277 accelerogram records from 67 Japanese earthquakes between 1956 and 1974. Spectral amplitudes at 18 periods of vibration are divided into 5 magnitude and 5 distance classes for sites with 4 different ground conditions. The relation takes the form of the product of three terms giving magnitude, epicentral distance and ground condition dependence, as given by Eqn. 3.3.

$$S_a(T) = f_m(T)\ f_\Delta(T)\ f_{gc}(T) \qquad (3.3)$$

where $S_a(T)$ = absolute acceleration response with 5 percent of critical damping
T = natural period of vibration
$f_m(T)$ = term giving magnitude dependence
$f_\Delta(T)$ = term giving epicentral distance dependence
$f_{gc}(T)$ = term giving ground condition dependence

The predicted spectral accelerations are for equivalent single degree of freedom structures with 5 percent of critical damping and are geometric mean values of the observed data in each class. The ratios of the observed to predicted spectral values, termed "residuals", were found to be log-normally distributed (that is, the common logarithms are normally distributed), with a mean of zero and a standard deviation σ_{10} of approximately 0.25. It is necessary to know the scatter in the spectral values about the predicted mean in order to carry out the hazard analysis.

The 5 magnitude classes are delimited by magnitudes of 4.5, 5.35, 6.05, 6.75, 7.45 and 7.9. The 5 epicentral classes are delimited by distances of 6 km, 20 km, 60 km, 120 km, 200 km and 400 km. The 4 ground conditions are, in short, bedrock (Type I), alluvium less than 10 m depth (Type II), alluvium less than 25 m depth including soft layers up to 5 m thick (Type III), and other than above, generally soft alluvium or reclaimed land (Type IV).

Most Japanese strong-motion records have been obtained from SMAC-B2 accelerographs which have a natural frequency of about 7 Hz. This results in relative suppression of high frequency ground acceleration measurement. Mulholland [3.4] applied a correction factor to the attenuation relation derived from the theoretical sensitivity versus frequency curve for the instrument.

A further modification was suggested by Peek [3.3] to the distance dependence term $f_\Delta(T)$ for the largest distance class (200 km to 405 km) by dividing it by 2. In some cases spectral amplitudes predicted by the originally published form of the attenuation relation were larger for greater epicentral distances. As is discussed later this makes very little difference to the uniform risk spectra, as most of the risk is contributed from earthquakes at much closer distances.

3.3.2 The Attenuation Relation of Okubo et al (1983)

The Okubo et al attenuation relation [3.10] is more recent than the Katayama relation and assumes a different functional form. Multiple regression analyses were performed on a larger data set of 394 horizontal components of Japanese strong-motion records including those

obtained from the 1978 Miyagi-ken-Oki (M=7.4) earthquake. Information from earthquakes at very short epicentral distances, particularly for large magnitude events, is still lacking in this data set. The pairs of horizontal accelerograms were combined, presumably vectorially, and maximum ground accelerations and absolute acceleration response spectra were calculated for single degree of freedom oscillators with 5 percent of critical damping. Corrections were made for instrument sensitivity.

Spectral ordinates at ten periods of vibration between 0.1 seconds and 3.0 seconds can be estimated as continuous functions of magnitude and epicentral distance using the expression in Eqn. 3.4.

$$S_a(T) = a(T)\ 10^{b(T)\,M}\ (\Delta + 30)^{c(T)} \qquad (3.4)$$

where $S_a(T)$ = absolute acceleration response with 5 percent of critical damping
T = natural period of vibration
M = local (Richter) magnitude
Δ = epicentral distance in km

The empirically derived coefficients a(T), b(T) and c(T) are given by Okubo et al in tabular form. The ground condition categories are generally the same as for the Katayama model, except ground condition Types II and III are combined in the Okubo model. As for the Katayama model the residuals of the observed spectral ordinates were found to closely match a log-normal distribution with standard deviations ranging from $\sigma_{10} = 0.211$ to 0.305 with an average value of 0.264.

3.3.3 The Attenuation Relation of Trifunac et al (1977)

The Trifunac attenuation relation [3.11] is based on statistical analysis of 182 strong-motion records from the western United States up to 1971. The expression given in Eqn. 3.5 is used.

$$\log_{10}[S(T),p] = M + \log_{10} A_o(\Delta) - a(T)p - b(T)M - c(T) - d(T)s - e(T)v - f(T)M^2 - g(T)\Delta \qquad (3.5)$$

where $S(T)$ = any spectral quantity (absolute acceleration, relative velocity, pseudo relative velocity, displacement etc)
T = natural period of vibration
M = local (Richter) magnitude
Δ = epicentral distance
A_o = epicentral distance attenuation function
p = confidence level - probability that given amplitude will not be exceeded by the observed data
s = site condition factor: = 2 for basement rock, = 1 for intermediate material, = 0 for alluvium
v = 0 for horizontal motion spectra, = 1 for vertical motion spectra

The factors a(T) to g(T) are regression coefficients and depend on the spectral amplitude quantity required and the fraction of critical damping. The coefficients for determining absolute spectral acceleration amplitudes are given by Trifunac and Anderson [3.11].

The standard deviation of residuals of the observed data is not explicitly given by the authors but may be deduced from Eqn. 3.5 by assuming that the residuals will be log-normally distributed and substituting exceedance probabilities for the standard normal variate and the confidence level p. Berrill [3.12] has calculated the standard deviations implied by the Trifunac attenuation model for absolute spectral accelerations and found them to range from 0.36 for short periods to 0.50 for long period oscillators. In this study the Trifunac data was further analysed and it was found that the standard deviations vary considerably depending on the confidence level considered.

As described later in this chapter, the computer program for seismic hazard analysis developed by Peek and Mulholland was modified to include the Trifunac attenuation model. The hazard analysis procedure calculates contributions to the risk from all possible distance and magnitude class combinations from the ranges considered. From each combination the number of standard deviations away from the geometric mean of the attenuation data is calculated. Clearly, the number of standard deviations will depend on the return period (exceedance probability) being sought. The hazard analysis results are quite sensitive to changes in the standard deviation, so it is important that an accurate estimate should be used. It should be noted that the standard deviation values for the Trifunac model are significantly larger than for the Katayama or Okubo models.

Because the calculated standard deviations were found to vary with the confidence level it is inferred that the Trifunac data is not in very good agreement with the log-normal distribution. However, for return periods of interest, between say 100 and 1000 years, the standard deviations calculated by Berrill were found to be satisfactory.

3.3.4 The Attenuation Relation of McVerry

McVerry [3.8] has examined the limited strong-motion data available from New Zealand earthquakes and found very good agreement of response spectral ordinates with those predicted by the corrected Katayama model. Slight variations were proposed to the Katayama attenuation relation to account for the New Zealand data. The suggested attenuation relation, given by the expression in Eqn. 3.6, is almost exactly the same as Katayama expression except that the term $f_\Delta(T)$, giving the epicentral distance dependence, has been adjusted and a correction factor CF(T) to allow for instrument sensitivity has been included. McVerry found that the available New Zealand data showed a slightly more rapid attenuation of shaking with distance than in the Japanese records.

$$S_a(T) = f_m(T)\ f_\Delta(T)\ f_{gc}(T)\ CF(T) \qquad (3.6)$$

The relation is appropriate for structures with 5 percent of critical damping. As this model was used for deriving hazard analysis predictions presented later in this chapter, for the whole of New Zealand, the values of the four period dependent weighting coefficients f_m, f_Δ, f_{gc} and CF are given in Table 3.2.

Table 3.2 Weighting Coefficients for McVerry Attenuation Relation

Response Period (sec)	Fm: Magnitude (M) 4.5-5.35	5.35-6.05	6.05-6.75	6.75-7.45	7.45-9.0	FΔ: Epicentral Distance Δ (km) 0-20	20-60	60-120	120-200	200-400	Fgc: Ground Condition Type I	Type II	Type III	Type IV	CF Correction Factor
0.10	0.208	0.278	0.296	0.399	1.0	4.478	2.650	1.153	0.657	0.371	126.	107.	120.	106.	1.445
0.15	0.225	0.274	0.297	0.448	1.0	5.358	3.053	1.252	0.684	0.371	155.	130.	141.	125.	1.445
0.20	0.185	0.280	0.288	0.449	1.0	6.086	3.376	1.326	0.715	0.371	169.	149.	161.	129.	1.318
0.25	0.171	0.254	0.283	0.534	1.0	6.717	3.650	1.388	0.721	0.371	135.	129.	143.	129.	1.245
0.30	0.164	0.269	0.280	0.548	1.0	6.220	3.435	1.340	0.708	0.371	109.	130.	147.	131.	1.202
0.35	0.161	0.274	0.302	0.588	1.0	5.830	3.263	1.300	0.697	0.371	92.8	126.	149.	142.	1.164
0.40	0.152	0.268	0.311	0.557	1.0	5.511	3.121	1.267	0.688	0.371	83.0	122.	145.	144.	1.138
0.50	0.108	0.237	0.309	0.593	1.0	5.013	2.897	1.214	0.674	0.371	76.6	113.	140.	156.	1.091
0.60	0.0889	0.246	0.321	0.618	1.0	4.643	2.727	1.173	0.662	0.371	32.1	101.	134.	159.	1.054
0.70	0.0730	0.222	0.315	0.644	1.0	4.351	2.590	1.138	0.652	0.371	50.1	88.8	118.	148.	1.023
0.80	0.0683	0.214	0.294	0.595	1.0	4.110	2.477	1.110	0.644	0.371	47.9	91.0	115.	145.	1.000
0.90	0.0672	0.214	0.285	0.581	1.0	3.913	2.382	1.084	0.636	0.371	46.4	90.5	113.	136.	1.000
1.00	0.0653	0.204	0.284	0.636	1.0	3.743	2.300	1.063	0.630	0.371	43.3	89.3	107.	125.	1.000
1.50	0.0503	0.138	0.204	0.534	1.0	3.346	2.105	1.010	0.614	0.371	33.0	56.5	68.5	84.6	1.000
2.00	0.0605	0.148	0.215	0.585	1.0	3.090	1.977	0.974	0.603	0.371	24.7	36.8	44.1	46.2	1.000
2.50	0.0587	0.136	0.183	0.405	1.0	2.905	1.883	0.947	0.594	0.371	21.9	32.7	35.8	33.0	1.000
3.00	0.0660	0.138	0.194	0.391	1.0	2.763	1.810	0.925	0.588	0.371	18.8	26.6	28.5	26.6	1.000
4.00	0.0704	0.144	0.187	0.395	1.0	2.552	1.700	0.893	0.577	0.371	15.7	20.3	24.1	19.1	1.000

3.3.5 Examples of Comparisons Between Attenuation Relations

To illustrate the differences between the four attenuation relations discussed, some specific examples were considered. Fig. 3.2 shows the attenuation of spectral accelerations with epicentral distance from a magnitude 6.4 earthquake predicted by the four models for structures with a natural period of 0.2 seconds located on hard ground. The Trifunac relation predicts the largest response accelerations for epicentral distances less than about 40 km with very large accelerations for distances less than 20 km. It is interesting that the Okubo model curve is considerably higher than the Katayama (and McVerry) curves as this is based largely on the same data set.

Figs. 3.3 and 3.4 show similar comparisons for 1.0 second structures from a magnitude 7.7 earthquake and 3 second structures from a magnitude 7.7 earthquake respectively, for hard ground sites. Similar trends are shown in both of these examples, with the Trifunac model giving much higher spectral accelerations at small epicentral distances.

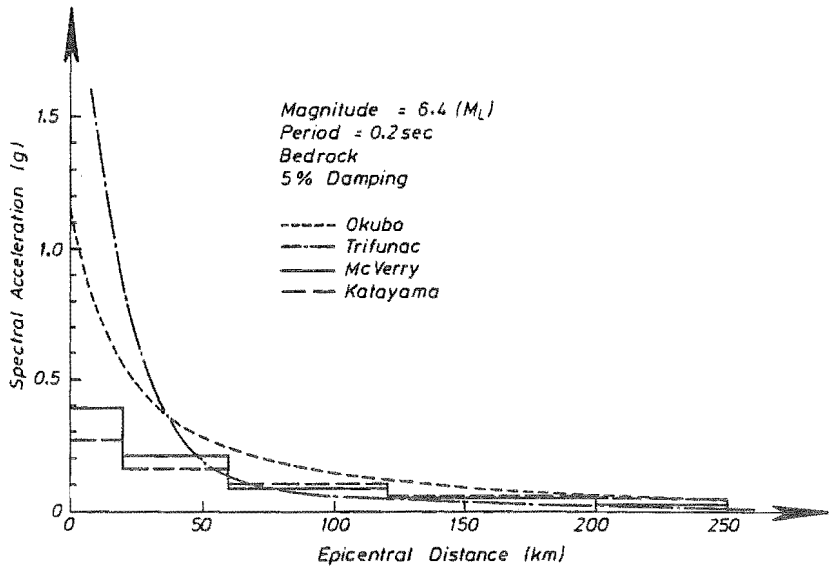

Fig. 3.2 Comparison of Attenuation Models for Hard Ground, M=6.4, T=0.2 sec

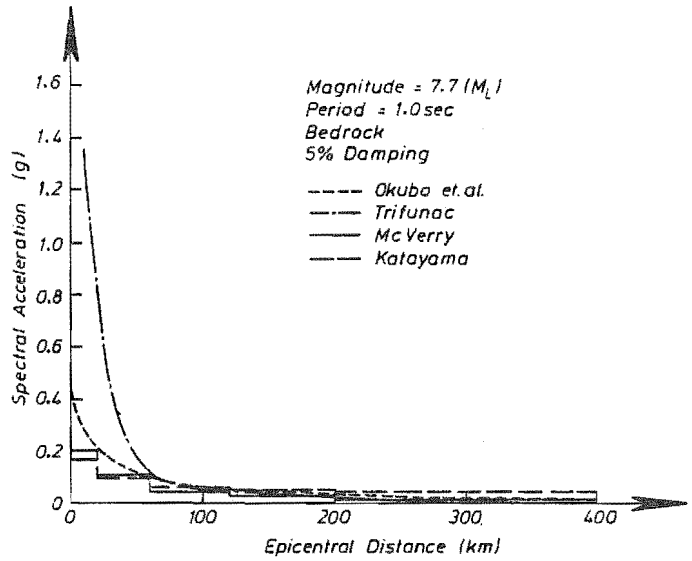

Fig. 3.3 Comparison of Attenuation Models for Hard Ground, M=7.7 , T=1.0 sec

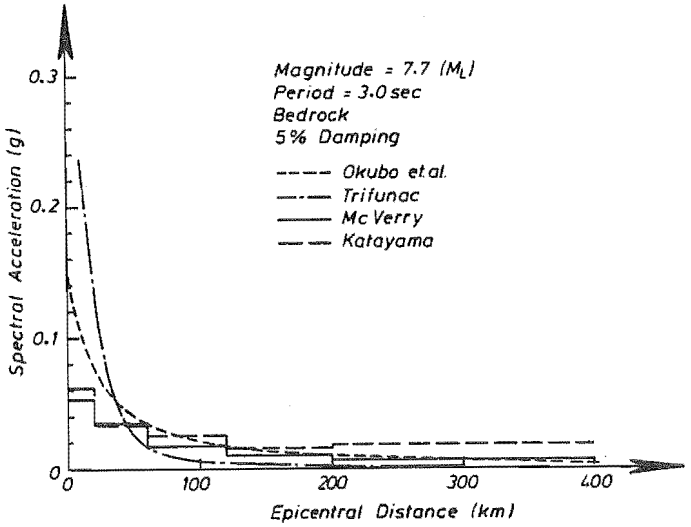

Fig. 3.4 Comparison of Attenuation Models for Hard Ground, M=7.7, T=3.0 sec

3.4 HAZARD ANALYSIS RESULTS

In this section the results of seismic hazard analyses are discussed. Uniform risk spectra have been calculated using the hazard analysis computer program developed by Peek and Mulholland. The most recently proposed seismicity model of New Zealand, due to Smith and Berryman [3.5], was used. The computer program was extended recently to include the McVerry modifications to the Katayama attenuation model. Further adaptions were made by this author to examine the effects of using the Okubo and Trifunac attenuation relations. Comparisons of uniform risk spectral accelerations were made for various return periods using the different attenuation models for a site near the Maui gas field, off the western coast of New Zealand.

The McVerry, Okubo and Trifunac attenuation models give results for periods of vibration up to 4.0, 3.0 and 7.5 seconds respectively. In the uniform risk spectra presented in this section the results have been extrapolated in each case up to periods of 8.0 seconds.

The extrapolation of the spectral curves was done by fitting a least squares hyperbolic curve through the last few data points on each curve, generally for the points at periods greater than 1 second. This was accomplished by fitting a least squares line through the logarithms of both the periods and spectral amplitudes. A hyperbolic variation is expected to fit the data quite well. On theoretical grounds it can be justified because the spectral displacement of long period structures tends to the maximum ground displacement. The response accelerations will then be proportional to the reciprocal of the period squared. In a study of displacement seismograph records by Katayama and Shino [3.13] it was found that the average Fourier spectra from 27 horizontal records showed almost constant amplitude in the period range from 2 to 20 seconds. If Fourier amplitude of acceleration is taken as a measure of spectral velocity then this suggests that a flat Fourier spectrum results in an acceleration response spectrum which varies as the reciprocal of period. In all cases the exponent for the extrapolated curves was between the values of -1.0 and -2.0. The additional uncertainties involved with this extrapolation were not considered too serious in light of the large differences predicted in the uniform risk spectra by the various attenuation models.

3.4.1 Uniform Risk Spectra Based on the McVerry Attenuation Relation

Uniform risk acceleration response spectra calculated using the McVerry (modified Katayama) attenuation relation are presented in Fig. 3.5 for a site near the Maui offshore gas field (latitude 39.65 degrees, longitude 173.35 degrees). The various curves correspond to return periods of 100, 1000 and 10 000 years, with the solid lines being for a hard ground (bedrock) site and the dashed lines being for a very soft site. The very soft site results would probably be appropriate for an offshore foundation where sediments are present to great depths. The spectra are expected acceleration response values assuming that both the structure and foundation remain elastic. Response ordinates for the very soft site condition are less than for the bedrock site values for periods below 0.3 seconds but greater for longer periods. The ratio of the soft to hard ordinates is exactly as given by the attenuation relation, thus if the attenuation relation is doubled, so is the uniform risk spectrum. For a structure with a natural period of 0.8 seconds located on a very soft foundation the predicted spectral acceleration is 3 times the acceleration on a bedrock site.

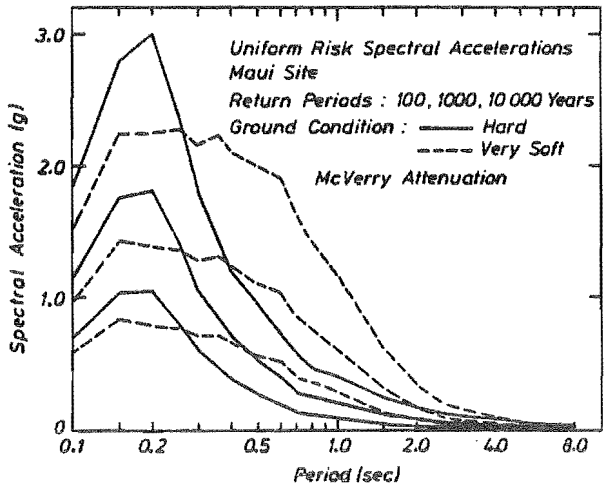

Fig. 3.5 Uniform Risk Response Spectra for Maui Site Using McVerry Attenuation

Table 3.3 Relative Risk - McVerry Attenuation, Period = 0.5 sec, Return Period = 1000 years, Hard Ground, Maui Site

Magnitude Class Range	Distance Class Range (km) 0-20	20-60	60-120	120-200	200-400	Total
4.5-5.35	0.06	0.02	0.	0.	0.	0.08
5.35-6.05	0.21	0.16	0.	0.	0.	0.37
6.05-6.75	0.09	0.08	0.	0.	0.	0.17
6.75-7.45	0.07	0.15	0.01	0.	0.	0.23
7.45-9.0	0.03	0.10	0.02	0.	0.	0.15
Total	0.46	0.51	0.03	0.	0.	1.00

For each response period the hazard analysis procedure calculates the contribution to the total risk from each combination of distance and magnitude class. For the McVerry (or Katayama) model the attenuation model subdivides the distance and magnitude ranges into classes. Table 3.3 shows the proportions of risk contributed by each distance and magnitude class combination for a particular case. It assumes a natural period of 0.5 seconds on hard ground at the Maui offshore site for a return period of 1000 years. Approximately 50 percent of the risk is contributed from earthquakes with epicentres within each of the distance ranges 0 to 20 km and 20 to 60 km with only a very small contribution from more distant events. The

distribution with magnitude shows that the greatest contribution (37 percent) is from small to moderate sized earthquakes with magnitudes in the range 5.35 to 6.05 and about 20 percent from earthquakes with magnitudes in each of the ranges 6.05 to 6.75, 6.75 to 7.45 and 7.45 to 9.0.

For longer natural periods there is a marked shift in the distribution of risk to larger magnitude earthquakes at greater epicentral distances. An example of this is shown in Table 3.4 for structures with natural periods of 4 seconds on hard ground at the Maui site, again for a return period of 1000 years. This effect is consistent with suggestions made by others [3.4, 3.10] and may be due to the greater influence of long period surface waves which are expected to attenuate less rapidly than body waves.

Table 3.4 Relative Risk - McVerry Attenuation, Period = 4.0 sec, Return Period = 1000 years, Hard Ground, Maui Site

Magnitude Class Range	Distance Class Range (km) 0-20	20-60	60-120	120-200	200-400	Total
4.5-5.35	0.03	0.02	0.	0.	0.	0.05
5.35-6.05	0.07	0.10	0.01	0.	0.	0.18
6.05-6.75	0.03	0.05	0.01	0.	0.	0.09
6.75-7.45	0.05	0.13	0.03	0.01	0.	0.22
7.45-9.0	0.04	0.20	0.12	0.06	0.40	0.46
Total	0.22	0.50	0.17	0.07	0.04	1.00

3.4.2 Uniform Risk Spectra Based on the Okubo Attenuation Relation

Using the Okubo et al attenuation model the uniform risk spectra shown in Fig.3.6 were obtained for the Maui site. The curves for the hard ground condition show quite good agreement with the results based on the McVerry attenuation model except for the lack of a peak in the spectra for natural periods of about 0.2 seconds. The reason why the peak response accelerations occur at 0.1 seconds with the Okubo model is the large difference in values of the standard deviation σ_{10}. At 0.1 and 0.2 second periods the standard deviations for hard ground are 0.2627 and 0.2296 respectively. For a larger standard deviation it is necessary to deviate further from the mean of the attenuation relation distribution in order to give the exceedance probability corresponding to the required return period.

The uniform risk acceleration response spectra for very soft site conditions are given by the dashed lines in Fig. 3.6 and are rather lower than those based on the McVerry model at natural periods less than about 0.3 seconds. There is also a very large peak centred around 0.7 seconds. This is due to the large amplification of responses predicted by the attenuation relation, being a characteristic of the original data.

For periods longer than about 3 seconds the uniform risk spectra are close to the values predicted using the McVerry model.

The proportions of risk contributed by the various distance and magnitude class combinations for 0.7 second period structures on hard ground at the Maui offshore site for a return period of 1000 years are given in Table 3.5. The distribution with magnitude is low up to a magnitude of 5.75 (total 9 percent) but fairly uniform over magnitudes ranging from 5.75 to 8.25 (total 91 percent). The distribution of risk with epicentral distance is fairly uniform for distances between 10 km and 50 km (total 70 percent) with a lower contribution of risk from distances between 50 and 100 km (total 20 percent).

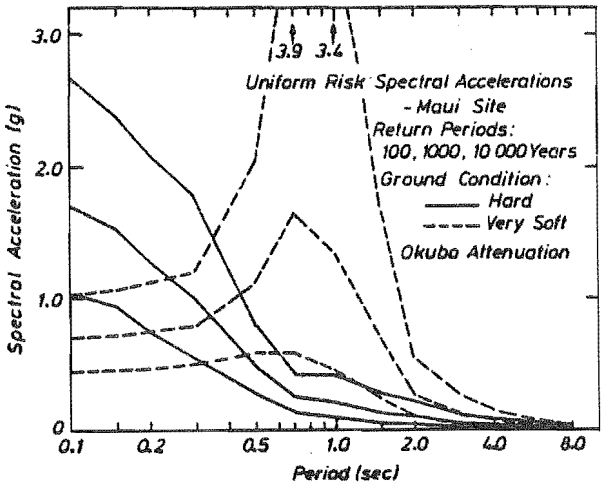

Fig. 3.6 Uniform Risk Response Spectra for Maui Site Using Okubo Attenuation

Table 3.5 Relative Risk - Okubo Attenuation, Period = 0.7sec, Return Period = 1000 years, Hard Ground, Maui Site

Magnitude Class Range	Distance Class Range (km) 0-10	10-20	20-30	30-40	40-50	50-60	60-80	80-100	100-200	200-300	Total
4.25-4.75	0.	0.	0.	0.	0.	0.	0.	0.	0.	0.	0.
4.75-5.25	0.	0.01	0.01	0.	0.	0.	0.	0.	0.	0.	0.02
5.25-5.75	0.01	0.02	0.02	0.01	0.01	0.	0.	0.	0.	0.	0.07
5.75-6.25	0.01	0.04	0.04	0.02	0.01	0.01	0.01	0.	0.	0.	0.14
6.25-6.75	0.02	0.05	0.05	0.04	0.02	0.01	0.01	0.	0.	0.	0.20
6.75-7.25	0.02	0.04	0.05	0.04	0.03	0.02	0.02	0.01	0.	0.	0.23
7.25-7.75	0.01	0.02	0.03	0.03	0.03	0.02	0.03	0.01	0.01	0.	0.19
7.75-8.25	0.	0.01	0.02	0.02	0.02	0.02	0.02	0.02	0.02	0.	0.15
Total	0.07	0.19	0.22	0.16	0.12	0.08	0.09	0.04	0.03	0.	1.00

3.4.3 Uniform Risk Spectra Based on the Trifunac Attenuation Relation

The Trifunac attenuation relation was used to obtain the uniform risk acceleration response spectra for the Maui offshore field shown in Fig. 3.7. Overall the uniform risk curves are somewhat higher than the results from the McVerry or Okubo attenuation models. This was expected as the Trifunac relation gave relatively large spectral values at close distances (refer Figs. 3.2 to 3.4). The 10 000 year risk spectra are very large with peak response accelerations of 4 to 5 times gravity predicted. Although these results are so large, they are not considered particularly relevant as the 10 000 year event has such a small probability (about 0.003) of being exceeded during the design life of a platform structure of say 30 years. The return period of 10 000 years also results in rather extreme extrapolation of the historical strong motion data which is only available for a few decades.

The hazard analysis procedure assumes that the residuals of the observed data are log-normally distributed. It has already been pointed out that the Trifunac data does not seem to fit the log-normal assumption very well. Because the standard deviations estimated for the Trifunac data are relatively high compared with the figures from Japanese data, the uniform risk spectral ordinates for large return periods could be substantially inflated because of the logarithmic influence. Some further rationalisation of the standard deviations may result in lower values and more modest uniform risk spectral predictions.

Table 3.6 shows an example of the contributions to the total risk from the various distance and magnitude class combinations. The results are for the case of 0.5 second structures on hard ground at the Maui site for a return period of 1000 years. Most of the risk is contributed by moderate magnitude earthquakes (M = 6.25 to 6.75) at very close epicentral distances (less than 10 km). This is due to the relatively high spectral ordinates predicted by the Trifunac attenuation relation at close distances.

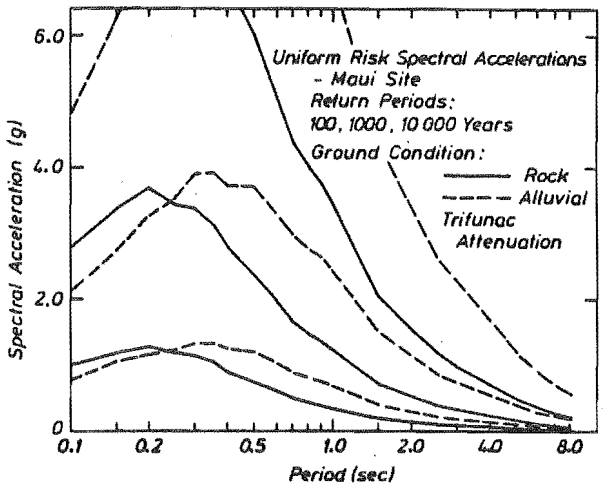

Fig. 3.7 Uniform Risk Response Spectra for Maui Site Using Trifunac Attenuation

Table 3.6 Relative Risk - Trifunac Attenuation, Period = 0.7sec, Return Period = 1000 years, Hard Ground, Maui Site

Magnitude Class Range	Distance Class Range (km)										Total
	0-10	10-20	20-30	30-40	40-50	50-60	60-80	80-100	100-200	200-300	
4.25-4.75	0.	0.	0.	0.	0.	0.	0.	0.	0.	0.	0.
4.75-5.25	0.	0.	0.	0.	0.	0.	0.	0.	0.	0.	0.
5.25-5.75	0.02	0.	0.	0.	0.	0.	0.	0.	0.	0.	0.02
5.75-6.25	0.14	0.07	0.01	0.	0.	0.	0.	0.	0.	0.	0.22
6.25-6.75	0.16	0.16	0.04	0.	0.	0.	0.	0.	0.	0.	0.36
6.75-7.25	0.08	0.12	0.05	0.01	0.	0.	0.	0.	0.	0.	0.26
7.25-7.75	0.02	0.05	0.03	0.01	0.	0.	0.	0.	0.	0.	0.11
7.75-8.25	0.01	0.01	0.01	0.	0.	0.	0.	0.	0.	0.	0.03
Total	0.43	0.41	0.14	0.02	0.	0.	0.	0.	0.	0.	1.00

Consideration was given to the possibility of a near field truncation of the attenuation relation for distances of less than say 10 km or 20 km. This would be physically reasonable as it allows for the effect of a finite, and possibly large, rupture zone dimensions. However Trifunac et al [3.11] show that the model gives acceptable predictions of actual strong motion records at close distances, such as the El Centro 1940 (Δ = 15 km) and Pacoima Dam 1971 (Δ = 9 km) records. The uniform risk acceleration response spectra derived using the Trifunac attenuation model must be accepted as being fair representations of likely hazard from western United States type earthquakes. It has already been pointed out that these may not be typical of New Zealand type ground motions.

3.4.4 Comparison of Uniform Risk Spectra Based on Different Attenuation Relations

The uniform risk spectral acceleration curves derived using the attenuation relations of McVerry , Okubo et al and Trifunac are compared in Figs. 3.8 to 3.11 for a site at the Maui offshore gas field. The examples are for return periods of 100 and 1000 years which are considered to represent appropriate levels of response corresponding to a design level earthquake and an extreme earthquake. Figs. 3.8 and 3.10 are for hard ground conditions and Figs. 3.9 and 3.11 are for very soft alluvial sites. The spectra based on the Okubo et al and McVerry (essentially Katayama) attenuation relations agree reasonably well, but the spectra based on the Trifunac attenuation are approximately twice as large over most of the range of natural periods.

The results serve to highlight the large discrepancies which can be given by the hazard analysis using two different attenuation expressions based on the best available data sets in their respective countries of origin. As discussed in section 3.2 the Japanese data is thought to be more appropriate for use in New Zealand. The hazard analysis results presented in Section 3.6 are based on the McVerry attenuation relation, which is an adaption of the Katayama model to allow for the small amount of New Zealand strong-motion data.

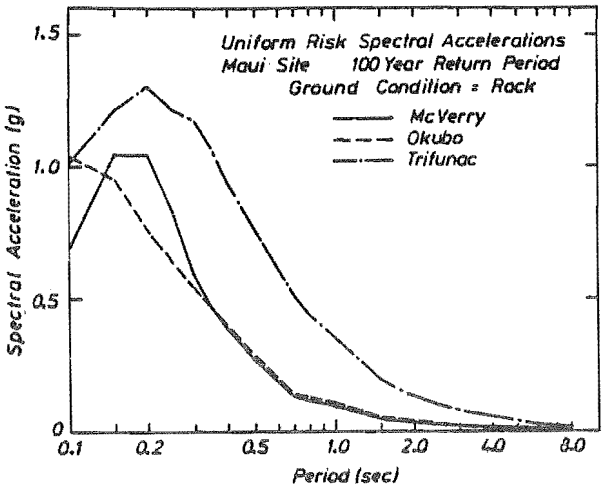

Fig. 3.8 Comparison of 100 Year Rock Spectra for Hard Ground at Maui Offshore Site

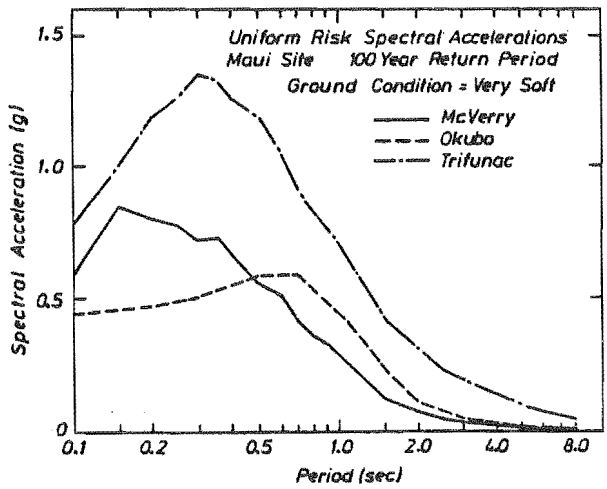

Fig. 3.9 Comparison of 100 Year Rock Spectra for Very Soft Ground at Maui Offshore Site

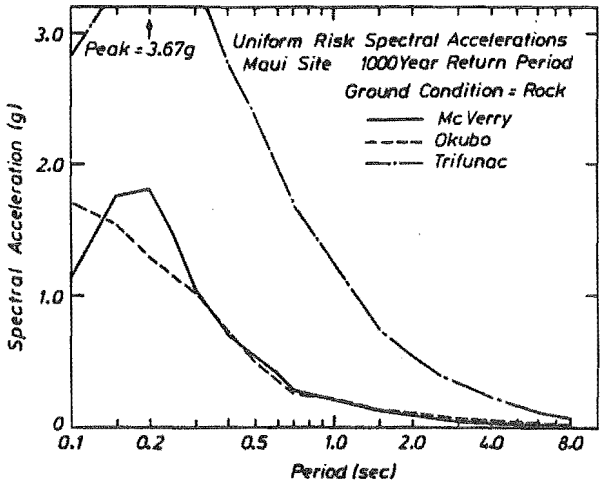

Fig. 3.10 Comparison of 1000 Year Rock Spectra for Hard Ground at Maui Offshore Site

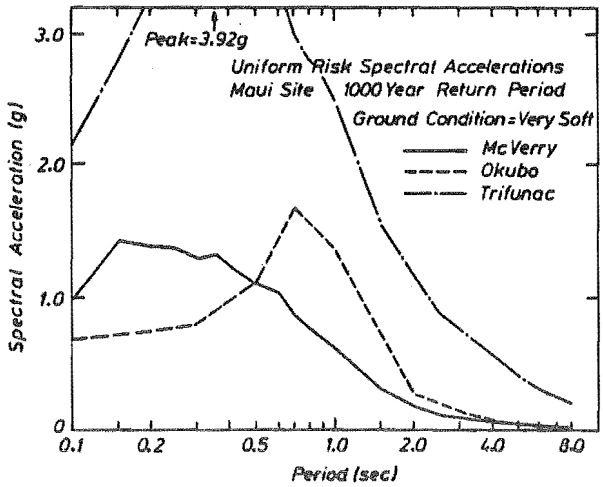

Fig. 3.11 Comparison of 1000 Year Rock Spectra for Very Soft Ground at Maui Offshore Site

3.5 RECENT LARGE EARTHQUAKES

3.5.1 Details of Some Recent Large Recorded Earthquakes

Modern strong-motion instruments for recording ground accelerations have been in use for about fifty years. Over this time many recordings have been made and the maximum recorded ground accelerations have progressively increased. However, there are still only relatively few recordings from the epicentral region of large earthquakes.

The El Centro record of the 18 May 1940 Imperial Valley, California earthquake indicated a maximum ground acceleration of approximately 0.35 g which was considered abnormally high at the time. Theories were advanced that the record was not representative of likely ground motions at close epicentral distances. As subsequent records have been obtained similar arguments have often been made to try to discount the validity of these extreme measurements. At present (1987) the strongest recorded horizontal ground shaking appears to be that from the Coyote Lake Dam site during the 1984 Morgan Hill, California earthquake where 1.3 g was measured. Ambraseys [3.14, 3.15] discussed the likely upper limits on intensity of ground shaking and suggested that the ability of the ground to transmit motions to the surface is probably only restricted by the finite shear strength of the material.

Table 3.7 lists some of the earthquakes and sites from which extreme strong-motion records have been obtained. Also tabulated are the maximum ground accelerations, epicentral distances and focal depths. In the remainder of this section a summary of the salient features of some of these earthquakes and recorded accelerograms is given.

Table 3.7 Details of some Extreme Strong-Motion Records

Earthquake	Local Magnitude	Depth (km)	Recording Site and Component	Epicentral Dist. (km)	Max. Ground Accel. (g)
Western U.S.					
Imperial Valley, 1940	6.7		El Centro NS	15	0.34
San Fernando, 1971	6.4		Pacoima Dam S14W	9	1.25
Imperial Valley, 1979	6.6	12	El Centro Array 5 230°	24	0.37
			El Centro Array 6 230°	24	0.44
			El Centro Array 7 230°	24	0.46
Morgan Hill, 1984	6.2	8	Coyote Lake Dam 285°	25	1.30
Other Earthquakes					
Miyagi-ken-Oki, 1978	7.4	30	JNR Sendai NS	100	0.44
Tabas, Iran, 1978	7.6	33	Tabas N16W	~ 60	0.96
Mexico City, 1985	8.1	20	SCI Compound	400	0.20

Imperial Valley, California, 1940 Earthquake [3.16]

The record from the El Centro site is one of the earliest strong-motion accelerograms obtained from the epicentral region of a moderate sized earthquake (M=6.7). This remained as the strongest record of ground shaking until the Parkfield earthquake in the 1960's. As a result many codes have used the El Centro record as a basis for earthquake resistant design requirements. It has been suggested that the mechanism of energy release in this earthquake was a complex multiple rupture mechanism which propagated away from the recording station and resulted in less intense levels of shaking than might have been expected. The peak horizontal ground acceleration measured in the El Centro record (0.34 g) is somewhat lower than has been measured in the epicentral region of recent earthquakes of similar magnitude.

San Fernando, California, 1971 Earthquake [3.17]

Although only a moderate magnitude earthquake (M=6.4), the Pacoima Dam record from the San Fernando earthquake indicated a peak horizontal ground acceleration of 1.25 g, the strongest measured up to that time. It has been proposed that the rupture propagated on a complex faulting plane upwards and towards the the Pacoima Dam site. Much debate has ensued among seismologists and earthquake engineers as to whether the the measured strength of shaking was representative for events of this magnitude. It is thought by some that the topographic relief at the Pacoima Dam site, combined with strong directivity effects, may have resulted in significant amplification of the free-field motions. Recently, Brune [3.18] conducted an experimental investigation using a scale model of the area and measured the relative amplitudes of the the motion at various locations. It was found that the Pacoima Dam site did not exhibit amplification for near vertical angles of incidence of ground waves. The study confirmed findings of theoretical studies that ground motion is amplified at the top of ridges while motion at the bottom of valleys tends to be reduced. The Pacoima Dam accelerograph was sited on a small rocky ridge near the bottom of a large canyon. Brune found from his model tests that the reduction in motion due to the effects of the canyon dominated any amplification effects due to the small ridge. Discussions of whether or

not the ground shaking at the Pacoima Dam site were exceptional will no doubt continue until more records are obtained with similar intensity, such as that from the 1984 Morgan Hill earthquake, discussed below.

Imperial Valley, California, 1979 Earthquake [3.19]

A comprehensive set of strong-motion accelerograph records was obtained from an array of instruments during this earthquake. The array traversed a known active fault and the closest of the recording sites was only about one kilometre perpendicular distance from the fault line. The epicentre was located approximately 25 km away and rupture propagated towards the instrument array. Thus it was expected that a strong directivity pattern would have developed with the recording stations being favourably sited to detect a large directivity effect. Calculated acceleration response spectra indicate very large response accelerations for structures with natural periods greater than about 2.5 seconds.

Morgan Hill, California, 1984 Earthquake [3.20]

The peak horizontal ground acceleration of 1.3 g measured at the Coyote Lake Dam during this magnitude 6.2 earthquake now supersedes the Pacoima Dam record as the largest instrumentally recorded horizontal ground acceleration. The acceleration response spectrum for structures with 5 percent of critical damping is also greater than the Pacoima Dam spectrum for vibration periods between 0.5 and 1.0 seconds, although the long and short period ordinates are somewhat less.

Miyagi-ken-Oki, Japan, 1978 Earthquake [3.21]

Unfortunately there were no strong-motion instruments located close to the epicentre of this large earthquake (M=7.4). There were a number of distant, moderate intensity, recordings obtained, with the strongest of these being at a distance of 100 km (JNR Sendai).

Tabas, Iran, 1978 Earthquake [3.22]

This large magnitude earthquake (M=7.6) occurred very close to a populated area of Iran and caused considerable damage and loss of life. The town of Tabas at an epicentral distance of approximately 60 km was almost completely destroyed. An accelerograph sited in Tabas recorded a maximum ground acceleration of 0.96 g. Response spectra computed from uncorrected accelerogram data by the author indicate that maximum response accelerations of 3.5 g are predicted for 0.2 second structures with 5 percent damping (cf 2.6 g for Pacoima Dam and 1.75 g for Morgan Hill records). The response accelerations for structures with long natural periods is also very large. Although the accelerogram data used was uncorrected, this was not expected to significantly affect the results.

3.5.2 Response Spectra from Recent Strong-Motion Recordings

Acceleration response spectra from the strong-motion earthquake recordings discussed in the previous section are presented in Figs. 3.12, 3.13 and 3.14 for single degree of freedom oscillators with 5 percent of critical damping.

Fig. 3.12 shows the response spectra for three Californian earthquake records from the 1940 Imperial Valley (El Centro record), 1971 San Fernando (Pacoima Dam record) and 1984 Morgan Hill (Coyote Lake Dam record) earthquakes. The maximum response spectral accelerations for structures with 5 percent damping from these records are approximately 1.0 g, 2.6 g and 1.75 g respectively. Normally a record with a larger peak ground acceleration will give larger response spectral accelerations. However, the Coyote Lake Dam record gives smaller responses than the Pacoima Dam record over most of the period range.

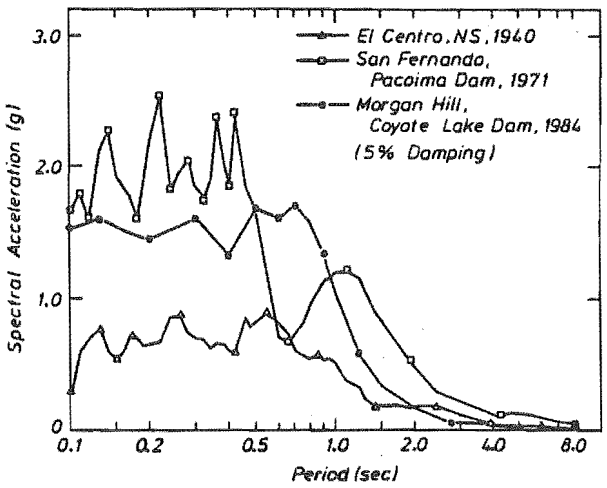

Fig. 3.12 5% Damped Acceleration Response Spectra from Three Californian Earthquakes

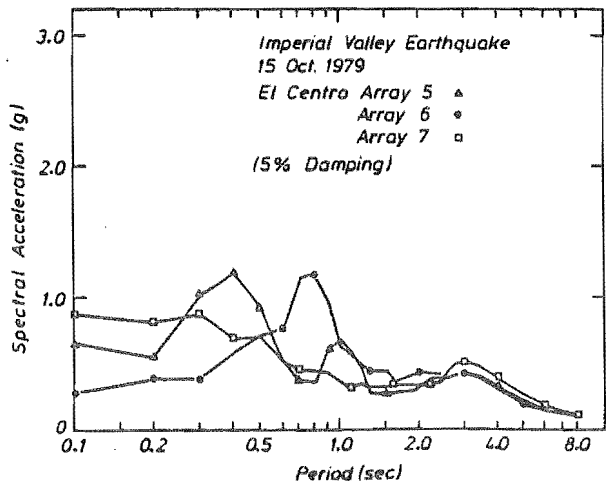

Fig. 3.13 5% Damped Acceleration Response Spectra from 1979 Imperial Valley Earthquake

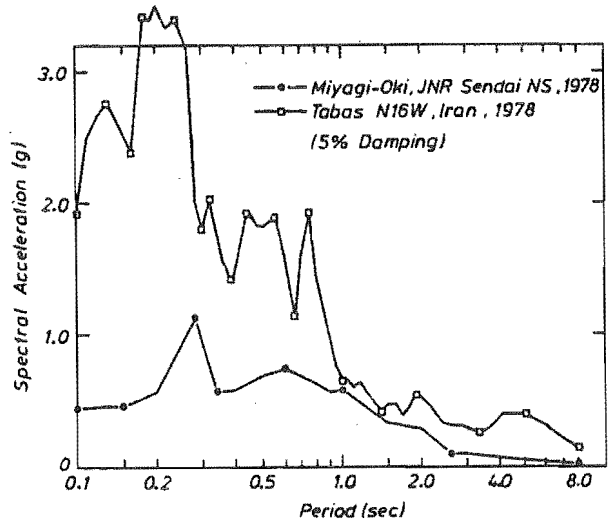

Fig. 3.14 5% Damped Acceleration Response Spectra from Earthquakes Outside U.S.

Acceleration response spectra for three records from the 1979 Imperial Valley earthquake are shown in Fig. 3.13. The response accelerations, which peak at about 1.2 g, are not as large as for some of the other spectra from large earthquakes but the ordinates of about 0.5 g for natural periods of around 3 seconds are larger than for any of the other records.

Fig. 3.14 shows response spectra for two large earthquakes from outside the United States. The 1978 Miyagi-ken-Oki earthquake gave the strongest Japanese instrumentally recorded horizontal free-field ground acceleration of 0.44 g even though the instrument was located at quite a large epicentral distance of 100 km. The maximum response spectral acceleration of 1.15 g occurs for natural periods of about 0.3 seconds.

Fig. 3.14 also shows the acceleration response spectrum for the 1978 Iranian earthquake recorded at Tabas. Response accelerations are very high over the period range 0.1 to 0.3 seconds. The response acceleration of 0.4 g for 4 to 5 second periods is also extremely large. The author computed the response spectrum in for the Tabas earthquake from uncorrected accelerogram data. It is not known what data processing would have been already carried out in converting the raw analogue recording from the instrument (SMA-1) to digital form. Normally, [3.16] low-pass filtering of the uncorrected data would be carried out to remove high frequency digitisation errors, and high-pass filtering to remove low frequency errors associated with matching of film segments (normally with about 10 seconds of record on each) and other effects. Baseline corrections are also performed to reduce any implied ground velocity at the end of the record to zero. It is thought that these corrections would not change the response spectra significantly over the range of periods of vibration of interest.

3.6 HAZARD ANALYSIS PREDICTIONS FOR NEW ZEALAND

3.6.1 Refined Presentation of Hazard Analysis Results

Hazard analyses have previously been carried out by Peek [3.3] and Mulholland [3.4]. Until the number of strong-motion earthquake records is more comprehensive or a substantially different attenuation relation is developed, the hazard analysis predictions will not change significantly. However, there have been minor recent changes in the seismicity and attenuation models. The risk maps available at present do not cover a very large area off the New Zealand coast. Also, those results have not been presented with long period structures, typical of offshore gravity platforms, in mind. A new analysis was completed as part of this study, specifically to provide information on the seismic hazard for offshore structures. For structures located on the New Zealand onshore area with natural periods up to about 2 seconds it is expected that these results will not differ greatly from those already available.

The Smith and Berryman seismicity model [3.5] was used by Mulholland [3.4] and is considered to be the best available model at present. The recently proposed McVerry attenuation relation, in which the Katayama et al relation was modified to account for the small set of New Zealand strong-motion data, is thought to be the most appropriate available at present. The limited New Zealand data agrees well with the Japanese data and the seismo-tectonic setting of the two countries is known to be quite similar.

The seismic hazard analysis results presented in this chapter are based on the Smith and Berryman seismicity model and the McVerry attenuation relation. It should be emphasised that both the seismicity and attenuation models are based on limited data, albeit the best available at present. The occurrence of large earthquakes in the future could significantly alter the seismicity model. Strong-motion recordings from such events could also substantially improve our predictions for attenuation of ground shaking.

Uniform risk acceleration response spectra were calculated for approximately 600 sites spaced at half degree intervals of latitude and longitude over New Zealand including a strip about 200 km wide around the coast. Spectral amplitudes were calculated for sites with hard ground conditions for return periods of 50, 100, 200, 500, 1000, 5000, and 10 000 years.

Peek and Mulholland both suggested that the shape of the spectra did not vary significantly over the country. While this was reasonable for structural response periods up to about 0.4 seconds, the differences for longer periods were up to about 100 percent. As the present study is concerned with offshore structures, often having significant response periods of 2 seconds or longer, it was decided to normalize the results from this study at 2 seconds. A uniform risk map of 2 second response accelerations for a return period of 200 years is shown in Fig. 3.15. The 200 year return period was chosen as it was expected to represent some sort of intermediate between likely design level and extreme level return periods. Uniform risk spectra for other return periods can be estimated from these values also.

Normalized risk spectra were derived for many sites by dividing by the 2 second ordinate, and the resulting spectra were plotted together. Some of those covering the range obtained are shown in Fig. 3.17. The maximum spectral accelerations occur predominantly at a period of 0.15 seconds with the normalized peak values varying between about 11 and 32. The shapes of the normalized spectra are all very similar, varying in a predictable manner depending on the peak value. Excellent prediction of normalized spectra at any site can be obtained by interpolating between the curves shown.

A map of uniform risk spectral acceleration ordinates for 0.15 second period structures is shown in Fig. 3.16 for return periods of 200 years on rock sites. These can be used together with the 2 second ordinates in Fig. 3.15 to determine the peak value of the normalized spectrum. The appropriate normalized spectrum can then be interpolated from Fig. 3.17 and the actual uniform risk acceleration response spectrum can be calculated by scaling by the 2 second ordinate. This two-parameter normalization appears to give a much better fit to the hazard analysis results over the entire range of response periods than the single parameter scaling used by Peek and Mulholland.

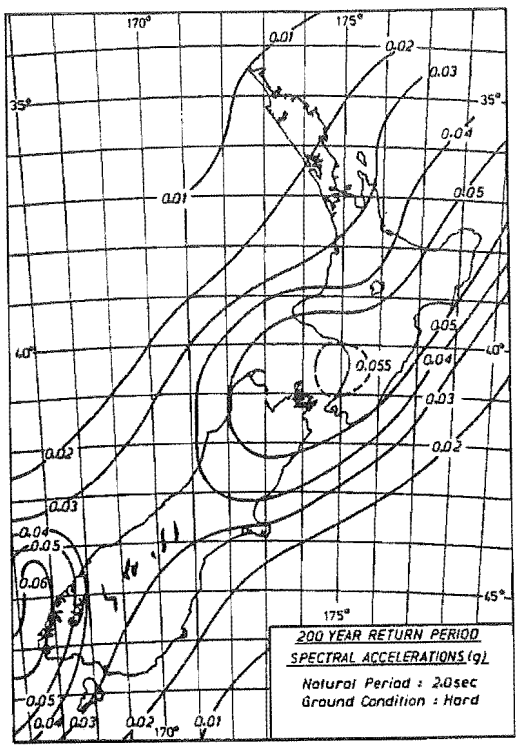

Fig. 3.15 Map of 2 Sec. Spectral Ordinates for 200 Year Return Period on Hard Ground

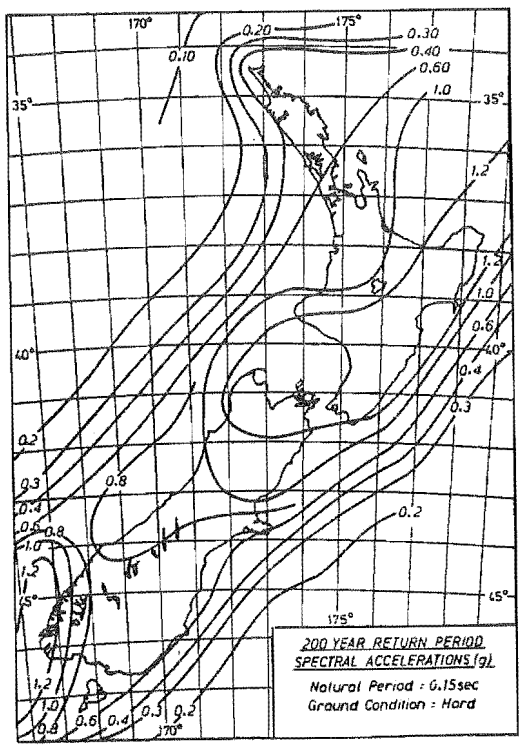

Fig. 3.16 Map of 0.15 Sec. Spectral Ordinates for 200 Year Return Period on Hard Ground

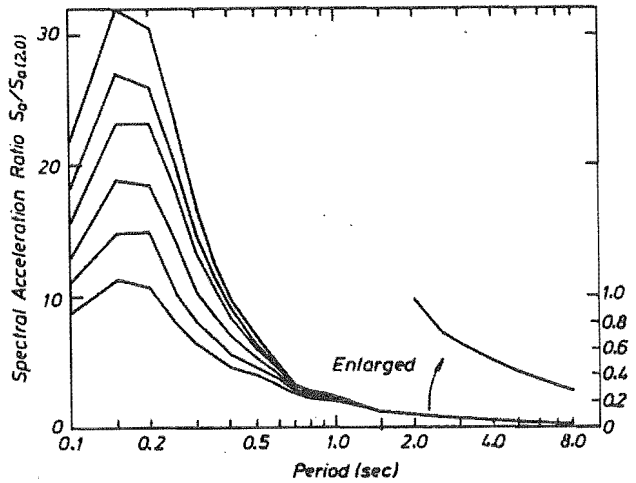

Fig. 3.17 Normalized Acceleration Response Spectra

The 2 second normalized spectra in Fig. 3.17 are effectively coincident for periods between 1 and 4 seconds. The single curve was extrapolated out to periods of 8 seconds using linear extrapolation of the logarithms of the periods and spectral ordinates, as discussed in Section 3.4.

It is interesting to compare the spectral contour maps in Figs. 3.15 and 3.16 with those produced previously by others. The maps derived in this study appear to give a better overview of the variation of hazard over New Zealand than previous maps in which the contours were restricted to mainly land coverage. It should be noted that judicious smoothing of the calculated contours was performed in obtaining the contour maps shown. In both maps there is a clear band of hazard which can be related to the historical pattern of seismic activity along the crustal plate boundaries. The remarkably parallel nature of the contours could lead to the suggestion that the real long-term hazard distribution is a very regular band and that irregularities in the derived contour maps may be a consequence of the limited duration for which earthquake records are available. However, some variation is likely due to geologic and tectonic variations over the country.

Previous studies [3.3, 3.4] have found that adequate estimates of spectra for a range of return periods can be made by simple scaling of the normalized spectral shape. Results from the present study confirmed this and scaling factors for return periods between 50 years and 10 000 years are shown in Fig. 3.18. Average scaling factors are shown for 0.15 second and 2.0 second

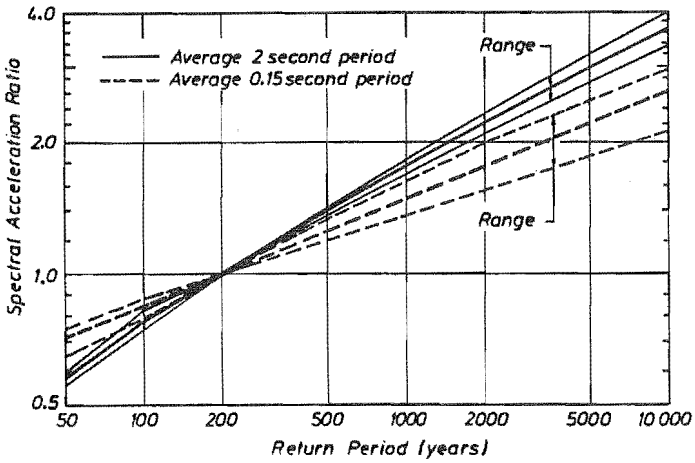

Fig. 3.18 Influence of Return Period on Spectral Acceleration Ratios

period ordinates together with the range of values found from the results at all sites considered. As suggested by McVerry [3.8], the relationship plotted using logarithmic scales, is effectively linear for the 0.15 second period and almost linear for the 2.0 second period results.

It was noted in Section 3.4.1 that uniform risk spectra for site conditions other than hard rock can be derived from the rock spectra by simply scaling the spectral ordinates by the ratio of the ground condition factors from the attenuation relation. The scaling factors for other ground condition types are given in Table 3.8. The factors for periods greater than 4 seconds have been estimated by the author.

Table 3.8 Scaling Factors for Ground Conditions Other Than Rock (McVerry Attenuation Relation)

Natural Period	Ground Condition		
	Type II	Type III	Type IV
0.1	0.85	0.95	0.841
0.15	0.84	0.91	0.806
0.2	0.88	0.95	0.763
0.25	0.95	1.06	0.955
0.3	1.19	1.35	1.20
0.35	1.36	1.61	1.53
0.4	1.47	1.75	1.73
0.5	1.48	1.83	2.04
0.6	1.62	2.16	2.56
0.7	1.78	2.36	2.96
0.8	1.90	2.40	3.03
0.9	1.95	2.43	2.93
1.0	2.06	2.47	2.88
1.5	1.71	2.08	2.56
2.0	1.49	1.79	1.87
2.5	1.49	1.60	1.51
3.0	1.41	1.52	1.41
4.0	1.29	1.54	1.22
5.0	1.20	1.40	1.10
6.0	1.10	1.25	1.05
7.0	1.05	1.10	1.02
8.0	1.00	1.00	1.00

3.6.2 Summary of Method for Determining Hazard Spectra

The method for determining uniform risk acceleration response spectra for any site, return period and ground condition is summarised below. The method is similar to that proposed by Peek [3.3] and Mulholland [3.4] but considers a two parameter normalized spectrum.

1) Read off 200 year rock site spectral ordinates for 0.15 second and 2.0 second period structures from Figs. 3.15 and 3.16.

2) Calculate ratio of 0.15 second to 2.0 second ordinates and determine appropriate normalized spectrum by linear interpolation between the curves in Fig. 3.17.

3) Scale the normalized spectrum by the 2.0 second spectral ordinate obtained in 1) to give the 200 year hard ground uniform risk spectrum.

4) Scale the 200 year spectrum by the factor obtained from Fig. 3.18 to adjust the spectrum to the desired return period.

5) Scale the rock spectrum by the factors given in Table 3.8 for the appropriate ground condition at the site.

6) If spectral ordinates are required for structures with natural periods greater than 4 seconds log-log linear extrapolation up to periods of about 8.0 seconds is considered reasonable.

3.7 ACCELERATION RESPONSE SPECTRA FOR DESIGN

In comparing results presented in the previous sections it is apparent that uniform risk acceleration response spectra predicted by the hazard analysis are significantly less than spectral ordinates calculated from accelerograms of some of the large recorded earthquakes, even for return periods of one thousand years or more. This applies particularly for periods of vibration greater than about 2 seconds. It is noted that longer period structures will in general be large, important structures and that attenuation relations are probably less reliable at these longer periods. It seems prudent therefore, in using hazard analysis results to develop acceleration response spectra for design purposes, to make allowances for these apparent defficiencies and to adopt suitably cautious estimates.

Recently a draft amendment was proposed to NZS 4203, The New Zealand Standard Code of Practice for General Structural Design and Design Loadings for Buildings. As part of this amendment a revised method of determining design earthquake loadings for building structures has been suggested, based on recent seismic hazard analysis work and the assumption of a constant pseudo spectral velocity at large periods of vibration.

The revised NZS 4203 method calculates the total horizontal design shear force V for a structure using the formula in Eqn. 3.7.

$$V = C_\mu R Z W_t \qquad (3.7)$$

where C_μ = Basic seismic spectral acceleration coefficient
R = A factor to allow for the return period of earthquake shaking
Z = A zone factor to account for the regional variation of seismic hazard
W_t = Total seismic weight of the structure

The basic seismic spectral acceleration coefficient C_μ is found from Fig. 3.19. The coefficient depends on the fundamental natural period of vibration, the soil condition and the available structure displacement ductility factor μ which is considered appropriate. The factor R is found from Fig. 3.20 and allows for return period, or its reciprocal, the annual probability of exceedance f_E. The basic spectral coefficients are appropriate for a return period of approximately 150 years in which case R = 1.0. The zone factor Z is obtained from Fig. 3.21 and allows for variations in hazard over New Zealand, as predicted by seismic hazard analysis.

Acceleration response spectra obtained from the hazard analysis presented in this section are compared with design spectra from the proposed amendment to NZS 4203 in Figs. 3.22 and 3.23. Those figures show 1000 year return period spectra for structures with 5 percent damping at the Maui offshore site, for hard and soft ground conditions. Also shown is the envelope of spectra presented in Section 3.5.2 from extreme strong-motion earthquake records.

The spectra from the proposed amendments to NZS 4203 appear to provide a realistic compromise between the results from seismic hazard analysis and available strong-motion records. The author suggests that they provide an adequate presentation of the current state of knowledge of earthquake hazard to structures in New Zealand and could be used for design purposes.

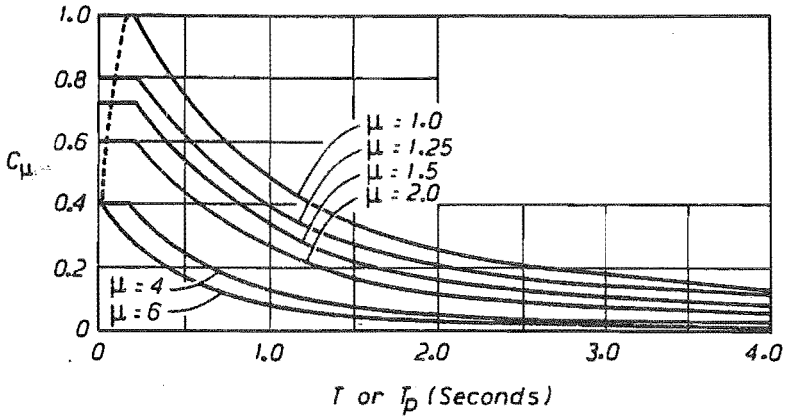

(a) NORMAL SOILS

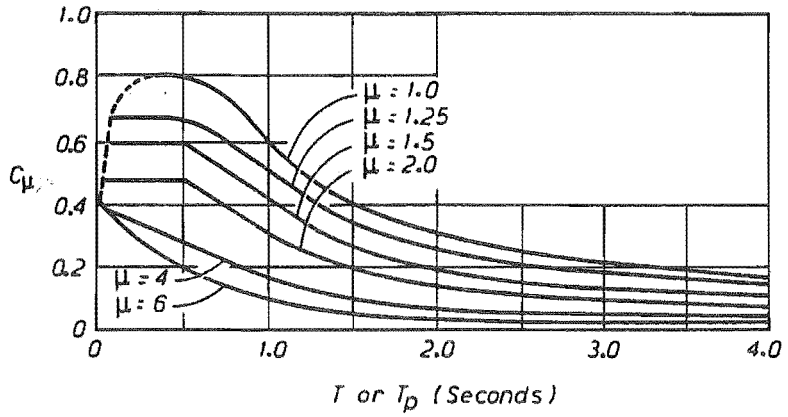

(b) SOFT SOILS

Fig. 3.19 C_μ Values for Proposed NZS 4203 Earthquake Loading Determination

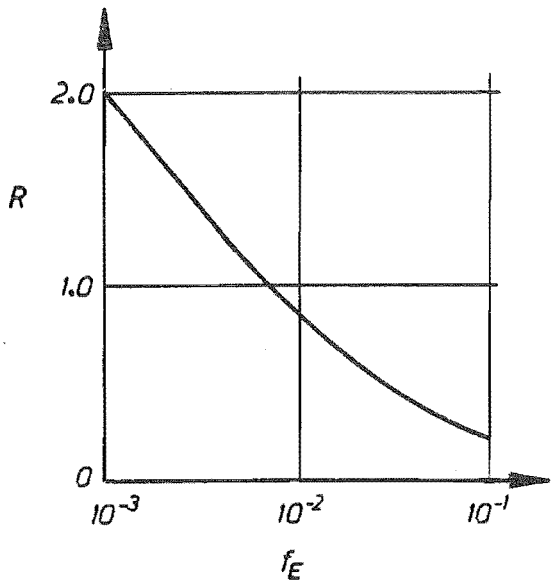

Fig. 3.20 Return Period Factor R for Proposed NZS 4203 Earthquake Loading Determination

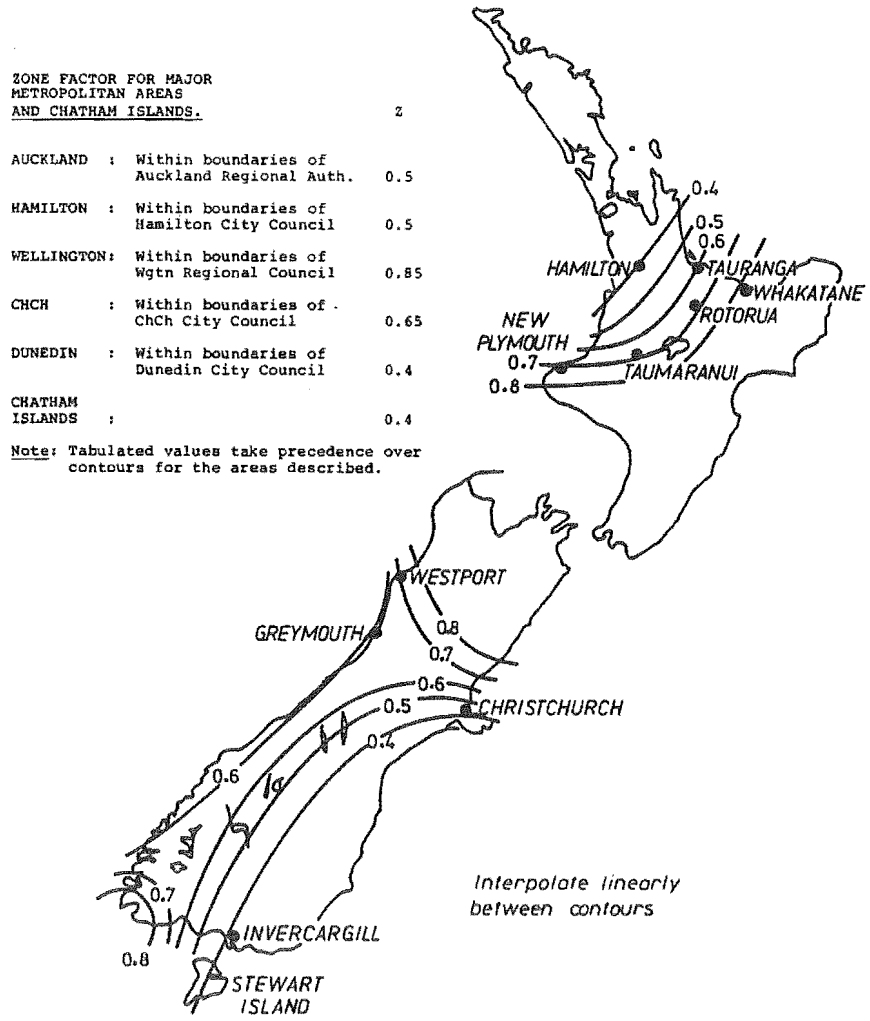

Fig. 3.21 Zone Factor Z for Proposed NZS 4203 Earthquake Loading Determination

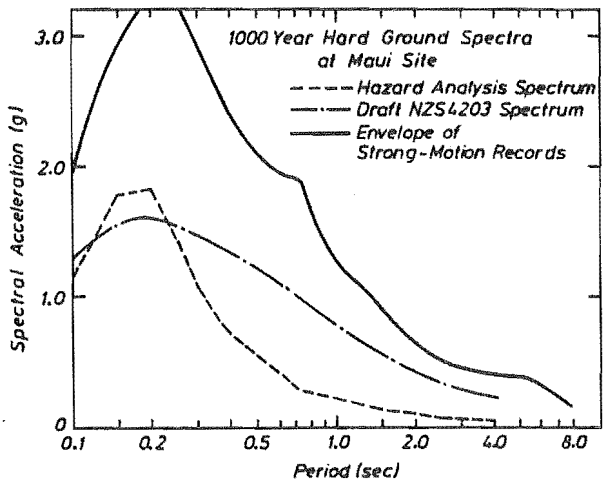

Fig. 3.22 Comparison of Hazard Analysis Results with Proposed NZS 4203 Spectra for Hard Ground

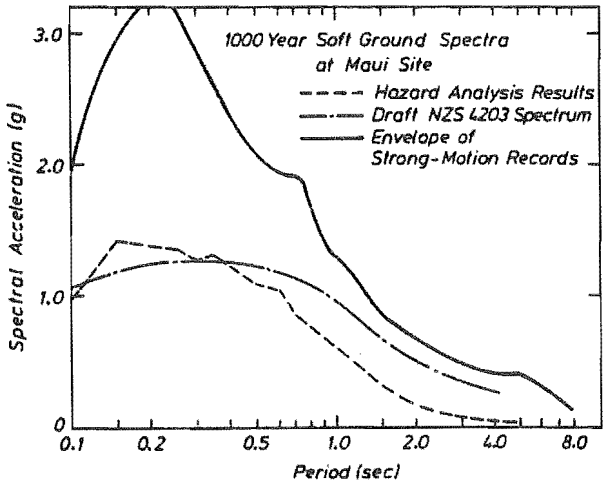

Fig. 3.23 Comparison of Hazard Analysis Results with Proposed NZS 4203 Spectra for Soft Ground

3.8 CONCLUSIONS

1. Seismic hazard analysis predictions are now being used as a basis for earthquake design spectra specified by structural design codes. Details of the seismicity model and attenuation relation, which are combined probabilistically in a seismic hazard analysis, were discussed. Recently proposed seismicity models and attenuation relations for New Zealand were presented.

2. Attenuation relations from the western United States and Japan were compared. These gave large differences in predicted intensity of structural response and uniform risk acceleration response spectra for some particular examples investigated. Uniform risk spectral magnitudes are quite sensitive to the implied scatter of recorded data about the mean of the attenuation relation. United States attenuation data appears to show greater scatter about the mean attenuation predictions and this results in substantially higher uniform risk values than obtained using the Japanese attenuation relation. The seismo-tectonic setting of New Zealand is expected to be more similar to Japan than that of the western United States. This is supported by limited New Zealand data.

3. Results of a seismic hazard analysis conducted by the author for New Zealand and the surrounding offshore area were presented. The recently proposed seismicity model, and attenuation relation based mainly on Japanese data, were used. Results were presented with particular emphasis on long period offshore structures in mind. This resulted in a slightly refined presentation compared with similar results presented by others in the past.

4. Design of large, important structures for earthquake effects normally considers very intense earthquake shaking corresponding to return periods of the order of one thousand years or more. It is considered prudent to ensure that design spectra corresponding to such extreme events should not differ too greatly from the response spectra of the few large earthquake records that have been obtained worldwide to date. Recent large earthquakes and the acceleration response spectra derived from their accelerograms were discussed. A suitable compromise between the hazard analysis results and available extreme earthquake records is made by the design spectra in the recently proposed amendment to the New Zealand Loadings Code NZS 4203.

3.8 REFERENCES - CHAPTER 3

3.1 Cornell, C. A. , "Engineering Seismic Risk Analysis", Bulletin of Seismological Society of America, Vol. 58, No. 5, 1968, pp 1583-1606.

3.2 McGuire, R. K. , "Seismic Structural Risk Analysis, Incorporating Peak Responses, Regressions on Earthquake Magnitude and Distance", Dept. of Civil Engineering, Research Report R74-51, Massachusetts Institute of Technology, Cambridge, Massachusetts, 1974.

3.3 Peek, R. , "Estimation of Seismic Risk for New Zealand, A Seismicity Model and Preliminary Design Spectra", Dept. of Civil Engineering Research Report 80-21, University of Canterbury, 1980. 84 pp.

3.4 Mulholland, W. M. , "Estimation of Design Earthquake Motions for New Zealand", Dept. of Civil Engineering Research Report 82-9, University of Canterbury, 1982, 97 pp.

3.5 Smith, W. D. and Berryman, K. R. , "Revised Estimates of Earthquake Hazard in New Zealand", Bulletin of the New Zealand National Society for Earthquake Engineering, Vol. 16, No. 4, 1983, pp259-272.

3.6 Eiby, G. A. , "Earthquakes", Heinemann, 1980, 209 pp.

3.7 Adams, J., "Paleoseismicity of the Alpine Fault Seismic Gap, New Zealand", Geology, Vol. 8, 1980, pp 72-76.

3.8 McVerry, G. H. , "Uncertainties in Attenuation Relations for New Zealand Seismic Hazard Analysis", Bulletin of the New Zealand National Society for Earthquake Engineering, Vol. 19, No. 1, March 1986, pp 28-39.

3.9 Katayama, T. , Iwasaki, T. and Mitsuaki, S. , "Statistical Analysis of Earthquake Acceleration Response Spectra", Trans. Japan Society of Civil Engineers, Vol. 10, 1978, pp 311-318.

3.10 Okubo, T. , Arakawa, T. and Kawashima, K. , "Attenuation of Peak Ground Motions and Absolute Acceleration Response Spectra With Use of Japanese Strong Motion Data", International Symposium on Lifeline Earthquake Engineering, ASME PVP-77, Portland, Oregon, 1983, pp 378-385.

3.11 Trifunac, M. D. and Anderson, J. G. , "Preliminary Empirical Models for Scaling Absolute Acceleration Spectra", Department of Civil Engineering Report No. CE 77-03, University of Southern California, August 1977.

3.12 Berrill, J. B. , "Distribution of Scatter in New Zealand Accelerograph Data", Bulletin of the New Zealand National Society for Earthquake Engineering, Vol. 18, No. 2, 1985, pp151-164.

3.13 Katayama, T. and Shino, I. , "An Engineering Study of Long-Period Strong Motion Using Displacement Seismograph Records", Proc. 8th World Conference on Earthquake Engineering, Vol. 2, San Francisco, 1984, pp 289-296.

3.14 Ambraseys, N. N. , "Dynamics and Response of Foundation Materials in Epicentral Regions of Strong Earthquakes", Proc. 5th World Conference on Earthquake Engineering, Rome, 1974, pp CXXVI - CXLVIII.

3.15 Ambraseys, N. N. , "Factors Controlling the Earthquake Response of Foundation Materials", Proc. 3rd European Symposium on Earthquake Engineering, 1970, pp 309-317.

3.16 Hudson, D. E. , "Reading and Interpreting Strong Motion Accelerograms", Earthquake Engineering Research Institute, Berkeley, California, 1979.

3.17 "Analyses of Strong Motion Earthquake Accelerograms", California Institute of Technology, Earthquake Engineering Research Laboratory Series.

3.18 Brune, J. N. , "Preliminary Results on Topographic Seismic Amplification Effect on a Foam Rubber Model of the Topography Near Pacoima Dam", Proc. 8th World Conference on Earthquake Engineering, San Francisco, 1984, Vol II, pp 663-670.

3.19 Brady, A. G. , Perez, V. and Mork, P. N. , "The Imperial Valley Earthquake, October 15 1979. Digitisation and Processing of Accelerograph Records", United States Department of the Interior, Geological Survey, Seismic Engineering Data Report 80 - 703, April 1980.

3.20 "The 1984 Morgan Hill, California Earthquake", California Department of Conservation, Division of Mines and Geology, Special Publication 68, 1984.

3.21 "Miyagi-ken-Oki, Japan Earthquake, June 12 1978", Earthquake Engineering Research Institute, Reconnaissance Report, December 1978.

3.22 Moinfar, A. A. and Adinazari, H. , "The Tabas Earthquake of 16th. Sept. 1978, Main Shock Acceleration - Time History and Related Uncorrected Data", Islamic Republic of Iran, Ministry of Housing and Urban Development, Building and Housing Research Center, July 1982.

3.23 NZS 4203: 1984, "Code of Practice for General Structural Design and Design Loadings for Buildings", Standards Association of New Zealand, Wellington, 100 pp.

3.24 Berrill, J. B. , "Seismic Hazard Analysis and Design Loads", Bulletin of the New Zealand National Society for Earthquake Engineering, Vol. 18, No. 2, June 1985, pp139-150.

Chapter 4

ANALYSIS OF SITE RESPONSE EFFECTS

4.1 INTRODUCTION

In Chapter 3 results of seismic hazard analyses were used to predict uniform risk acceleration response spectra for structures in New Zealand. The hazard analysis results, and the final spectra suggested as being suitable for design purposes, allowed for hard and soft ground conditions. It is likely that the results for soft ground conditions would be more appropriate for most offshore sites where marine sediments often extend to great depths. Because offshore platform structures are such important facilities it may be appropriate to investigate the response characteristics of each particular site to establish how the actual foundation materials may influence the character of the ground motions expected there. Offshore structures are normally installed for recovery of subsea resources so it is likely that the exploration phase would have provided detailed borelog information regarding the distribution of material properties with depth. Soil samples may also have been recovered enabling the dynamic response properties of the materials to be determined.

It is widely recognised that local site conditions modify the nature of ground motions arriving from the far-field. Sites with flexible material can significantly amplify the strength of ground shaking above the level which would be felt on a relatively rigid rock site. Material damping and nonlinear stress-strain behaviour can also attenuate the strength of ground shaking. The behaviour of soft nonlinear foundation materials is complex and not easily quantified.

In this brief study the site response of some well defined example sites was considered to investigate how particular ground motions arriving at a site could be modified by the presence of flexible nonlinear soil deposits. Dynamic time history analyses of simple one-dimensional offshore site models, representing saturated soil deposits over competent bedrock, were carried out. Methods of dynamic analysis including equivalent linear and nonlinear methods were compared. Other factors investigated were the effects of dynamic model complexity, depth of soil deposit, intensity of input excitation, and the type of stress-strain behaviour used for nonlinear analysis. Simple two-dimensional site models were also investigated in which a typical concrete gravity platform was modelled, in order to assess the foundation-structure interaction effects.

4.2 HASKELL'S LAYERED SITE ANALYSIS

Haskell [4.1] presented a theoretical method for predicting the amplitude of the free surface displacement due to plane SH waves incident at the base of a layered crust. The method is based on the principles of wave propagation through elastic media and does not allow for any material damping. Wave fronts impinging at any angle of incidence to the base layer, and any number of layers can be considered.

For the case of a single surface layer with vertically incident plane SH waves the surface displacement is given in terms of the incident wave amplitude by the expression in Eqn. 4.1.

$$D_s / 2 D_i = (\cos^2 Q + r^2 \sin^2 Q)^{-1/2} \qquad (4.1)$$

where D_s = amplitude of surface displacement response
D_i = amplitude of incident displacement wave at base of layer
Q = $\omega d / c_s$ = a dimensionless frequency parameter
ω = circular frequency of incident wave
d = thickness of surface layer

r = $\rho_s c_s / \rho_b c_b$ the acoustic impedance ratio
ρ_s = mass density of surface layer
ρ_b = mass density of basement material
c_s = shear wave propagation speed in surface layer
c_b = shear wave propagation speed in basement material

This expression is a transfer function with the amplitude ratio being given as a function of frequency of the ground waves. The factor of two is included to allow for the free surface doubling effect.

For the case of a soft soil over competent basement rock the acoustic impedance of the soil will be much less than that of the rock and Eqn. 4.1 will have an infinite number of maxima at periods of vibration given by Eqn. 4.2.

$$T_m = 4d / mc_s \qquad m = 1, 3, 5, \ldots \tag{4.2}$$

These are the natural periods of vibration of a uniform shear beam. At all natural periods Eqn. 4.1 takes the values given by Eqn. 4.3, with the amplitude ratio being equal to the reciprocal of the acoustic impedance ratio of the two materials.

$$\begin{aligned} D_s / 2 D_i &= 1/r \\ &= \rho_b c_b / \rho_s c_s \end{aligned} \tag{4.3}$$

A complete transfer function was calculated for the case of the simple site which is shown in Fig. 4.1. A 200 m thick layer of uniform dense sand over bedrock was assumed. The mass densities of soil and rock were assumed to be 1600 kg/m^3 and 2600 kg/m^3 respectively and the shear wave speeds were assumed to be 300 m/s and 3000 m/s respectively. The complete transfer function is shown in Fig. 4.2. The first few natural periods of the site are 2.67 sec, 0.889 sec, 0.533 sec, 0.381 sec . . . and so on. The maxima in the transfer function all have a value of 16.25.

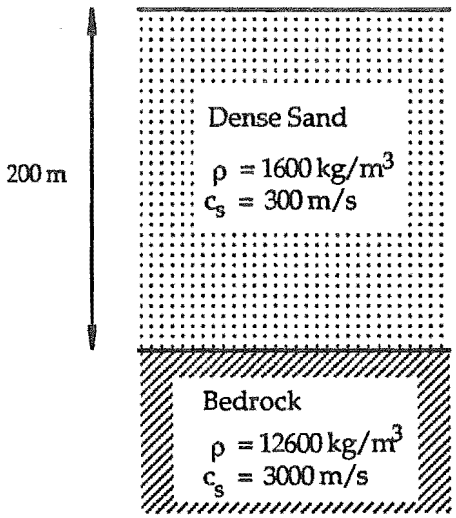

Fig. 4.1 Simple Site Profile for Haskell Analysis

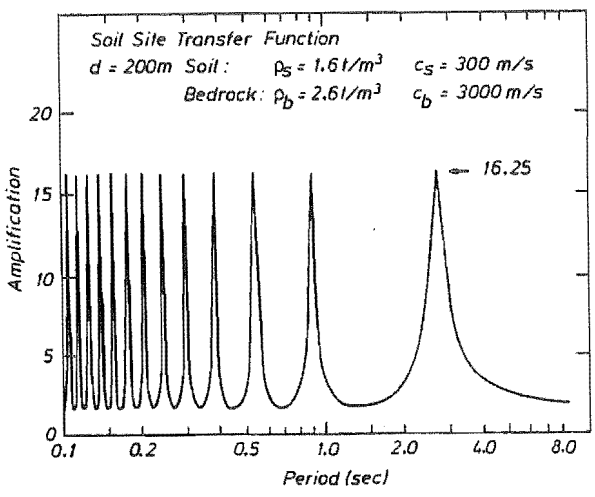

Fig. 4.2 Transfer Function Derived Using Haskell Method

It is possible to allow for the variation in soil properties which would normally occur with depth at a site by considering many layers, each with different properties. Theoretically, the complete transfer function for the site could be determined and the steady-state surface response could be calculated for any basement input motion in the frequency domain. This

would require transforming the input motion to the frequency domain, multiplying the resulting Fourier amplitude spectrum by the transfer function, and transforming back to the time domain. Non-periodic motions associated with earthquake shaking could also be considered and transformed to the frequency domain using discrete Fourier transforms. Thus, in theory, it would be possible to estimate the response at the surface of a soil deposit due to input ground motions from the underlying bedrock.

In practice the Haskell analysis is likely to be of very limited use for predicting the amplitude of ground surface motions due to earthquake shaking. The method is only applicable to the steady-state response of elastic undamped systems. From the results of nonlinear site response analyses described later in this chapter, it is clear that typical soil deposits would have substantial shear strains induced in them during shaking caused by moderate to large earthquakes. This would cause large changes in shear stiffness and would be associated with substantial amounts of material damping. The undamped response predictions would be expected to grossly over-estimate the real levels of response which would occur. The response is also transient rather than steady-state and the resonant response in each frequency may not have time to develop.

4.3 DYNAMIC SOIL PROPERTIES

In order to carry out dynamic analyses of site response effects it is necessary to have information on the dynamic properties of the materials present. Rock materials probably respond elastically up to quite large ground motion intensities but soils are expected to be highly nonlinear. Accurate prediction of dynamic response of soil deposits may require the use of nonlinear constitutive relations. Such relations could be determined from laboratory testing of actual soil samples. In this study approximate methods of representing the nonlinear stress-strain behaviour of soil were considered.

Seed et al [4.2] presented dynamic soil moduli from a large number of steady-state and free vibration tests on soil samples, mainly sands. Fewer results were presented for cohesive materials and a greater scatter is evident. An idealised steady-state nonlinear soil shear stress versus shear strain behaviour is shown in Fig. 4.3. The amount of nonlinearity is generally dependent on the level of shear strain imposed on the soil during the response, with greater nonlinearity being expected for larger soil shear strains. Nonlinear behaviour can be approximated as an equivalent linear response by specifying the secant stiffness and an equivalent amount of viscous damping. The secant stiffness is simply the stress divided by the strain at the point of load reversal. The amount of viscous damping can be related to the energy dissipated in each complete cycle of response, which can be calculated from the area within the stress-strain hysteresis loop.

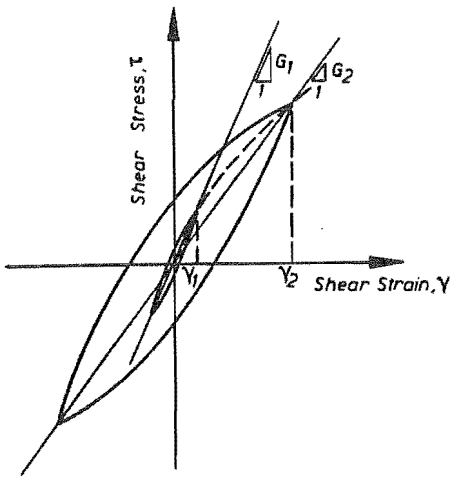

Fig. 4.3 Nonlinear Soil Stress-Strain Behaviour

The shear modulus of sands can be estimated from the expression given by Seed et al in Eqn. 4.4. It should be noted that this expression is a metric version adapted from the original equation which used imperial units.

$$G = 220\, K_2(\gamma)\, (\sigma_m')^{0.5} \qquad (4.4)$$

In this equation G is the shear modulus (kPa units), K_2 is a constant depending on the level of shear strain γ, and σ_m' is the mean effective confining stress (kPa units), which depends on the depth of overburden and its properties.

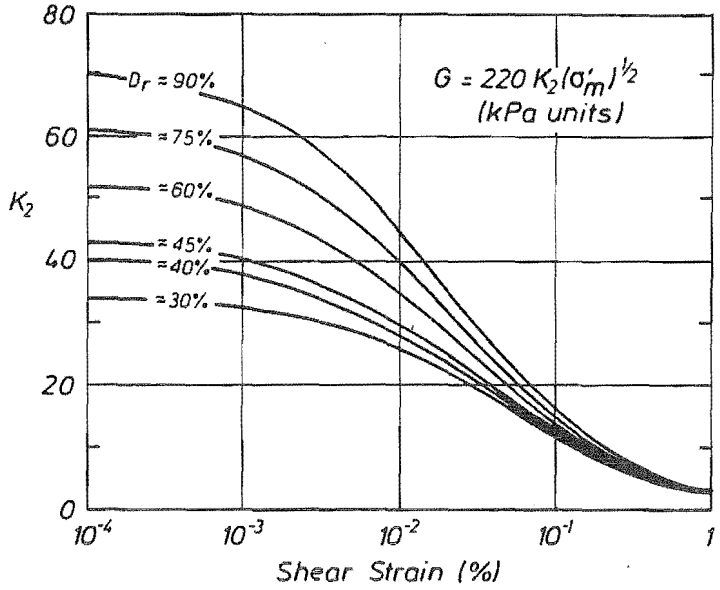

Fig. 4.4 Dependence of Softening Parameter K_2 on Soil Shear Strain

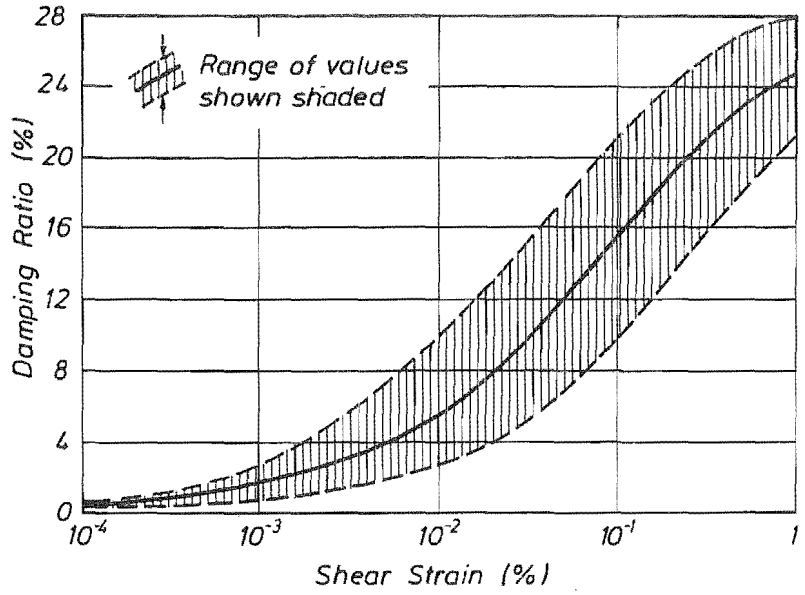

Fig. 4.5 Dependence of Viscous Damping Ratio λ on Soil Shear Strain

Values for the parameter K_2 are given by Seed et al and are reproduced here as Fig. 4.4. The actual values depend on the relative density of the sand. For a dense sand with relative density of 90 percent, which was assumed in this work, K_2 varies from a small strain value of 70 for $\gamma < 10^{-4}$ percent to a large strain value of 3 for $\gamma > 1$ percent. Soil softens and the shear modulus decreases as the level of shear strain increases. It was convenient to define a stiffness reduction factor $k(\gamma)$ giving the ratio of the shear modulus G at any particular soil shear strain to the initial small strain shear modulus G_i as in Eqn. 4.5.

$$k(\gamma) = G(\gamma) / G_i \qquad (4.5)$$

Equivalent viscous damping is also plotted by Seed et al as in Fig. 4.5 which gives the percentages of critical damping as a function of soil shear strain. The values range from a small strain value of 0.5 percent for $\gamma < 10^{-4}$ percent to a large strain value of 25 percent for $\gamma >$ 1 percent.

4.4 EQUIVALENT LINEAR DYNAMIC ANALYSIS OF SITE RESPONSE

For structural systems which are only slightly nonlinear the equivalent linear method of analysis can be used to approximate the actual nonlinear load versus deformation behaviour. The nonlinear response of soil deposits was investigated in this study using nonlinear stress-strain soil models but a limited number of analyses were also performed using the equivalent linear method. Secant shear moduli and equivalent viscous damping percentages were estimated using the values given by Seed et al.

In applying the equivalent linear method it is necessary to use an iterative approach to allow for the nonlinear soil response. For example, the secant stiffness and damping ratios can be based on estimated maximum soil shear strains, and a dynamic analysis carried out. From the maximum soil shear strains predicted during the analysis the equivalent linear properties can be reestimated. This procedure is repeated until convergence is obtained.

There is a difficulty in using the equivalent linear method with regard to damping. The maximum soil shear strains generated in each member of the dynamic model will in general be different, thus leading to different equivalent viscous damping levels being required in each member. It is not possible to derive a damping matrix which corresponds to specified fractions of critical damping in each member. An average level of damping from all members must be used in order to estimate the damping matrix for the subsequent analysis iteration. Where there is a substantial variation in soil shear strains this could be a rather severe limitation.

It appears that the more direct approach of modelling the nonlinear stress-strain behaviour of soil with an appropriate hysteresis rule is more realistic and simpler to apply.

4.5 NONLINEAR DYNAMIC ANALYSIS OF SITE RESPONSE

4.5.1 Comparison of Equivalent Viscous Damping and Nonlinear Hysteresis

The actual stress-strain behaviour of most soils is highly nonlinear for levels of strain which are likely to develop during ground shaking caused by moderate to large earthquakes. The best predictions of dynamic response of soil deposits are likely to be obtained by using dynamic analysis procedures incorporating realistic representations of the nonlinear stress-strain behaviour.

In this study nonlinear dynamic analysis of soil deposits was carried out using various hysteresis rules for soil stress-strain behaviour. It was still necessary to use an iterative approach to complete an analysis. The parameters for controlling the hysteresis behaviour were calculated in each iteration using the reverse procedure to that used by Seed et al in deriving the equivalent linear soil stiffnesses and damping moduli. Five quantities were

known for every member after each iteration of analysis. These were the maximum force and internal displacement (strain), the initial shear modulus, the secant shear modulus and the fraction of critical damping implied by the level of soil shear strain. It was thus possible to uniquely determine up to five parameters to govern the hysteresis behaviour. Bilinear and Ramberg-Osgood hysteresis rules were both used as these could be completely defined using five parameters.

The initial stiffness was calculated from the small strain shear modulus. The secant shear modulus could be estimated from Eqn. 4.1 knowing the maximum shear strain in the soil. Also, the area within the hysteresis loop could be estimated from the level of equivalent viscous damping by assuming steady-state harmonic response.

The relationship between viscous damping and equivalent hysteretic damping can be determined by considering the resonant steady-state response of a single degree of freedom oscillator. If the damping forces F_D are plotted against the displacement d over a complete cycle of response an ellipse is generated as shown in Fig. 4.6 with length of the horizontal axis equal to $2d_{max}$, where d_{max} is the maximum displacement, and length of the vertical axis equal to $2F_{Dmax}$, where F_{Dmax} is the maximum damping force. The area of the ellipse represents the work done , or energy dissipated, by the viscous damping forces per cycle, W_D as given by Eqn. 4.6. This can be equated to the area within the force versus displacement hysteresis loop in an equivalent nonlinear system.

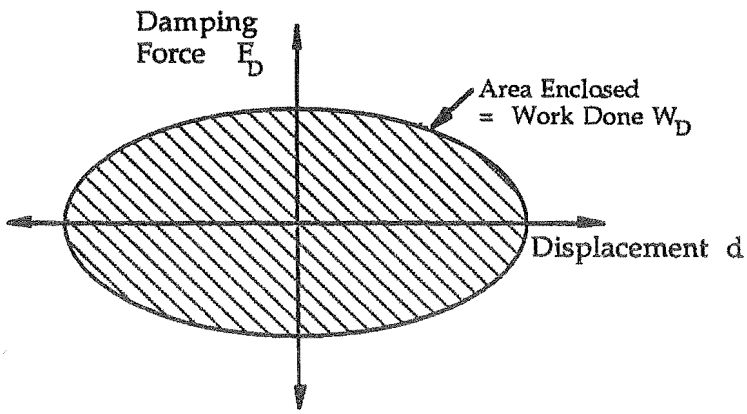

Fig. 4.6 Single Degree of Freedom Steady State Damping Forces Versus Displacement

$$W_D = \pi F_{Dmax} d_{max} \qquad (4.6)$$

The maximum damping force F_{Dmax} in the viscously damped system given by Eqn. 4.7 where C is the damping coefficient, v_{max} is the maximum velocity and ω is the circular natural frequency of response.

$$F_{Dmax} = C v_{max}$$

$$= C\omega d_{max} \qquad (4.7)$$

The damping coefficient C can be expressed in terms of the fraction of critical damping λ and the critical damping coefficient C_c which is dependent on the mass M or spring stiffness K and circular frequency as in Eqn. 4.8.

$$C = \lambda C_c$$

$$= \lambda 2M\omega$$

$$= \lambda 2K/\omega \qquad (4.8)$$

These expressions can be substituted into Eqn. 4.6 to equate the area in the nonlinear hysteresis loop to the fraction of critical damping λ, and the maximum elastic force F_{max} and displacement d_{max}, as indicated by Eqn. 4.9.

$$W_D = 2\pi \lambda F_{max} d_{max} \qquad (4.9)$$

where $F_{max} = K d_{max}$ (4.10)

4.5.2 Bilinear Hysteresis Model

Bilinear force versus displacement behaviour is shown in Fig. 4.7. F is force and d is displacement. F_y and d_y are the yield force and the yield displacement, and F_{max} and d_{max} are the maximum elastic force and displacement attained in each cycle of response. K_i is the initial loading stiffness which in this case is assumed to be equal to the unloading stiffness as indicated. βK_i is the second slope stiffness after yielding has occurred. K_s is the secant stiffness, which for shear type members can be related to the initial stiffness by the expression in Eqn. 4.11.

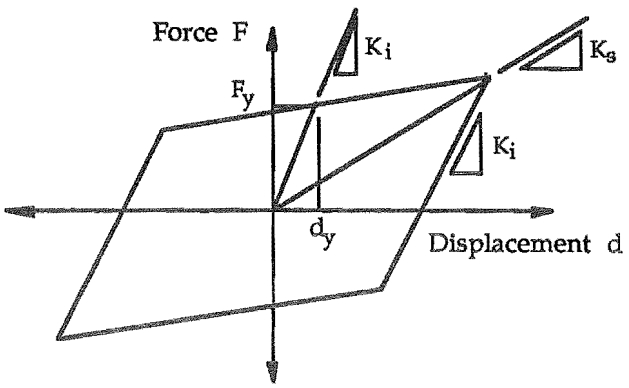

Fig. 4.7 Bilinear Force Versus Displacement Hysteresis

$$K_s = k(\gamma) K_i \qquad (4.11)$$

A ductility factor μ can also be defined relating the maximum displacement to the yield displacement, as in Eqn. 4.12.

$$\mu = d_{max} / d_y \qquad (4.12)$$

The load reversal point (d_{max}, F_{max}) lies on the secant stiffness line and the bilinear second stiffness line. By equating the expressions for each, Eqn. 4.13 can be derived.

$$\beta = (k\mu - 1)/(\mu - 1) \qquad (4.13)$$

The area inside the hysteresis loop can be related to the fraction of critical damping of an equivalent viscously damped system using Eqn. 4.9. This has been done by Otani [4.3] and gives the relationship in Eqn. 4.14.

$$\lambda = 2 (\mu - 1 + \beta - \mu\beta) / [\pi \mu (1 - \beta + \mu\beta)] \qquad (4.14)$$

On substituting for β Eqn. 4.15 is obtained.

$$\lambda = 2(1-k)/\pi\mu k \qquad (4.15)$$

In the dynamic analysis of site response an iterative procedure was required. After each iteration the maximum force F_{max} and shear strain γ induced in each shear member was noted. From the maximum shear strain the stiffness reduction factor $k(\gamma)$ and the appropriate fraction of critical viscous damping λ could be determined from Figs. 4.2 and 4.3. The parameters controlling the bilinear hysteresis for the next iteration were then calculated using Eqns. 4.16 to 4.18.

$$\mu = 2(1-k)/\pi\lambda k \qquad (4.16)$$

$$\beta = (k\mu - 1)/(\mu - 1) \qquad (4.17)$$

$$F_y = F_{max}/[1 + \beta(\mu - 1)] \qquad (4.18)$$

Iteration was continued until there was little change in the maximum member actions during the analysis.

An example of bilinear stress-strain response is shown by the dashed lines in Fig. 4.8. The hysteresis loops were calculated using the above procedure for a dense sand sample located at a depth of 10 m beneath the seabed surface. The effective unit weight of soil was assumed to be 6 kN/m^3. This gave a mean effective normal stress of 45 kPa. Three bilinear hysteresis loops are shown for maximum shear strain levels of 0.1 percent, 0.5 percent and 1.0 percent.

It should be noted that the material models developed here may only be appropriate to represent the undrained behaviour of dilatant (dense) sands. In a drained material the maximum shear stresses which develop should be limited to the effective vertical stress multiplied by the tangent of the internal angle of friction. In loose saturated sands positive pore pressures could develop and reduce the strength further, but in dense sands negative pore pressures could develop and strengthen the material.

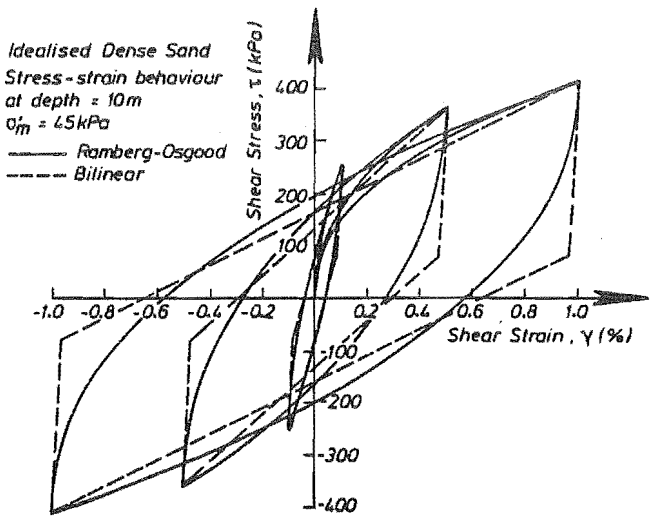

Fig. 4.8 Example of Bilinear and Ramberg-Osgood Hysteresis Behaviour

4.5.3 Ramberg-Osgood Hysteresis Model

Ramberg-Osgood force versus displacement behaviour varies as a continuous curve as shown in Fig. 4.9. The slope of the initial loading curve is to be equal to K_i, the stiffness based on the

small strain shear modulus G_i of the soil. Reversed cyclic loading is considered up to maximum positive and negative displacements of d_{max} and forces of F_{max}. The secant stiffness at the load reversal point is given by Eqn. 4.19.

$$K_S = F_{max} / d_{max} \tag{4.19}$$

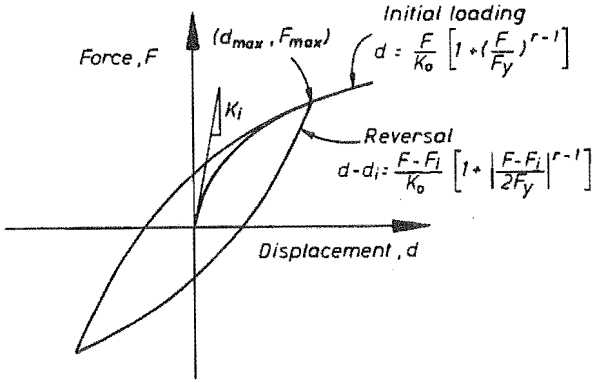

Fig. 4.9 Ramberg-Osgood Hysteresis Behaviour Description

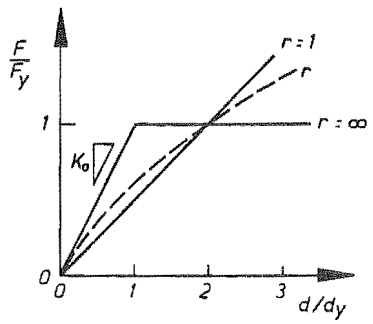

Fig. 4.10 Ramberg-Osgood Parameter R

For the initial loading curve the displacement d can be written in terms of the force F by the exponential expression in Eqn. 4.20.

$$d = F\,[\,1+(F/F_y)^{r-1}\,]\,/\,K_o \tag{4.20}$$

K_o is related to the tangent stiffness at the origin, F_y is like a yield force and r is the Ramberg-Osgood parameter. The Ramberg-Osgood behaviour can be better understood with reference to the nondimensional plot in Fig. 4.10 in which F/F_y is plotted versus d/d_y. d_y is analogous to a yield displacement. For r=1 the behaviour is linear elastic and the stiffness is equal to $K_o/2$. For r=∞ the behaviour is elasto-plastic and the initial stiffness is equal to K_o. For values of r between 1 and ∞ (all cases considered here) the behaviour ranges from elastic toward elasto-plastic but all curves have initial stiffness equal to K_o (= K_i) and all pass through the point ($d = 2d_y$, $F = F_y$).

For load reversal from the point (d_{max}, F_{max}) the displacement can be written in terms of the force by the expression in Eqn. 4.21.

$$d - d_{max} = (F - F_{max})\,[\,1+|(F - F_{max})/2F_y\,|^{r-1}\,]\,/\,K_o \tag{4.21}$$

The | | denotes the absolute value of the enclosed term. The five parameters required to define the load versus displacement behaviour are the maximum force F_{max}, the maximum displacement d_{max}, the yield force F_y, the yield displacement d_y and the Ramberg-Osgood parameter r. After any analysis iteration the known parameters were the maximum force F_{max}, the maximum internal displacement d_{max} (or the shear strain γ), the initial stiffness K_i, the secant stiffness K_s and the fraction of critical damping required λ. K_s and λ depended on the level of soil shear strain predicted by the iteration.

Otani [4.3] also gives the required expression for relating the fraction of equivalent viscous damping to the area within the hysteresis loop, as given by Eqn. 4.22.

$$\lambda = (2/\pi)\,(1-2/(r+1))\,(1-K_s/K_i) \tag{4.22}$$

This can be solved for the Ramberg-Osgood parameter r as in Eqn. 4.23 in which the stiffness reduction factor k(γ) has been included.

$$r = [\,2\,(1-k)+\lambda\pi\,] \,/\, [\,2\,(1-k)-\lambda\pi\,] \qquad (4.23)$$

Because the load reversal point lies on both the initial loading curve and the secant stiffness line it is possible to solve both equations simultaneously to find the Ramberg-Osgood yield force F_y given by Eqn. 4.24, and the yield displacement d_y given by Eqn. 4.25.

$$F_y = F_{max}\,[\,k/(1-k)\,]^{1/(r-1)} \qquad (4.24)$$

$$d_y = F_y / K_i \qquad (4.25)$$

Analysis iteration can be continued with updated Ramberg-Osgood parameters until convergence of the solution is achieved.

An example of Ramberg-Osgood stress-strain response is shown by the solid curves in Fig. 4.8 for direct comparison with the example bilinear stress-strain hysteresis loops calculated in the previous section. The hysteresis loops were calculated using the same assumed soil data used for the bilinear hysteresis example. It can be seen that the loading and unloading stiffnesses of the loops based on the two hysteresis rules are identical. The areas enclosed by the hysteresis loops are also identical for each level of maximum shear strain.

4.6 ONE - DIMENSIONAL DYNAMIC ANALYSIS MODELS

4.6.1 Description of Site Response Analyses

Site response analyses were carried out in this study of a number of very simple example sites. These sites were considered to be deposits of dense saturated sand over bedrock and were assumed to be of infinite horizontal extent. It was also assumed that during earthquake shaking only vertically propagating SH waves would be present so that all points at a particular level would undergo identical response. This enabled a simple one-dimensional model of the site to be considered, representing a unit area in plan. The dynamic analysis models consisted of a stack of several nodes with lumped masses interconnected by shear beam members. Only that part of the site above the bedrock to soil interface was modelled. A typical example site and dynamic analysis model is shown in Fig. 4.11. In this case the 200 m depth of sand was modelled using 6 nodes and 4 vertical shear beam soil members over the height. One node represented a fixed point in the underlying rock and the other five represented the lumped soil masses. The soil nodal points were only allowed to translate horizontally with vertical and rotational degrees of freedom restrained to zero.

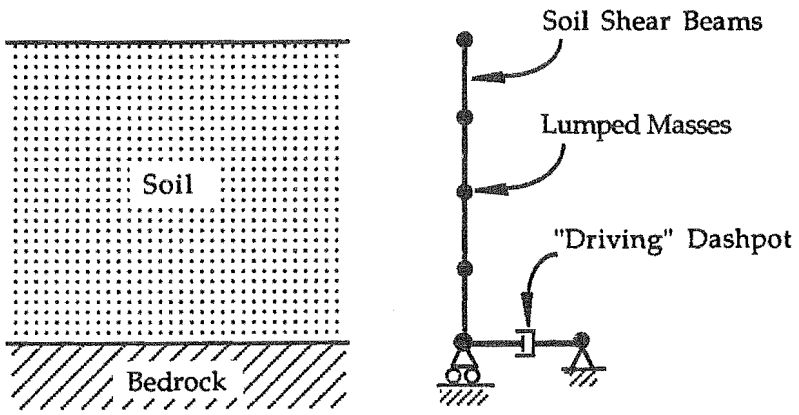

Fig. 4.11 Idealised Site and One-Dimensional Dynamic Analysis Model

Earthquake excitation was input through the fixed bedrock node at the base and the soil was "driven" through a viscous dashpot with its damping coefficient set equal to the acoustic impedance (ρc_s) of the bedrock times the assumed plan area of the model. ρ is the mass density and c_s is the shear wave speed in the rock material. This follows the method of Tsai [4.4] and is claimed to provide an exact analogue of the dynamic stiffness of the one dimensional system. No other members were required to model the connection between the soil and bedrock.

For the six node model representing the 200 m site each shear beam member represented a 50 m depth of soil. The nodes at the top and bottom had lumped masses representing a 25 m height of the soil column and the nodes over the central region had lumped masses representing a 50 m height of the column.

The shear stiffness of the vertical shear beam members was based on the shear modulus calculated using Eqn. 4.1. Because the shear modulus is strain dependent an iterative approach was necessary. The distribution of maximum shear strains was estimated for the first iteration of the analysis.

The shear modulus is also dependent on the mean effective normal stress. The vertical effective stress was calculated at the mid-depth of each member assuming an effective unit weight of overburden equal to 6 kN/m^3 which corresponds to a bulk density of approximately 1600 kg/m^3. A coefficient of lateral earth pressure of approximately 0.6 was assumed for the other two principal directions, corresponding to a slightly over-consolidated material. The resulting mean effective normal stress was 75 percent of the vertical effective normal stress.

Dynamic analysis was carried out using the two-dimensional inelastic frame time history analysis computer program RUAUMOKO already described in previous sections. The equations of motion are solved directly in the time domain using step by step integration techniques. This program has the facility to calculate the total displacement response of the degrees of freedom, rather than the response relative to the ground which is often calculated by dynamic analysis programs. Where the equivalent linear method was used, only the elastic analysis features of the program were required, but where nonlinear site response analyses were performed, inelastic members were used to model the soil hysteresis behaviour. Output results consisted of nodal displacements, velocities and accelerations and internal member actions at required time intervals.

In the program RUAUMOKO response is calculated for an input time history of ground accelerations, normally an actual earthquake accelerogram. For most of the site response analyses carried out in this work the excitation motion used was the first ten seconds of the north-south component of the El Centro record of the 1940 Imperial Valley, California earthquake. The El Centro record has no special significance but was a suitable real record for the purposes of this study. The maximum ground acceleration which occurred during this record was approximately 0.35 g. It was intended to input a known excitation motion, representing incoming ground waves, at the base of the dynamic model and to study the response over the height of the soil profile. In particular, it was intended to study the response motion at the ground surface.

The results of interest were the maximum acceleration and the acceleration response spectrum of the input accelerogram, and the corresponding response at the node representing the seabed surface at the top of the model. The nodal response accelerations from the dynamic time history analysis were output at time intervals of 0.02 seconds which is consistent with the digitisation time step of many accelerograms. The acceleration response spectrum of the seabed response accelerogram was then calculated using a spectral analysis program. Time histories of any output quantity could also be plotted from the dynamic analysis results.

Several site response analysis models were investigated in this study. The aims of carrying out the various analyses were to:

1. Examine the effects of nonlinear soil behaviour

2. Compare the predictions of nonlinear and equivalent linear methods.
3. Examine the effect of various depths of soil over bedrock.
4. Examine the effect of intensity of bedrock excitation on surface response.
5. Examine the effect of mesh refinement and model complexity.
6. Examine the effect of hysteresis rule used in the nonlinear analyses.

In order to examine the effects of nonlinear soil behaviour on the response of the seabed surface it was necessary to use a realistic intensity of input motion at the base of the model. It was considered that the El Centro earthquake record was adequate for this purpose. Results showed that a substantial level of shear strain and nonlinear behaviour was induced over the soil profiles by this level of shaking. The level of intensity was varied by determining the response for input motions of half and twice the El Centro record.

Equivalent linear and nonlinear analyses were carried out with dynamic models of the same soil profiles. Both types of analysis required iteration as the stiffness and damping properties were response dependent. For the equivalent linear analysis it was necessary to use an average value of damping appropriate to the whole soil profile. It was not possible to specify different damping levels in each member depending on the maximum level of shear strain induced by the previous iteration.

The effect of depth of soil present at a site was examined by considering sites with 50 m and 200 m of dense sand over bedrock.

The effect of model complexity was examined by refining the mesh size of the one-dimensional shear beam models. As discussed in Chapter 2 the mesh size, shear wave speed and analysis time step all influence the range of frequencies over which accurate predictions of dynamic response can be obtained.

The nonlinear analysis of site response requires that a hysteresis rule be specified to govern the stress-strain behaviour of the soil material. Experimental stress-strain curves for soil generally show a continuous variation of shear modulus with strain. This suggested that a Ramberg-Osgood type of hysteresis rule would be most appropriate. However, that rule tends to be computationally expensive because of the constant updating of member properties which is required. For most of the site response analyses a bilinear hysteresis rule was used, as this involved considerably less computational effort. It was of interest to compare the results of analyses of the same simple site profiles using both bilinear and Ramberg-Osgood hysteresis rules.

4.6.2 Discussion of Modelling Assumptions

A number of simplifying assumptions were made in developing dynamic analysis models for the study of site response effects. Some of the important assumptions are briefly discussed in the following paragraphs.

The simple sites are assumed to consist of horizontal layers of infinite extent. Subsurface strata at real sites may differ somewhat from horizontal but, in general, it is expected that offshore sites will satisfy the assumption better than for onshore sites. The irregular surface and subterranean features surrounding many onshsore sites would often make the assumption of simple layered site of infinite extent inappropriate.

Another major assumption is that the ground motion is generated by vertically propagating plane SH (horizontally polarized shear) waves. Consideration of theoretical expressions for far-field displacement magnitudes due to idealised source mechanisms [4.5] indicate that, of the total energy associated with body waves, perhaps 95 percent would be due to S waves, with only 5 percent due to P (compression) waves. The assumption of vertical incidence appears to be reasonable provided that the site is not very close to the source, such as in a very shallow focus earthquake. The reduction in shear modulus and hence propagation speeds of body waves, towards the ground surface, tends to refract the raypaths toward vertical. This can be predicted theoretically using Snell's Law.

The analysis ignores the presence of surface waves. There is little quantitative information available on how much of the total energy can be attributed to body wave motion and how much to surface wave motion. It could be argued that surface wave effects are included in the seismic hazard analysis predictions of uniform risk acceleration response spectra. As the attenuation relations used in the hazard analysis are based on actual earthquake records, all types of waves have been accounted for already. In Chapter 3 the results of a seismic hazard analysis carried out by the author showed that, for very long period structures, a greater proportion of the risk was contributed from earthquakes at large epicentral distances than for short period structures.

Recent work by Bard [4.6] has shown that Love waves can be generated when plane SH waves impinge on curved boundaries between materials of different rigidities. In a sediment filled valley this can result in Love waves that become trapped inside the valley, travelling up and down, reflecting off the boundaries for long periods of time. Curvature of material interfaces can also cause body waves to be focussed at particular points.

The simple site models used in these dynamic site response analyses were "driven" through viscous dashpot members rather than being attached to the input motion through a member with real stiffness. This follows the method of Tsai [4.4]. A rigid base would be inappropriate because seismic energy input at the base of the system would become trapped and could only be dissipated by internal damping mechanisms in the soil. In reality some of the kinetic energy of the responding system can be transmitted back into the basement material. An exact analog of the required dynamic stiffness is provided by a viscous dashpot with damping coefficient equal to the acoustic impedance of the basement material.

Salt [4.7] discusses some of the shortcomings of simple site response models with lumped masses and shear beam members. There is no doubt that in many cases such simple representations would be inadequate. Even for well defined, regular sites, where the major assumptions appear to be reasonable, it is most unlikely that detailed predictions of actual site response could ever be made. Although the subject is very much in its infancy, engineers and seismologists face the problem of making some assessment of the influence of factors such as local site response effects. By the very nature of earthquakes there will always be considerable uncertainty involved with this kind of work. The results of the simple site response analyses carried out in this study represent real effects but it is acknowledged that there will be other contributing and complicating factors which have not been considered.

4.7 RESULTS OF SITE RESPONSE ANALYSES

In this section results of the site response analyses carried out in this study are presented. In all cases a dense sand site over bedrock was assumed.

The simplest site response model used in this study was a 6 node model of a 200 m deposit of dense sand. This was analysed using both equivalent linear and nonlinear analysis methods. Bilinear hysteresis behaviour was assumed for the nonlinear analysis. Fig. 4.12 shows the acceleration response spectrum of the El Centro input motion and the response motion predicted at the surface of the soil for the two analyses. For periods of vibration greater than about 1.5 seconds both analyses predicted maximum response accelerations greater than the spectral accelerations from the El Centro input motion, thus indicating some amplification. For periods of vibration less than about 1.3 seconds both analyses predicted maximum response accelerations which were much smaller than the El Centro spectrum. The high frequency components were filtered out leaving only the low frequency response. This can be attributed to two main effects. Firstly, the motion is dominated by the long period response of the site and secondly, the model used quite a coarse mesh to represent the site. There were effectively only 4 modes of vibration contributing to the response of the site.

It is possible to estimate the natural periods of the site using the equivalent linear method. The maximum soil shear strains varied over the depth of the site but strains of about 0.13 percent were predicted in most of the members. It was thus possible to estimate secant shear

moduli (approx 90 MPa) and corresponding shear wave speeds (approx 230 m/s) over the height of the soil deposit. Using this information it was possible to calculate the first 4 natural periods of the site using the Haskell method (Section 4.2). This gave periods of approximately 3.4, 1.1, 0.7 and 0.5 seconds. Use of a coarse mesh does not result in numerical instability but the model will be insensitive to input motions with frequencies higher than the highest natural frequency (lowest natural period) of the system. From the discussion in Chapter 2 on dynamic analysis fundamentals it was pointed out that, as a rule of thumb, accuracy could only be expected for periods greater than about four times the smallest natural period of the system. In this case it would be expected that the response for periods less than about 2 seconds would be underestimated.

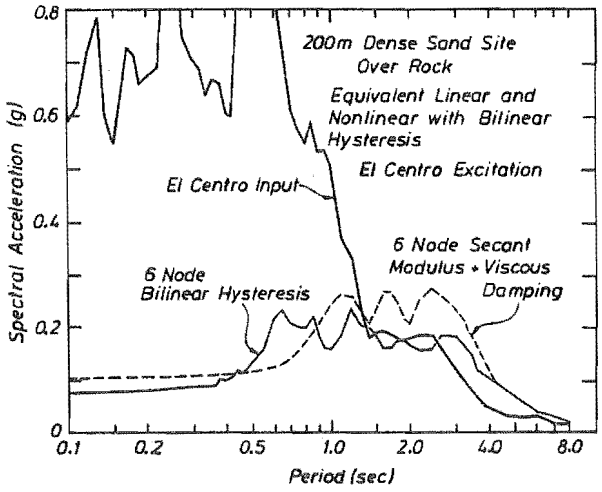

Fig. 4.12 Surface Response Spectra for 200 m Bilinear Site

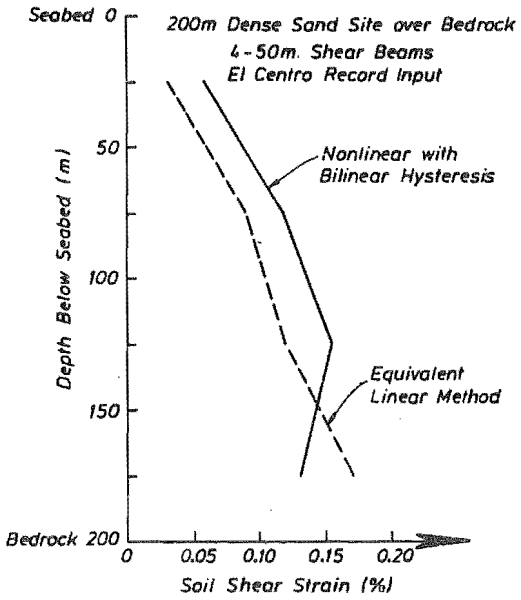

Fig. 4.13 Maximum Soil Shear Strain Distributions for 200 m Bilinear Site

There is up to 50 percent difference in the response spectra predicted by the equivalent linear and nonlinear methods of analysis. The relative peaks and troughs in the response spectra derived from the surface motion do not occur at the same periods. The acceleration time histories of the seabed surface node were also somewhat different in appearance indicating that the response predicted by the two methods is significantly different.

Fig. 4.13 shows the distributions of maximum soil shear strains with depth predicted by the equivalent linear and nonlinear methods. In the equivalent linear analysis the trend is for the strains to increase with depth. In the nonlinear analysis the strains are more uniform over most of the depth and decrease near the surface. For both analysis methods the maximum strains near the surface are predicted to be about 0.05 percent, while near the bottom of the soil deposit they reach about 0.15 percent. These results agree quite well with values obtained from similar analyses by Seed et al [4.8].

The response of the same 200 m dense sand site was also predicted using smaller mesh sizes with 12 nodes (20 m shear beams) and 18 nodes (12.5 m shear beams). Nonlinear soil behaviour was assumed with bilinear stress-strain response in each case. Fig. 4.14 shows the acceleration response spectrum of the three nonlinear analyses of the 200 m sand site using 6, 12 and 18 node meshes. The three analyses give similar predictions of response for long periods of vibration but, as expected, the discrepancies become large as the period reduces. It would be expected that the response predictions should converge as the finite element mesh is refined. However there are differences in the spectra even for long period response ordinates.

Based on an average secant stiffness value over the depth of the site and the Haskell method it was estimated that response predictions from the 6, 12 and 18 node models should have been reasonable for periods above 2.0 seconds, 0.7 seconds and 0.4 seconds respectively. For a realistic assessment of spectral ordinates below these periods a smaller mesh size would be necessary.

The distribution of maximum soil shear strains predicted by the three analyses are shown in Fig. 4.15. The distributions agree quite well, with an average strain of about 0.14 percent over most of the depth. In the upper 50 m the strains generally decrease to about 0.05 percent. As the mesh-size is refined the strains appear to remain more uniform over a greater depth and reduce more sharply close to the surface.

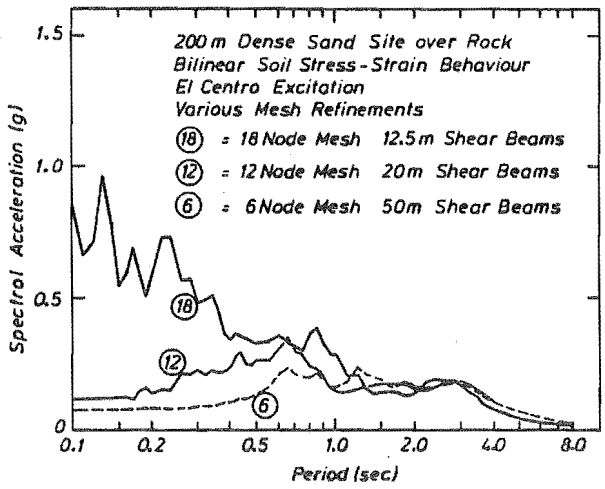

Fig. 4.14 Effect of Mesh Refinement on Surface Response Spectra for 200 m Bilinear Site

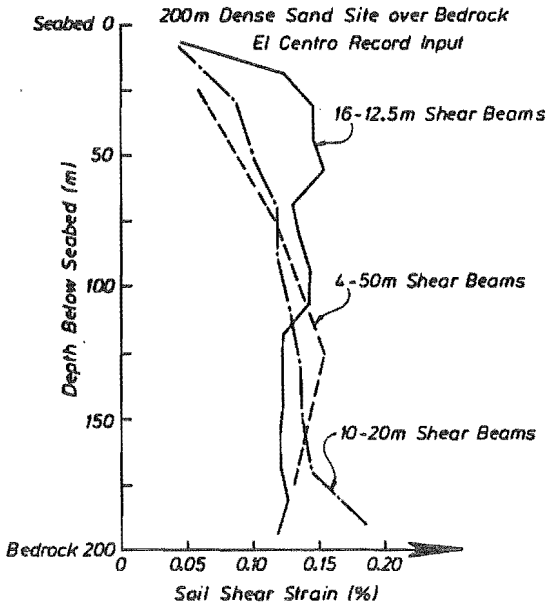

Fig. 4.15 Maximum Soil Shear Strain Distributions from models with Mesh Refinements

The influence of the depth of soil over bedrock was briefly studied by comparing the 200 m site (18 nodes) with a 50 m site (6 nodes). Both models had shear beam members 12.5 m in length. Fig. 4.16 shows the acceleration response spectra obtained from the acceleration histories predicted at the seabed surface nodes. Also shown is the spectrum from the El Centro earthquake record used as the basement input motion to the models. The 200 m site gives some amplification of response for structures with periods of about 2.5 seconds or greater, whereas the 50 m site gives amplification over the El Centro input for structures with periods greater than about 1.2 seconds. For periods up to about 1 second both sites show about the same level of response, which is somewhat less than the El Centro input amplitude. For periods greater than about 1.2 seconds the response of the 50 m site is about twice the response of the 200 m site.

The distribution of maximum soil shear strains with depth shows a similar trend in the 50 m site as for the 200 m site except the magnitudes are greater. Over the lower half of the 50 m site the maximum strains predicted were about 0.35 percent, approximately twice those predicted in the 200 m site.

The effect of intensity of the basement rock excitation was examined by studying the 50 m dense sand site model. This model used 12 nodes and 10 shear beam members over the depth, with bilinear stress-strain hysteresis. Three levels of earthquake intensity were used; 0.5, 1.0 and 2.0 times the El Centro record. Fig. 4.17 shows the acceleration response spectra obtained from the predicted response motion at the seabed surface node for the three levels of

excitation. For most periods there is a general trend for the response to increase with an increase in excitation level. However, this is not true for all periods of vibration. In some cases the maximum spectral accelerations are predicted for the smallest input intensity. For long period structures, with periods greater than about 3 seconds, the response level is almost linear with intensity.

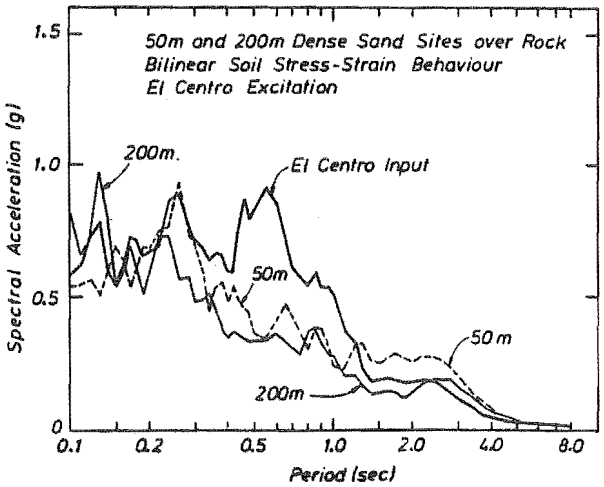

Fig. 4.16 Influence of Soil Depth on Surface Acceleration Response Spectra

The distributions of maximum soil shear strains predicted over the depth of the soil deposits are shown in Fig. 4.18. There is a clear trend for increase in the level of shear strain with intensity but the dependence is not exactly linear. For 1.0 times the El Centro record a maximum shear strain of about 0.35 percent is predicted over much of the depth. For the case of 0.5 times El Centro input motion this reduces to about 0.1 percent and for 2.0 times El Centro the level of shear strain increases to about 0.8 percent.

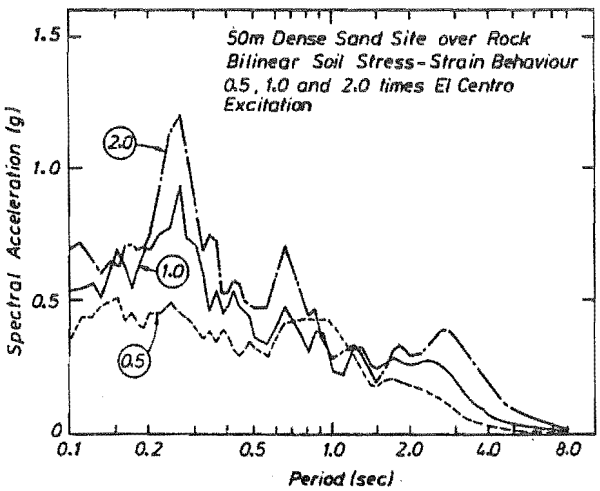

Fig. 4.17 Influence of Excitation Level on Surface Acceleration Response Spectra

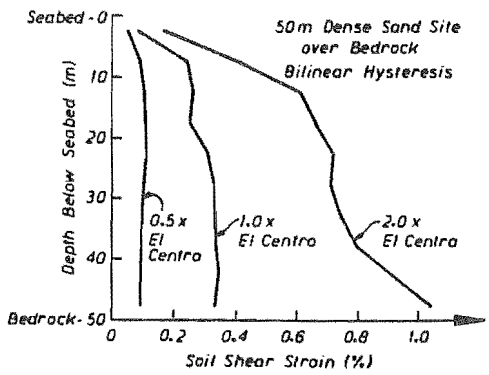

Fig. 4.18 Influence of Excitation Level on Maximum Soil Shear Strain Distributions

The nonlinear dependence of the spectral amplitudes and maximum shear strains on the intensity of input motion from the basement rock is due to the nonlinear behaviour of the soil.

As the intensity increases the soil shear strains increase causing a decrease in stiffness and an increase in the hysteretic damping in accordance with the assumed variation of dynamic soil properties.

The analysis using two times the El Centro earthquake record as the input motion predicted maximum soil shear strains of up to 1 percent. This was the upper limit for which dynamic properties of soils were presented in the work by Seed et al [4.2]. In Figs. 4.4 and 4.5 the trend indicated at the 1 percent upper strain limit is for both the shear modulus and the damping ratio to remain about constant with increasing strain. However, it is likely that some form of failure and gross modification of the soil would take place if shear strains greater than this magnitude were imposed.

The influence of the hysteresis rule used in the nonlinear analysis of site response was examined by using the 50 m nonlinear site model with 12 nodes and 10 shear beams over the depth. The unscaled El Centro record was used as the excitation motion at the basement rock level. Bilinear and Ramberg-Osgood stress-strain hysteresis was compared. Fig. 4.19 shows the acceleration response spectra obtained from the predicted response motion at the seabed surface node for the analyses using the two nonlinear hysteresis rules. Also shown is the result from an equivalent linear analysis of the same site. The spectral ordinates are very similar for periods greater than about 3 seconds for the two nonlinear analyses but there are substantial differences for periods less than about 1 second. The equivalent linear analysis predicts large response spectral accelerations for structures with periods greater than 2 seconds. The ordinates are approximately twice those predicted by the nonlinear analyses. There is an obvious filtering effect in the equivalent linear spectrum for periods less than about 0.5 seconds.

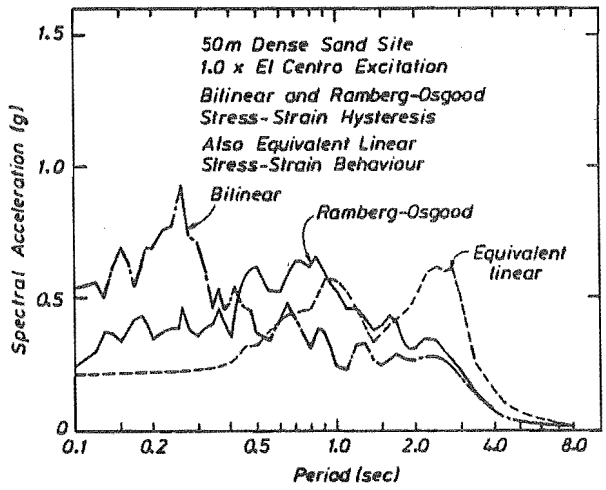

Fig. 4.19 Effect of Nonlinear Hysteresis Rule on Surface Acceleration Response Spectra

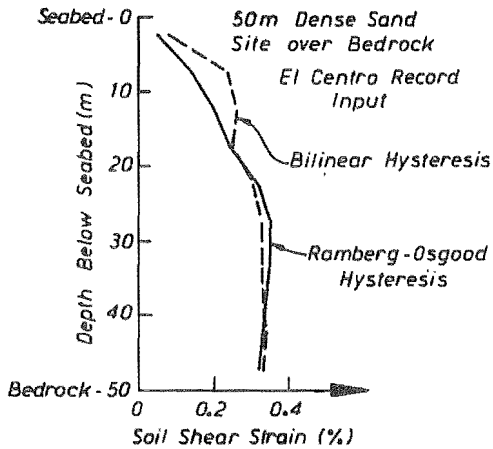

Fig. 4.20 Effect of Nonlinear Hysteresis Rule on Maximum Soil Shear Strain Distributions

Equivalent linear analyses tend to result in peaks occurring in the response spectra at periods corresponding to the natural periods of the particular site model. The effect is similar to the amplification of wave amplitudes predicted by the Haskell method (Section 4.2) at the natural frequencies of an elastic undamped site. This was masked considerably in the results of these equivalent linear site response analyses by the large fractions of damping which were implied by the strain response levels in the soil. Analyses carried out with much smaller levels of excitation showed considerable amplification of response spectra in the vicinity of the natural periods of vibration. It should be noted that where substantial nonlinear soil behaviour is induced in the soil, the natural periods of vibration corresponding to the secant stiffnesses of the soil members are not physically meaningful as the stiffnesses

are constantly changing. Thus the use of the equivalent linear method may lead to fictitiously large response ordinates for periods close to the natural periods of the site based on the secant stiffnesses assumed.

The distribution of maximum soil shear strains induced over the depth of the soil deposit is shown in Fig. 4.20. The two nonlinear analyses gave reasonable agreement with strains varying from about 0.05 percent near the surface to about 0.35 percent over the lower half of the 50 m depth of sand.

4.8 SUMMARY OF RESULTS FROM ONE - DIMENSIONAL SITE RESPONSE ANALYSES

Results of site response analyses based on the equivalent linear and nonlinear analysis methods show a substantial difference in predictions. The site response analyses carried out in this study showed that large shear strains (up to about $\gamma = 1$ percent) could be expected in soil deposits excited by moderate to high intensity earthquake shaking. It was evident that the dynamic properties of soils, such as the dense sand materials studied here, are strongly influenced by the level of shear strain induced in the soil and this resulted in highly nonlinear behaviour. It is expected that the equivalent linear method of analysis is not appropriate where significant inelastic deformations occur. The effects of resonance close to the natural periods of the equivalent linear system may lead to fictitious amplifications of the response in those period ranges.

For levels of response where only small strains are induced in the soil materials, up to say an order of magnitude greater than the small strain ($\gamma = 10^{-4}$ percent) level for which soils remain effectively linear, the equivalent linear method is likely to be adequate.

For elastic systems it is possible to estimate the necessary mesh size and analysis time step required to give accurate predictions of dynamic response of vibration modes up to particular frequencies. For nonlinear systems the problem is complicated because the dynamic properties of the system are not constant. However, it is considered that accuracy can be expected for periods greater than about four times the shortest natural period of the equivalent linear system. This criteria appears to be applicable to the nonlinear response of one-dimensional site models.

The distribution of maximum soil shear strains over the depth of simple soil sites was sensitive to the depth of soil over bedrock and the intensity of the basement rock input motion. In general the distributions increased with depth from the surface down to about half the depth, after which they remained about constant. Greater maximum strains were predicted for sites with less soil over bedrock. Maximum strain profiles were found to increase with increasing input motion intensity, but not proportionally.

Response spectral accelerations were generally found to be greater for shallower soil deposits. In some cases the spectral ordinates from the input motion were amplified and in other cases they were reduced. As a general trend the spectral ordinates increased with increasing input motion intensity, although this did not apply for all periods of vibration in the examples studied.

The Ramberg-Osgood and bilinear hysteresis used in the nonlinear site response studies appeared to give quite similar stress-strain response for the soil. Results of analyses for the same site using the two hysteresis models showed very similar distributions of maximum soil shear strain with depth but somewhat different acceleration response spectra derived at the seabed surface.

These studies have not been extensive enough to make detailed conclusions about the influence of flexible non-linear material on the response spectra which should be used for design of structures located on the seabed surface. For small amplitude ground motions it is quite likely that amplification would occur, but for large amplitude ground motions the significant nonlinear response that is expected in typical soils may well attenuate rather than amplify

the motion. It is suggested that until these effects are quantified by extensive further research, the soft ground spectra presented in Chapter 3 should be used for design purposes.

4.9 SIMPLE PLATFORM - NONLINEAR SITE INTERACTION STUDIES

4.9.1 One-Dimensional Platform-Nonlinear Site Interaction Analysis

The one-dimensional site response modelling was adapted to include the presence of a simple North Sea type concrete gravity platform. An example site/platform combination was chosen, consisting of a 200 m dense sand site over bedrock, supporting the Frigg TP1 platform. The assumed layout and the dynamic analysis model used are both shown in Fig. 4.21. The platform and site members are offset from each other to allow the rotational compliance effects to be modelled. The horizontal member between the platform base and the seabed surface was axially rigid but had flexural stiffness corresponding to the estimated rotational stiffness provided by the foundation.

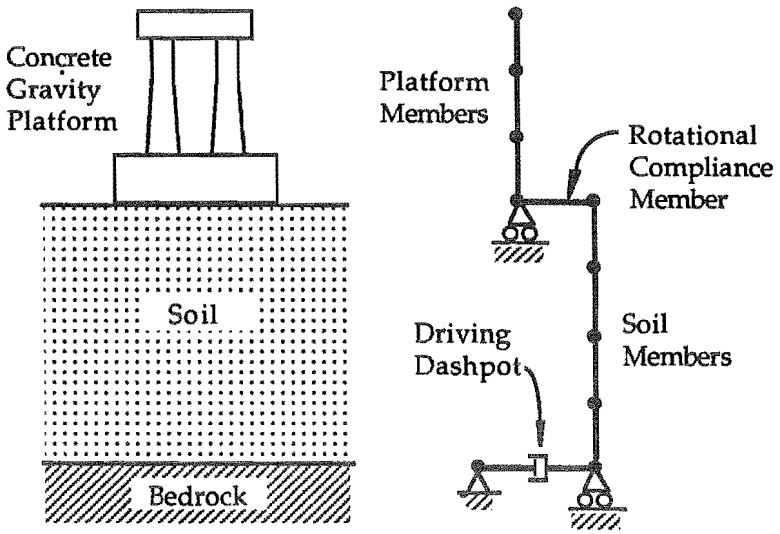

Fig. 4.21 Simple One-Dimensional Site/Platform Model

The soil members were arbitrarily chosen to represent a 200 m by 200 m column. Subsequent analyses were carried out using two-dimensional models to assess the influence of local interaction effects around the platform base. The overburden effects of the platform were assumed to disperse at 45 degrees with depth and influenced the calculation of the soil shear modulus determined at the mid-depth of each soil member. This tended to stiffen the members above the values used for the site only response analysis with the influence being substantial for the uppermost member but insignificant for the lower members. Bilinear stress-strain hysteresis behaviour was assumed in the soil. Properties for the initial iteration of the analysis were estimated from the corresponding site-only analysis.

Damping in the platform structure was provided by damping members placed parallel to the main flexural members. Rayleigh damping coefficients were determined from a separate analysis of the platform only in which 5 percent of critical damping was specified in two of the modes of vibration. The damping matrix in the platform could then be built up by specifying the mass and stiffness appropriate to each damping member.

Response of the site and platform system was calculated for the El Centro earthquake record input through the basement rock at the base of the model. Several iterations were required to converge to the response obtained, with the soil stress-strain behaviour being based on the maximum induced shear strain from the previous iteration.

Fig. 4.22 shows the distribution of maximum soil shear strains induced over the soil profile. Also shown is the distribution found from the site only analysis. Clearly the presence of the platform did not significantly affect the soil response. The platform weight corresponded to only about 8 m of additional soil on top of the 200 m square column assumed.

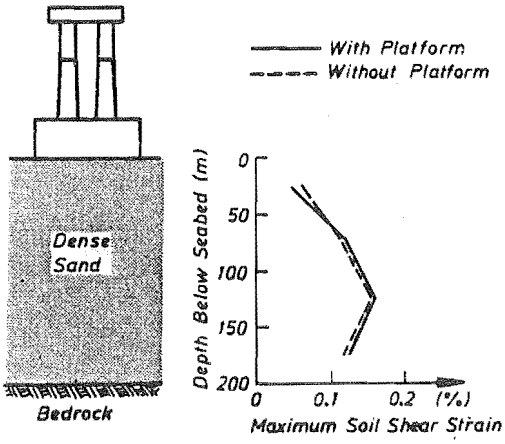

Fig. 4.22 Distribution of Maximum Soil Strains from 1-D Site/Platform Model

4.9.2 Two-Dimensional Platform-Nonlinear Site Interaction Analysis

In order to investigate the local interaction effects between the platform base and the surrounding soil more closely, a two-dimensional dynamic model of the same example site and platform presented in the previous section was developed, as is shown in Fig. 4.23. Some of the nodal numbers are identified as they are referred to in later presentations of analysis results. In this model the soil was represented by a number of vertical soil columns made up of shear beams and interconnected by horizontal linking members. This was effectively an extension of the so-called one-dimensional model. The site was considered to be symmetrical about a vertical line through the platform and only half of the total site/platform system was modelled. A uniform mesh was used with the columns representing 50 m widths of soil. Three dimensional effects were not allowed for in this model, which represented a 100 m thick slice of site. Platform modelling was identical to that used in the one-dimensional model.

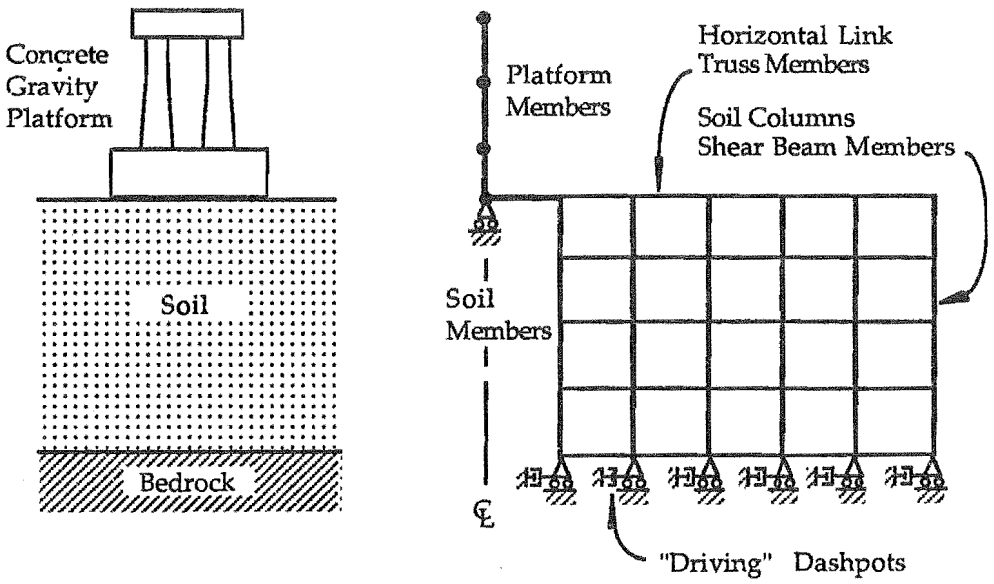

Fig. 4.23 Two-Dimensional Site/Platform Model with Uniform Mesh

The horizontal link members between the columns were modelled as elastic truss members, capable of transmitting only axial forces. The stiffness of these links was based on the estimated Young's modulus, calculated as a function of the shear modulus in the adjacent vertical shear members.

The two-dimensional site was "driven" through dashpot members located at the base of each soil column. The damping coefficient in each was set equal to the assumed acoustic impedance of the bedrock times the plan area of the column of soil. Vertical excitation of the site was not considered.

Response of the site platform model was calculated using the inelastic time history analysis program previously described. Nodal displacements, velocities and accelerations together with member actions were calculated. Of particular interest was the way in which the predicted motions varied at nodes along the seabed surface. The time histories of acceleration response predicted at each of the surface nodes was plotted and compared. Each response trace was different but all were similar in amplitude and frequency content. Because of the relatively coarse mesh used the high frequency components were filtered out of the response.

Fig. 4.24 shows the maximum soil strains induced in the soil members during the response. The figures for the vertical shear members are shear strains and the figures for the horizontal link members are axial strains. The maximum shear strains for the free-field, found from the site only analysis, are also shown. As expected there are large strains induced in the soil close to the platform base. The effects diminish away from the platform with the strains in the most distant soil column reducing to slightly below the free-field values. In Fig. 4.25 the equivalent viscous damping ratios in the vertical shear beams are shown and a similar trend is apparent.

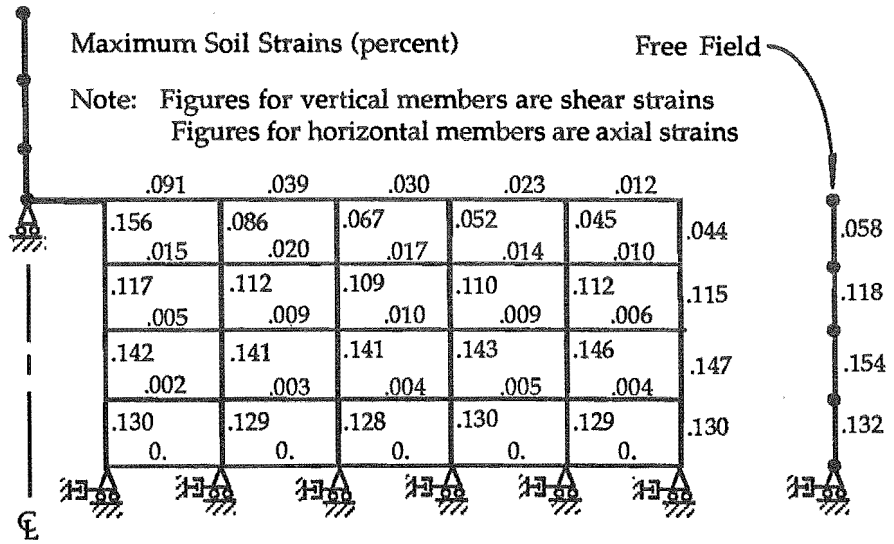

Fig. 4.24 Distribution of Maximum Soil Strains - Two Dimensional Site/Platform Uniform Mesh Model

It appears that the increase of response in the soil adjacent to the platform is compensated for by the reduction in response at a distance. The way in which the mesh is suddenly stopped at the far-field is of course unrealistic. Ideally it should be continued until the free-field response is predicted in the members at the extremities. Alternatively a suitable analogue of the far-field radiation condition could be incorporated in to the model.

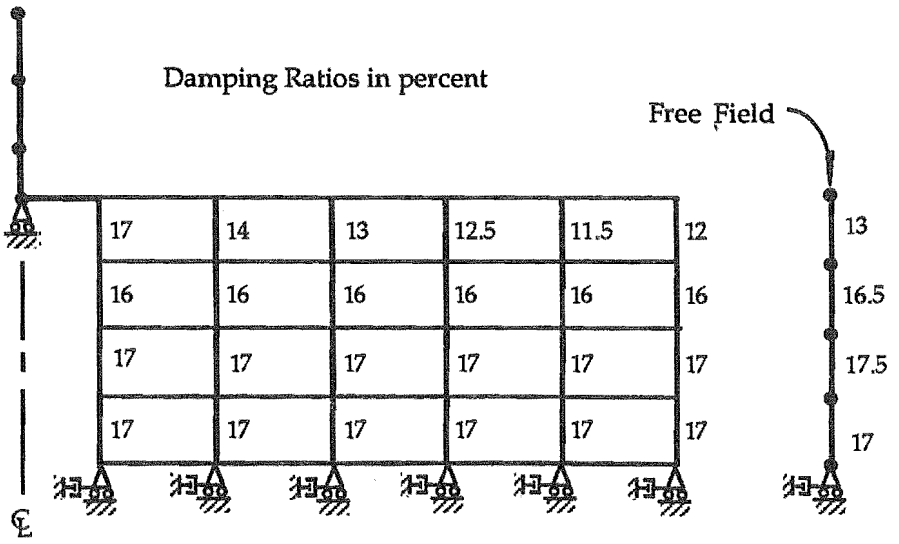

Fig. 4.25 Distribution of Equivalent Viscous Damping Ratios in Inelastic Soil Members Two-Dimensional Site/Platform Uniform Mesh Model

In an attempt to better model the far-field radiation condition a second analysis was carried out. As shown in Fig. 4.26 the mesh was graded horizontally so that the soil columns represented progressively larger amounts of soil for the columns further away from the platform. The soil column widths, starting at the column closest to the platform, were taken as 50 m, 70 m, 100 m, 140 m and 200 m. The far soil column was modified to represent the free-field by scaling up the member properties and masses associated with this column by a factor of ten. The truss members used as the horizontal links between this column and the rest of the soil were replaced by dashpot members with damping coefficients equal to the acoustic

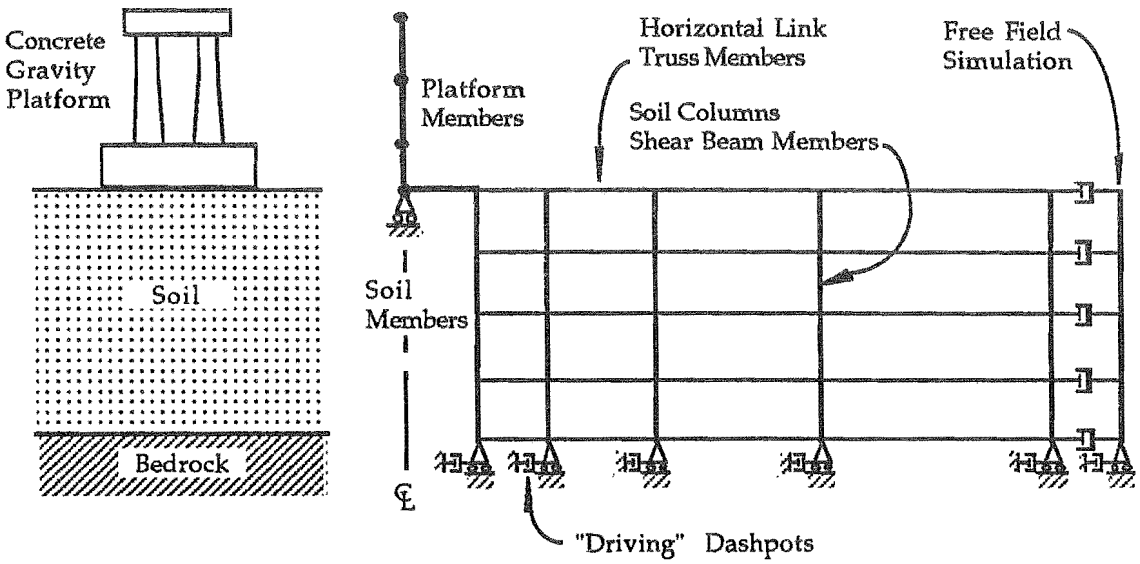

Fig. 4.26 Two-Dimensional Site/Platform Model - Graded Mesh with Free-Field Constraint

impedance to compression waves times the contact area. This resulted in the site being "driven" from the side by the free-field response. Differential motion between the edge of the soil model and the free-field would cause damping forces to be generated and energy associated with the relative motion to be dissipated.

The response of the platform was found to be almost identical with the response predicted by the other two-dimensional site/platform analysis. Horizontal acceleration time history

responses at nodes along the seabed surface showed very similar behaviour with only small differences in maximum acceleration amplitude. Figs. 4.27 and 4.28 show the horizontal acceleration time history responses predicted at nodes 6 and 35 (refer Fig. 4.23) which were located adjacent to the platform base and at the free-field respectively. The peak accelerations differ by about 25 percent. Note that the maximum acceleration of the free field response is about 0.07 g, only 20 percent of the maximum acceleration of the input El Centro record. This is mainly due to the coarse mesh size used which filtered out the high frequency components of the response.

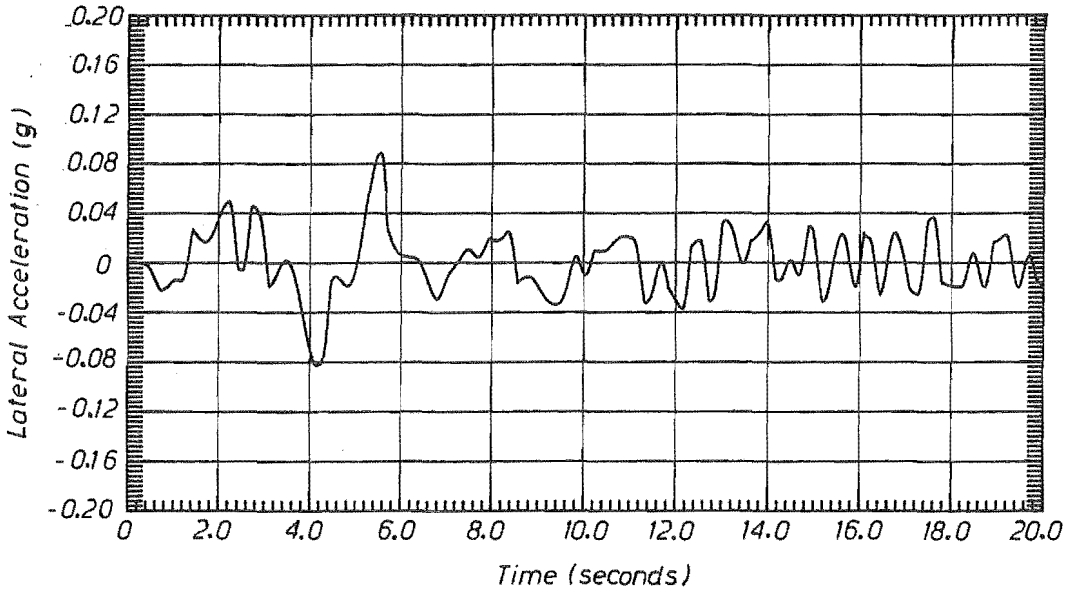

Fig. 4.27 Acceleration Time-History at Platform Base Node

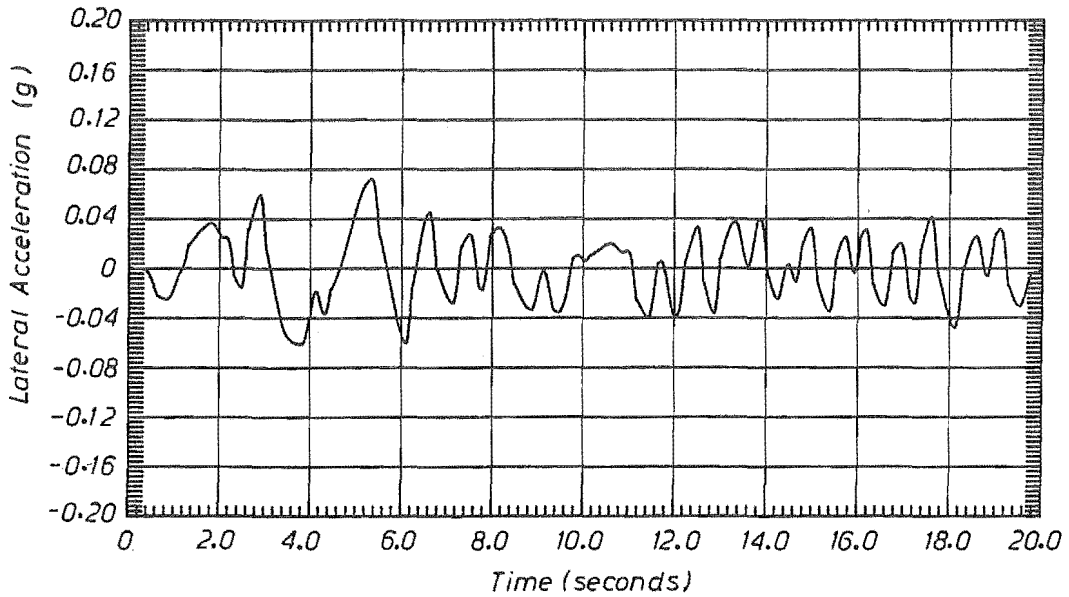

Fig. 4.28 Acceleration Time-History at Free-Field Node

Fig. 4.29 shows response spectra calculated from the absolute acceleration response histories at the platform base (node 6), the free-field (node 35) and at an intermediate node (node 15) along the surface of the soil. Although the acceleration response spectra have about the same overall magnitude, variations at particular natural periods are substantial, as large as 50 percent for some periods. Comparison of the spectra for the free-field and platform base motions shows an amplification of response for long periods. This indicates, as expected, that

there is effectively a flexible connection between the free-field and the platform base. It appears reasonable, at present, to model these foundation interaction effects using simple compliance members such as the spring and dashpot members discussed in Chapter 2.

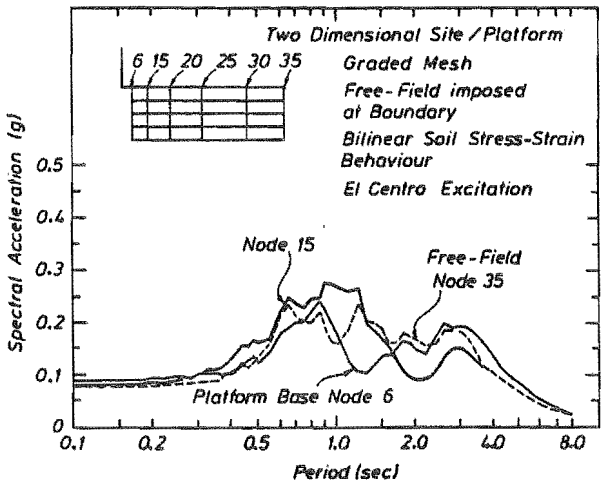

Fig. 4.29 Acceleration Response Spectra at Nodes Along Soil Surface

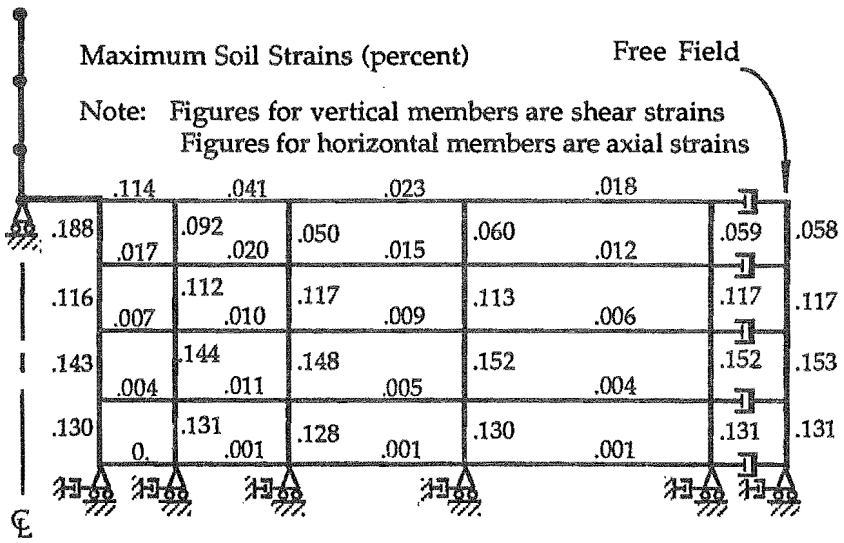

Fig. 4.30 Distribution of Maximum Soil Strains - Two Dimensional Site/Platform Graded Mesh Model

The distribution of maximum soil strains predicted by the dynamic analysis is shown in Fig. 4.30. The maximum soil shear strains are locally increased due to the presence of the platform with the maximum shear strain in the vertical shear member just below the base being about three times the free-field strain. The distribution of equivalent viscous damping ratios in the vertical shear beam members are shown in Fig. 4.31. The distributions of both maximum strains and damping ratios are very similar to the results from the uniform mesh model.

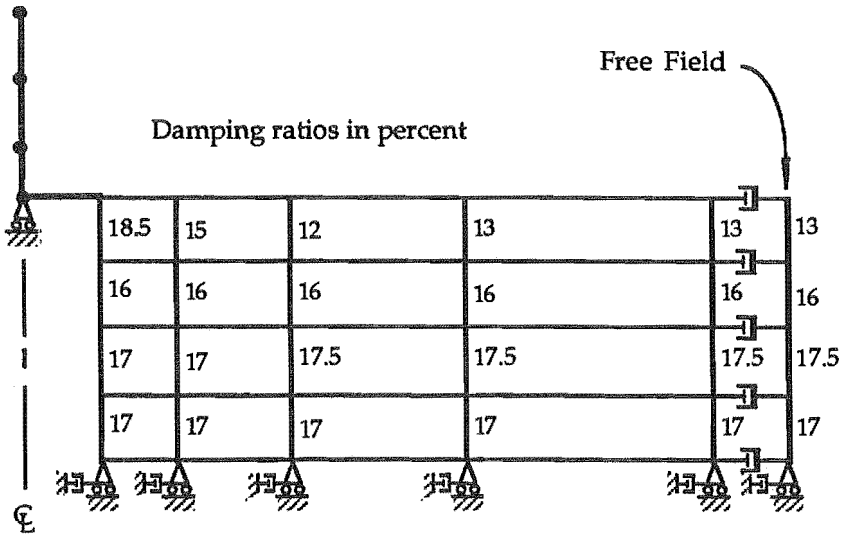

Fig. 4.31 Distribution of Equivalent Viscous Damping Ratios in Inelastic Soil Members Two-Dimensional Site/Platform Graded Mesh Model

4.10 SUMMARY OF RESULTS FROM SIMPLE PLATFORM - NONLINEAR SITE RESPONSE ANALYSES

The analyses carried out in this brief study involved great simplification of the actual platform/site system but the results have given some indication of the behaviour which could be expected. Ideally a much more detailed three-dimensional nonlinear finite element model of the entire foundation would be desirable. It would not be adequate to simply model the soil in the immediate vicinity of the platform base using nonlinear elements as the soil in the free-field is also expected to be nonlinear.

The model used in this study considered only simple nonlinear shear behaviour of the soil. While this may be a reasonable simplification for the soil located at some distance from the discontinuity caused by the platform, the soil beneath the platform base will be subject to complex dynamic triaxial stress histories. To realistically predict the behaviour of this material it would be necessary to use three dimensional constitutive relations. A further complication arises because of the soil saturation, as changes in pore water pressures could significantly modify the dynamic response of the soil. For accurate predictions of response at frequencies of interest for most structures, quite small mesh sizes would be necessary, resulting in very large computational models. Clearly, with the present state of knowledge, there would be serious difficulties in attempting a complete soil-structure interaction analysis of an offshore platform subject to high intensity earthquake excitation. The large uncertainty in the characteristics of the incoming ground motions should also be kept in mind. However, the simple analyses carried out in this study have highlighted some useful results.

The one-dimensional site and platform analysis indicated that the platform did not significantly modify the response at the surface of the soil deposit if the soil column dimensions were significantly larger than the platform. For the case considered the platform represented only a small additional mass on top of the soil column. It is thought that this gave an over simplification of the response of the platform/foundation system as it masked the local effects which would be expected in the immediate vicinity of the platform base.

The two-dimensional platform/site analysis displayed some of the local effects in the soil around the platform base which might be expected. Although the element mesh used in the model was quite coarse, there was a significant variation in maximum soil strains in the members close to the platform base. The maximum shear strain in the vertical shear members immediately below the platform base was about three times the predicted free-field value.

Sensitivity studies could be conducted to determine if more detailed modelling of the foundation affected this result.

Acceleration response spectra were calculated from the acceleration responses at nodes along the soil surface. Results indicated that interaction between the platform and foundation is likely to result in the excitation motion to the platform being somewhat different from the free-field response of the soil surface. It is inferred from this that it is not appropriate to simply use the horizontal free-field motion to directly excite the platform base. Neither is it feasible, at present, to attempt a complete nonlinear analysis of the combined structure and foundation system. Instead, it seems appropriate to analyse only the structure with some form of simplified foundation interaction to account for the differential motion which can occur between the platform base and the free-field.

While this has not been investigated further, it appears that dynamic analysis models should incorporate foundation compliance members in the form of soil spring and dashpot members such as those given by Veletsos and Verbic, discussed in Chapter 2. It appears reasonable in estimating the foundation compliance to take account of the likely levels of soil strain which would be induced in soil deposits by the level of earthquake excitation being considered. This approach was applied in carrying out preliminary design studies of two different offshore concrete gravity platform structures in this research. Details of these design studies are reported in Chapter 8.

4.11 REFERENCES - CHAPTER 4

4.1 Haskell, N. A., "Crustal Reflection of Plane SH Waves", Journal of Geophysical Research, Vol. 65, No. 12, Dec. 1960, pp 4417-4150.

4.2 Seed, H. B. and Idriss, I. M., "Soil Moduli and Damping Factors for Dynamic Response Analyses", Report No. EERC 70-10, Earthquake Engineering Research Center, University of California, Berkeley, Dec. 1970, 38pp.

4.3 Otani, S., "Hysteresis Models of Reinforced Concrete for Earthquake Response Analysis", Journal of the Faculty of Engineering, The University of Tokyo (B), Vol. XXXVI, No. 2 (1981).

4.4 Tsai, N. C., "Influence of Local Geology on Earthquake Ground Motion", Ph.D. Thesis, California Institute of Technology, Pasadena, California, 1969, 201pp.

4.5 Kasahara, K., "Earthquake Mechanics", Cambridge University Press, 1981, 248 pp.

4.6 Bard, P.-Y. and Bouchon, M., "The Seismic Response of Sediment Filled Valleys. Part 1. The Case of Incident SH Waves", Bulletin of the Seismological Society of America,Vol. 70, No. 4, August 1980, pp 1263-1286.

4.7 Salt, P. E. , "Seismic Site Response", Bulletin of the New Zealand National Society for Earthquake Engineering, . Vol. 7, No. 2, June 1974, pp 62-74.

4.8 Seed, H. B., Lysmer, J. and Hwang, R., "Soil Structure Interaction Analyses for Evaluating Seismic Response", Report No. EERC 74-6, Earthquake Engineering Research Center, University of California, Berkeley, April 1974, 25pp.

Chapter 5

ARTIFICIAL EARTHQUAKE RECORDS FOR USE IN DYNAMIC ANALYSES

5.1 INTRODUCTION

In this study extensive use is made of dynamic time history analyses in investigating the response of offshore concrete platform structures to earthquake motions. In carrying out a dynamic time history analysis it is necessary to supply a digitised ground acceleration record to the analysis. There are relatively few real accelerograms available with the intensity appropriate to very severe earthquake shaking.

Structural designers normally design for earthquake effects by using simplified acceleration response spectra. These are available from design codes or from special seismic hazard studies. Designs are carried out using either an equivalent distribution of static forces or dynamic analysis methods based on the chosen acceleration response spectrum. Design spectra are expected to represent some sort of smoothed average to the acceleration response spectra which might be obtained from many earthquakes with about the same return period. Response spectra derived from individual records tend to be quite irregular over the range of periods of vibration, and no real record would ever match the design spectrum over the entire period range.

Because of the irregularities in real earthquake records, it is common to select a suite of accelerograms, and a dynamic analysis is carried out with each of the records as an input ground motion to the structural model. Records are often scaled to achieve some consistent intensity of motion. Problems arise in determining how records with completely different characteristics should be scaled to a consistent intensity. Scaling can be carried out to give similar maximum ground accelerations or average response spectral accelerations over some period range. However, the natural variability of earthquake motions makes it very difficult to scale real records to satisfy all but very limited criteria.

Inelastic response of structures can only be accurately predicted using analysis in the time domain for which digitised accelerograms are required.

It is very desirable to be able to generate artificial earthquake records having response spectra which closely match any chosen design spectrum. In this study an existing computer program for generating artificial earthquake records was used to generate a suite of ground motion records to match the elastic design spectra suggested in proposed changes to the New Zealand Loadings Code NZS 4203. These records were used in the design studies reported in Chapter 8 to investigate the feasibility of using an offshore concrete gravity platform off the coast of New Zealand.

The existing program generates a ground motion from the superposition of sinusoidal components. Amplitudes of the individual components are based on the intensity of the power spectral density function corresponding to the desired response spectrum. A criticism sometimes levelled at the use of this technique is that results don't resemble real earthquake records. An alternative approach to generating artificial earthquake records was investigated in this study also. An existing earthquake record is used, and the motion is massaged in the frequency domain to match a target acceleration response spectrum supplied by the user. The resulting artificial record retains much of the character of the input motion but overall the response spectrum can give a reasonable match to the required spectrum.

5.2 THE PROGRAM "SIMQKE"

A computer program SIMQKE was developed by Gasparini and Vanmarcke [5.1] for generating artificial ground motions to match a user specified target velocity or acceleration response spectrum appropriate to a particular proportion of critical damping, or power spectral density function. The Fourier analysis principle, that any periodic function can be generated from an infinite trigonometric series, is used. A non-periodic function such as an arbitrary earthquake record can be considered as periodic provided the period is assumed to be longer than the duration of the record.

A function F(t) with period T can be expanded as an infinite series of sine functions as in Eqn. 5.1.

$$F(t) = \sum_{i=1}^{\infty} A_i \sin[(2\pi i/T)\, t + \varnothing_i)] \qquad (5.1)$$

The values A_i are the amplitudes of the individual sine functions (related to the Fourier Amplitudes) and the values $\varnothing_i$ are the corresponding phase angles. The amplitudes A_i can be related to the single sided power spectral density function $G(\omega)$, where $\omega = 2\pi/T$, using the expression in Eqn. 5.2.

$$G(\omega_i) = A_i^2/2 \qquad (5.2)$$

The program calculates the required sinusoid amplitudes from the power spectral density function supplied by the user. For the case where the input is a target response spectrum the power spectral density function is estimated first. A seed number is input by the user and a random number generator is used to choose phase angles between the values of zero and 2π. By choosing different selections of phase angles earthquake motions with similar overall characteristics but slightly different details can be generated. It is thus possible to generate a suite of earthquakes from the same target spectrum.

The individual sinusoidal components are combined, as in Eqn. 5.1, to give the earthquake motion at the required digitisation time step. Any duration of ground shaking can be specified but the generated acceleration time-history tends to contain many acceleration peaks of about the same amplitude. In order to obtain a more realistic looking motion the record is scaled by an intensity function supplied by the user. This enables the build-up to intense ground shaking at the beginning of the record and the decay of intense shaking at the end of the record to be simulated. Various intensity envelopes with trapezoidal, exponential or a combined trapezoidal-exponential shape can be applied. The program also applies so-called base-line corrections to to ensure that the ground velocity reduces to zero at the end of the record. A further adjustment is made to enable the maximum ground acceleration to be specified by the user. The peak acceleration in the record is found and compared with the desired value provided by the user. If the desired maximum acceleration is smaller than the current value, the whole record is scaled down by the ratio of the two. In the present version of the program only the instantaneous peak acceleration is scaled up if its value is less than the value required.

The response spectrum is then calculated from the final ground acceleration record. Either the velocity or acceleration response spectrum, or the power spectrum is calculated, depending on the input target spectrum type. The spectrum from the generated motion is compared with the target spectrum at a specified number of control frequencies, to measure the precision of the match. Linear interpolation of the input spectrum is assumed between the coordinates supplied. The program then provides an iterative procedure to improve the match to the target spectrum. The iteration procedure involves scaling the power spectral density function $G(\omega)$, at all of the control frequencies, by the ratio of the spectral ordinate of the current generated motion to the target spectral value. The user is able to specify the number of iterations which are to be carried out, but the User's Guide to the program suggests that there is little point in using more than about four iterations.

The user can specify the range of frequencies from which contributions to the ground motion will be considered, thus only frequencies of interest need be included. It would be possible to generate several earthquake records which each match the target spectrum over part of the period range only, and fall away from the target outside the matching interval. This would give a suite of earthquakes, with each record having its own predominant range of frequency content.

The technique used by the program SIMQKE is extremely useful. However, one problem with this approach to generating artificial earthquake records is that the distribution of frequency content is stationary throughout the duration of shaking. In real earthquake accelerograms the frequency content varies throughout the record. This is one of the reasons why artificial earthquake records generated using this method sometimes look rather contrived.

5.3 ARTIFICIAL EARTHQUAKE RECORDS GENERATED USING SIMQKE TO MATCH THE PROPOSED NZS 4203 DESIGN ACCELERATION RESPONSE SPECTRA

The proposed amendment to the New Zealand Loadings Code for building structures NZS 4203 [5.2] for determining design acceleration response spectra was discussed in Chapter 3 (refer Section 3.7). The computer program SIMQKE was used to generate a suite of artificial earthquake records to match the elastic acceleration response spectra suggested for design of structures on soft ground.

A suite of three artificial earthquake records was generated for the soft ground elastic spectrum. These can be used for any soft site in New Zealand or for any return period by simple scaling of the records by the appropriate zone and return period factors given in the derivation of the design spectra. Artificial records corresponding to the hard ground spectra were also generated but are not discussed here as only the soft ground records were used in the offshore platform design studies reported in Chapter 8.

Typical input information to the program SIMQKE used to obtain the artificial records is given in the following:

Smallest period in range of frequencies contributing to simulation	=	0.2 sec
Largest period in range of frequencies contributing to simulation	=	8.0 sec
Trapezoidal intensity envelope used - Build-up time	=	1.0 sec
- Level time	=	15.0 sec
Duration of generated accelerogram	=	20.0 sec
Discretization interval for generated accelerogram	=	0.02 sec
Desired maximum ground acceleration	=	0.4 g
Seed number provided for selection of random phase angles	=	arbitrary
Number of iteration cycles for improvement of match to target spectrum	=	3
Number of points used to describe the target spectrum	=	25
Percentage of critical damping appropriate to target spectrum	=	5 percent

Fig. 5.1 shows a typical accelerogram generated by the computer program SIMQKE. The acceleration response spectra of the three generated accelerograms and the target spectrum for single degree of freedom oscillators with 5 percent of critical damping are shown in Figs. 5.2 to 5.4. It can be sen that a reasonable match is achieved over most of the period range but there are local variations with a maximum error of about 20 percent. This is fairly typical of the match which can be expected from the program. It is expected that the effects of local variations in the response spectra are diminished by using a suite of similar accelerograms.

Many engineers seem sceptical about the validity of using artificial earthquake records. A better understanding of how such records are generated, and experience with the results which can be expected from these procedures, should help to allay doubts. Artificial records sometimes look rather contrived with many acceleration peaks of about the same magnitude or with obvious excesses or absences of particular frequency contents. While this may seem significant, the most important test is how well the response spectrum of the generated motion

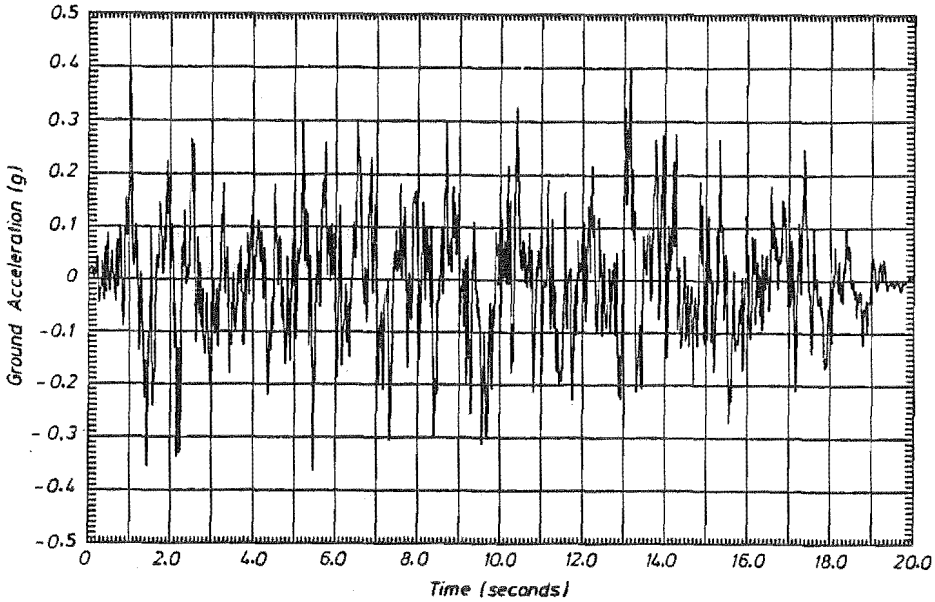

Fig. 5.1 Artificial Accelerogram Generated by SIMQKE to Match Proposed NZS 4203 Soft Ground Design Acceleration Response Spectrum

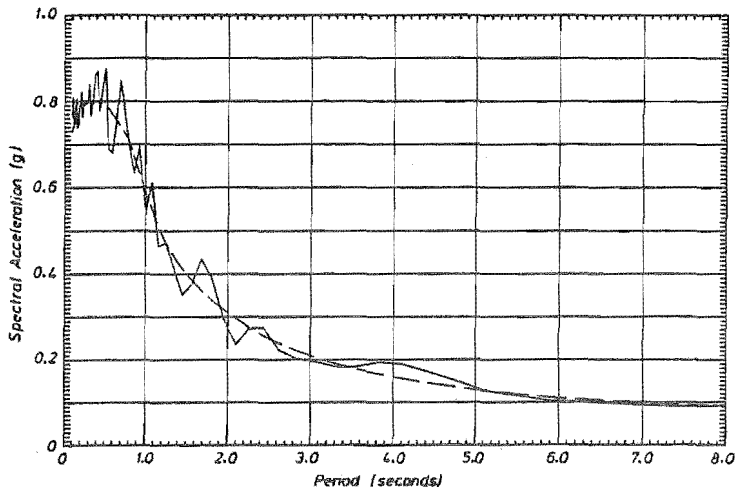

Fig. 5.2 Match of Acceleration Response Spectrum and Target Spectrum - Artificial Motion 1

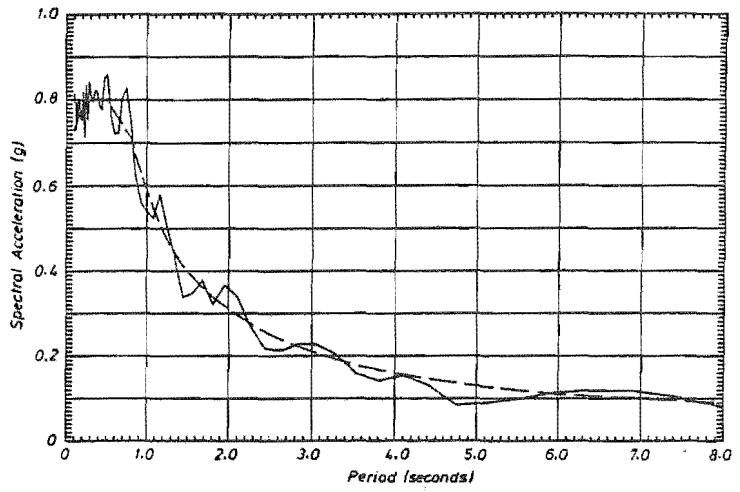

Fig. 5.3 Match of Acceleration Response Spectrum and Target Spectrum - Artificial Motion 2

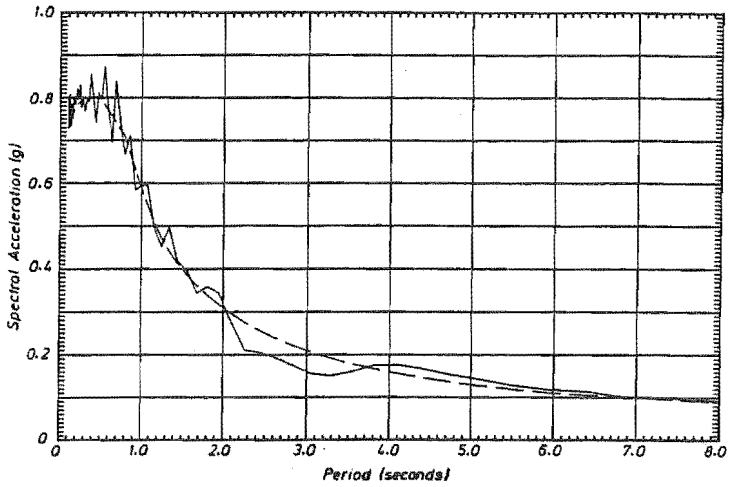

Fig. 5.4 Match of Acceleration Response Spectrum and Target Spectrum - Artificial Motion 3

matches the target spectrum. If a good match is achieved over the range of frequencies of interest then the principal aim of the simulation has been achieved and the actual details of the generated record are of less importance. However, some simple precautions can be taken to ensure that the generated motion will be reasonable. These include choosing a realistic duration of strong shaking, intensity envelope, maximum ground acceleration, and a range of contributing frequencies which envelopes the range of frequencies of interest in the structures to be analysed. Generally the maximum response spectral acceleration for single degree of freedom oscillators with about 5 percent of critical damping will be about 3 times the maximum ground acceleration. The maximum ground displacement and velocity, and the displacement and velocity response spectra can also be checked to see that they are realistic for the intensity of ground shaking being simulated.

5.4 AN ALTERNATIVE APPROACH:- "MASSAGING" OF REAL EARTHQUAKE RECORDS

An alternative approach to generating artificial earthquake records was briefly investigated in this study also. The method is similar to the approach used in the program SIMQKE except that it uses an existing earthquake accelerogram and "massages" the record to try and give a match between the response spectrum and the required target spectrum. A computer program was developed by the author to generate artificial earthquake records using this method.

The program read in a digitised accelerogram and calculated the acceleration response spectrum corresponding to the percentage of critical damping required. A target acceleration response spectrum was also input as a number of period versus spectral acceleration pairs. By taking the discrete Fourier transform, the input record was transformed to the frequency domain, with both real and imaginary components being obtained. A fast Fourier transform (FFT) algorithm was incorporated in the program to calculate the discrete Fourier transform. The program then scaled the frequency domain record at each frequency depending on the discrepancy between the response spectrum of the input record and the target spectrum. The inverse Fourier transform was then calculated to transform the record back to the time domain. The acceleration response spectrum of the massaged record was calculated and compared with the target spectrum.

The fast Fourier transform algorithm used was that given by Brigham [5.3]. To apply this algorithm the number of samples in the time domain must be chosen to be a multiple of 2. To avoid end-effects the duration of the record in the time domain is chosen to be at least twice as long as the actual record used.

A means of measuring the convergence of the procedure was incorporated. The calculated response spectrum was compared with the target values at each of the periods at which the target spectrum was specified. The calculated sum of squares of the differences was expected to reduce as a better match to the target spectrum was achieved. The procedure could be repeated as many times as required to seek a good match to the target spectrum. As for the similar procedure in the program SIMQKE, it was generally found that there was little improvement in the match after three or four iterations.

The scaling factor at each frequency was taken as the square of the ratio between the target spectrum and the actual response spectrum. The target spectrum was linearly interpolated between the specified periods. Satisfactory convergence was also obtained by using a scaling factor equal to the ratio of the target spectral ordinate to the current spectral ordinate but normally the procedure converged more quickly by squaring the ratio.

An example artificial motion was generated by massaging the El Centro north-south record of the 18 May 1940 Imperial Valley, California earthquake to match the elastic soft ground spectrum of the proposed amendment to the NZS 4203 code. Fig. 5.5 shows the acceleration time-history of the first 10 seconds of the El Centro earthquake record and Fig. 5.6 shows the acceleration time-history of the massaged record. It can be seen that the details of the motion have not been changed significantly. In this particular case the amplitude of the acceleration pulses are not changed significantly in order to produce the required acceleration response amplitudes. In other cases the amplitudes may be scaled substantially.

Fig. 5.7 shows the 5 percent damped acceleration response spectra of the input motion, the massaged earthquake motion and the target spectrum. The match between the spectrum from the massaged earthquake record and the target spectrum is reasonable but not quite as good as

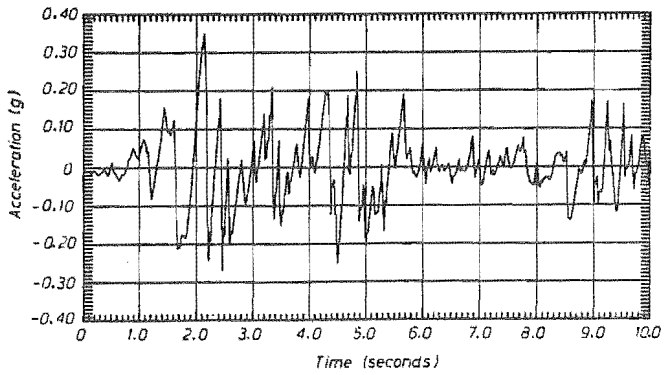

Fig. 5.5 El Centro NS record of the 18 May 1940 Imperial Valley, California Earthquake

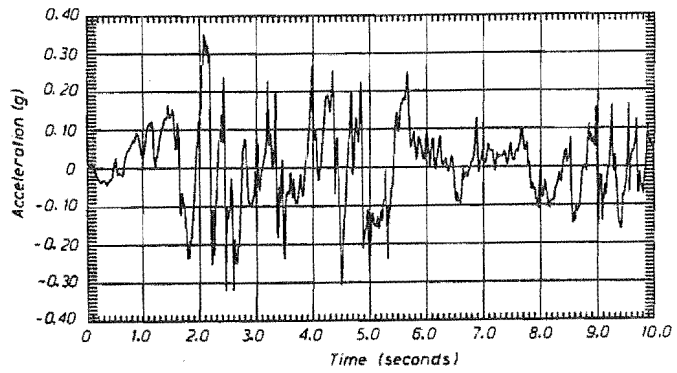

Fig. 5.6 Artificial Accelerogram Generated by Massaging El Centro Record to Match Proposed NZS 4203 Soft Ground Design Acceleration Response Spectrum

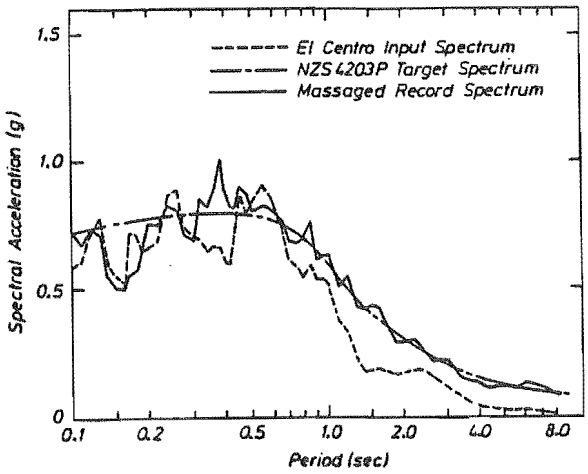

Fig. 5.7 Match of Massaged Record Response Spectrum Against Target Spectrum

the match obtained using the program SIMQKE. The overall spectral shape of the massaged record is governed by the target spectrum but the local troughs and peaks are governed by the original record.

5.5 CONCLUSIONS

1. Structural design for earthquake effects is normally based on smooth acceleration response spectra, obtained either from design codes or from special hazard analysis studies. Inelastic response of structures can only be accurately predicted using analysis in the time domain for which digitised accelerograms are required.

2. Response spectra from the few available real earthquake records seldom bear much resemblance to the smooth spectra adopted for design purposes.

3. Artificial earthquake records can be generated having response spectra which match the required smooth design spectra reasonably well.

4. The program SIMQKE, developed by Gasparini and Vanmarcke, was used to generate a suite of three artificial earthquake accelerograms with acceleration response spectra matching the design spectrum for soft ground from the proposed amendments to the New Zealand Loadings Code for buildings, NZS 4203. Quite good agreement was obtained with the desired target spectrum.

5. An alternative approach to simulating ground motions was investigated in which existing earthquake records were massaged. The match to the required target response spectrum was reasonable but not as good as obtained from the program SIMQKE. Artificial records generated using this approach tend to retain the details of the original record but an overall match to the required target spectrum can be obtained.

5.6 REFERENCES - CHAPTER 5

5.1 Gasparini, D. and Vanmarcke, E. H., "Simulated Earthquake Motions Compatible with Prescribed Response Spectra", M.I.T. Department of Civil Engineering, Research Report R76-4, Order No. 527, January 1976.

5.2 NZS 4203 : 1984, "Code of Practice for General Structural Design and Design Loadings for Buildings", Standards Association of New Zealand, Wellington. 100 pp.

5.3 Brigham, E. O., "The Fast Fourier Transform", Prentice Hall Inc., Englewood Cliffs, New Jersey, 1974, 252 pp.

Chapter 6

EXPERIMENTAL TESTS OF HOLLOW CIRCULAR CONCRETE MEMBERS FOR STRENGTH AND DUCTILITY

6.1 INTRODUCTION

An experimental testing programme was carried out as part of this research to investigate the strength and ductility of hollow circular concrete columns. Six test units were constructed to represent scale models of members which could be used in possible offshore concrete platform configurations. Testing was carried out to simulate severe earthquake loading effects.

Design for seismic resistance has not been a primary concern in the concrete gravity platforms already installed, mainly in the North Sea. Future concrete platforms used in seismically active areas, such as around New Zealand, will need to be capable of withstanding very large earthquakes without collapse. Although a suitably cautious approach will used in designing such platforms to resist earthquake effects, it is unlikely to be economically viable to proportion these structures to remain undamaged during very large earthquakes. It is likely that instead, a reasonable level of strength would be incorporated to enable small or moderate sized earthquakes to be sustained with little or no damage. Structures would also be carefully detailed to ensure that during very large earthquakes, ductile failure mechanisms could be relied upon to sustain the deformations expected. For North Sea type cantilever structures comprising a massive base supporting relatively slender legs, failure will tend to occur either in the foundation or in the legs. Previous research has indicated that both are possible in typical North Sea type structures.

The aim of this study was to investigate the inelastic behaviour of the hollow members which are normally used in offshore concrete platforms. To avoid collapse during severe earthquake shaking, ductile behaviour will be required from the critical sections where inelastic deformations are expected to concentrate. A great deal of information is available regarding the inelastic behaviour of solid concrete members but very little has been reported on the behaviour of hollow members. It was hoped that this series of tests would provide information on how these members could be designed and detailed to ensure satisfactory behaviour.

6.2 PREVIOUS EXPERIMENTAL WORK RELATED TO THE STRENGTH AND DUCTILITY OF HOLLOW CONCRETE MEMBERS

Extensive experimental investigations conducted at the University of Canterbury and elsewhere in recent years have given a good understanding of the post-elastic behaviour of solid reinforced, prestressed and partially prestressed concrete members. Results of such research programmes are summarised by Priestley and Park [6.1]. Important findings from such studies have been incorporated in the New Zealand Concrete Design Code NZS 3101 [6.2]. Only very limited results are available to indicate the likely post-elastic behaviour of hollow concrete members.

Regan and Hamadi [6.3] tested four hollow circular members with an outside diameter of 800 mm and a wall thickness of 40 mm. Two layers of 2.5 mm diameter steel wire mesh were used, one located close to each of the inner and outer faces. A number of 5 mm diameter pretensioned prestressing wires were placed at the centre of the wall to provide between 2 MPa and 4 MPa axial prestress to the units. Some of the test units also contained deformed high strength longitudinal reinforcing bars placed at the centre of the wall. No external axial loads were applied. Testing was carried out by loading the members as cantilevers with concentrated end lateral loads until failure. The members displayed little ductility capability and failures were generally sudden with large loss of strength. In some cases tensile fracture of the

longitudinal mesh bars occurred at the welds. In most cases buckling of the longitudinal bars on the compression side of the section led to collapse of the concrete compression zone and subsequent loss in moment of resistance. Although not considered unsatisfactory by the authors, such non-ductile behaviour would be unsuitable for seismic resistance. A review of these tests would suggest that better performance could have been achieved if ductile longitudinal reinforcement had been used and sufficient closely spaced transverse reinforcement had been present to adequately confine the concrete in the compression zone and prevent premature buckling of the longitudinal bars.

Mander et al [6.4] carried out experimental testing of four hollow reinforced concrete piers with square cross sections. The columns had a shear span of about 3 m with an outside dimension of 750 mm and a wall thickness of 120 mm. Two layers of longitudinal reinforcement were used with one placed close to each of the inner and outer faces and the two layers were tied through the wall thickness by transverse hoops. The piers were tested as cantilevers under sustained axial load and high intensity reversed cyclic lateral loading. Levels of axial load and quantities of transverse hoop reinforcement in the plastic hinge region were varied. The tests showed that well detailed hollow members can perform as well as solid concrete members and are capable of sustaining substantial plastic hinge rotations. It was found reasonable and conservative to detail the transverse reinforcement according to the provisions for solid columns in the New Zealand Concrete Design Code NZS 3101.

Zahn et al [6.5] conducted tests on circular hollow reinforced concrete column members to assess their strength and ductility characteristics. Three pairs of columns were tested, all units being reinforced as for similar solid members, with longitudinal and spiral reinforcement present in only one layer near the outside face. No attempts were made to confine the concrete on the inside face of the section. The columns were about 4 m in height and lateral loading was applied at a central stub. The outside diameter of the circular sections was 400 mm and wall thicknesses of 94 mm, 75 mm and 55 mm were used. This gave outside diameter to wall thickness ratios of 4.26, 5.33 and 7.27 respectively. The two columns of each wall thickness were tested with different levels of applied axial load to investigate the influence on the available ductility. The results showed that the units with low axial load and wall thicknesses of 94 mm and 75 mm behaved in a ductile manner with stable load deformation hysteresis and excellent energy dissipation characteristics. The columns with higher axial load ($P_e > 0.2f_c'A_g$), and those with low axial load and only 55 mm wall thickness, showed unstable hysteretic behaviour and extremely limited available ductility. It was concluded that this poor performance was due to high concrete compressive strains at the inside face of the sections causing spalling of the concrete and loss of the concrete compression zone.

6.3 TYPICAL FEATURES OF CONCRETE GRAVITY PLATFORM MEMBERS

To date approximately fifteen offshore concrete gravity platforms have been installed in the North Sea area in water depths ranging from 70 m to approximately 150 m. Typically, these structures have had massive cellular bases supporting from one to four hollow circular leg members (shafts) of variable diameter and wall thickness. Typical leg members have been about 100 m high with wall thicknesses at the base of about 1 m and outside diameters at the base ranging from about 12 m to 25 m. Diameters and wall thicknesses have generally been tapered to smaller dimensions at the water line and above, where the flexural demands are smaller. The resulting outside diameter to wall thickness ratios (D/t) near the base of the shafts has been in the range of approximately 15 to 25. Lateral load design of the leg members has been governed by wave loading considerations.

In order to ensure floating stability of concrete gravity platforms at all times during the deck mating, tow-out and sinking phases of installation, substantial positive buoyancy is necessary in the legs of these structures. Very simply, the centre of buoyancy must be kept sufficiently above the the centre of gravity to maintain stability. Clearly, the presence of mass such as the deck and topside facilities, above the water-line during installation, makes it desirable to have significant buoyancy in those portions of the shafts floating just below the water surface. It is easily shown that if the mass per unit length of hollow circular concrete member (with no internal water) is to be less than the displaced mass of water, then the outside

diameter to wall thickness ratio D/t must be at least 8.22, assuming a concrete to sea water density ratio of 2.34.

The earliest offshore concrete platform structures used concretes with compressive cylinder strengths in the range of 30 to 40 MPa. High strength concretes with compressive cylinder strengths in the region of 50 MPa to 60 MPa are now being used quite commonly in platform structures. There may be a future trend toward the use of very high strength concretes. Recent developments in concrete materials for offshore applications include the use of concretes with cylinder strengths of up to 100 MPa. With admixtures such as silica fume, strengths of this order can readily be achieved. Super-plasticisers are normally used also, as they significantly reduce the water required to achieve a workable mix.

Axial loads are induced in leg members due to the weight of the platform deck and topside facilities and also due to self-weight. For typical platform structures used to date the axial stress levels imposed on sections at the base of the shafts appear to have been equal to about 10 percent of the concrete cylinder strength. Additional axial loads are induced by hydrostatic pressures in any shafts which are not flooded. The effect depends on water depth and shaft geometry. For example, considering a typical shaft layout, at 100 m depth axial stresses of about 3 MPa could be induced.

Axial prestress is generally provided in the members of offshore concrete platforms to provide better fatigue life, crack control and corrosion resistance. Levels of prestress which have been used appear to have been in the range of 10 to 20 percent of the concrete compressive cylinder strength. Design codes such as the American Concrete Institute "Guide for the Design and Construction of Fixed Offshore Structures" [6.6] warn against the excessive use of prestressing in platform structures designed to resist earthquakes.

Little information is published regarding details of longitudinal and transverse reinforcement which have actually been used in the shafts of platforms constructed to date. However, normal limits suggested by design codes would be appropriate. Back calculation of information published on the Shell Brent B platform [6.7] indicates that a longitudinal reinforcement content of approximately 2.5 percent of the gross section area was provided at base of the shafts.

6.4 DETAILS OF TEST UNITS

6.4.1 Test Unit Layout

Six hollow circular concrete columns were constructed to model the leg members of offshore concrete platform structures. Details of the layout and dimensions of the six test units are shown in Fig. 6.1 and details of the reinforcement provided in the units is shown in Fig. 6.2. The shear span of the members was about 3.2 m and the outside diameter of the circular cross-section was 800 mm. The columns were thus only about one twentieth of typical full size members. A solid concrete base was used to introduce the lateral loading to the members. The critical section in the hollow circular tube was located just above the base. The upper part of the member was cast solid to enable external loads to be applied.

Units 1 and 2 had a wall thickness of 100 mm and thus had a rather low outside diameter to wall thickness ratio (D/t = 8). Units 3 to 6 used tube wall thicknesses of 50 mm (D/t = 16) giving proportions more representative of typical leg members of North Sea platforms. The 50 mm wall thickness represented a practical lower limit using conventional reinforced concrete construction techniques.

The shear span to member diameter used in these tests was approximately 3.9 which was considered to be a reasonable representation of the member geometry used in North Sea concrete platform structures.

The thickness of cover concrete provided to the transverse reinforcement was 10 mm in Units 1 and 2, 5 mm in Units 3 and 4, and 4 mm in Units 5 and 6. Thus about 10 percent of the gross

concrete area consisted of cover concrete on the inside and outside of the sections which was expected to spall off when large deformations were imposed on the members. The Det norske Veritas design rules [6.8] specify a minimum cover to nonprestressed longitudinal reinforcement of 50 mm in the splash zone and submerged areas. At least 100 mm cover is required to the ducts of prestressing tendons. The British Code of Practice for Fixed Offshore Structures BS 6235 [6.9] specifies minimum nominal cover thicknesses of 60 mm for both internal and external surfaces in submerged areas for nonprestressed reinforcement, and 75 mm for prestressed reinforcement.

Cover thickness has an important effect on the post-elastic behaviour of concrete members as the moment of resistance of a section often reduces when the cover concrete spalls off. For a prototype sized member with a wall thickness of about 1 m and 60 mm cover to the longitudinal reinforcement, the cover thickness ratio would be approximately 0.05. The cover thicknesses used in the test units are thus conservative and the deterioration of flexural resistance due to cover loss would be more severe than in the prototype.

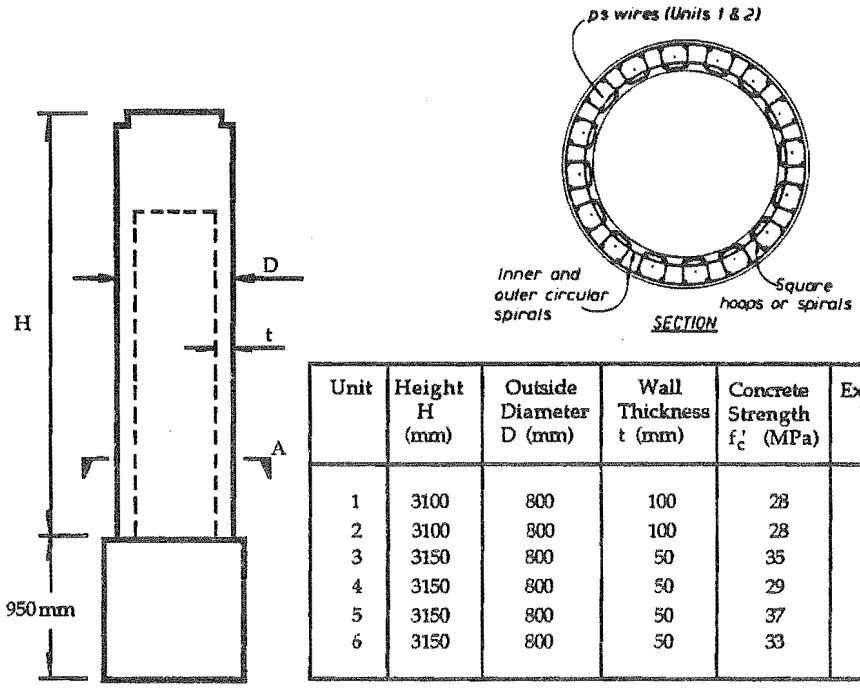

Unit	Height H (mm)	Outside Diameter D (mm)	Wall Thickness t (mm)	Concrete Strength f_c' (MPa)	External Axial Load Level $P_e/f_c'A_g$	Axial Prestress Level $P_{ps}/f_c'A_g$
1	3100	800	100	28	0.125	0.125
2	3100	800	100	28	0.3	0.125
3	3150	800	50	35	0.3	-
4	3150	800	50	29	0.3	-
5	3150	800	50	37	0.3	-
6	3150	800	50	33	0.3	-

Fig. 6.1 Layout and Dimensions of Column Tests Units

6.4.2 Axial Load Level

Levels of external axial load which were applied to the test units during testing are given in the table in Fig. 6.1. In Unit 1 an external axial load level of $0.125f_c'A_g$ was used but in all other units a higher axial load level of $0.3f_c'A_g$ was applied. From a survey of available information on existing platforms it was found that this level of axial load represented an upper bound to the likely levels at critical sections. In Units 1 and 2 axial prestress was also present to a level of $0.125f_c'A_g$. In Units 3 to 6 no axial prestress was used.

Previous experimental research [6.1] has highlighted the influence of axial load level on the available ductility of reinforced and prestressed concrete members. It has been found that the quantity of transverse reinforcement required in a member to achieve a given ductility increases with axial load level. This is recognised in the New Zealand Concrete Design Code NZS 3101 [6.2].

As the expected levels of axial prestress were quite moderate and did not appear to adversely affect the performance of Units 1 and 2, it was decided to omit prestressing from the subsequent test units. This resulted in a considerable simplification to the construction of these members.

6.4.3 Longitudinal Reinforcement

Non-prestressed longitudinal reinforcement was provided in Units 1 and 2 by sixty four Grade 315 (yield stress = 315 MPa) deformed 10 mm diameter bars, giving a volumetric steel content of 2.3 percent. Axial prestress was provided by sixteen 7 mm diameter single wire tendons located at the centre of the wall thickness. Units 3 to 6 contained 120 Grade 430 deformed 6 mm diameter nonprestressed bars giving a steel content of 2.9 percent. The typical arrangement of reinforcement can be seen in the sectional view of Fig. 6.1.

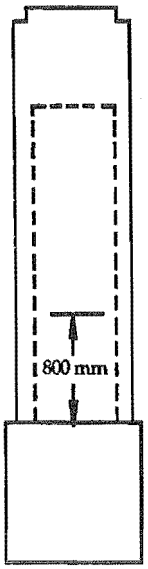

	Transverse Reinforcement	
	Unit 1	Unit 2
Circular spirals	2 - R6 Grade 320 @ 80	2 - R6 Grade 325 @ 80
Circular spirals	2 - R6 Grade 325 @ 50	2 - R6 Grade 325 @ 40
Square ties (dimensions)	R6 Grade 325 @ 50 (80 mm x 80 mm)	R6 Grade 325 @ 40 (80 mm x 80 mm)

Longitudinal Reinforcement Units 1 and 2
Non prestressed: 64 - D10 Grade 315
Prestressed: 16 - 7 mm tendons

a) Reinforcement Provided in Test Units 1 and 2

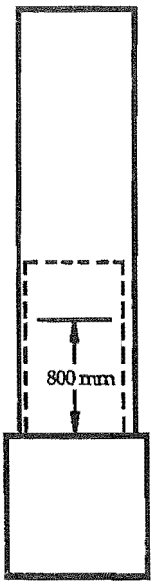

	Transverse Reinforcement			
	Unit 3	Unit 4	Unit 5	Unit 6
Circular spirals	2 - R3.15 Grade 310 @ 50	R4 Grade 255 @ 50	R4 Grade 255 @ 50	R3.15 Grade 245 @ 50
Circular spirals	2 - R3.15 Grade 310 @ 30	R4 Grade 255 @ 30	R4 Grade 255 @ 25	R3.15 Grade 245 @ 25
Circular spirals	2 - R3.15 Grade 310 @ 30	R4 Grade 255 @ 30	R4 Grade 255 @ 25	R3.15 Grade 245 @ 25
Folded spirals (dimensions)	R4 Grade 255 @ 30 (50 mm x 40 mm)	R4 Grade 255 @ 30 (50 mm x 40 mm)	R4 Grade 300 @ 25 (62 mm x 42 mm)	R4 Grade 300 @ 25 (62 mm x 42 mm)
U - bar links	—	—	—	R4 Grade 225 @ 25

Longitudinal Reinforcement Units 3 to 6 120 - D6 Grade 430

b) Reinforcement Provided in Test Units 3 to 6

Fig. 6.2 Reinforcement Provided in Test Units

The stress-strain characteristics of the reinforcement used in the various test units are shown in Figs. 6.3 to 6.5. Fig. 6.3 shows the measured tensile stress-strain behaviour of the prestressing tendons used in Units 1 and 2 and Fig. 6.4 shows the measured tensile stress-strain behaviour of the nonprestressed longitudinal reinforcement.

The nonprestressed longitudinal reinforcement in all units was provided in two layers, one close to each of the inner and outer faces. This was considered essential so that a well confined core of concrete would remain after any cover concrete had spalled from the inner and outer faces of the member. The spacing of the longitudinal bars around the circumference was chosen so as not to exceed about 75 percent of the overall wall thickness. This was done to limit the penetration of spalling between the bars into the core of the section. It should be noted that this violated the requirement of the New Zealand Concrete Design Code NZS 3101 that the centre to centre spacing of the longitudinal bars should not exceed one fifth of the least lateral dimension of the cross-section, that is, one fifth of the wall thickness. While this bar spacing limitation is reasonable in full size members, practical restrictions made this too difficult to meet in the small scale test units. Thus the area of effectively confined core concrete was conservatively modelled.

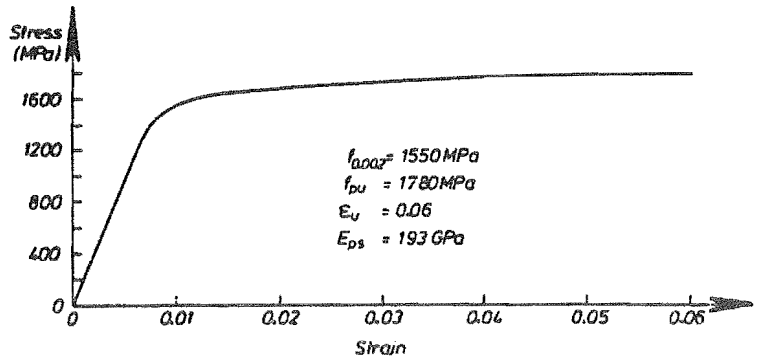

Fig. 6.3 Measured Stress-Strain Behaviour of Prestressing Tendons

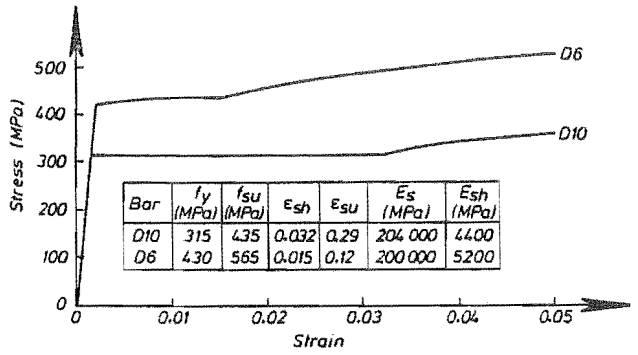

Fig. 6.4 Measured Stress-Strain Behaviour of Nonprestressed Longitudinal Reinforcement

6.4.4 Transverse Reinforcement

The typical layout of transverse reinforcement used in the test units is shown in the section view of Fig. 6.1. All transverse reinforcement used was from plain round bar, and sizes used in the test units were 6 mm (R6) in Units 1 and 2, and 3.15 mm (R3.15) or 4 mm (R4) in Units 3 to 6. Fig. 6.5 shows the measured tensile stress-strain behaviour of the transverse reinforcement. It should be noted that three different grades of 4 mm bar and two different grades of 3.15 mm bar were used in the units. The grades used in each test unit were distinguished in Fig. 6.2.

Quantities of transverse reinforcement were determined generally according to the requirements of the New Zealand Concrete Design Code NZS 3101. Special provisions are made in that code for the design of members for seismic resistance. There are three main requirements in the design of transverse reinforcement. Firstly, it is required to help provide a shear resistance mechanism, secondly to provide confinement to the concrete in the core of the section and thirdly to restrain longitudinal bars from premature buckling.

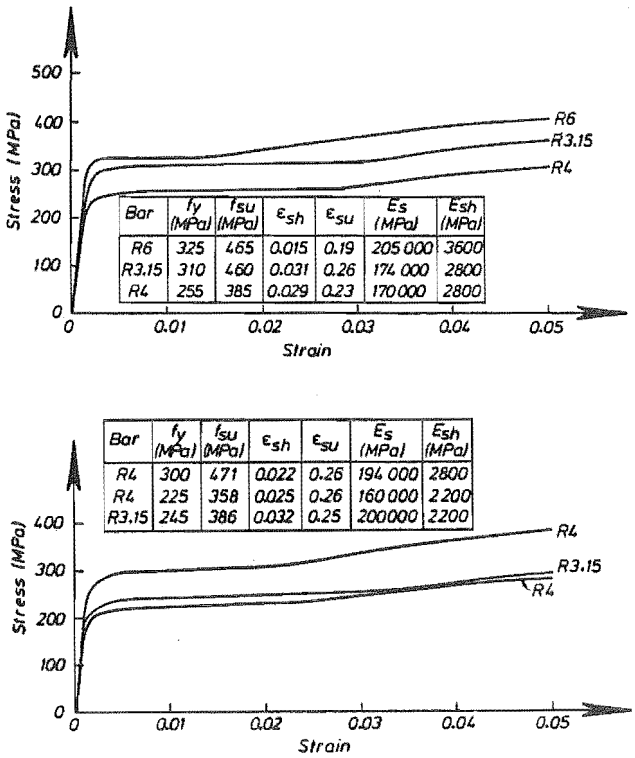

Fig. 6.5 Measured Stress-Strain Behaviour of Transverse Reinforcement

Shear:

The undesirable nature of shear failures in reinforced concrete members has led to the current design philosophy to ensure that shear failures are guarded against in favour of ductile flexural hinging in carefully detailed plastic hinge zones. Capacity design methods ensure that the ideal shear capacity V_t is greater than the shear V_o associated with the expected flexural overstrength of the member. It is generally expected that the overstrength capacity will be about 25 percent in excess of the shear V_i associated with the ideal flexural capacity based on nominal material strengths. This is partly to account for the actual material strengths exceeding the nominal values and partly to account for strain hardening in the reinforcement and strength enhancement of the confined concrete.

The NZS 3101 code approach for shear design assumes that part of the total shear resistance V_t will be contributed by concrete shear resistance mechanisms ,V_c, and the remainder by a steel shear resisting mechanism V_s. The total ideal shear resistance is given by Eqn. 6.1.

$$V_t = V_c + V_s \quad > V_o \tag{6.1}$$

The shear carried by concrete mechanisms is given by Eqn. 6.2.

$$V_c = v_c b_w d \tag{6.2}$$

v_c is the concrete shear stress, b_w is the equivalent width of the section web and d is the effective depth of the section. The quantity $b_w d$ represents an area on which the concrete

shear stress can be assumed to act. For the hollow circular sections of interest here an equivalent $b_w d$ value was derived by considering a uniform shear flow around the tube walls. Assuming a thin-walled tube with centre line diameter D and wall thickness t with a uniform shear stress v acting around the circumference, the average shear stress v_{av} acting in the direction of the applied shear force can be derived, as in Eqn. 6.3.

$$v_{av} = \frac{4 \int_0^{\pi/2} vtD/2 \sin\phi \, d\phi}{\pi D t}$$

$$= (2/\pi)\, v \qquad (6.3)$$

The resulting effective area is equal to $2/\pi$ (about 64 percent) times the gross area of the section.

In plastic hinge regions the concrete shear stress term v_c is given by Eqn. 6.4.

$$v_c = 4 v_b \sqrt{[(P_e/f_c' A_g) - 0.1]} \qquad (6.4)$$

v_b is the basic concrete shear stress, given by Eqn. 6.5.

$$v_b = (0.07 + 10\rho_w)\sqrt{f_c'} \qquad \leq 0.2\sqrt{f_c'} \qquad (6.5)$$

where P_e = design axial compression load on the section
f_c' = concrete compressive cylinder strength
A_g = gross section area
ρ_w = volumetric ratio of tension reinforcement = $A_s/2A_g$
A_s = Total area of nonprestressed longitudinal reinforcement

For the case where $P_e/f_c'A_g < 0.1$, or where the axial force is tensile, then v_c is to be taken as zero.

Outside plastic hinge regions the concrete shear stress is given by the expression in Eqn. 6.6 for columns subject to axial compression and by Eqn. 6.7 for columns subject to axial tension.

$$v_c = (1 + 3P_u/f_c'A_g)\, v_b \qquad (6.6)$$

$$v_c = (1 + 12P_u/f_c'A_g)\, v_b \qquad (6.7)$$

P_u is the factored axial load on the cross-section. In Eqn. 6.7 P_u is taken as negative.

The steel shear resistance mechanism is based on a truss analogy. A 45 degree diagonal crack is assumed and the shear force V_s resisted by transverse shear reinforcement is taken to be the sum of the components of the yield forces of all bars crossing the crack in the direction of loading. NZS 3101 gives the expression in Eqn. 6.8 for V_s.

$$V_s = A_v f_y d/s \qquad (6.8)$$

A_v is the total area of hoop legs with yield stress f_y in each layer parallel to the direction of the applied shear, d is the effective depth of the section and s is the hoop set spacing. No distinction is made in NZS 3101 between rectangular and circular sections. For a circular spiral of area A_{sp} wound with diameter d_s and pitch s, Ang [6.10] has shown that the shear resistance provided by the components of spiral bar forces crossing a 45 degree crack is given by Eqn. 6.9.

$$V_s = (\pi/2) A_{sp} f_y d_s/s \qquad (6.9)$$

For members in these tests containing two circular spirals, such as in Units 1 to 3, where inner and outer spirals were able to engage a layer of longitudinal bars, both spirals were considered to be effective at resisting shear.

NZS 3101 also requires a check that the total shear stress level v_d associated with the design shear force V_d in plastic hinge regions is less than the value given by Eqn. 6.10.

$$v_d = V_d/b_w d \qquad \leq 0.9\sqrt{f_c'} \qquad (6.10)$$

The equations presented were used to check the shear capacity of the test units.

Confinement:

The New Zealand Concrete Design Code NZS 3101 specifies minimum quantities of transverse confining reinforcement to be provided in plastic hinge regions. These quantities were used as a basis for the amounts chosen in the test units.

For confinement provided by circular spirals NZS 3101 specifies the minimum volumetric confinement ratio ρ_s to be the greater of the values obtained from Eqns. 6.11 and 6.12.

$$\rho_s = 0.45\,[(A_g/A_c)-1]\,f_c'/f_{yh}\,[0.5 + 1.25\,(P_e/\phi f_c' A_g)] \qquad (6.11)$$

or

$$\rho_s = 0.12\,(f_c'/f_{yh})[0.5 + 1.25\,(P_e/\phi f_c' A_g)] \qquad (6.12)$$

where

$$\rho_s = 4\,A_{sp}/d_s s \qquad (6.13)$$

and A_g = gross area of concrete section, A_c = area of confined concrete core, f_{yh} = yield strength of transverse hoop bars, P_e = design axial compression load on the section and ϕ = strength reduction factor normally to be taken as 0.9 for a confined column, f_c' = concrete compressive cylinder strength, A_{sp} = cross sectional area of spiral bar, d_s = diameter of spiral turns and s is the spiral pitch.

For columns with confinement provided by rectangular hoops, with or without supplementary cross-ties, the total area of hoop legs across the section in each direction, A_{sh}, is specified to be the greater of Eqns. 6.14 and 6.15.

$$A_{sh} = 0.3\,s_h\,h''[(A_g/A_c) - 1]\,f_c'/f_{yh}\,[0.5 + 1.25\,(P_e/\phi f_c' A_g)] \qquad (6.14)$$

$$A_{sh} = 0.12\,s_h\,h''\,(f_c'/f_{yh})[0.5 + 1.25\,(P_e/\phi f_c' A_g)] \qquad (6.15)$$

s_h = spacing between the hoop sets, h" = dimension of the concrete core of the section measured perpendicular to the direction of the hoop bars to the outside of the peripheral hoop, and the other terms are as for columns confined with circular spirals.

The above equations recognise the greater efficiency of circular spirals over rectangular hoops. This is because spiral bars acting in tension can apply continuous confining pressure around the circumference of a section whereas rectangular hoops apply non-uniform confining pressures. Good confinement may be provided near the corners of rectangular hoops, but between hoop corners the hoop leg can bend outwards and the concrete core is less well confined.

The NZS 3101 equations specify quantities of transverse confining reinforcement to enable members to sustain ductility levels consistent with those implied by current loadings codes for buildings [6.11] and bridges [6.12]. It is thought that structures designed to those loadings codes would undergo displacement ductility factors of approximately 4 during an earthquake with a return period of about 150 years. The commentary of NZS 3101 states that the critical sections of members detailed to the provisions of that code should be capable of sustaining

curvature ductility factors of approximately 20. For the design of unusual structures such as offshore platforms it is likely that quite different levels of ductility capability will be required from the critical sections. Design earthquake loadings are likely to be more severe and ductility demands are likely to be significantly less than for most structures. It was thus appropriate to investigate the available ductility from members with a range of contents of transverse confining reinforcement.

Antibuckling:

Longitudinal bars are restrained against longitudinal buckling by the corners of the transverse bars which engage them. Eventually even longitudinal bars restrained by transverse reinforcement are likely to buckle, but tests have shown that if the transverse bars are spaced closely enough, buckling can be prevented until quite large compression strains have been sustained in the reinforcement. After buckling of the longitudinal reinforcement does occur the confined concrete core in the compression zone of the member deteriorates rapidly and results in loss of flexural resistance. Extensive experimental testing on reinforced concrete members using a wide range of longitudinal bar sizes and transverse hoop spacings has led to the so-called antibuckling requirement of the NZS 3101 code that the centre to centre spacing of circular spirals or rectangular hoops in plastic hinge regions should not exceed six longitudinal bar diameters. This ensures that buckling of the longitudinal bars will be delayed until high compression strains have been reached.

Mander et al [6.4] presented an analytical approach, based on the double modulus of the yielded bar, to determine the maximum compression strain for a given hoop spacing. An example presented for a typical 16 mm Grade 275 bar indicated that a compression strain of about 0.05 could be sustained during monotonically applied compression loading if the bar was restrained at spacings of six longitudinal bar diameters.

Transverse reinforcement was provided in the test units by circular spirals, and square ties or folded rectangular spirals around each group of longitudinal bars. The actual layouts used in each of the test units are shown in Fig. 6.6. The circular spirals provided shear reinforcement and confinement in the circumferential direction. The square ties (Units 1 and 2) or folded rectangular spirals (Units 3 to 6) provided confinement to the concrete contained within them in both the circumferential and radial directions. They also restrained the longitudinal bars from premature buckling.

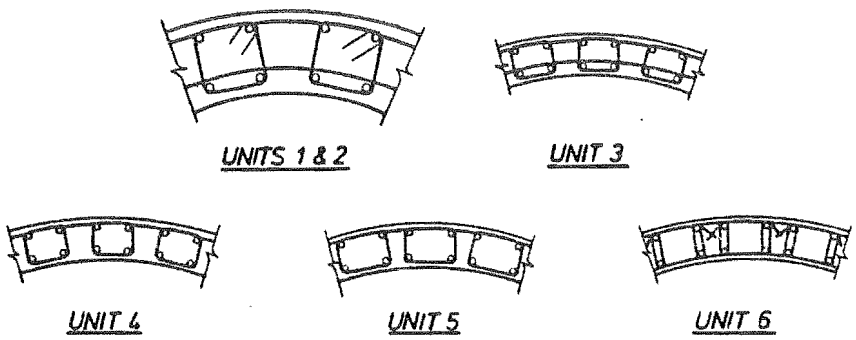

Fig. 6.6 Transverse Reinforcement Layouts in Compression Zones of Plastic Hinge Regions

It should be noted that in Units 1 to 3 an inner circular spiral was also used and was located on the core side of the inner layer of longitudinal bars. While it was appreciated that construction would have been easier if this spiral had been placed within the inside cover concrete, it was expected that the spiral would have then been able to burst through the cover. The inner circular spirals were only effective as both shear and confining reinforcement because they could bear against the tied longitudinal bars.

In Unit 6 the folded rectangular spirals were interlinked in the compression areas (about the outer third of the section depth on either side) of the plastic hinge zone by U-shaped ties with their ends bent around the outer longitudinal bars. Over the middle third of the section depth these additional links were not provided as the longitudinal compression strains in the concrete were not expected to be large.

Quantities of transverse confining reinforcement provided in the six test units for the circumferential and radial (through wall) directions are given in Table 6.1. The quantities are presented as the ratio of the transverse confining stress f_l on the concrete core when the hoops yield to the unconfined compressive cylinder strength f_c'. The fractions of the quantity required by the New Zealand Concrete Design Code NZS 3101 for rectangular hoops are also given. The bar spacings in the test units were quite large compared with the dimensions of the confined concrete core and it was evident that spalling of the cover concrete penetrated some distance into the core between the longitudinal and transverse bars. It was reasoned that the arrangements of transverse bars were less effective because of this and a confinement efficiency factor of about 0.8 was incorporated in calculating the quantities of confining reinforcement provided. The actual efficiency factors assumed for each of the test units are also given in Table 6.1.

It can be seen that in all test units considerably more confinement was provided in the circumferential direction than was required by the NZS 3101 code. However, in the radial (through-wall) direction quantities ranged from about 58 percent to 135 percent of the code amount.

Table 6.1 Quantities of Transverse Confining Reinforcement Provided in Test Units

Unit	Confining stress ratios		Fraction of NZS 3101 Requirements		Confinement Efficiency Factor
	Circumferential f_{lc} / f_c'	Radial f_{lr} / f_c'	Circumferential	Radial	
1	0.206	0.075	2.62	0.95	0.79
2	0.270	0.099	2.57	0.94	0.83
3	0.164	0.061	1.56	0.58	0.75
4	0.158	0.071	1.50	0.68	0.75
5	0.189	0.084	1.80	0.80	0.80
6	0.162	0.142	1.54	1.35	0.80

The efficiency factors were estimated by considering the confining action provided by the arrangements of circular spirals and rectangular hoops. When spalling of the cover concrete occurred there was some penetration of damage into the core of the section in the spacings between successive levels of transverse reinforcement. It was assumed that the concrete would arch between the the sets of transverse bars, as illustrated in Fig. 6.7. A parabolic arch shape was considered with 45 degree entrant angles and it was assumed that concrete on the outside of this arch would not be effectively confined. The concrete core thickness to the outside of the hoops was taken as t_c and the spacing between the hoops as s. The efficiency factor k_e was calculated by determining the proportion of the total core area which was effectively confined. Simple geometric analysis gives the expression in Eqn. 6.16.

$$k_e = 1 - (s / 3t_c) \qquad (6.16)$$

The theoretical margins provided against shear failure in the test units are given in a later section of this chapter (refer Table 6.4). The capacity design methods incorporated in the New Zealand Concrete Design Code NZS 3101 would normally result in a reserve shear capacity ratio V_t/V_i of about 1.15. Flexural performance was of most interest in the test units and large reserves of shear capacity were available in Units 1 to 3. However, it was also

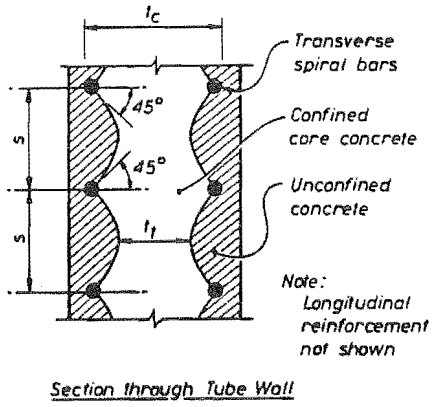

Fig. 6.7 Assumed Arching Action Between Spiral Bars

important to determine whether the method used for shear design was conservative, as it had been adapted from methods used for solid members. Hollow sections are efficient in flexure and could become critical in shear, particularly if the shear span was quite small compared with the member diameter. The reserve shear capacities in Units 4 to 6 were kept to a minimum to investigate the adequacy of the chosen shear design method.

6.4.5 Concrete

Because of the congested reinforcing arrangements, small wall thicknesses and very small cover concrete thicknesses, small aggregate concrete mixes were used in tubular portions of the test units. In order to achieve satisfactory placement and compaction of the concrete it was necessary to have a highly workable concrete and super-plasticisers were used where necessary to increase workability. Ordinary Portland Cement and clean river-run greywacke aggregates were used in all concrete mixes. Actual mix details were varied in each unit depending on the strength and workability required, but the following quantities and characteristics are representative.

Water/cement ratio = 0.56
Aggregate/cement ratio = 5.0

Mix quantities (for 1 m^3):

Cement (OPC)	360. kg
Water	202. kg
Aggregate	1800. kg

Aggregate grading:

Size Range (mm)	Proportion	Mass (kg)
< 0.15	0.025	45
0.15 - 0.3	0.075	135
0.3 - 0.6	0.10	180
0.6 - 1.2	0.10	180
1.2 - 2.4	0.20	360
2.4 - 5.0	0.20	360
5.0 - 10.0	0.30	540
Total	1.00	1800

Air entraining agent (AEA Darex): Dosage 15 ml/100 kg cement = 54 ml
Super-plasticiser (WRDA - FL): Dosage 0.005 times cement mass = 1.8 kg

Slump before adding super-plasticiser = 45 mm
Slump after adding super-plasticiser = 180 mm

28 day compressive cylinder strength = 35 MPa

In Units 3 and 4 the aggregate grading was slightly different as the 5 mm to 10 mm size range was not used. This resulted in a mortar-like concrete. After the poor performance of Units 3 and 4 had been obtained it was suspected that the very small aggregate concrete may not display the required expansive behaviour at large strains to allow the passive confining action of the transverse reinforcement to develop. As this may have contributed to the relatively poor performance of those test units the larger size fractions of aggregate were included in Units 5 and 6 to try to minimise such effects.

The compressive cylinder strengths obtained at the time of testing for each of the test units are given in the table in Fig. 6.1.

For the portions of the test units other than the hollow sections, ready mixed concrete was purchased from a commercial concrete manufacturer. This had a maximum aggregate size of 13 mm and a minimum specified 28 day compressive cylinder strength of 40 MPa.

6.4.6 Construction Details

Construction of the test units was completed with four concrete pours, one for the solid base block, one for the 1200 mm height of hollow tube and two for the solid infilled circular portion at the top. The construction procedure is outlined below.

Base Block:

1. The 900 x 900 x 10 mm plate forming the underside of the base was drilled to locate the vertical reinforcing bars. For Units 1 and 2 additional holes were drilled for the sixteen prestressing tendons and short lengths of steel tube to form the beginning of the duct were attached.

2. Longitudinal nonprestressed bars were located at welded to the base plate.

3. About two turns of circular spiral and small rectangular ties were placed around the longitudinal reinforcement just below the top surface of the block. After the base concrete was poured the circular spirals were continued up into the walls of the hollow tubular portion of the test units. Longitudinal bars were held in place by plywood templates while the transverse steel was fixed and concrete was placed.

4. For Units 1 and 2 prestressing duct formers, consisting of lengths of 20 mm diameter rubber tubing were passed down the middle of each group of four vertical bars. These fitted neatly into the short lengths of steel tube already attached to the base plates. The rubber formers were held straight with lengths of 6 mm steel rod pushed inside.

5. Shear reinforcement for the base block was fixed in place. This consisted of 5 pairs of overlapping D20 Grade 275 U-shaped bars placed between the upper and lower sets of bolts for fixing the inclined steel loading arm. Light basketting reinforcement consisting of approximately D10 L-shaped bars at 200 centres was also fixed in place.

6. Formwork for the base block consisted of construction plywood and 100 x 50 mm timber framing. The two end forms were positioned and bolted down. Lengths of 25 mm OD PVC conduit were passed through the reinforcing cage and into holes in the forms. These formed clear holes through the base so that the steel rods attaching the inclined steel loading arm could be removed and reused. In Units 3 to 6 it was necessary to offset some of the longitudinal reinforcing bars in the base to pass around the conduits. These bars were cranked back to their required position just below the top surface of the base block.

7. The 20 mm high strength steel rods were inserted to hold the formwork.

8. The side forms were placed and bolted to the end forms. All joints were sealed to minimise leakage.

9. Concrete was placed and vibrated. Test cylinders were cast. A retarding agent was applied to the construction joint surface over the area where the tube wall would continue.

10. The following day retarded concrete was removed from the construction joint area and the surface was roughened. The rubber duct formers were pulled out to leave a clear straight duct hole. This was temporarily plugged to prevent the intrusion of debris. Exposed concrete was covered with wet sacking and polythene and left to cure. Formwork was removed after about one week.

1200 mm Hollow Circular Portion:

1. For Units 1 and 2 the layout of circular spirals and separate ties was continued up and fixed in place to the longitudinal reinforcement. For Units 3 to 6 the folded square spirals were preformed and dropped down over the longitudinal bars. The outer and inner circular spirals, where appropriate, were then fixed in place.

2. For Units 1 and 2 the spirals had been wound from 6 m lengths of straight bar. Laps were made by arc welding in place as necessary. Units 3 to 6 used continuous wire spirals supplied in coil form. A manageable amount was cut off and fixed in place with overlapping splices being used. The ends of each length were hooked around a longitudinal bar to ensure anchorage.

3. Strain gauges were attached to the circular spirals at the required positions. The ties for Units 1 and 2, and the folded spirals for Units 3 to 6 were strain gauged prior to assembly.

4. The temporary plugs were removed from the the prestressing ducts holes in the previous concrete pour. The rubber duct formers were passed down through the reinforcing cages and the tapered ends were pushed a short distance into the existing concrete.

5. Steel formwork was assembled and positioned on the inside and outside of the reinforcing cages. This formwork consisted of semicircular steel shells made from 2 mm steel sheet rolled to the required internal or external diameter of the concrete tube. Steel rings were welded to the shells to provide stiffening. Two steel channels were fabricated to bolt between the halves of the inner formwork to allow easy removal. The form work was sealed and fixed down to the base block.

6. Purpose made studs were fabricated to space the inner and outer formwork shells. These were cast in to the tube walls and some were used for mounting instrumentation during testing.

7. Concrete was placed and compacted using external vibrators attached to the outer formwork. A small internal vibrator was also pushed down through the reinforcing wherever possible. Concrete test cylinders were cast and placed in a fog room the following day.

8. Formwork was left in place for about one week to reduce moisture loss.

Solid Circular Upper Portion:

In Units 1 and 2 the hollow walls were slip-formed up to a total height of 2.3 m above the the base following a similar procedure to that just described. Above that level the circular column was made solid. In Units 3 to 6 only the lower 1.2 m was hollow and the remainder was cast solid with two separate concrete pours. The solid portions of the columns were constructed as follows:

1. A stiffened circular plywood disk was fitted inside the concrete tube level with the top of the previous concrete pour. This formed the soffit of the solid portion and was supported on wooden blocks bolted to the studs cast in the wall below.

2. The outer circular spiral was continued up at the required spacing and fixed to the longitudinal reinforcement. Where an inner spiral was also provided in the tube wall this was continued for a few turns in to the solid portion.

3. The outer formwork shells were placed with 100 mm vertical overlap to the previous pour. As the two halves were bolted together they clamped on to the concrete below.

4. Concrete was placed and compacted. As there was a considerable weight of wet concrete to be supported by the stiffened plywood disk, this was done in two stages. Initially only about 100 mm of concrete was placed. This was allowed about three days to gain sufficient strength to support the remaining concrete to be placed.

5. A final solid section was cast on top of the columns. This contained a number of bolts which were used to attach the top loading plate assembly and some plates cast in to the sides to which lifting brackets could be attached.

6. In Units 1 and 2 it was necessary to form a 100 mm wide step at the top of the columns to locate anchorage assemblies for the sixteen prestressing tendons. These consisted of bearing plates with short lengths of steel tube attached to the underside. Several turns of spiral wire were also provided around the anchorage zone to control bursting effects. Small tubes were attached to provide injection points for tendon grouting.

6.4.7 Prestressing

Units 1 and 2 were post-tensioned with sixteen 7 mm solid prestressing tendons. The prestressing system is shown in Fig. 6.8. A modified form of the BBR system was used with a forged button head at one end of the tendon and a barrel and wedge arrangement at the other end. This enabled the tendon to be inserted in the preformed duct after the column was completed. The barrel and wedge anchorages were used at the "dead-end" with the barrels located to bear against 20 mm thick plates which sat against the 10 mm plate on the underside of the base block. The 20 mm plates were drilled through the side to allow grout to be pumped to waste at that end.

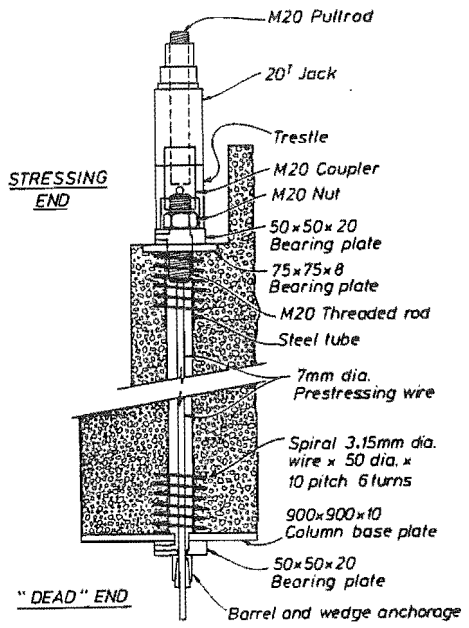

Fig. 6.8 Prestressing Tendon System

At the stressing end the tendons had forged button heads. The button could bear against the end of a length of M20 threaded rod through which a neat hole had been drilled to allow the tendon itself to pass. Tubes were provided on each stressing anchorage for grout injection and also for leads to pass to strain gauges, which were attached to some of the tendons.

The stressing jack was arranged with a coupling nut to attach on to the end of the threaded rod and a saddle to push against the bearing plate. The jack extended the tendon and threaded rod by the required amount and the nut on the threaded rod was then wound down finger tight against the bearing plate. The jack force could then be released and the tendon force was transferred to the nut. The tendons were stressed one at a time.

A load cell was also attached to the jack to monitor the applied jack force. A few tendons were also fitted with strain gauges. This enabled a check to be made on the amount of force lost in the tendon due to the stressing sequence, transfer of the force to the nut, and relaxation effects. It was found that 1.9 percent of the tendon force was lost during the transfer operation of removing the jack. A further 2 percent relaxation loss was measured in the strain gauged tendons over the next few days. Stressing was carried out by sequentially stressing tendons diametrically opposite each other around the circumference to minimise any bending effects, although they were expected to be small. Elastic shortening of the concrete reduced the force in the first tendons stressed by less than 1 percent by the time the final tendon had been installed.

All tendons were stressed to 50.4 kN (0.73 times the ultimate tensile stress UTS). After transfer and relaxation it was estimated that the force remaining in each tendon was 48.5 kN (0.71 UTS), giving a total axial prestress force in each unit of 775 kN.

The tendons were grouted within a few days of stressing. Mix proportions for the cement grout were as follows:

10 kg	Ordinary Portland Cement
4 kg	water
0.1 kg	Interplast (non-shrink agent)

The stressing and grouting operations were carried out with the test units lying on the ground. The units were inclined slightly so that the upward flow of grout would expel air from the ducts. Before grouting each duct was filled with water to wet the inside surface and also to check for leaks. It was necessary to seal the anchorages at both ends with dental plaster. Grout was run to waste until an even flow was obtained with no remaining air bubbles and the plastic waste tube was then wired closed. The ducts were pressurized to at least 350 kPa before sealing off the inlet tube. Three 100 mm x 50 mm diameter test cylinders of grout were cast. By the time of testing this had reached a compressive strength of approximately 40 MPa. The units were left for approximately one week before being returned to the upright position for testing.

6.4.8 Test Rig

The loading equipment used for testing the column members had previously been used by others [6.4, 6.13]. Fig. 6.9 shows a typical test unit in the loading rig and the loading actions. A DARTEC 10 MN capacity universal testing machine was used to apply the required constant axial compression force to the test unit. An inclined steel cantilever arm was bolted to the solid base of the unit and a horizontal jack between the end of the arm and the top of the column unit was used to introduce moment and shear to the test unit. This resulted in a triangular distribution of bending moments over the height with the critical maximum moment section being just above the solid base. Roller bearings were provided at the top and bottom of the column to allow the ends to rotate with a minimum of restraint. An instrument frame and counterbalance arm were bolted to the other side of the base.

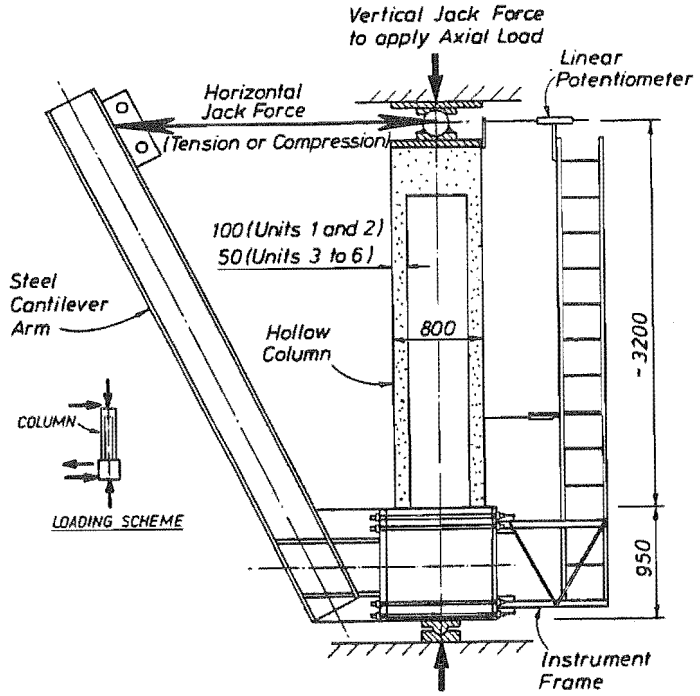

Fig. 6.9 Testing Arrangement for Column Units

6.4.9 Instrumentation

Instrumentation used to monitor performance of the test units consisted of load cells, linear potentiometers, and strain gauges. All instruments except the load cells were connected to an electronic data logger and instantaneous readings were made frequently during the cyclic loading programme. Output from the data logger was transferred to a computer for processing and analysis.

Load-Displacement Behaviour:

Axial load was maintained constant during the test by the servo-hydraulic DARTEC test machine. Lateral load applied by the horizontal hydraulic jack was monitored by the output from a calibrated load cell with two independent Wheatstone bridge circuits. One was used to drive the vertical axis on an X-Y plotter and the other was connected to a strain indicator calibrated to read load. These load values were recorded manually at each increment.

Lateral displacement at the top of the units was measured using a large travel linear potentiometer mounted on the instrument frame which was bolted to the solid base block. The top of the column was located in the cross-head of the DARTEC test machine and was free to rotate in a roller bearing. Application of lateral load from the horizontal jack caused the base block to rotate and resulted in a relative displacement between the top of the instrument frame and the top of the column. Output from the linear potentiometer was used to drive the horizontal axis of the X-Y plotter and a channel on the data logger. The continuous output of load versus displacement hysteresis behaviour was displayed during the test. Applied displacements at the top of the column were accurately monitored during the test using a digital voltmeter.

Longitudinal Strains and Curvatures:

Linear potentiometers were mounted on the sides of the the columns to measure the extreme fibre bending strains, as indicated in Fig. 6.10. Six potentiometers were used on each side of Units 1 and 2 to measure average longitudinal strains over successive gauge lengths of 80, 120, 200, 300, 400 and 500 mm. Shorter gauge lengths were used close to the base block as the strains were expected to be changing more rapidly in that region.

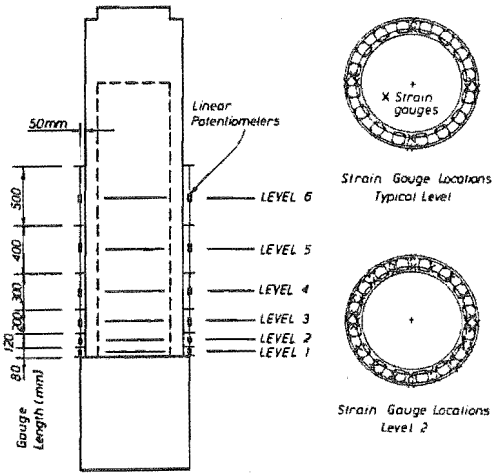

Fig. 6.10 Typical Linear Potentiometer and Strain Gauge Instrumentation Details

In Units 3 to 6 the upper 500 mm gauge length was not used as results from Units 1 and 2 had shown that elastic behaviour could be expected in that region. Instead, an additional gauge point was placed approximately 20 mm away from the face of the base block. This enabled a clearer definition to be made of the strain distributions very close to the face, and contributions from inside the base block.

The twelve linear potentiometers measuring longitudinal strain were monitored by the electronic data logger. Average curvatures over each of the gauge lengths were calculated after the test by a data analysis computer program.

Transverse Reinforcement Strains:

Electrical resistance strain gauges were attached to the transverse reinforcement to measure strains induced during testing. The locations of the gauges used in Units 1 and 2 can be seen in the section views of Fig. 6.10. For Units 3 to 6 a similar arrangement was used except that the gauges were attached to the radial legs of the folded rectangular spirals. Units 4 to 6 had fewer gauges as they did not contain an inner circular spiral. All strain gauges were monitored by the electronic data logger.

As the bar sizes were very small 2 mm long strain gauges were used. It is desirable to use strain gauges in pairs with one gauge attached to each side of a reinforcing bar. In this way any bending effects in the bar can be accounted for. With only a single gauge it is impossible to distinguish between axial and bending strains. However, because of the congested nature of the reinforcing layouts and the small sized bars used in these test units only single strain gauges were used at each location.

6.5 TEST PROCEDURE

Just prior to testing concrete control cylinders were tested to determine the concrete cylinder compressive strength. The external axial load to be applied during the test was determined based on the required axial load level and the measured concrete strength. The ideal flexural strength of the column at the critical section was calculated using the ACI (also NZS 3101) flexural strength method based on the measured material strengths.

For the first loading cycle a lateral load of 75 percent of the calculated ideal lateral load capacity was applied in each direction. This corresponded approximately to the load to cause first yield of the longitudinal tension reinforcement. From the experimentally measured lateral displacement at the top of the column the yield displacement was determined by linear extrapolation to a value corresponding to the ideal lateral load capacity. The tests proceeded by imposing lateral displacements corresponding to increasing displacement

ductility factors (multiples of the yield displacement) in each direction. In Units 1 and 2 two complete cycles of displacement were imposed to displacement ductility factors of $\mu = \pm 2, \pm 4, \pm 6, \pm 8$, and further until either the useful load carrying capacity was exhausted or the displacement limits of the test rig were reached. In Units 3 to 6 two complete cycles were imposed to displacement ductility factors of $\mu = \pm 2, \pm 3, \pm 4, \pm 5, \pm 6$. In some of these test units failure occurred before all of these cycles were completed.

Testing was carried out over a period of days for each unit. During each cycle the lateral load was frequently held while instrument readings were taken. At the peak of each displacement cycle the lateral load was recorded, instruments were scanned by the electronic data logger, a visual examination was made, cracks were marked with felt-tipped pens and photographs were taken. During the early cycles, when cover concrete was still intact, maximum crack widths were measured at the peak of the loading cycle and after removal of the lateral load. During testing of Units 1 and 2 the imposed lateral displacements were sometimes greater than than the available jack stroke. Unloading and reblocking of the jack was then required which resulted in some additional hysteresis in the load-deformation response. The reblocking hysteresis has been omitted from the load-deformation hysteresis curves presented in the following section for the sake of clarity.

6.6 EXPERIMENTAL RESULTS

In this section the experimental results obtained from the six hollow circular concrete column members are presented. A general description of the behaviour of each unit is given, followed by a more detailed analysis of the instrument measurements. A summary of the details of test units was given in Fig. 6.1. Reference is sometimes made in the text to north, south, east and west faces of the columns. The test units were positioned in the test rig with the inclined loading arm on the east side and so the lateral loading was applied in the east-west direction. Reference to positive loading cycles means that the west side of the column was in compression.

6.6.1 General Observations

A general description of the typical behaviour of all units is presented followed by particular observations for each test unit.

All Units

On the initial loading cycle the lateral load was increased incrementally to a maximum of about 75 percent of the calculated ideal lateral load capacity in each direction. The measured stiffness of the members was generally within about 10 percent of the expected values.

First flexural cracking was always observed on the initial loading cycle in each direction at lateral loads very close to the expected values. As the lateral load was increased on subsequent cycles, a well defined crack pattern developed and spread rapidly up the height of the columns. In later cycles, as maximum lateral loads were attained, cracking normally extended well into the upper solid portions, up to about 70 percent of the height between the critical section and the point of application of the lateral load. Cracks initiated on the tension side of the member, due to the effects of shear, extended around the walls to become inclined flexure-shear cracks. Each crack initiated on the tension side of the column coincided with the position of a transverse circular spiral bar running around the outside of the section. Above the potential plastic hinge region where the transverse bar spacing was increased, the crack spacing also increased. The diameter of the spiral bars was quite large compared with the thicknesses of cover to the transverse reinforcement. It appears that this created a distinct weakness in the cover concrete, although this did not seem to detrimentally affected the behaviour.

The next significant observation was generally the first occurrence of damage to cover concrete in compression. This was evident by the appearance of small vertical splitting cracks and signs of concrete crushing, normally about 100 mm above the top of the base block (the theoretical critical section). On average this occurred at displacement ductility factors of about $\mu = \pm 3$. However, in the units which sustained very large ductilities crushing did not occur until $\mu = \pm 4$, and in units which displayed only limited ductility crushing tended to occur at lower ductilities of about $\mu = \pm 2$. In general crushing of the cover concrete occurred at compression strains of about 0.004, which is lower than has been found in tests of solid members. This is probably due to the larger strain gradient present in the cover of solid members. In these hollow members the variation of longitudinal compression strains through the thickness is quite small.

Spalling of damaged cover concrete occurred soon after first crushing was observed. For the units which sustained large ductilities the spalling of cover spread progressively until a considerable amount of cover had been lost. For units which displayed only limited ductility spalling of the cover concrete did not spread far from where it initiated.

Final failure is described for each particular unit in the following paragraphs.

Unit 1:

This test unit was a partially prestressed concrete member with fairly stocky walls (diameter to wall thickness ratio D/t = 8.0) and a low level of externally applied axial load ($P_e/f_c'A_g$ = 0.125). Design of this member was carried out assuming a concrete compressive cylinder strength of 40 MPa. Transverse reinforcement was proportioned using the New Zealand Concrete Design Code NZS 3101 equations for shear and confinement based on this assumed strength. However, the actual cylinder strength, measured just prior to testing, was only 28 MPa. The quantity of transverse confining reinforcement provided in the circumferential direction was thus considerably in excess of that required. In the radial (through-wall) direction the quantity provided was quite close to the requirements of NZS 3101, allowing for a reduced efficiency of the layout of transverse steel due to the relatively large bar spacings.

The first signs of cover concrete crushing and spalling occurred on the first loading cycle to $\mu = \pm 4$. After three complete cycles to $\mu = \pm 8$ cover had spalled over an area of approximately 600 mm around the circumference by 400 mm high on each side.

Longitudinal bars began to buckle outwards at a displacement ductility factor of $\mu = 6$. These buckles straightened almost completely on the following cycle when the lateral load was reversed and the bar was strained in tension. On subsequent cycles the buckles reformed during compressive strainings and straightened during tensile strainings. The buckling was more pronounced as cycles to $\mu = \pm 8$ were imposed and several longitudinal bars snapped during tension straining due to the effects of low cycle fatigue. After the third cycle to $\mu = \pm 8$ five bars had failed but no obvious drop in the lateral load resistance of the member was apparent.

Damage to the concrete core of the tube wall was clearly accelerated by the occurrence of longitudinal bar buckling at large imposed displacement ductility factors. Concrete from the core was progressively lost as cycling of the lateral load continued. When the test was stopped one of the prestressing tendons, which was centrally located in the 100 mm thick wall, was visible.

The test was stopped after three complete cycles of loading to $\mu = \pm 8$ had been completed. Because of limitations with the test-rig it was not possible to impose larger displacements.

The sequence of photographs in Fig. 6.11 shows the progression of damage which was sustained by the plastic hinge region of Unit 1 during the test.

Unit 2:

This test unit was a partially prestressed concrete member with fairly stocky walls (diameter to wall thickness ratio D/t = 8.0) and a moderate level of externally applied axial load ($P_e/f_c'A_g = 0.3$). As for Unit 1 transverse confining reinforcement was designed approximately to the provisions of NZS 3101 assuming a concrete compressive cylinder strength of 40 MPa, whereas the actual strength at the time of testing was only 28 MPa. The quantity of transverse confining reinforcement provided in the circumferential direction was considerably in excess of that required but the quantity provided in the radial direction was close to the required amount.

For displacement cycles up to $\mu = \pm 2$ cracks closed completely upon removal of the lateral load. For cycles at $\mu = \pm 4$ a small residual crack width was observed and measured after load removal, and for larger displacement cycles increased crack widths were observed at the peak of the cycle and after load removal.

The first sign of spalling of the cover concrete occurred at approximate displacement ductility factors of $\mu = \pm 3$. The corresponding extreme fibre compression strain was estimated to be 0.0035. Cover concrete was progressively lost as displacement cycling was continued. After the last loading cycle, to $\mu = +12$ and $\mu = -10$ was completed, an area of cover concrete approximately 700 mm by 500 mm had spalled off each side of the plastic hinge region.

During the first loading cycle to $\mu = -4$ there was a sudden, but not severe, loss of stiffness as the base block developed some horizontal cracks. After this, some of the displacement imposed on the unit during negative displacement cycles appeared to be contributed by deformation of the base block. This would have slightly reduced the deformations imposed on the plastic hinge region of the member during subsequent negative displacement cycles.

Although extensive spalling of the cover concrete occurred, there was no evidence of longitudinal bar buckling, even when a displacement ductility of $\mu = +12$ was imposed. The transverse reinforcement was spaced at only four longitudinal bar diameters in this case and provided excellent restraint to those bars. The quantity of transverse reinforcement was also sufficient to confine the concrete core, even at the large longitudinal strains imposed.

The test was concluded after displacement ductilities of $\mu = +12$ and $\mu = -10$ had been imposed, as the test rig could not accommodate larger displacements.

The sequence of photographs in Fig. 6.12 shows the progression of damage which was sustained by the plastic hinge region of Unit 2 during the test.

Unit 3:

This test unit was a reinforced concrete member with only 50 mm thick walls (diameter to wall thickness ratio D/t = 16.0) and a moderate level of externally applied axial load ($P_e/f_c'A_g = 0.3$). As for Units 1 and 2, two circular spirals were provided in this unit, with one engaging the inner layer of longitudinal bars and the other engaging the outer layer.

The quantity of transverse confining reinforcement was designed to be somewhat less than had been used in Units 1 and 2. With reference to Table 6.1 the quantity of transverse confining reinforcement provided in the circumferential direction was still in excess of that required by the NZS 3101 code by about 50 percent, but the quantity provided in the radial direction was only about 60 percent of that required by NZS 3101.

Cover concrete began to crush and spall at displacement ductility factors of $\mu = \pm 2$, rather earlier than in previous tests.

At displacement ductility factors of $\mu = +2.5$ and $\mu = -3.5$ this column suffered a sudden loss of lateral load resistance. This was accompanied by severe concentrations of damage in the compression zones on each side of the member. A band of highly strained concrete was evident

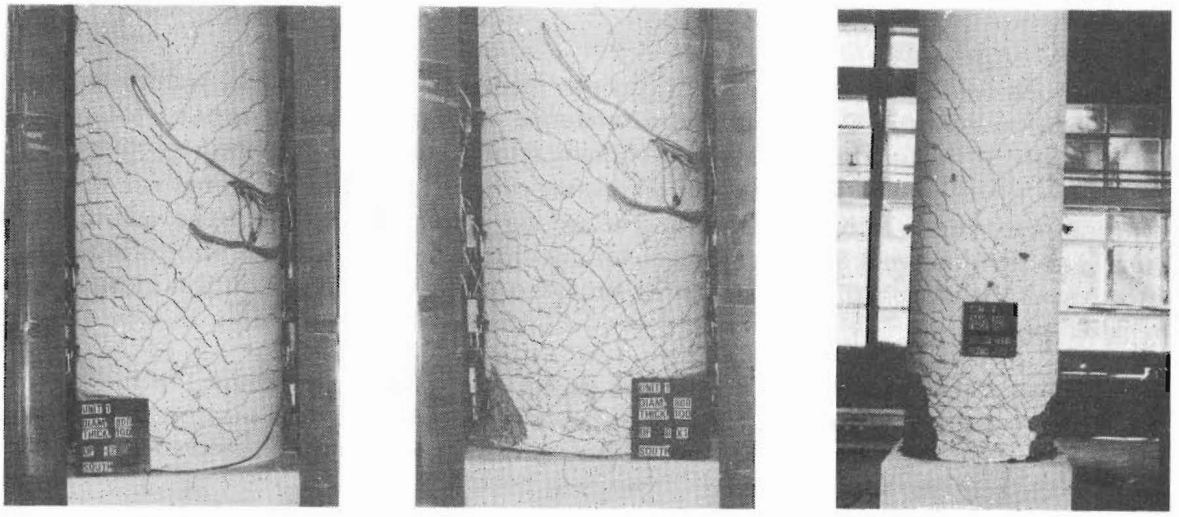

a) $\mu = 2$ b) $\mu = 6$ c) $\mu = 8$ (end of test)

Fig. 6.11 Sequence of Damage Sustained by Unit 1

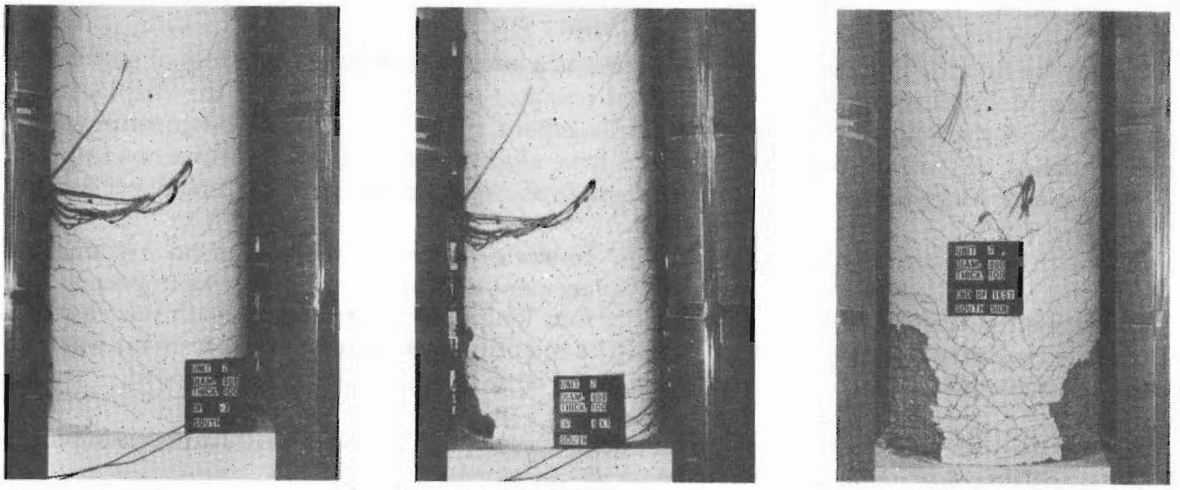

a) $\mu = 2$ b) $\mu = 6$ c) $\mu = 12$ (end of test)

Fig. 6.12 Sequence of Damage Sustained by Unit 2

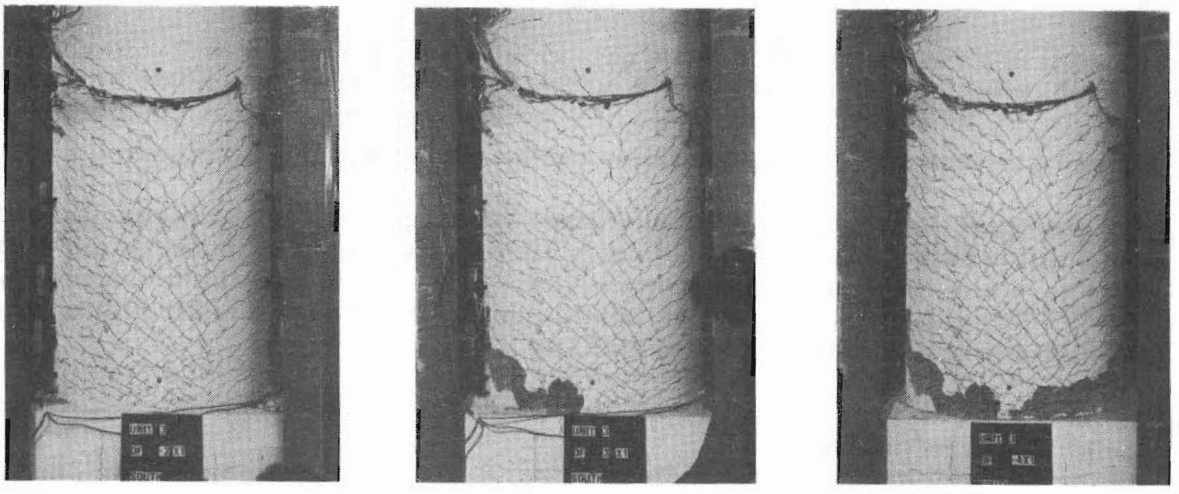

a) $\mu = 2$ b) $\mu = 3$ c) $\mu = 4$ (end of test)

Fig. 6.13 Sequence of Damage Sustained by Unit 3

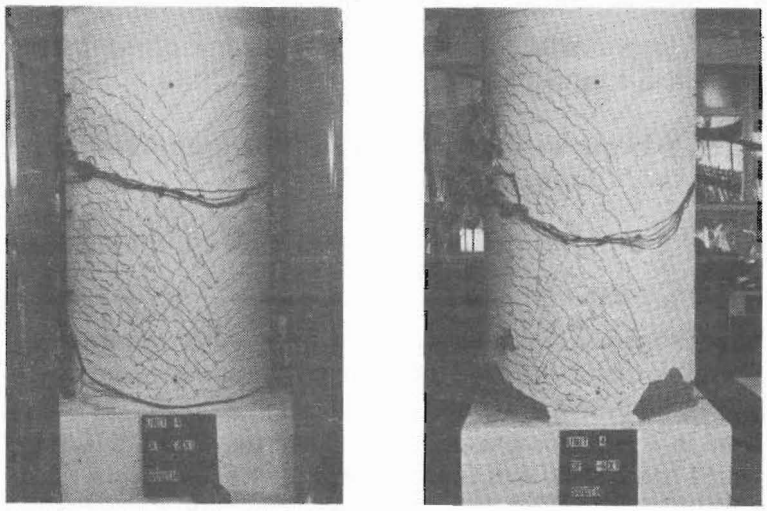

a) $\mu = 2$ b) $\mu = 4$ (end of test)

Fig. 6.14 Sequence of Damage Sustained by Unit 4

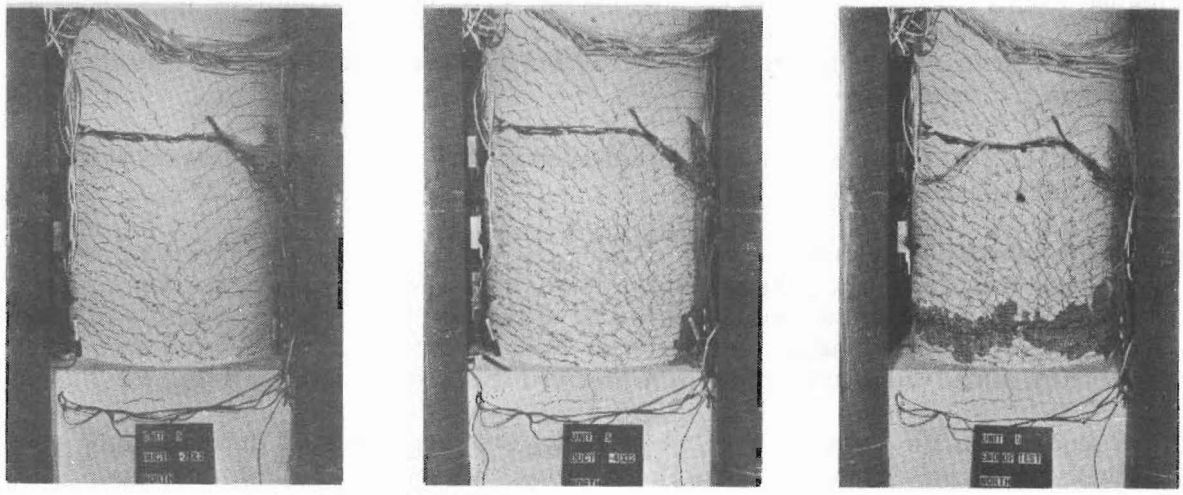

a) $\mu = 2$ b) $\mu = 4$ c) $\mu = 5$ (end of test)

Fig. 6.15 Sequence of Damage Sustained by Unit 5

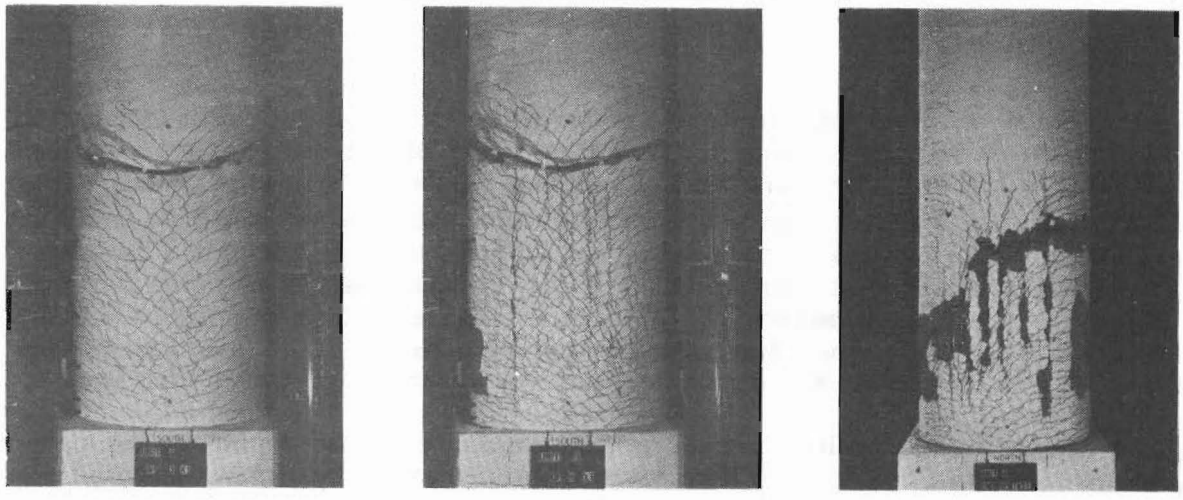

a) $\mu = 2$ b) $\mu = 6$ c) $\mu = 7$ (end of test)

Fig. 6.16 Sequence of Damage Sustained by Unit 6

around the circumference. Buckling of longitudinal bars and fractures of some of the folded rectangular spirals were observed within this band of damage.

The sequence of photographs in Fig. 6.13 shows the progression of damage which was sustained by the plastic hinge region of Unit 3 during the test.

Unit 4:

This test unit was a reinforced concrete member with only 50 mm thick walls (diameter to wall thickness ratio D/t = 16.0) and a moderate level of externally applied axial load ($P_e/f_c'A_g$ = 0.3). Although similar to Unit 3, this unit had no inner circular spiral. Instead, the outer circular spiral was increased in area to compensate. (Unit 3 had two 3.15 mm Grade 310 spirals at 30 mm centres, and Unit 4 had one 4.0 mm Grade 255 spiral at 30 mm centres). It was of interest to determine whether the inner circular spiral was necessary as it caused construction difficulties and it would be desirable to omit it if possible.

The quantities of transverse reinforcement were similar to Unit 3 but the concrete strength was only 29 MPa (compared with 35 MPa in Unit 3) so the level of confinement was slightly higher. With reference to Table 6.1 the quantity of transverse confining reinforcement provided in the circumferential direction was still in excess of that required by the NZS 3101 code by about 50 percent, but the quantity provided in the radial direction was only about 70 percent of that required by NZS 3101.

As in Unit 3, cover concrete began to crush and spall at displacement ductility factors of $\mu = \pm 2$, rather earlier than in previous tests.

At displacement ductility factors of $\mu = +3.5$ and $\mu = -3.0$ this column also suffered a sudden loss of lateral load resistance. As in Unit 3, this was accompanied by severe concentrations of damage in the compression zones on each side of the member. A band of highly strained concrete was evident around the circumference. Buckling of longitudinal bars and fractures of some of the folded rectangular spirals were observed within this band of damage.

The sequence of photographs in Fig. 6.14 shows the progression of damage which was sustained by the plastic hinge region of Unit 4 during the test.

Although the performance of Units 3 and 4 was rather poor, there was no evidence that either of the arrangements of transverse reinforcement resulted in superior confinement or shear resistance. It was inferred from this that adequate confinement and shear reinforcement could be provided using only an outer circular spiral.

Unit 5:

This test unit was a reinforced concrete member with only 50 mm thick walls (diameter to wall thickness ratio D/t = 16.0) and a moderate level of externally applied axial load ($P_e/f_c'A_g$ = 0.3). A similar arrangement of transverse reinforcement was used in this unit as had been used in Unit 4, with only a single circular spiral, except that the quantity of confining reinforcement was increased by reducing the spacing to 25 mm. The folded rectangular spirals were also elongated more so they would enclose a larger proportion of the core of the tube wall. It was expected that the more effective confinement provided in Unit 5 would enhance the confined strength of the wall after spalling of the cover concrete and encourage the compression zone damage to spread over a greater length than in Units 3 and 4.

The increase in the quantity of transverse reinforcement was offset slightly by the higher concrete strength (37 MPa). With reference to Table 6.1 the quantity of transverse confining reinforcement provided in the circumferential direction was in excess of that required by the NZS 3101 code by about 80 percent, and the quantity provided in the radial direction was about 80 percent of that required by NZS 3101.

Cover concrete began to crush and spall at displacement ductility factors of $\mu = \pm 3$, slightly later than in Units 3 and 4.

Ductile behaviour was obtained from this column up to displacement ductility factors of $\mu = \pm 4$. However, as ductilities of $\mu = 5$ were approached in each direction a similar severe loss of lateral load resistance and concentration of damage occurred, as had been observed in Units 3 and 4. Although spalling of the cover concrete spread slightly more than in Units 3 and 4, final failure was the same.

The sequence of photographs in Fig. 6.15 shows the progression of damage which was sustained by the plastic hinge region of Unit 5 during the test.

Unit 6:

This test unit was a reinforced concrete member with 50 mm thick walls (diameter to wall thickness ratio D/t = 16.0) and a moderate level of externally applied axial load ($P_e/f_c'A_g = 0.3$). The arrangement of transverse reinforcement was changed slightly in this unit from the arrangement used in Units 4 and 5. It was estimated that in those units the transverse confining stress effective in the circumferential direction was substantially higher than the confining stress in the radial direction (refer Table 6.1). In order to provide a high level of confinement in both transverse directions the arrangement shown in Fig. 6.6 was used. The folded rectangular spirals were interlinked by U-shaped bars fitted from the inside and having their ends bent around the outside longitudinal bars into the core of the tube wall. This provided about twice the quantity of confining reinforcement in the radial direction as had been used in Unit 5. The U-shaped bars were only used in the portions of the tube walls which were expected to be within the compression zones of the section for loading in either direction. They were thus used over a length of about one quarter of the circumference on each side of the section. Over the remainder of the circumference the folded rectangular spirals were used around each group of longitudinal bars, but these were not interlinked.

With reference to Table 6.1 the quantity of transverse confining reinforcement provided in the circumferential direction was in excess of that required by the NZS 3101 code by about 54 percent, and the quantity provided in the radial direction was about 35 percent more than required by NZS 3101. It was expected that compression zone damage would be encouraged to spread and ductile behaviour would be obtained up to large displacement ductility factors.

Shear reinforcement was deliberately kept to a minimum in this test unit to closely check the method used for shear design. Only a single 3.5 mm circular spiral was used around the outside of the section.

Cover concrete began to crush and spall at displacement ductility factors of $\mu = \pm 3$.

Ductile behaviour was obtained from this column up to displacement ductility factors of $\mu = \pm 6$. As the second cycle to $\mu = +6$ was being imposed a compression zone failure started to occur outside the expected plastic hinge region and the lateral load was removed. Confining reinforcement was provided over a length of one member diameter (800 mm) from the critical section. Outside this area the only transverse reinforcement present was the outer circular spiral which would have provided only a small amount of confinement to the concrete in the wall. There was no restraint provided to the inner layer of longitudinal bars outside the confined region.

Substantial diagonal shear cracking occurred in the webs of this member. In those areas the groups of four longitudinal bars surrounded by folded rectangular spirals were not interlinked by additional U-shaped bars. The areas between these small "columns" of reinforcement had only horizontal spirals traversing them. Vertical cracking appeared in those lightly reinforced areas at displacement ductility factors of about $\mu = \pm 4$ and as loading continued substantial lateral offsets were observed across these cracks during lateral load reversals.

Lateral loading was resumed in the negative loading direction and a displacement ductility of $\mu = -7$ was achieved. As larger deformations were imposed the unit suffered a drastic loss of lateral strength and showed severe concentrations of compression zone damage within the confined region. Although spalling of the cover concrete had spread considerably more than in Units 3, 4 and 5, final failure was very similar.

The sequence of photographs in Fig. 6.16 shows the progression of damage which was sustained by the plastic hinge region of Unit 6 during the test.

6.6.2 Lateral Load Versus Displacement Hysteresis

Lateral load versus deformation behaviour is perhaps the most important information obtained from experimental tests studying the strength and ductility behaviour of structural members. The hysteresis loops obtained show the strength which is mobilized by a member, as well as the amount of ductility sustained. The overall shape of the hysteresis loops gives an indication of the ability of the member to dissipate energy, which may be an important factor in limiting the response of structures during earthquake shaking.

An X-Y plotter was used to continuously monitor the lateral load versus lateral displacement hysteresis behaviour of the test units and the behaviour obtained is shown in Figs. 6.17 to 6.22. In each of these the ideal lateral load capacity V_i based on ACI (or NZS 3101) flexural strength theory is also shown on the vertical axis and displacement ductility factors (μ) are indicated parallel to the horizontal displacement axis. It should be noted that the ideal lateral load capacity reduces with displacement due to the so-called P-delta effect. As the column base rotates, the critical section just above the base block, is displaced horizontally from the line of action of the applied axial load. Thus an additional moment is applied to all sections equal to the externally applied axial load multiplied by the horizontal displacement of the centroid of the section from the axial load axis.

Excellent lateral load versus displacement behaviour was shown by Units 1 and 2 (refer Figs. 6.17 and 6.18). Lateral load carrying capacity was maintained at well above the ideal capacity based on flexural strength theory to displacement ductility factors in excess of $\mu = \pm 8$ with minimal loss of strength. Although near the end of the tests some degradation of strength is apparent in successive load cycles, the lateral loads continued to rise relative to the sloping line representing the ideal capacity. As only minor strength degradation had occurred in these units it was evident that even larger deformations could have been sustained by both units before the end of useful load carrying capacity.

Figs. 6.19 and 6.20 show the lateral load versus lateral displacement hysteresis behaviour obtained from Units 3 and 4. The behaviour of these two units was rather poor with only limited ductility being available. At displacement ductilities of between $\mu = 2.5$ and 3.5 both units suffered sudden losses of lateral load carrying capacity. Prior to those sudden failures the load carrying capacity was very good with approximately 30 percent above the ideal lateral load capacity being available in each unit.

Figs. 6.21 and 6.22 show the lateral load versus lateral displacement hysteresis behaviour obtained from Units 5 and 6. The behaviour of these two test units was quite good with displacement ductility factors of about 5 and 6 being reliably attained in Units 5 and 6 respectively. The load carrying capacity in these members was as for Units 3 and 4, with about 1.2 times the ideal lateral load capacity being maintained until the characteristic sudden failure occurred.

Obvious features of the lateral load versus displacement hysteresis loops obtained from the members which sustained substantial ductilities (Units 1, 2, 5 and 6), are the loss of stiffness on reloading as the imposed displacements increased, and the slight pinching of the loops.

The loss of stiffness on reloading is a common feature of the hysteretic behaviour of reinforced and prestressed concrete members and is due mainly to the cyclic stress-strain behaviour of

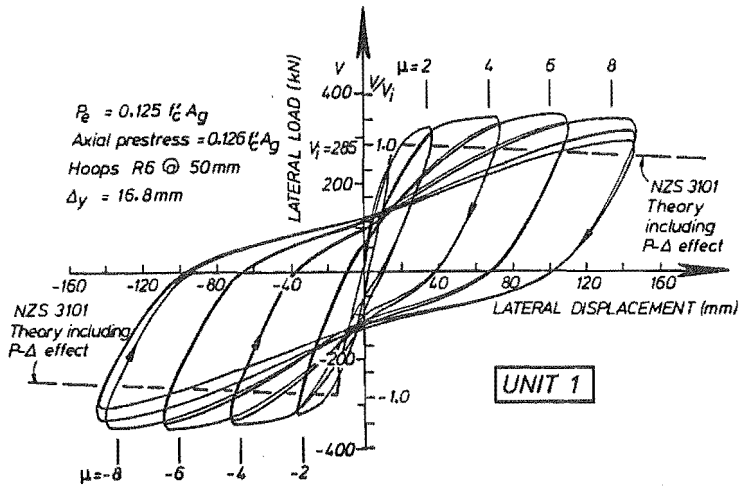

Fig. 6.17 Experimental Lateral Load versus Lateral Displacement Behaviour - Unit 1

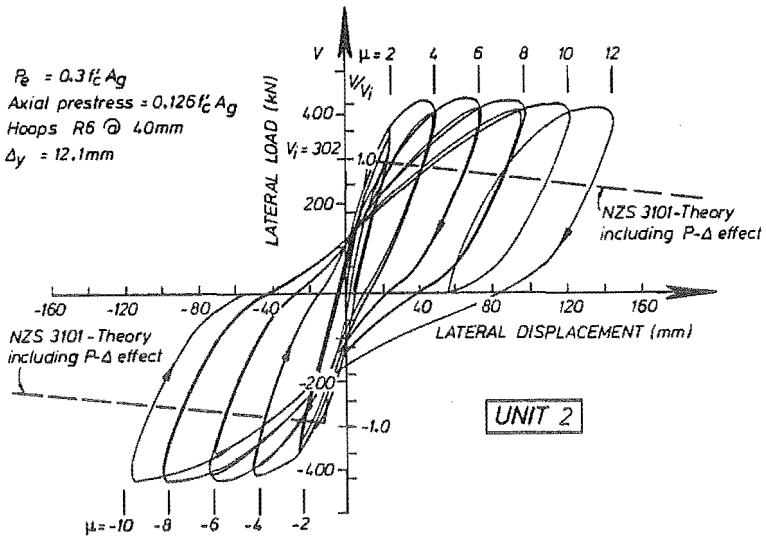

Fig. 6.18 Experimental Lateral Load versus Lateral Displacement Behaviour - Unit 2

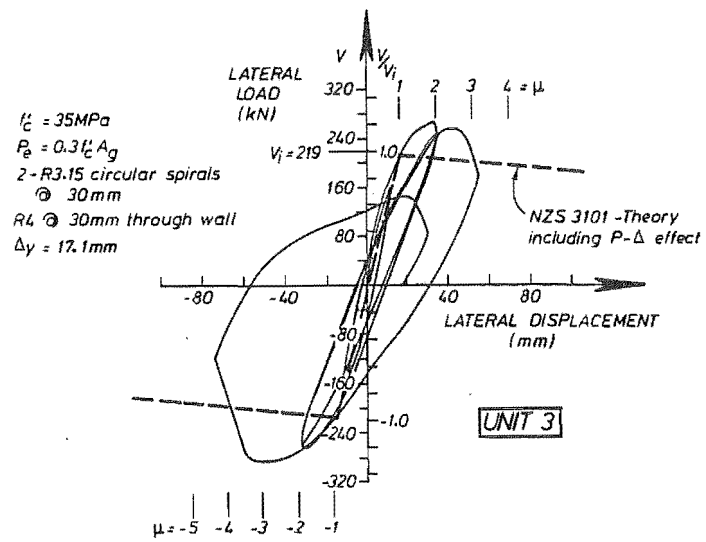

Fig. 6.19 Experimental Lateral Load versus Lateral Displacement Behaviour - Unit 3

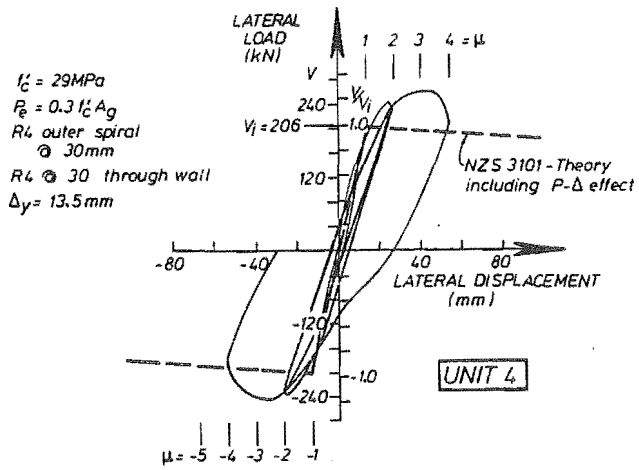

Fig. 6.20 Experimental Lateral Load versus Lateral Displacement Behaviour - Unit 4

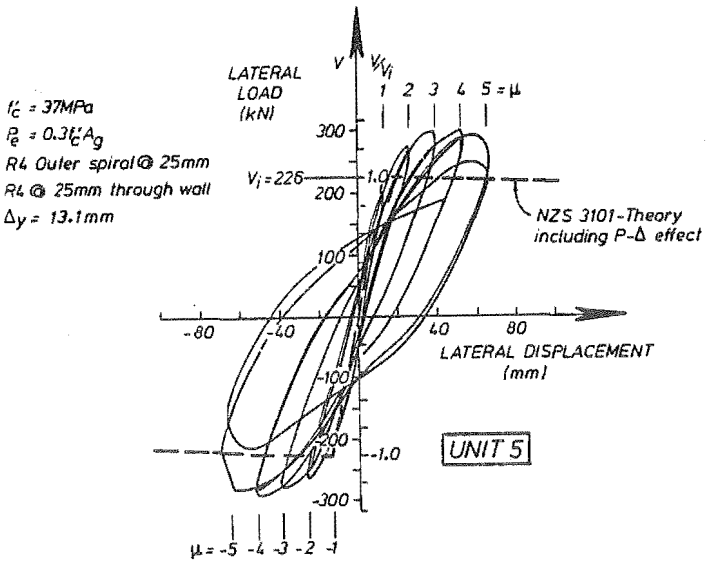

Fig. 6.21 Experimental Lateral Load versus Lateral Displacement Behaviour - Unit 5

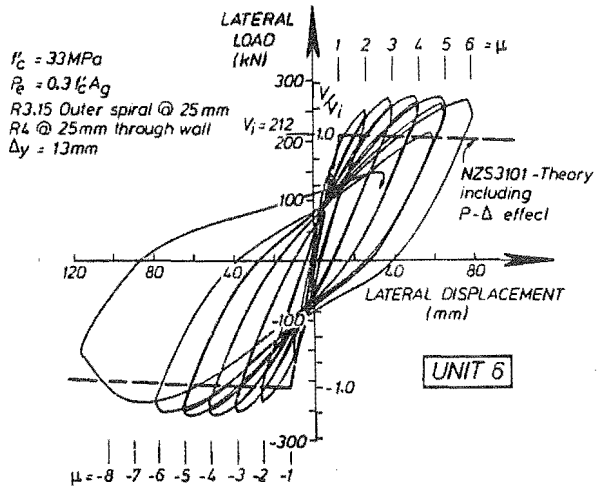

Fig. 6.22 Experimental Lateral Load versus Lateral Displacement Behaviour - Unit 6

compressed concrete. The idealised uniaxial cyclic stress-strain behaviour of compressed concrete is shown in Fig. 6.23. It is evident that in order to mobilize the the stress achieved in previous loading cycles the compression strains must reach the maximum previously attained levels. Also there is a significant softening of the concrete at high strains.

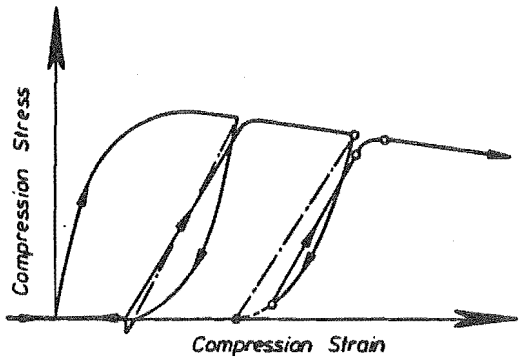

Fig. 6.23 Idealised Uniaxial Stress-Strain Behaviour of Confined Concrete

The pinching effectin the hysteresis loops is also common in concrete members and is often related to the level of externally applied axial load. Where a member undergos deformations into the inelastic range and is then unloaded, elastic unloading of both the concrete and longitudinal reinforcement in the section occurs. The unloaded section may be left with wide open cracks remaining. Until the cracks close the flexural stiffness of the section can be quite low. Where the section has been subject to high intensity loading in both directions it may be left with a full depth crack at the critical section and the flexural stiffness may only be contributed by the tangent stiffness of the yielded longitudinal reinforcement. It is often necessary to impose substantial reversed curvatures on a member in order to close these cracks and allow concrete compression stresses to develop. Where substantial axial load is present on the section the neutral axis depth is greater and a significant area of concrete is maintained at all times to carry the axial load. In that case removal of the lateral load will not leave the section with such a severe loss of stiffness and residual cracking. Thus the tendency is for more pinching in members with low axial load levels.

The maximum lateral loads mobilized in the test units V_{max} are given in Table 6.2 as multiples of the ideal lateral load capacity V_i based on ACI or NZS 3101 flexural strength theory. Also shown in the table is the axial load level. For Units 1 and 2, which were partially prestressed, the axial load level corresponds to the sum of the internal prestress force and the externally applied axial load. A justification for this is given in Chapter 7 (refer Section 7.8.7.1).

Table 6.2 Maximum lateral loads sustained by test units

Unit	Axial load level $P/f_c'A_g$	V_{max}/V_i
1	0.25	1.25
2	0.425	1.42
3	0.3	1.32
4	0.3	1.32
5	0.3	1.32
6	0.3	1.32

Recent work by Ang [6.10] collated the measured flexural strength enhancements from approximately thirty experiments on solid reinforced concrete columns tested at the University of Canterbury in recent years. Those results are shown in Fig. 6.24 and it is apparent that an increase in axial load level resulted in an increase in the flexural strength enhancement. It was found that the average behaviour followed the solid curve and that most results fell within the the shaded region representing a variation of ±15 percent from the average. This effect is due to the increase in the concrete strength due to confinement by transverse reinforcement. In members with a higher level of axial load, a greater proportion of the flexural strength is contributed by concrete compression forces so the enhancement is more significant.

The enhanced strength ratios for the test units from this study are also shown in Fig. 6.24. Observed flexural strength enhancements for all of the test units lie within the shaded area encompassing the solid column results and in fact lie quite close to the average curve. It appears that the relationship between flexural strength enhancement and axial load level found for solid columns is also appropriate for hollow circular members.

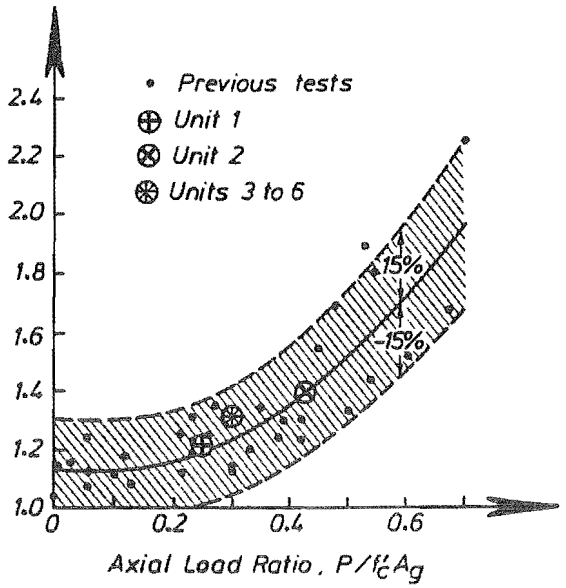

Fig. 6.24 Flexural Strength Enhancement Found from Experimental Tests

6.6.3 Measured Curvature Distributions

Measurements from the six linear potentiometers mounted up each side of the test units were read by the electronic data logger and from the results it was possible to calculate average longitudinal strains and curvatures over the gauge lengths. The derived profiles of curvature up the height of each member are shown in Figs. 6.25 to 6.30. In each case the calculated average curvature values are assumed to be appropriate to the midheight levels of the gauge lengths, as indicated by the horizontal lines. The maximum curvatures measured on loading cycles to each displacement ductility factor were plotted and the points joined to indicate the variation over the length of the plastic hinge region. The distributions for positive and negative loading cycles are shown on either side of the figures.

The results for Units 1 and 2, shown in Figs. 6.25 and 6.26, are fairly typical of the curvature profiles which have been measured in numerous past tests of reinforced and prestressed concrete members. In general, curvatures are large close to the critical section but reduce to the elastic straight line curvature distribution at a distance of about one member diameter from the critical section.

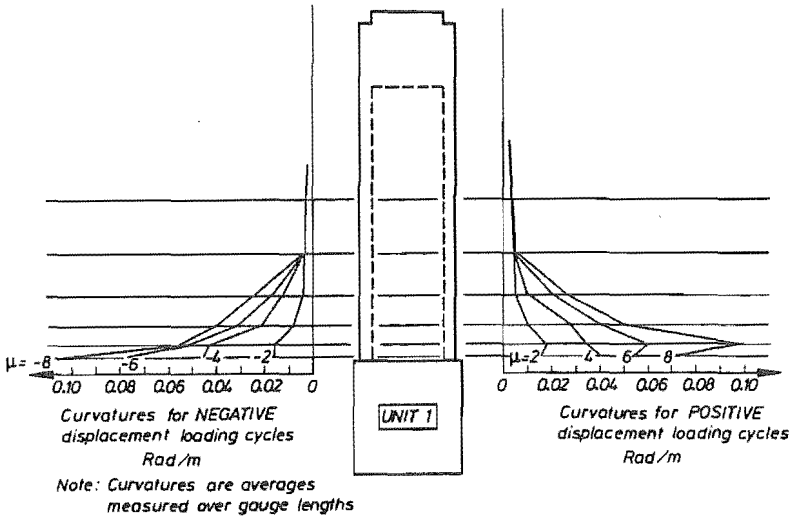

Fig. 6.25 Measured Curvature Profiles in the Plastic Hinge Region - Unit 1

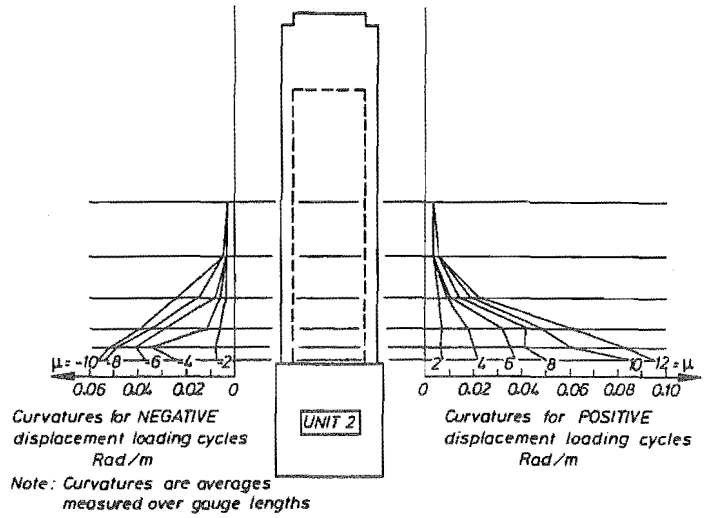

Fig. 6.26 Measured Curvature Profiles in the Plastic Hinge Region - Unit 2

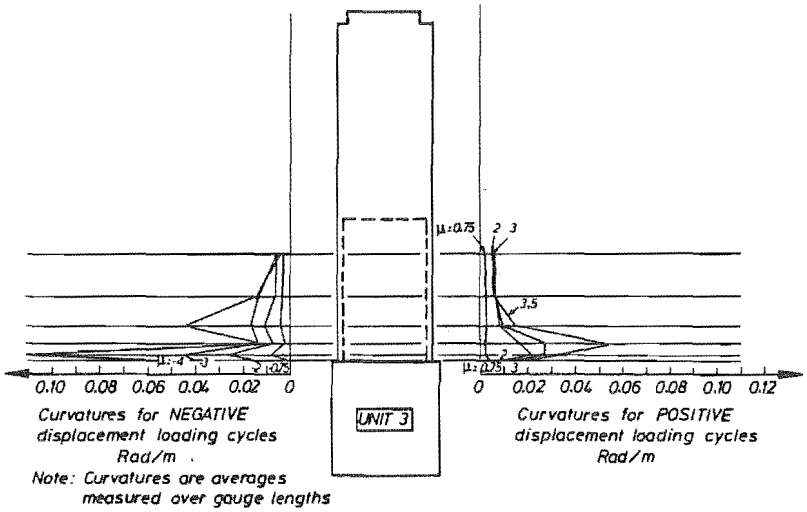

Fig. 6.27 Measured Curvature Profiles in the Plastic Hinge Region - Unit 3

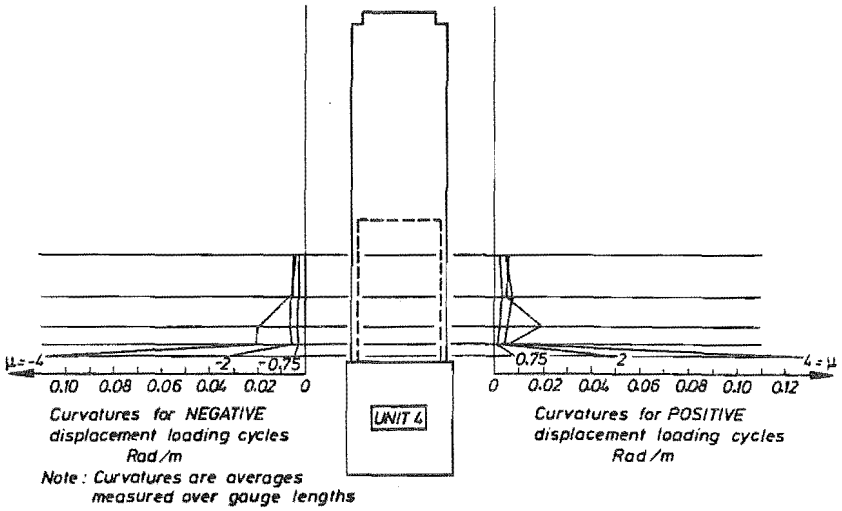

Fig. 6.28 Measured Curvature Profiles in the Plastic Hinge Region - Unit 4

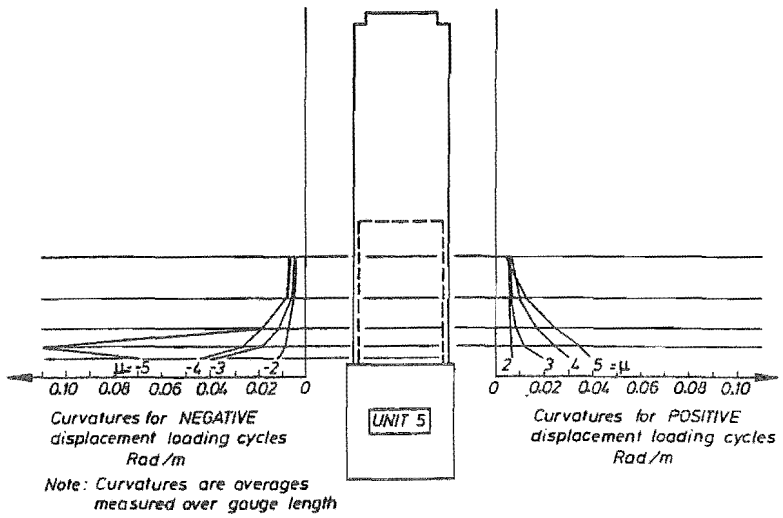

Fig. 6.29 Measured Curvature Profiles in the Plastic Hinge Region - Unit 5

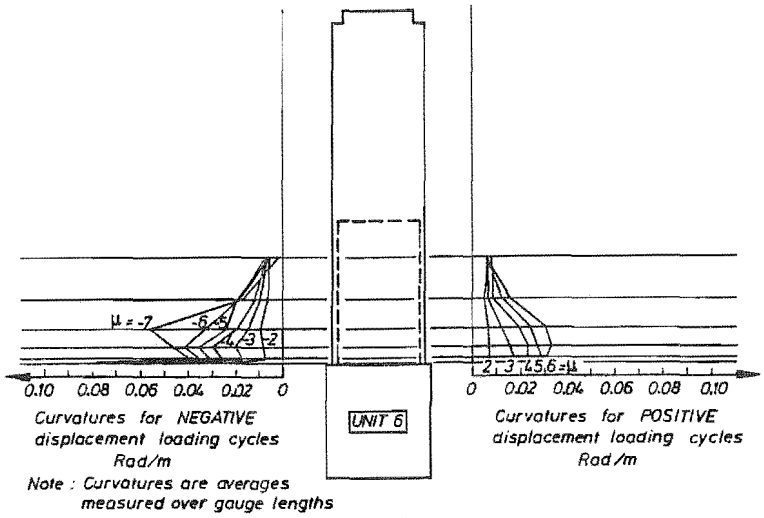

Fig. 6.30 Measured Curvature Profiles in the Plastic Hinge Region - Unit 6

It is thought that there was significant error involved in the measurement of the peak curvature in the gauge length adjacent to the critical section. The hollow members in this study were attached to a solid base block which had a slightly larger dimension than the outside diameter of the circular tube. In the gauge length closest to the critical section longitudinal strains were measured between studs embedded in the tube wall and the face of the base block. It was expected that the block would be effectively rigid and would contribute very little extra deformation to the measurements over that gauge length.

Previous researchers have used similar measurement techniques and noted that the effects of yield penetration into the member joint region contribute part of the strain measured on the tension side of the member in the first gauge length. During reversed cyclic loading the deterioration of bond can result in significant longitudinal bar strains in the joint zone. Priestley and Park [6.1] discussed the likely spread of the curvature distribution into the joint zone due to the effects of yield penetration, and also along the member due to the effects of shear (the so-called T-jd effect).

The nominal gauge length adjacent to the base block was 80 mm in Units 1 and 2. Examination of the distributions of extreme fibre strains and curvatures from the initial elastic cycle of loading indicated that the effective gauge length was about 160 mm, approximately double the nominal value. The distributions of curvature shown in Figs. 6.25 and 6.26 were calculated assuming the adjusted gauge lengths adjacent to the critical section. It is thought that this gives a more realistic estimate of the actual curvatures in those gauge lengths.

In Units 3 to 6 this measurement problem was overcome by casting the first instrument mounting stud in the tube wall as close as practicable to the critical section (about 20 mm). Measurements taken over the first gauge length did not then include contributions from any deformations in the base block. As a check on the effects of block deformation and yield penetration another instrument was used to measure deformations between the face of the block and the second stud cast into the wall, a distance of about 80 mm from the face of the block.

The curvature distributions for Units 3 to 6, shown in Figs. 6.27 to 6.30, are somewhat erratic over the plastic hinge region and this is probably due to several factors. It is possible that the instrument mounting studs cast in the wall could have moved slightly when cracking occurred, thus increasing the apparent strain in one gauge length and decreasing in the adjacent gauge length. Because the member walls were relatively thin, it is possible that variations in the properties of the wall could have resulted in irregular distributions of longitudinal strain over the plastic hinge region. Problems were encountered with placement of the concrete in the critical regions of Units 3 and 4 and it is possible that this could have accentuated the variability of the properties. In solid members there is likely to be a better compatibility of strains through the section even if there are local variations in material properties.

6.6.4 Equivalent Plastic Hinge Lengths

For design purposes a useful way a characterizing the distribution of curvatures is to introduce the concept of an equivalent plastic hinge length. A method for determining the equivalent plastic hinge length l_p for cantilever members is given by Priestley and Park [6.1]. The analysis assumes the idealised behaviour shown in Fig. 6.31 for a column of height L. The total lateral displacement at the top of the column Δ is assumed to consist of an elastic component equal to the yield displacement Δ_y and a plastic component Δ_p. The curvature distribution is idealised as in Fig. 6.31b comprising a triangular distribution of elastic curvatures up to the yield curvature ϕ_y and a rectangular distribution of plastic curvatures with a constant value of $(\phi_{max} - \phi_y)$ over a length of l_p. Using normal moment-area principles the expression in Eqn. 6.17 follows.

$$\Delta = \Delta_y + \Delta_p = \Delta_y + (\phi_{max} - \phi_y)\, l_p\, (L - 0.5 l_p) \qquad (6.17)$$

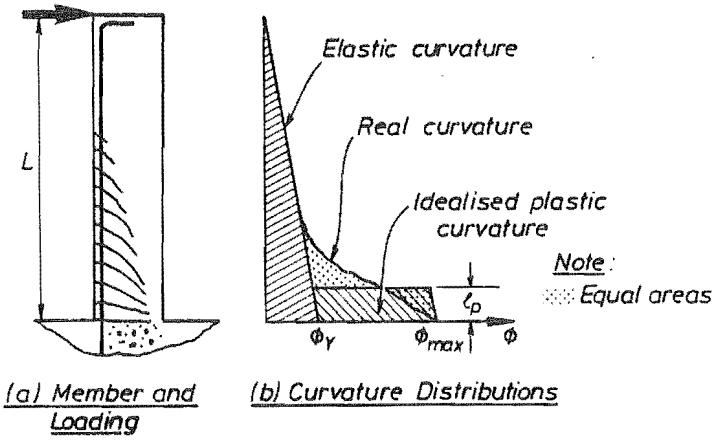

Fig. 6.31 Idealised Analysis for Determining Equivalent Plastic Hinge Length

Noting that the displacement ductility factor μ can be expressed in terms of the top lateral displacement and the yield displacement as in Eqn. 6.18 then the above expression can be solved for the equivalent plastic hinge length, given by Eqn. 6.19.

$$\mu = \Delta / \Delta_y \tag{6.18}$$

$$l_p / L = 1 - \{ 1 - 2(\mu-1)\Delta_y / [L^2 \phi_y ((\phi_{max} / \phi_y) - 1)] \}^{0.5} \tag{6.19}$$

The equivalent plastic hinge lengths calculated for each test unit are also given in Table 6.3. Those values were calculated from the measurements at deformation levels just prior to the occurrence of any concentrations of damage in the members.

The equivalent plastic hinge lengths of about half the member diameter obtained for Units 1 and 2 are consistent with the values for solid reinforced concrete members. The values obtained for the thinner walled Units 3 to 6 are some what erratic and this is due to the rather irregular distributions of curvature obtained for those members.

It should be noted that the equivalent plastic hinge lengths have been calculated based on the maximum curvature measured in the plastic hinge region but not including the effects of yield penetration or deformations in the base blocks. It is possible that some equivalent plastic hinge lengths calculated by others in the past may be conservatively low because of the method of measuring the maximum curvature. This may seem unimportant as the method of determining the equivalent plastic hinge length simply adjusts the idealised plastic curvature distribution magnitude and length to match the observed plastic rotation. However, this may have important effects on the relationships between displacement ductility, curvature ductility and equivalent plastic hinge length.

Table 6.3 Calculation of Equivalent Plastic Hinge Lengths

Unit	Height L (m)	Yield Displ. Δ_y (m)	Yield Curvature ϕ_y (rad/m)	Maximum Ductilities		l_p (m)	lp /Diameter
				μ_Δ	μ_ϕ		
1	3.10	0.0168	0.0048	8	20	0.45	0.56
2	3.10	0.0121	0.0042	12	23	0.51	0.63
3	3.15	0.0171	0.0055	2.5	9	0.19	0.24
4	3.15	0.0135	0.0057	2.5	10	0.13	0.16
5	3.15	0.0131	0.0055	5	9	0.40	0.50
6	3.15	0.0130	0.0055	6	7	0.70	0.88

The available curvature ductility μ_ϕ from a particular section layout may be determined using theoretical methods or from experimental evidence. The available displacement ductility μ_Δ can be determined from the curvature ductility and the expected equivalent plastic hinge length, as in Eqn. 6.20.

$$\mu_\Delta = \Delta / \Delta_y = 1 + (\mu_\phi - 1)\, \phi_y\, l_p\, (L - 0.5\, l_p)/\Delta_y \qquad (6.20)$$

Plastic hinge lengths based on erroneously high values of maximum curvature will be artificially short and the calculated available displacement ductility factors will be conservatively low. Conversely, if given displacement ductility factor is assumed for design an excessive curvature ductility demand will be predicted. While this is safe, more attention could be paid to determining maximum curvature values in future experimental work. More accurate estimates of equivalent plastic hinge lengths may lead to some design economies.

Priestley and Park [6.1] showed that the effects of yield penetration past the critical section in many previous experimental tests increased the equivalent plastic hinge length by about six longitudinal bar diameters. In the present tests the observed differences in maximum curvatures, measured with and without the effect of deformations beyond the critical section, confirm that yield penetration was taking place over approximately this equivalent distance into the joint.

The results for equivalent plastic hinge length from the test units appear to show a dependence on the the level of transverse confinement. However, as a conservative estimate it would seem that equivalent plastic hinge lengths of only about 20 percent of the member diameter could be assumed.

6.6.5 Transverse Confining Reinforcement Strains

Strain gauges were attached to the transverse reinforcement near the extreme fibres of the section to monitor the passive confinement action on the concrete. The gauges were attached to the radial legs of the ties or folded spirals through the thickness of the wall and also to the circular spirals, at about the midheight of each of the instrument gauge lengths. Both the inner and outer circular spirals were strain gauged in Units 1 to 3. In the following figures the strains measured at various levels in the test units have been plotted and joined by straight line segments to give an idea of the distribution of transverse reinforcement strains over the height of the plastic hinge region. Distributions are shown for each of the displacement ductility factors imposed during testing.

The strains measured at the peak of the loading cycles in the transverse confining reinforcement through the thickness of the walls are shown in Figs. 6.32 to 6.37. Strains in the through-wall confinement were often well in excess of the yield strain, also shown in the figures, and maximum strains of up to 5 percent were indicated by the strain gauges, although readings from strain gauges are normally only reliable up to strains of about 2 percent. As expected, the distributions of measured strains tend to follow the distributions of curvatures along the plastic hinge region and in general the measured strains increased with increasing displacement ductility factor.

The strains measured in the circular spirals near the extreme compression fibres at the peaks of the loading cycles are shown in Figs. 6.38 to 6.43. Very similar behaviour as in the through-wall confinement is evident, with the strain magnitudes increasing with displacement ductility factor and generally following the same trends as the curvature distributions. In general the strains are less than in the through-wall direction but this is probably due to the larger quantity of transverse confining reinforcement provided in the circumferential direction than in the radial direction. The strains measured in the circular spirals in Units 1 to 3 were similar for both the inner and outer spirals. In some cases the inner spiral gauges indicated larger strains than the outer spiral gauges but in other cases the opposite occurred.

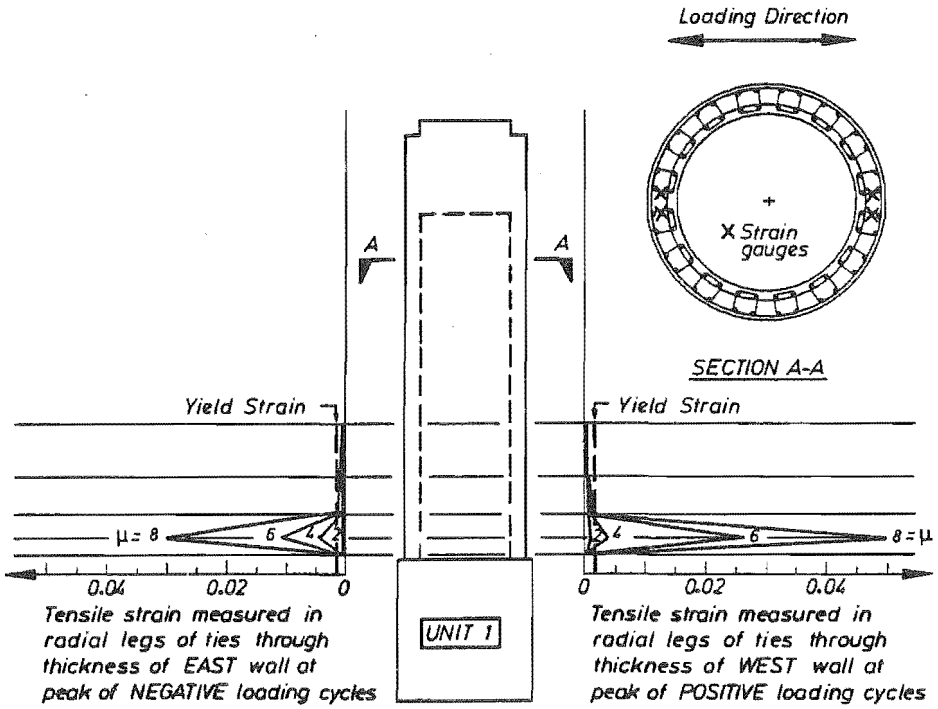

Fig. 6.32 Measured Through-Wall Confining Reinforcement Strains - Unit 1

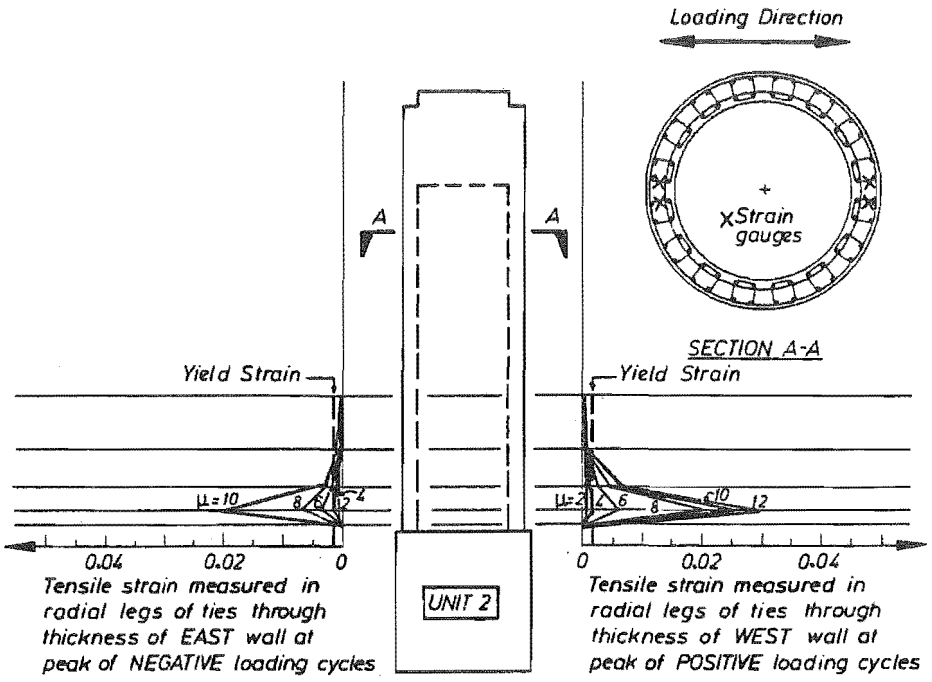

Fig. 6.33 Measured Through-Wall Confining Reinforcement Strains - Unit 2

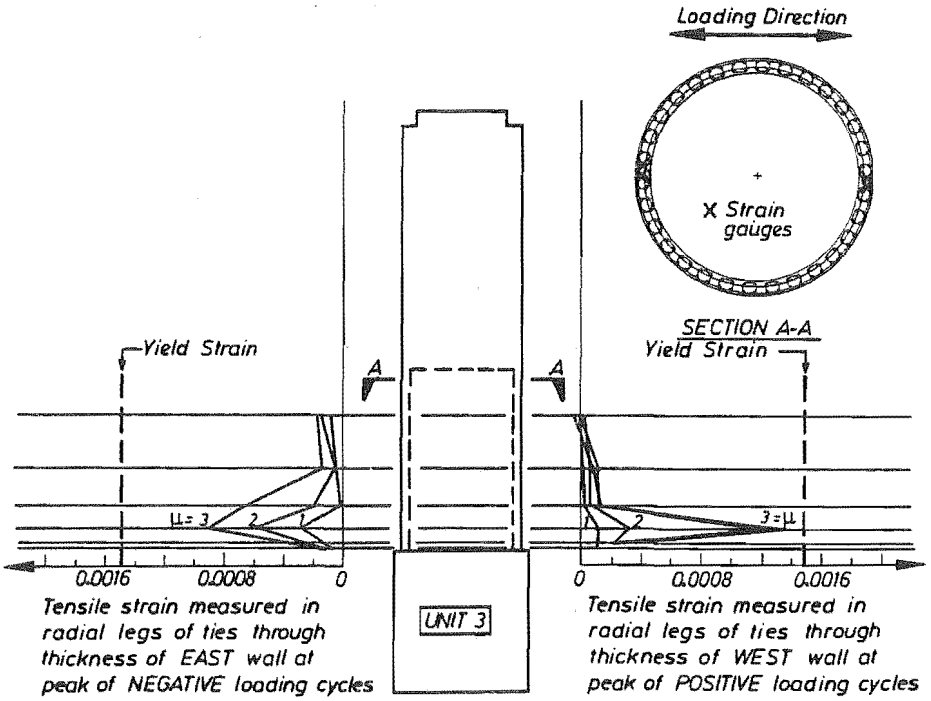

Fig. 6.34 Measured Through-Wall Confining Reinforcement Strains - Unit 3

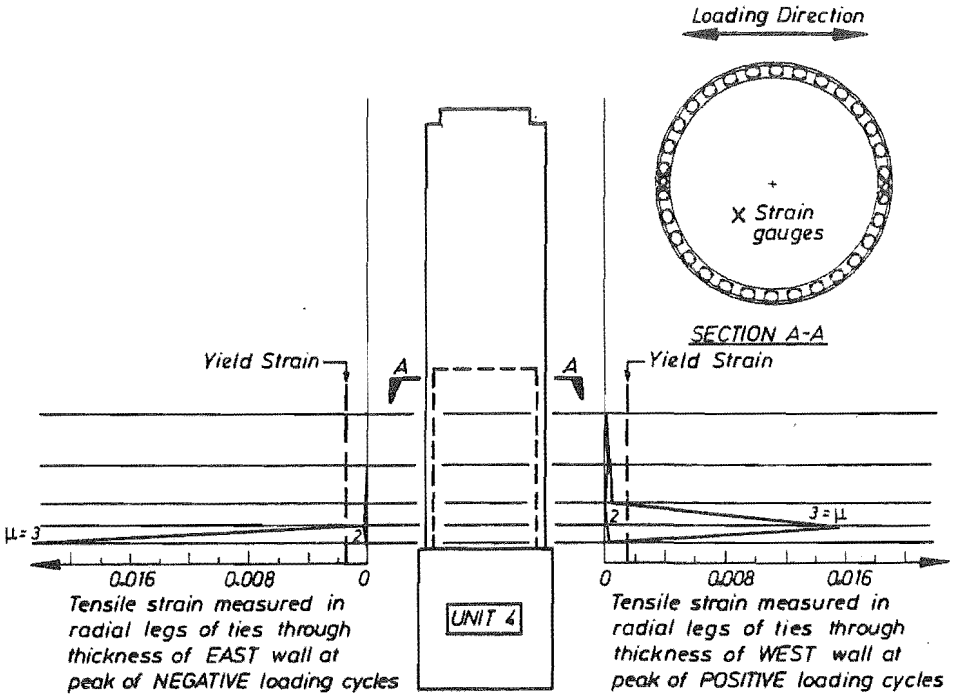

Fig. 6.35 Measured Through-Wall Confining Reinforcement Strains - Unit 4

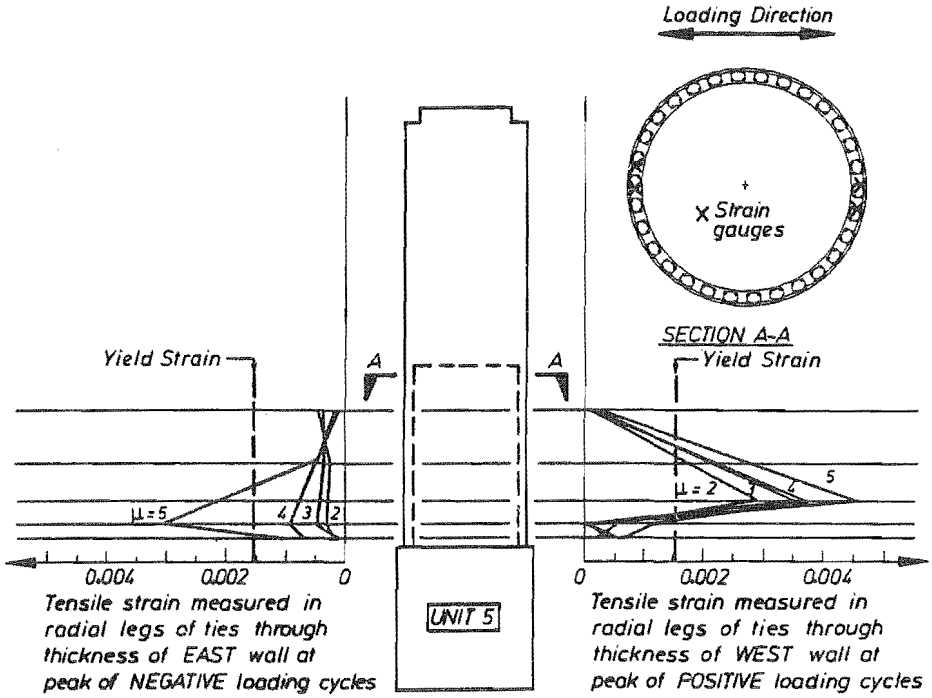

Fig. 6.36 Measured Through-Wall Confining Reinforcement Strains - Unit 5

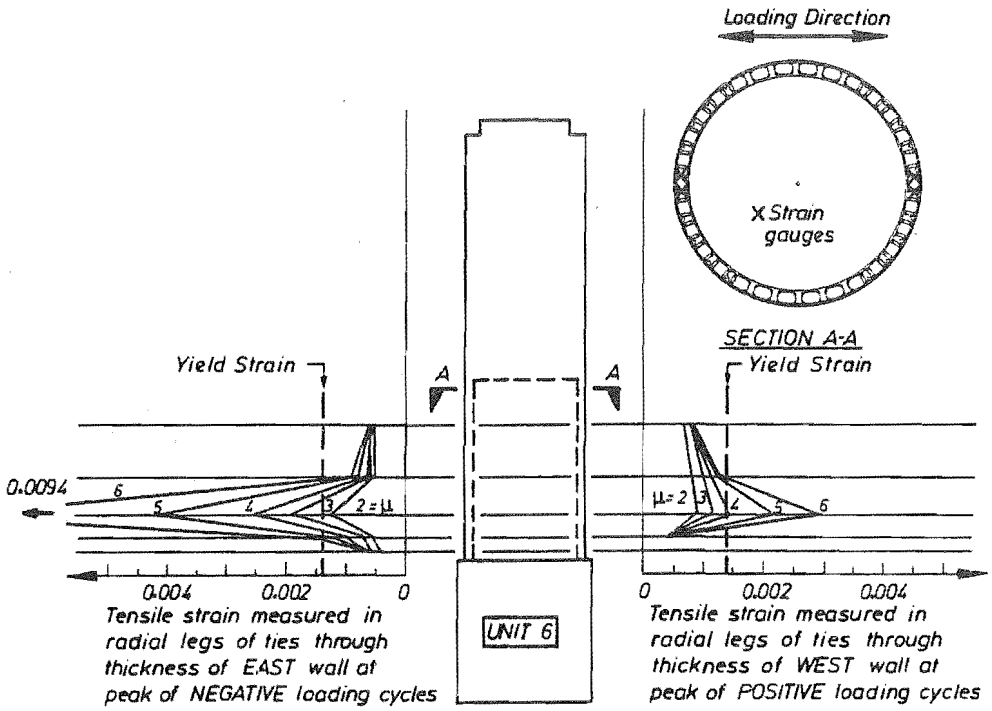

Fig. 6.37 Measured Through-Wall Confining Reinforcement Strains - Unit 6

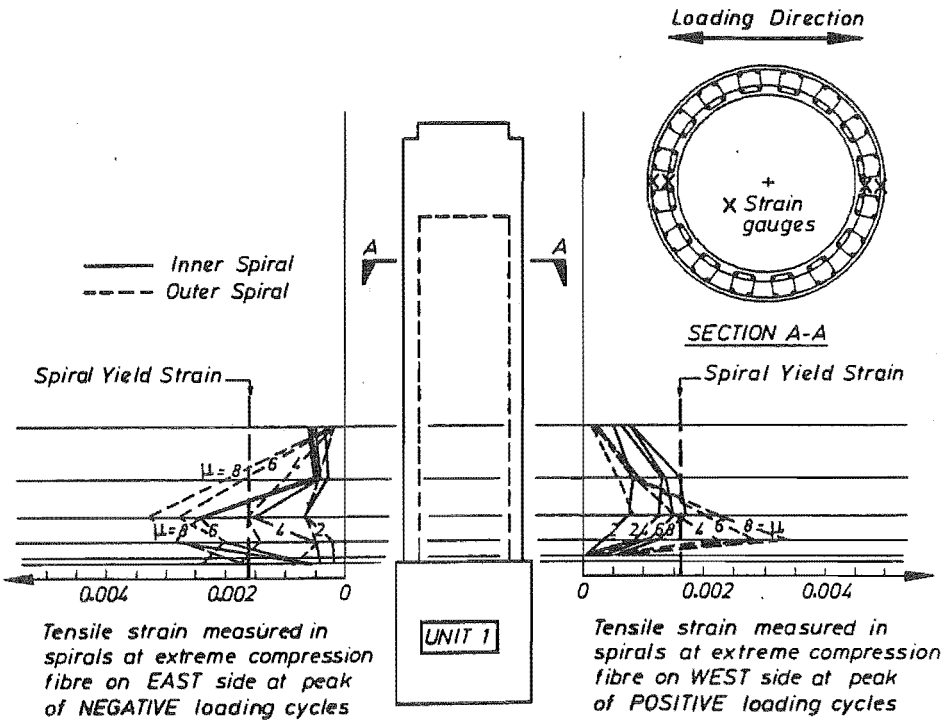

Fig. 6.38 Measured Circular Spiral Confining Reinforcement Strains - Unit 1

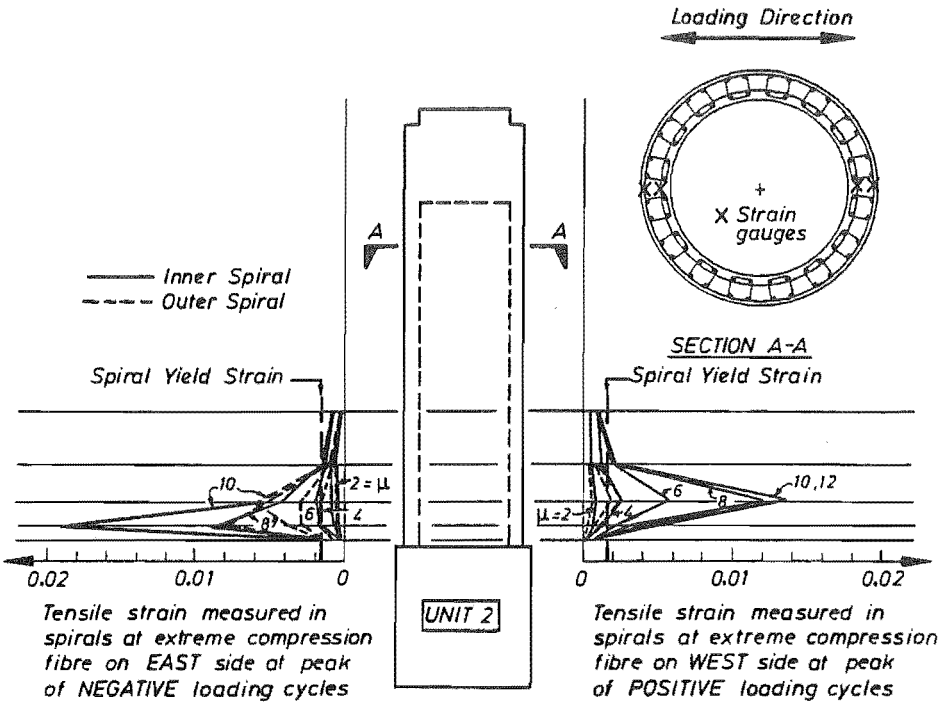

Fig. 6.39 Measured Circular Spiral Confining Reinforcement Strains - Unit 2

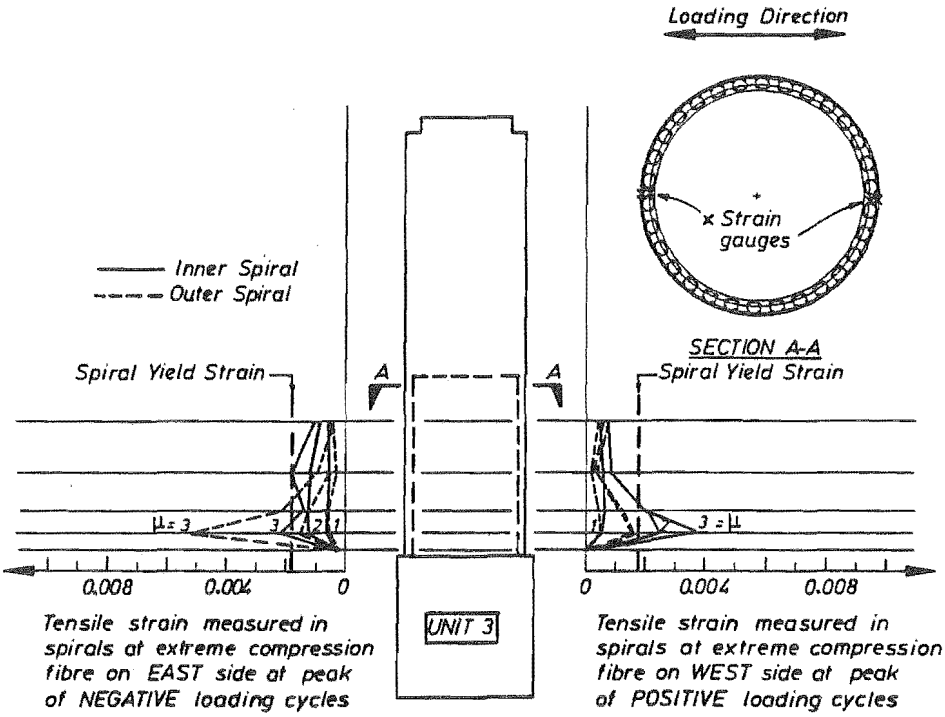

Fig. 6.40 Measured Circular Spiral Confining Reinforcement Strains - Unit 3

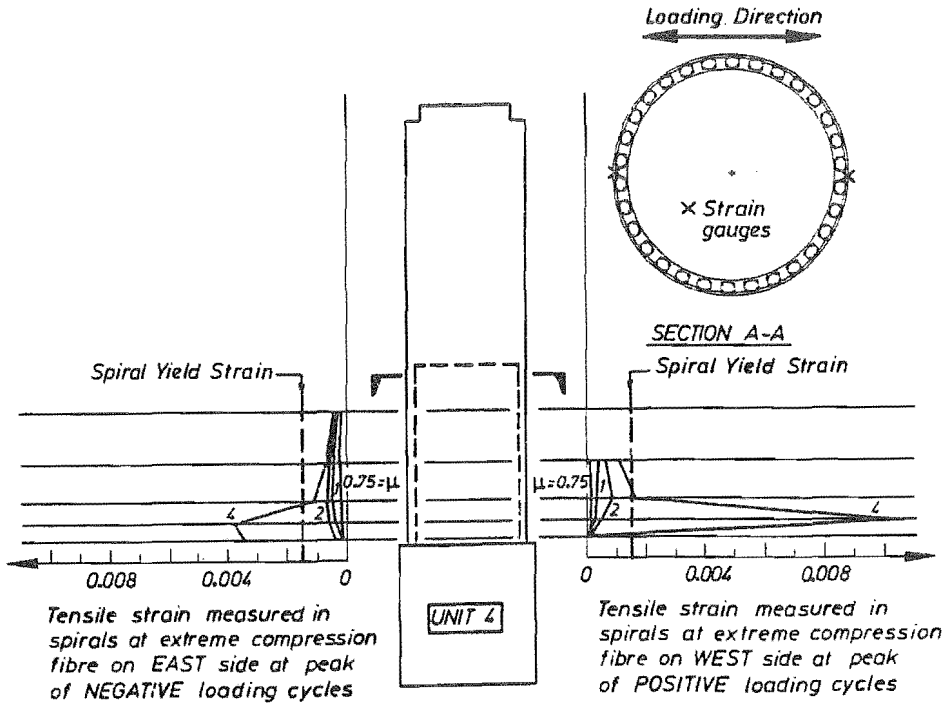

Fig. 6.41 Measured Circular Spiral Confining Reinforcement Strains - Unit 4

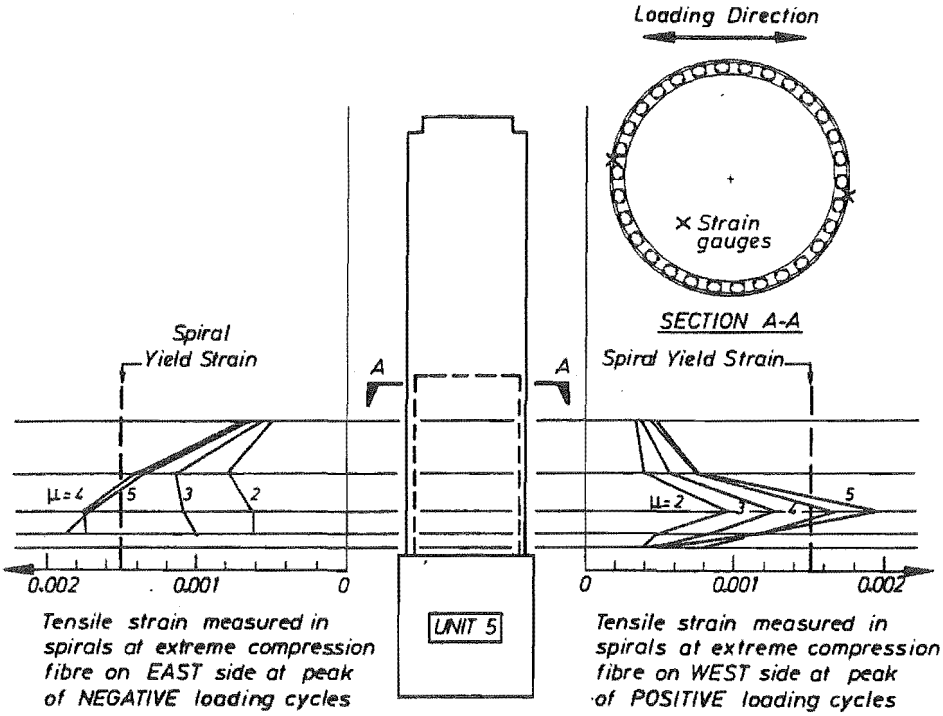

Fig. 6.42 Measured Circular Spiral Confining Reinforcement Strains - Unit 5

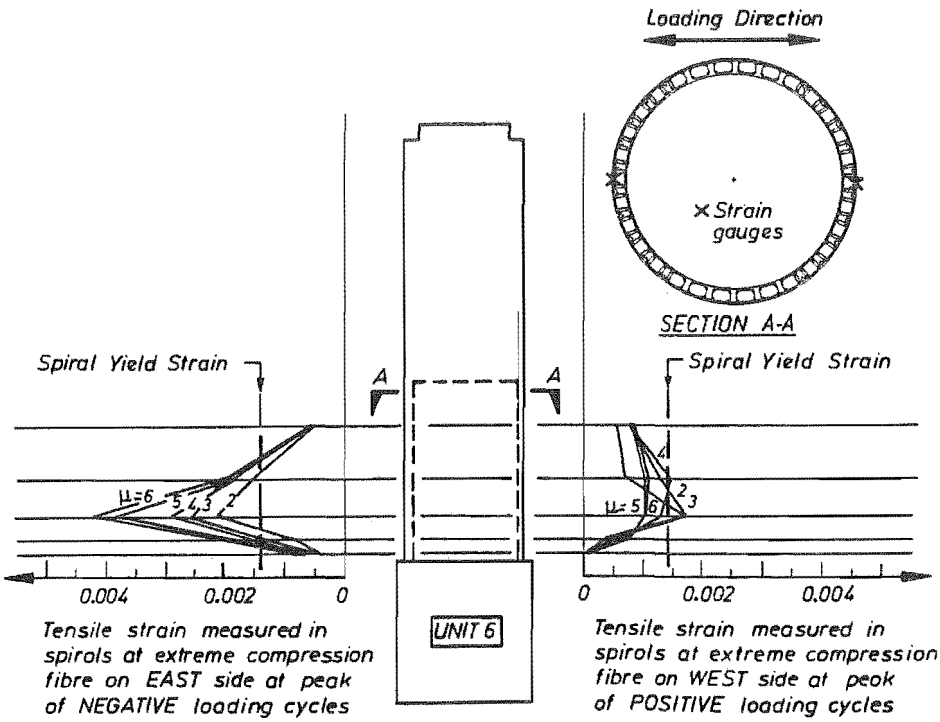

Fig. 6.43 Measured Circular Spiral Confining Reinforcement Strains - Unit 6

The mechanism of confinement provided by transverse reinforcement in concrete members is now quite well understood. As the concrete is compressed longitudinally, lateral strains develop due to Poisson's ratio effects. Extensive internal cracking in the concrete results in a rapid increase in the value of Poisson's ratio and an increase in volume as the concrete expands. The concrete bears out against any transverse hoops, which resist the expansion with a passive confining action. Effective confinement can be provided to the concrete contained within the hoops even after the transverse reinforcement has yielded. Because less confinement was provided in the radial direction than in the circumferential direction in the test units, the concrete would tend to expand more in the radial direction and thus induce larger strains in the transverse reinforcement provided in that direction.

The test unit results show that strains in the transverse confining reinforcement follow a similar trend to the curvatures except close to the critical section at the face of the base block. It is apparent that there is a significant additional confining effect provided by the solid base block. This effect has been observed by other researchers [6.1] for both solid and hollow members in which a stiff joint block was provided adjacent to the critical section.

It might have been expected that the inner circular spiral would be less effective at providing confinement than the outer spiral since the core of the concrete section is not actually contained inside the spiral. However, similar levels of strain were induced in both. Tensile strains induced in the either spiral will result in a circumferential compression stress in the concrete, which will provide a confining action. The outer spiral may also induce a radial confining action in the concrete. The confinement mechanism from the inner circular spiral relies on the spiral bars bearing against the inner layer of longitudinal bars which are restrained by the through-wall reinforcement. It appears from the test results that both inner and outer circular spirals are effective at providing confinement to the concrete if detailed in this way.

6.6.6 Transverse Shear Reinforcement Strains

Shear reinforcement was provided in the test units by the circular spirals around the inner and outer layers of longitudinal bars. Lateral loading was applied in the east-west direction so it was expected that the dominant effects of shear would be apparent in the "webs" of the section on the north and south sides of the member. Strain gauges were attached to the circular spirals near the centroidal axis of the columns. In the vertical direction the gauges were located near the middle of the gauge lengths used for longitudinal strain measurements. In Units 1 to 3 four gauges were attached at each level and in Units 4 to 6 only two gauges were used at each level, as there was only an outer circular spiral provided.

The strains measured in the spiral shear reinforcement in the test units are shown in Figs. 6.44 to 6.49. The figures show the average strain in all of the web strain gauges at each level as a fraction of the yield strain. The values have been shown as a distribution for each imposed ductility factor by joining the points with straight line segments. It can be seen from the figures that in Unit 1 some yielding of the spiral shear reinforcement occurred, but only over a limited length and then only at large displacement ductility factors. In Units 2 and 3 no yielding of the spiral shear reinforcement occurred on average. In Units 4, 5 and 6 only a single outer circular spiral was provided and some quite large strains were induced by shear effects. In Unit 6 the average spiral strains exceeded the yield strain over a considerable length of the hollow tube. It is recalled that significant diagonal cracking and signs of shear distress were observed in this member during testing.

The method used for shear design of the hollow circular columns assumed that separate concrete and steel shear resisting mechanisms would be acting. The assumed shear stress which can be carried by the concrete v_c in plastic hinge regions was taken from the NZS 3101 code and allows for the deterioration of concrete mechanisms during reversed cyclic loading. It is thus expected that initially the concrete would be capable of carrying substantially higher shear stresses, and stresses in any shear reinforcement would be quite low. As the member degrades due to reversed cyclic loading it is expected that the stresses in the shear reinforcement would progressively increase, even if the maximum shear force on the member

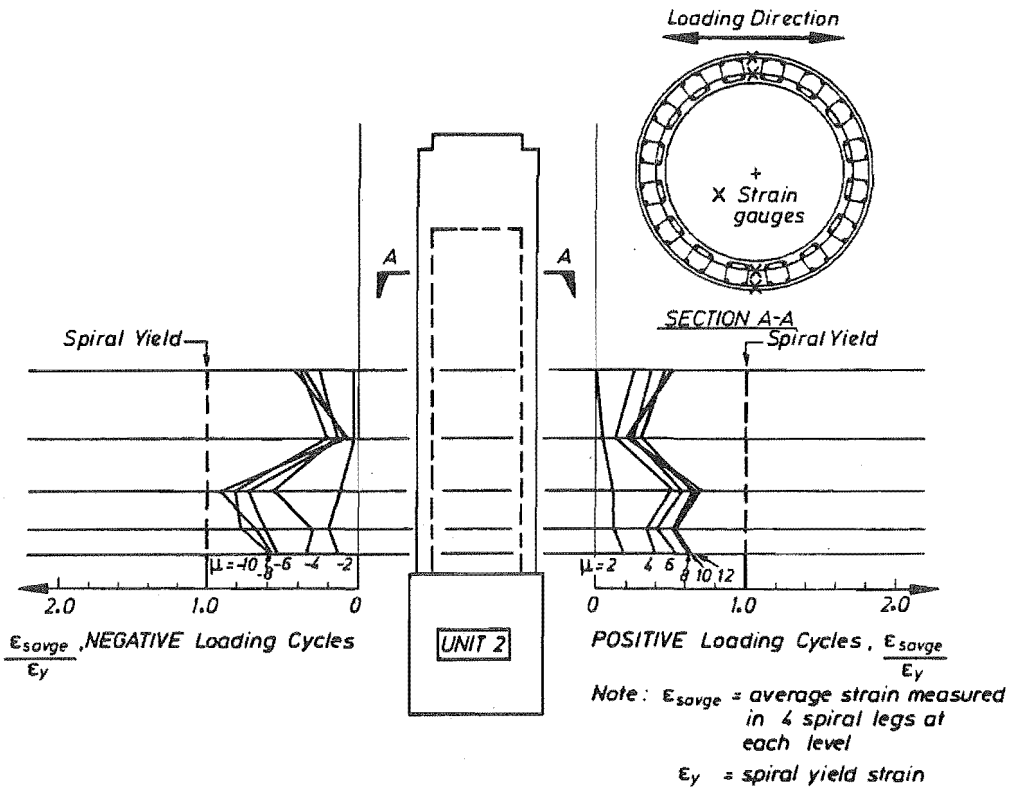

Fig, 6.44 Measured Circular Spiral Shear Reinforcement Strains - Unit 1

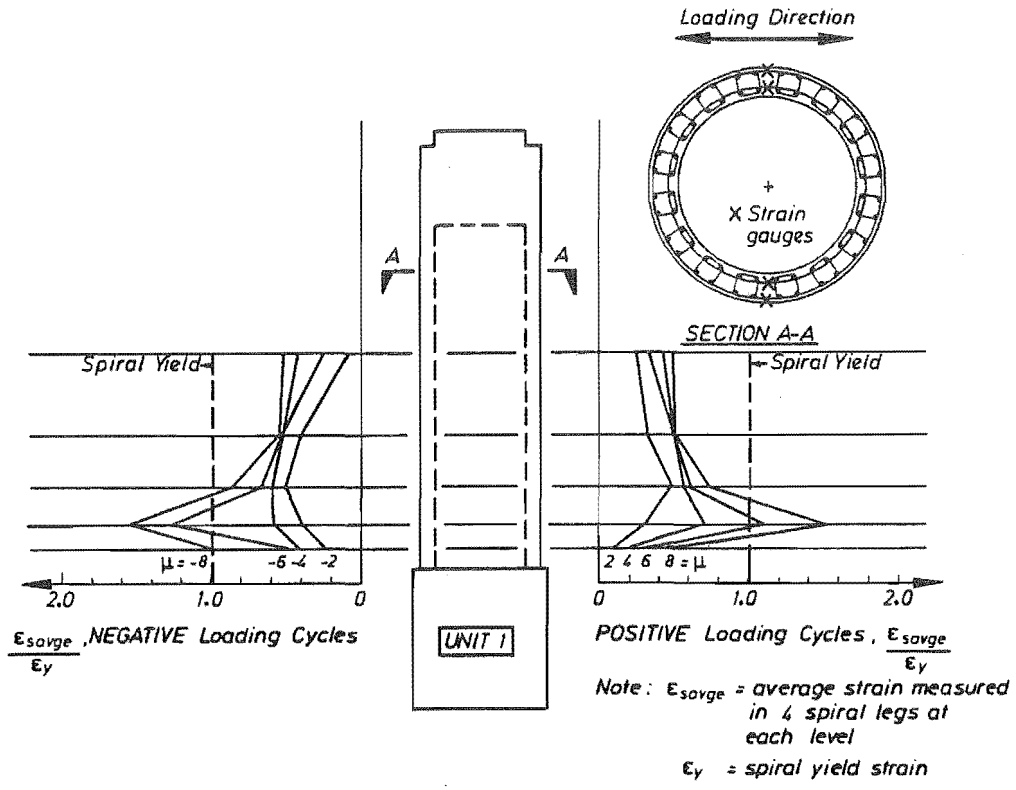

Fig, 6.45 Measured Circular Spiral Shear Reinforcement Strains - Unit 2

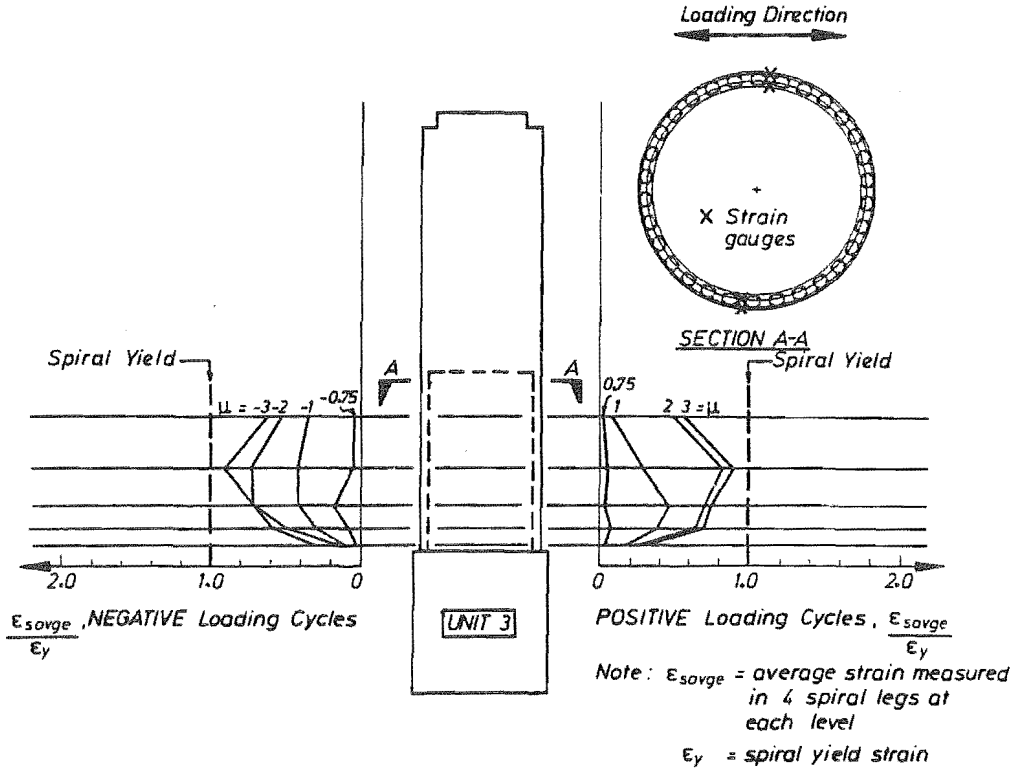

Fig, 6.46 Measured Circular Spiral Shear Reinforcement Strains - Unit 3

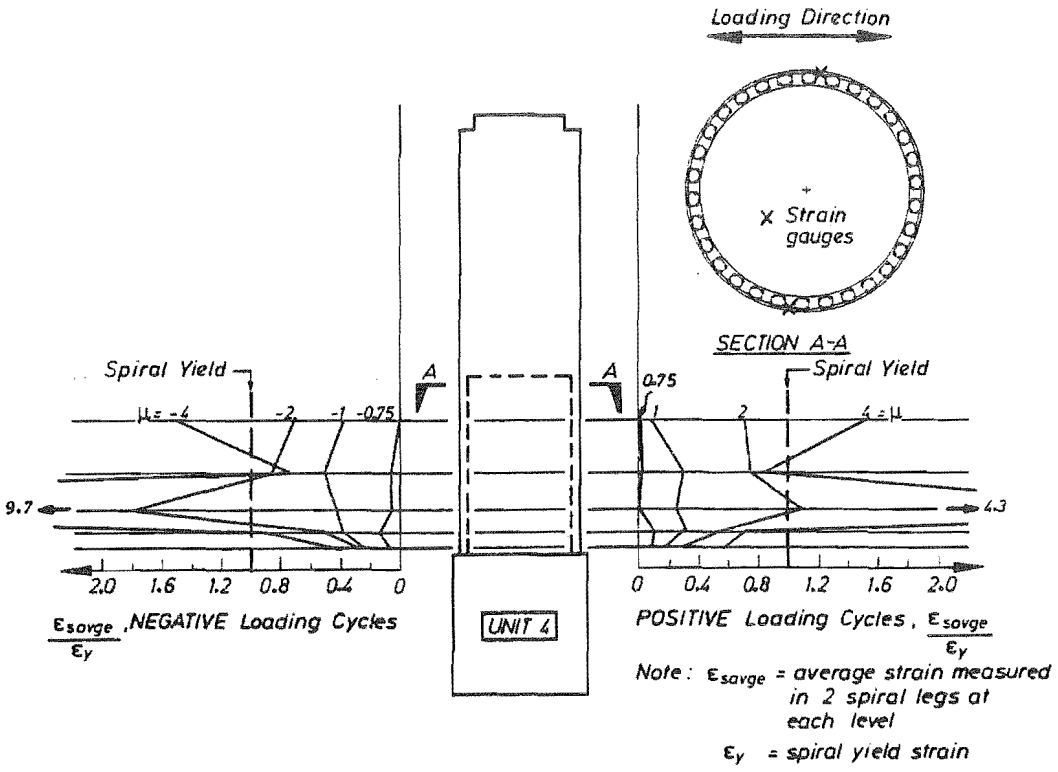

Fig, 6.47 Measured Circular Spiral Shear Reinforcement Strains - Unit 4

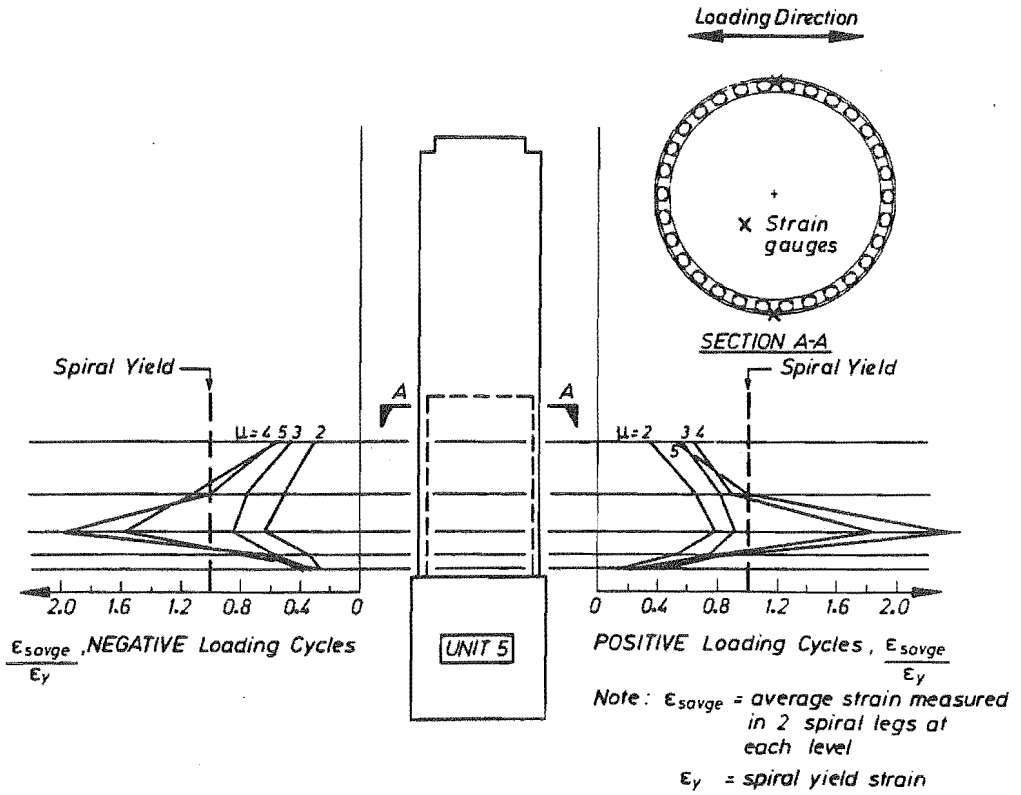

Fig, 6.48 Measured Circular Spiral Shear Reinforcement Strains - Unit 5

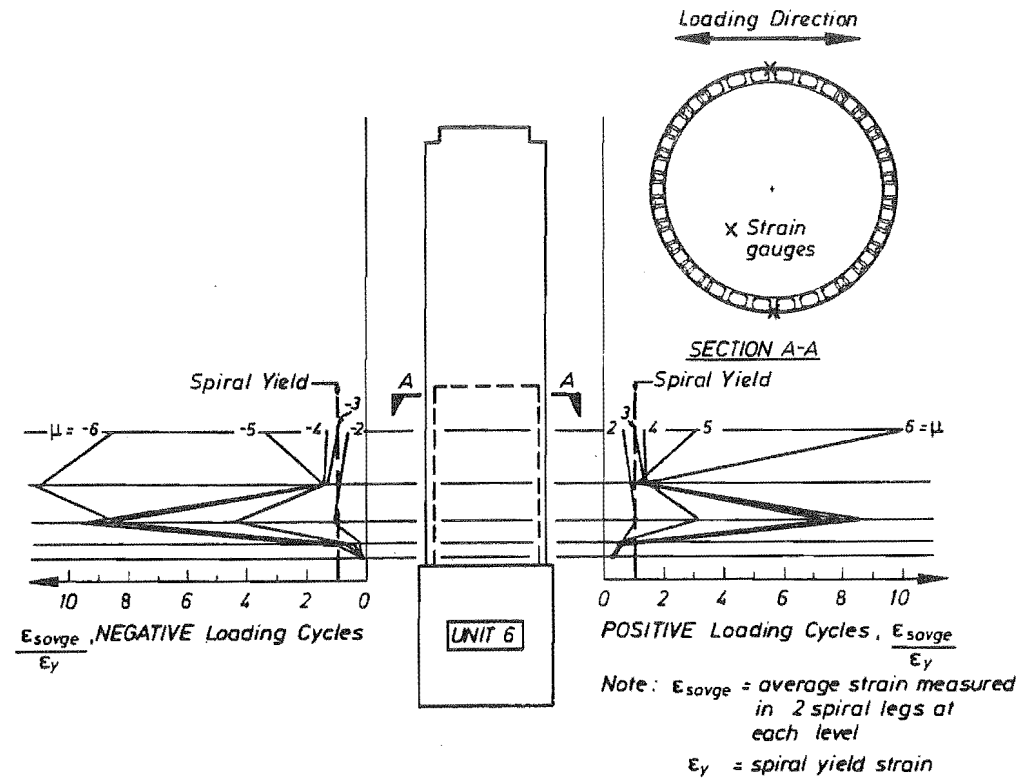

Fig, 6.49 Measured Circular Spiral Shear Reinforcement Strains - Unit 6

was not significantly increased. The steel shear resistance mechanism is based on determining the force which can be transmitted across an assumed 45 degree crack by the transverse bars when they reach their yield stress. For a full mechanism to develop it is expected that all of the bars crossing such an inclined crack would yield.

In reality both the concrete and steel shear resisting mechanisms are likely to degrade with load cycling, as the steel mechanism relies on the development of internal concrete compression forces and bond stresses.

From the observed crack pattern in the test units the 45 degree crack assumption was a reasonable approximation to the average crack inclination in the plastic hinge region. It was expected that if the strains in the spiral shear reinforcement did not reach yield over a substantial proportion of the plastic hinge zone then reserve shear resistance was available in the members. In Units 3 and 4 only a few cycles of reversed lateral loading were sustained before compression zone failures occurred. This makes it difficult to assess how much the concrete shear resistance mechanisms might have deteriorated. In Units 1, 2, 5 and 6 several reversed cycles were sustained by the members, so it is thought that the extent of yielding in the shear reinforcement gives a reasonable indication of the reserve shear capacity.

Table 6.4 summarizes the shear performance of the test Units. This table gives the design values of shear V_c and V_s contributed by concrete and steel shear resisting mechanisms, the ideal shear strength V_t, the shear required to mobilize the ideal flexural strength based on ACI (NZS 3101) flexural strength theory V_i, the maximum shear force resisted during testing V_{max}, the design margin against shear failure V_t/V_i, and the actual margin against shear failure V_t/V_{max}.

Table 6.4 Summary of Shear Performance

Unit	V_c (kN)	V_s (kN)	V_t (kN)	V_i (kN)	V_{max} (kN)	V_t / V_i	V_t / V_{max}
1	136	404	540	285	355	1.89	1.52
2	286	505	791	300	426	2.64	1.86
3	160	190	350	219	288	1.60	1.22
4	145	131	276	204	270	1.35	1.03
5	164	157	321	226	299	1.42	1.07
6	155	93	248	212	279	1.17	0.89

The extent of yielding in the spiral shear reinforcement matches the trends in the margins against shear failure given in Table 6.4 quite well. Very little sign of damage due to shear was observed in the test units with large margins against shear failure, but substantial damage was observed in the units which had only a small margin against shear failure. Theoretically, Unit 6 could have failed in shear as the design method gave no margin of reserve strength above the actual shear force resisted. Substantial cracking and deformation due to shear was observed in this member and it was considered to be very close to failure in shear.

Strains induced in the inner circular spiral were very similar to those in the outer spirals, although the values are not distinguished in the figures showing the shear reinforcement strains. As for the confining action provided by the inner spiral, it is apparent that its effectiveness for resisting shear is also dependent on the spiral being able to bear against the inner layer of longitudinal bars which were restrained by through-wall reinforcement.

The performance of the test units indicates that the method of shear design used was reasonable and conservative. Application of normal capacity design procedures, such as those

given by the New Zealand Concrete Design Code NZS 3101, in conjunction with the suggested method for calculating shear strength, is recommended. The margin of reserve strength above the shear associated with the ideal flexural strength should include realistic allowances for expected flexural strength enhancement and dynamic magnification effects.

6.6.7 Effective Flexural Stiffness

The so-called yield deflection of the members was estimated from the initial loading cycle, in which a lateral load of 75 percent of the ideal lateral load capacity V_i, based on the ACI flexural strength method, was applied. The yield deflection was taken as 1.33 times the measured displacement. The initial lateral stiffness of the members was thus assumed to be equal to the ideal lateral load divided by the measured yield displacement.

The contribution of shear to the yield displacement was estimated from the shear deformation measurements available from the linear potentiometer positioned at about one diameter away from the critical section. To calculate the effective flexural stiffness the shear displacement at the top of the member was estimated and subtracted from the total displacement to give the displacement due to flexure only Δ_f. The ratio of the effective second moment of area I_e to the gross second moment of area I_g was then calculated using Eqn. 6.21.

$$I_e/I_g = V_i L^3/3E_cI_g \Delta_f \qquad (6.21)$$

L is the height from the critical section to the point of lateral load application and E_c is the assumed Young's modulus for the concrete ($E_c = 5000\sqrt{f_c'}$).

The calculated reduction factors for the second moments of area are given in Table 6.5. The values vary from 0.59 to 0.85. The lowest value is for Unit 1 which had the lowest axial load level ($P/f_c'A_g = 0.25$ including prestress) and the highest value is for Unit 2 which had the highest axial load level ($P/f_c'A_g = 0.425$ including prestress). The other test units which had an axial load level of $P/f_c'A_g = 0.3$ gave an average value of about 0.75. Also shown in Table 6.5 are the theoretical reduction factors obtained from analytical moment-curvature studies presented in Chapter 7 (refer Section 7.8.3). There are some discrepancies and on average the experimental figures are about 10 percent greater than the theoretical values. This is to be expected as the theoretical analysis ignores the tension stiffening effect between cracks.

Table 6.5 Flexural Stiffness Reduction Factors

Unit	Experimental Reduction I_e/I_g	Theoretical Reduction I_{cr}/I_g	Ratio Experimental / Theoretical
1	0.59	0.58	1.02
2	0.85	0.70	1.21
3	0.61	0.65	0.94
4	0.83	0.70	1.21
5	0.80	0.65	1.23
6	0.76	0.65	1.17

6.6.8 Maximum Crack Widths

Crack widths were monitored at the extreme fibres of the column units during testing. A crack width measuring microscope was used to measure the maximum crack widths at the peak of loading cycles and after removal of the lateral load. Measurements were not taken after extensive spalling of the cover concrete had occurred. Typical results are shown in Fig. 6.50a

for the prestressed members (Units 1 and 2) and in Fig. 6.50b for the nonprestressed members (Units 3 to 6). It can be seen that the maximum crack widths due to flexure increased as larger deformations were imposed. An approximate linear relationship has been fitted to the results to indicate the trends. The residual crack widths measured after removal of the lateral load are approximated by the dashed lines.

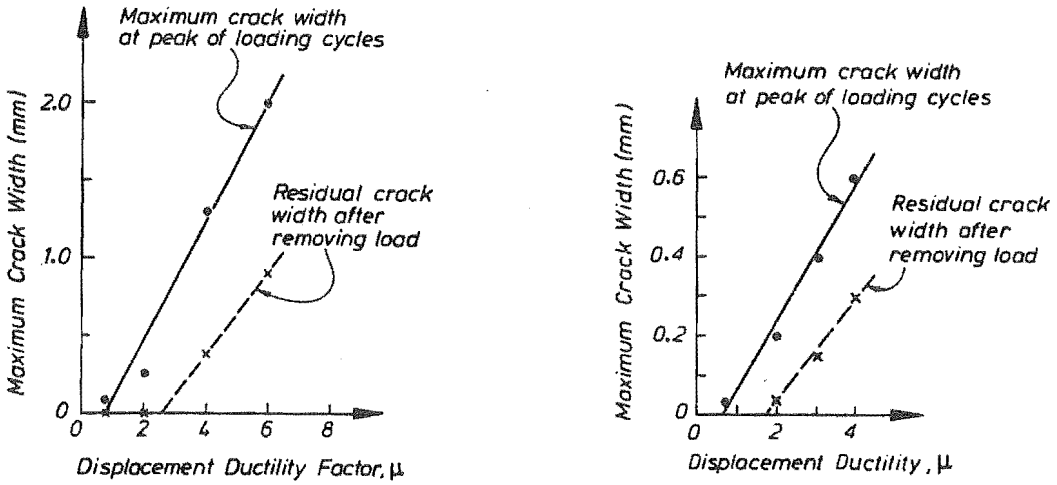

a) Prestressed Members (Units 1 and 2)

b) Nonprestressed Members (Units 3 to 6)

Fig. 6.50 Maximum Measured Crack Widths in Test Units

The maximum crack widths in the prestressed members (Units 1 and 2) were about twice as large as in the nonprestressed members (Units 3 to 6). This was because the crack positions were governed by the positions of transverse bars which were at wider spacings in Units 1 and 2 than in the other members.

In the prestressed members the cracks closed almost completely on removal of the lateral load and residual crack widths were very small for imposed displacement ductility factors up to about $\mu = \pm 3$. For the nonprestressed members similar behaviour was observed but effective crack closure occurred only up to displacement ductility factors of about $\mu = \pm 2$. The greater elastic recovery displayed by prestressed concrete members could be a useful feature in offshore platform structures where it would be desirable to minimise residual crack widths.

6.6.9 Discussion of Sudden Failure Behaviour

In Units 3 to 6 behaviour was initially ductile with progressive spread of cracking and spalling of compression zone cover concrete with increasing lateral displacements. However, in each case final failure was sudden with a drastic loss of strength and concentration of compression zone damage over a very narrow band.

This behaviour can be explained with reference to Fig. 6.51 which is adapted from Park and Paulay [6.14]. In Fig. 6.51a a cantilever member is considered with a point lateral load at the free end. The resulting triangular distribution of bending moment is shown together with a possible moment-curvature relationship. The curvature distribution along the beam can be predicted by translating points from the moment-curvature curve as is indicated by the dashed lines. At the critical section curvatures will increase rapidly after the member has yielded. Away form the critical section, in the unyielded portion of the member, the curvatures will follow the elastic straight line distribution.

The moment-curvature relationship will have a peak after which the moment of resistance of the section reduces with increasing curvatures. If imposed deformations on the member are increased until the curvature at the critical section is pushed beyond the peak in the moment-curvature curve, then the lateral load resistance of the member will be limited by the reduced

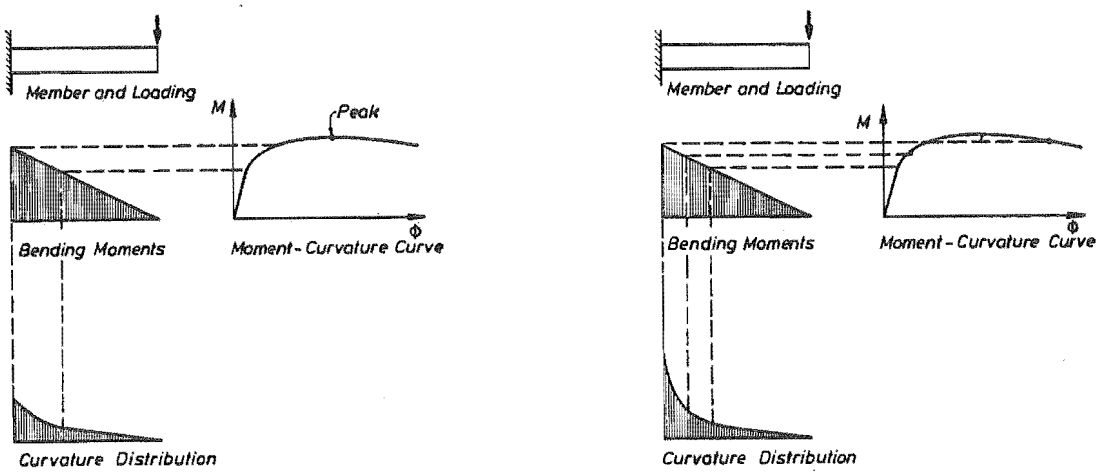

a) Behaviour Before Critical Section Reaches Peak of M-Ø Curve

b) Behaviour After Critical Section Reaches Peak of M-Ø Curve

Fig. 6.51 Idealised Moment-Curvature Behaviour of Cantilever Columns

moment of resistance at the critical section. At all other sections along the member elastic unloading will occur, as the bending moment diagram must remain triangular and reduce in size. This is illustrated in Fig. 6.51b and it is apparent that curvatures will increase dramatically at the critical section but actually reduce slightly at all other sections. Theoretically, any increase in imposed displacement at the free end would result in an infinite curvature demand at the critical section. However, this idealised analysis does not take into account factors which help spread yield in real concrete members. The presence of shear induces diagonal tension cracking which spreads the yielding of longitudinal reinforcement along the tension side of the member (the so-called T-jd effect). Deterioration of bond, particularly in members subject to reversed cyclic loading, also tends to spread yielding away from the critical section. Hence the plastic hinge will retain some finite length and the curvature demand over that length will not be as severe as suggested by Fig. 6.51.

Nevertheless, it seems that the idealised analysis discussed above, modified to account for some spread of yielding, can explain the sudden loss of strength observed in Units 3 to 6. Theoretically predicted lateral load versus lateral displacement behaviour is presented in Section 6.7 and reasonable agreement was achieved between the theoretical and experimental behaviour. It was possible to predict when the critical section in each test unit would reach the peak of the moment-curvature curve. For Units 1 and 2 the theoretical moment-curvature curves were still rising at deformations corresponding to the maximum experimentally imposed displacements. This is expected to account for their extremely ductile response. For Unit 6 analysis showed that the peak of the moment-curvature curve would have just been reached when failure occurred outside the well confined end region of the member.

6.7 THEORETICAL PREDICTION OF LOAD - DEFORMATION BEHAVIOUR

A computer program was developed by Mander et al [6.4] to predict the lateral load versus deformation behaviour of reinforced concrete columns. Details of this program are given in Chapter 7. The program calculates moment-curvature behaviour of arbitrarily shaped reinforced concrete sections to a prescribed series of imposed curvatures. Lateral load versus lateral displacement behaviour of cantilever members can also be determined. In that case the moment-curvature behaviour is assumed to be that appropriate to the critical section. The program assumes a parabolic variation of curvature over the yielded length of the beam and also accounts for shear deformations. The author has modified the program to include high strength steel prestressing tendons so that the behaviour of prestressed concrete members can also be predicted.

In the discussion in Section 6.6.9 it was suggested that one of the fundamental aspects of behaviour of these thin-walled tubular members was the sudden failures which were observed in several of the test units. This failure seems to be triggered when the curvature at the critical section reaches the peak in the governing moment-curvature relationship. The lateral load versus curvature at the critical section was derived for monotonic loading of each test unit to determine what deformations could theoretically be sustained before the peak of the moment-curvature curve was reached. The monotonic lateral load versus curvature relationships are shown in Figs. 6.52 to 6.57. The maximum curvature and lateral displacement corresponding to the predicted peak of the moment-curvature curves are noted for each unit.

The comparison between these results and the maximum deformations sustained by the test units before loss of load resistance is given in Table 6.6. Maximum predicted and experimentally measured curvatures are up to 50 percent different but the maximum lateral displacement figures agree quite well. The large discrepancies in available curvature arise because of the large variations in the shape of the measured curvature distributions over the plastic hinge regions. In some units (for example Units 3 and 4) the curvatures were not well spread and the equivalent plastic hinge lengths were quite a small proportion of the member diameter. In those cases the theoretical maximum available curvature at the critical section is smaller than the maximum measured value. In Unit 6 the reduction of curvature over the plastic hinge region appeared to be much more gradual and the equivalent plastic hinge length was quite a large proportion of the member diameter. In that case the theoretical maximum curvature is larger than the maximum measured value.

Table 6.6 Comparison of Maximum Experimentally Measured and Maximum Theoretically Predicted Deformations

Unit	Experimental Deformations		Theoretical Deformations	
	Displacement Δ_{max} (mm)	Curvature $\varnothing_{max}$ (rad/m)	Displacement Δ_{max} (mm)	Curvature $\varnothing_{max}$ (rad/m)
1	145	0.10	194	0.173
2	145	0.11	127	0.107
3	45	0.05	43	0.038
4	35	0.06	48	0.045
5	60	0.05	58	0.055
6	87	0.04	83	0.077

The distributions of curvature over the plastic hinge region assumed by the computer analysis program give predicted maximum plastic hinge rotations in reasonable agreement with the measured experimental values. That is why the theoretical maximum lateral displacements agree quite well with the experimental values.

It is theoretically possible to predict the variation in curvature over the plastic hinge region, as explained in Section 6.6.9. However, empirical allowances would be necessary to allow for the spread of yielding along the member. This approach may result in better agreement between theoretical and experimentally measured distributions of curvature, but it was not pursued in this study.

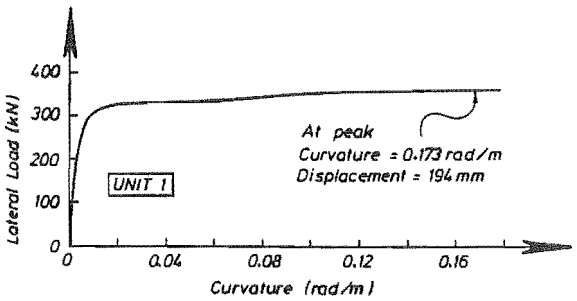

Fig. 6.52 Theoretical Monotonic Moment-Curvature Response at Critical Section - Unit 1

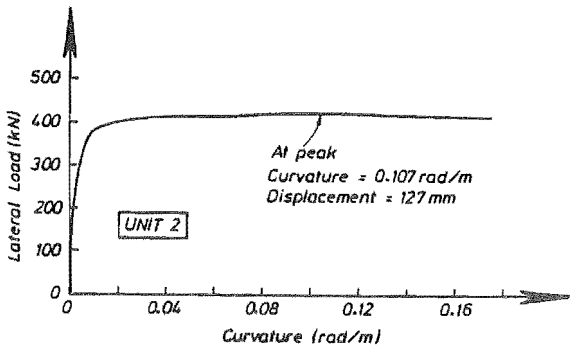

Fig. 6.53 Theoretical Monotonic Moment-Curvature Response at Critical Section - Unit 2

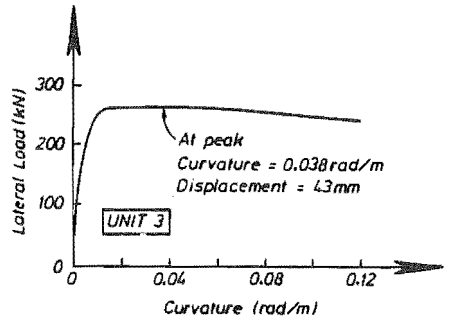

Fig. 6.54 Theoretical Monotonic Moment-Curvature Response at Critical Section - Unit 3

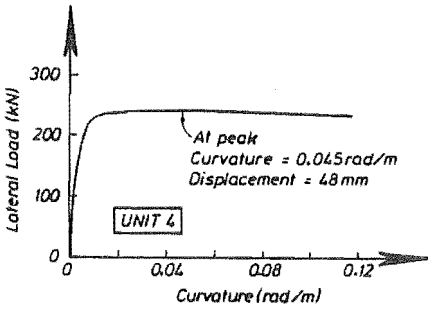

Fig. 6.55 Theoretical Monotonic Moment-Curvature Response at Critical Section - Unit 4

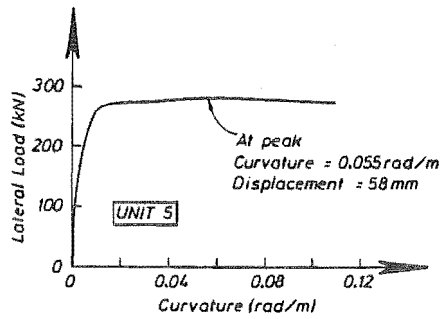

Fig. 6.56 Theoretical Monotonic Moment-Curvature Response at Critical Section - Unit 5

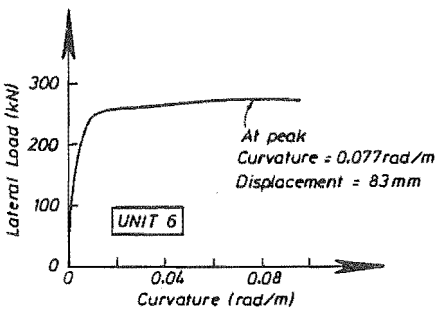

Fig. 6.57 Theoretical Monotonic Moment-Curvature Response at Critical Section - Unit 6

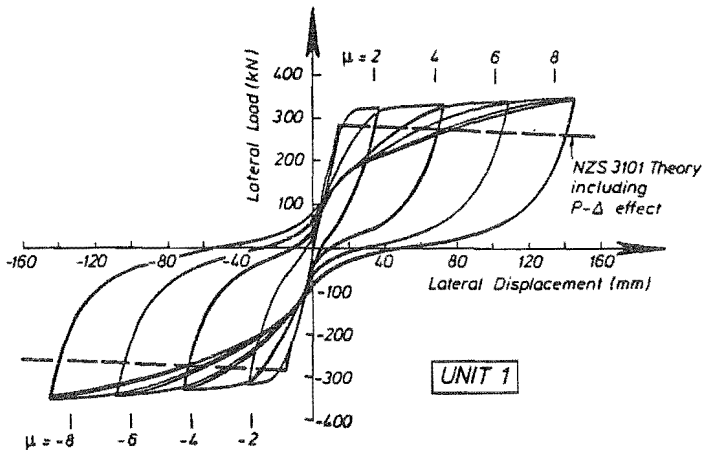

Fig. 6.58 Theoretical Cyclic Lateral Load versus Displacement Behaviour - Unit 1

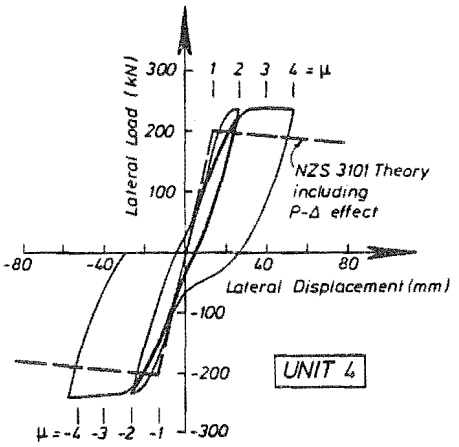

Fig. 6.61 Theoretical Cyclic Lateral Load versus Displacement Behaviour - Unit 4

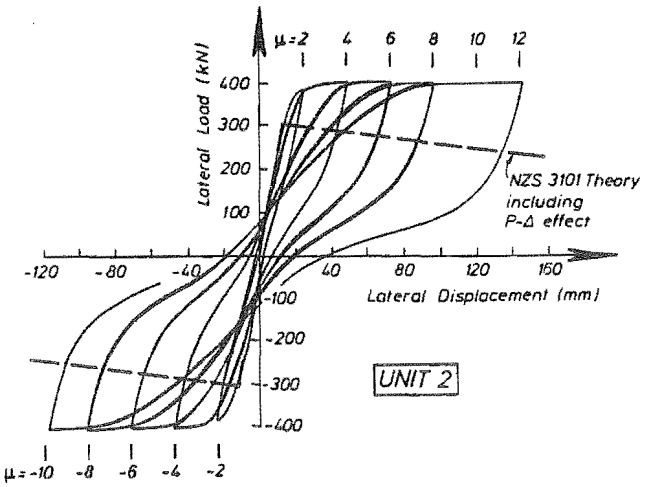

Fig. 6.59 Theoretical Cyclic Lateral Load versus Displacement Behaviour - Unit 2

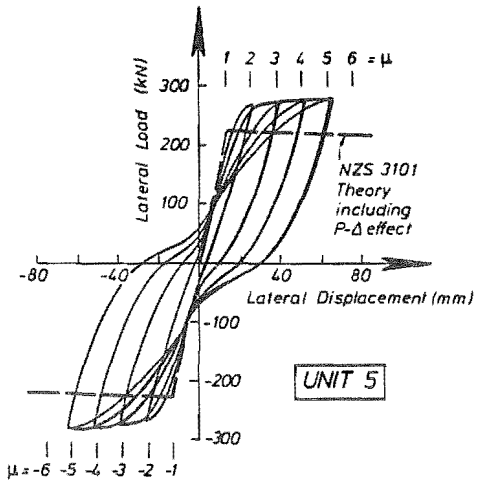

Fig. 6.62 Theoretical Cyclic Lateral Load versus Displacement Behaviour - Unit 5

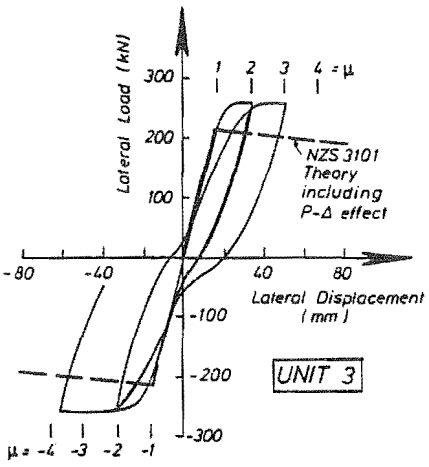

Fig. 6.60 Theoretical Cyclic Lateral Load versus Displacement Behaviour - Unit 3

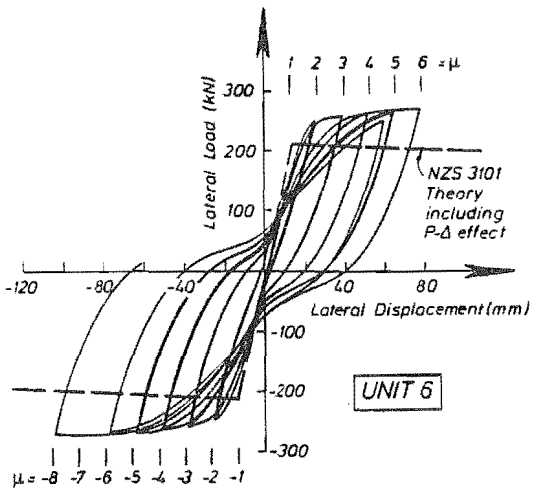

Fig. 6.63 Theoretical Cyclic Lateral Load versus Displacement Behaviour - Unit 6

In deriving the theoretical lateral load versus deformation behaviour it was necessary to adjust the parameters controlling the stress-strain behaviour of confined concrete. The model assumed for the stress-strain behaviour of confined concrete is presented in Chapter 7. The strain ε_{cc} at the confined strength f_{cc}' is determined from the unconfined compressive cylinder strength f_c', the peak strain in the unconfined stress-strain curve ε_{co} (assumed to be 0.002), and a parameter R, as given by Eqn. 6.22.

$$\varepsilon_{cc} = \varepsilon_{co} [1 + R((f_{cc}'/f_c') - 1)] \qquad (6.22)$$

Mander [6.4] suggested a value of R=5 was appropriate but noted that previous researchers had found values between about 3 and 10 from tests on confined concrete specimens. The lower limit of R=3 was found to give much better agreement between the theoretical and experimental load-deformation behaviour of the test units in this study. A value of R=3 was used in deriving the theoretical lateral load versus curvature curves. It is expected that this was because small aggregate concrete was used in the test units.

Figs. 6.58 to 6.63 show theoretical lateral load versus lateral displacement hysteresis behaviour derived for each of the test units using the computer analysis program. The cyclic loading history was prescribed to follow the same set of imposed displacements as in the experimental testing of each unit.

The agreement between the theoretical and experimental behaviour (Figs. 6.17 to 6.22) is quite good. In all cases the theoretical behaviour gave conservative estimates of the actual lateral loads resisted by the test units. The overall shape of the hysteresis loops is quite similar but the theoretical loops tend to be a little more "pinched" with slightly less area enclosed. This is probably due to the idealised closure of cracks which is assumed in the analysis. In real members crack closure is not perfect. Small pieces of concrete may be dislodged and shear slippage can occur while the crack is open . The theoretical behaviour does not show the sudden loss of load resistance, as the analysis assumes that there is always a gradual reduction of curvature along the plastic hinge region.

6.8 CONCLUSIONS FROM EXPERIMENTAL STUDY

1. Hollow circular reinforced or partially prestressed column members containing a sufficient quantity of well detailed transverse reinforcement can be expected to display similar ductile load-deformation behaviour to that available from well-detailed solid members.

2. Although initially ductile, thin-walled hollow concrete members appear to be less able to spread plastic hinging along the member as final failure is approached. The failures are characterised by a sudden loss of strength and severe concentrations of damage in the concrete compression zones. It appears that this damage is triggered when the curvature at the critical section exceeds the curvature at the peak of the moment-curvature response curve. The moment-curvature behaviour can be obtained theoretically and thus the range of ductile response can be predicted.

3. Flexural strength calculations based on the NZS 3101 and ACI 318 theoretical method, assuming a strength reduction factor of unity and the measured material strengths, gave quite conservative estimates of the actual flexural strength found from the test units. It appears that the enhancement of strength above these code method predictions is due mainly to the increase of concrete strength resulting from confinement. It is dependent on the level of axial load, to the same extent found in solid members.

4. Yield displacements of the test units were estimated from an initial loading cycle to approximately 75 percent of the ideal lateral load capacity based on the code

theoretical flexural strengths. The effective flexural stiffness of the members in this initial cycle was approximately 75 percent of the initial gross stiffness. This is a reasonable estimate of the effective flexural stiffness of members with an axial load level of $P_e/f_c'A_g = 0.3$. For higher axial load levels the effective stiffness is expected to increase and for lower axial load levels it will reduce.

5. Methods for shear design of hollow circular members are not generally provided by concrete design codes. For these test units the capacity design principles of the New Zealand Concrete Design Code were followed. A steel shear resistance mechanism based on bar forces across a 45 degree crack was assumed, together with a concrete resistance mechanism using 64 percent of the gross section area, and was found to be conservative. For design purposes, the ideal shear strength V_t of a hollow circular concrete column can be calculated from the expression in Eqn. 6.23.

$$V_t = 0.64A_g v_c + (\pi/2)\, A_{sp}\, f_{yh}\, d_s/s \qquad (6.23)$$

6.9 REFERENCES - CHAPTER 6

6.1 Priestley, M. J. N. and Park, R., "Strength and Ductility of Bridge Substructures", RRU Bulletin 71, National Roads Board, Wellington, New Zealand, 1984.

6.2 NZS 3101 : 1982 , "Code of Practice for the Design of Concrete Structures", Parts 1 and 2, Standards Association of New Zealand, Wellington.

6,3 Regan, P. E. and Hamadi, Y. D., " Behaviour of Concrete Caisson and Tower Members", Concrete in the Oceans, Technical Report No. 4, CIRIA/UEG, Cement and Concrete Association, Department of Energy, United Kingdom.

6.4 Mander, J. B., Priestley, M. J. N. and Park, R., "Seismic Design of Bridge Piers", Research Report 84-2, Department of Civil Engineering, University of Canterbury, February 1984.

6.5 Zahn, F. A., Park, R. and Priestley, M. J. N., "Design of Reinforced Concrete Bridge Columns for Strength and Ductility", Research Report 86-7, Department of Civil Engineering, University of Canterbury, March 1986.

6.6 American Concrete Institute, "Guide for the Design and Construction of Fixed Offshore Structures".

6.7 "Shell Brent B Instrumentation Project", Proceedings of the Seminar held on 14 November 1979, The Society for Underwater Technology, London.

6.8 "Rules for the Design, Construction and Inspection of Offshore Concrete Structures", Det norske Veritas, Norway, 1977.

6.9 BS 6235 : 1982, "Code of Practice for Fixed Offshore Structures", British Standards Institution.

6.10 Ang Beng Ghee, "Dynamic Shear Strength of Concrete Piers", Ph.D. Thesis, University of Canterbury, 1985.

6.11 NZS 4203 : 1984, "Code of Practice for General Structural Design and Design Loadings for Buildings", Standards Association of New Zealand, Wellington. 100 pp.

6.12 CDP 701/D, "Highway Bridge Design Brief", New Zealand Ministry of Works and Development, September 1978 (including 1978 addendum).

6.13 Goodsir, W. J., Paulay, T. and Carr, A. J., "The Design of Coupled Frame-Wall Structures for Seismic Actions", Research Report 85-8, Department of Civil Engineering, University of Canterbury, August 1985.

6.14 Park, R. and Paulay, T., "Reinforced Concrete Structures", John Wiley and Sons, New York, 1975,

Chapter 7

THEORETICAL STUDY OF STRENGTH AND DUCTILITY OF HOLLOW CIRCULAR CONCRETE MEMBERS

7.1 INTRODUCTION

Hollow circular concrete members are often incorporated in offshore concrete gravity platform structures. In conjunction with the experimental investigations reported in Chapter 6, a study was undertaken to examine the theoretical moment-curvature behaviour of hollow circular concrete column sections subject to axial load and reversed cyclic flexure. Variables included in the study were: axial load level, transverse confining stress, longitudinal reinforcement index, yield stress of longitudinal reinforcement, concrete compressive cylinder strength, cover to wall thickness ratio and level of axial prestress. Variables were considered in nondimensional form so that results were applicable for members of any size.

Results are presented in a form which will be of direct use to structural designers. Charts are provided which enable the strength and ductility characteristics of circular hollow sections to be estimated. The charts cover a range of variables applicable to structural members which could be used in offshore concrete platforms. Designers will be able to select quantities of transverse confining reinforcement necessary to sustain the ultimate curvatures anticipated in plastic hinge regions during severe earthquake loading.

Theoretical moment-curvature behaviour was predicted using a computer analysis program developed by Mander et al [7.1]. This program incorporates refined stress-strain models for confined concrete and reinforcing steel. Modifications were made to include prestressed longitudinal reinforcement also. Cyclic moment-curvature analyses of many example sections were carried out in order to examine the dependence of behaviour on different variables.

Moment-curvature analyses based on realistic stress-strain behaviour of confined concrete and reinforcing steels indicate that ideal flexural strengths based on conventional section analysis methods such as the ACI method [7.2], also incorporated in the New Zealand Concrete Design Code [7.3], are reasonable for low levels of axial load, but are unduly conservative for high levels of axial load. This has been observed in many previous experimental studies for both hollow and solid members. Charts are provided for estimating realistic ideal flexural capacities which should be available from these members. This would allow significant economies to be made in designing members with moderate to high levels of axial load.

Information regarding ultimate curvature ductility was also available from these investigations. Charts are provided for estimating yield curvature and available ultimate curvature from these sections.

7.2 APPLICATION OF MOMENT - CURVATURE RESPONSE INFORMATION

During large seismic disturbances it is expected that significant inelastic deformations may occur in a limited number of critical regions of offshore platform structures. Capacity design principles should be used to ensure that ductile flexural hinging will occur in carefully detailed potential plastic hinge zones. Structure are required to sustain the displacements likely to be imposed during such a disturbance with an acceptably low risk of collapse. It is expected that this can be achieved by ensuring that critical regions exhibit stable moment-curvature behaviour. If axial strength and a significant proportion of the lateral load carrying capacity can be preserved during earthquake shaking then collapse should be avoided, provided that secondary effects, such as the so-called P-delta loadings caused by lateral drift, do not become excessive. Stable hysteretic behaviour under reversed cyclic loading can also result in significant dissipation of kinetic energy and reduced levels of structural response. In this study it was intended to study the moment-curvature behaviour of

a large number of hollow circular concrete sections which could represent the critical regions of members in offshore concrete platform structures. Performance criteria were chosen to determine when moment-curvature behaviour became unsatisfactory.

Modern design codes, such as the New Zealand Concrete Design Code NZS 3101 [7.3] specify quantities of transverse confining reinforcement for solid members which have been found from experimental and theoretical research to give ductile load-deformation behaviour. The commentary to NZS 3101 [7.3] suggests that members detailed in accordance with that code should be capable of sustaining curvature ductility factors (ratio of maximum imposed curvature to curvature at yield) of approximately 20. NZS 3101 provisions for design and detailing of transverse reinforcement are intended to be consistent with the likely ductility demands for building and bridge structures designed to the appropriate loadings codes [7.4, 7.5]. For most structures designed to these loadings codes, maximum displacement ductility demands of approximately six are expected during very large earthquakes. The corresponding curvature ductility demands at the critical sections can be up to 3 or 4 times this, that is approximately twenty. Members designed according to the requirements of these codes are expected to display good inelastic behaviour and it is generally considered unnecessary to carry out specific checks to determine their ductility capabilities. However, it is appropriate for designers of unusually complex or important structures, such as offshore platforms, to have more detailed methods of assessing the design and detailing requirements specific to the ductility demands which may be expected. Offshore platform structures are designed to resist the effects of large storm waves without damage. This requires considerable strength to be provided. It is likely that the ductility demands during large earthquakes are quite different from those which are expected in typical building or bridge systems.

In practice the strength of offshore platform structures will be proportioned to safely carry the chosen design loadings for waves and moderate sized earthquakes. Consideration of maximum credible earthquake events will indicate the overall displacements which the structure will be required to withstand. Using simple collapse mechanism theories, or more complex computer analysis methods, the required plastic hinge rotations, and hence the maximum curvature demands, could be estimated. The design aid charts presented here could then be used to determine the transverse confining reinforcement required to reliably attain those curvature demands.

7.3 COMPUTER ANALYSIS PROGRAM

A computer program for determining the load-deformation behaviour of arbitrarily shaped reinforced concrete members was developed by Mander et al [7.1]. Refined stress-strain models for confined concrete and reinforcing steels were incorporated in the program. The member cross-section of interest was considered as a series of parallel strips which lie perpendicular to the direction of the applied load. It is assumed that this is the critical maximum moment section of a cantilever member with axial load and variable lateral load at the free end. The distribution of flexural strains is always assumed to be linear through the depth of the section. Analysis proceeds by incrementing the curvature at the critical section in a series of small steps. The position of the neutral axis is obtained by iteration until equilibrium of the internal forces is achieved, after which the moment of resistance of the section is calculated. In this way the moment versus curvature behaviour of the critical section is followed piece-wise.

Lateral load versus lateral displacement behaviour of cantilever members can also be determined by specifying the distance from the critical maximum moment section to the free end, and parameters governing shear deformations along the member. Only moment-curvature behaviour was of interest in this study.

Reversed cyclic loading histories could be simulated by specifying the required maximum curvature at the peak of successive loading cycles. Cyclic moment curvature analyses can give realistic predictions of strength and stiffness degradation which might be observed from experimental tests.

An energy balance method is incorporated in the program to calculate the strain energy stored in the critical hoop tie leg. By comparing this with the estimated strain energy capacity of the tie it is possible to predict the occurrence of hoop fracture, considered to mark the end of useful load carrying capacity of the member. Initially it is assumed that the strain energy absorbed by the member is stored in the concrete. Strain energy in excess of the capacity of the unconfined concrete is subsequently assumed to be stored in the transverse confining reinforcement. Half of the strain energy increase at each curvature increment is assumed to be stored in the hoop legs in each of the transverse directions. Hoop fracture is predicted when the strain energy accumulated in the hoops exceeds the expected fracture energy.

Although the program had features for adjusting material behaviour for dynamic loading rates, they were not used in this study.

7.4 RANGE OF VARIABLES CONSIDERED

Variables expected to have a significant influence on the moment-curvature response were: - axial load level, transverse confining stress, longitudinal reinforcement content and yield stress, concrete strength, cover concrete thickness, spacing of longitudinal bars, and number of loading cycles sustained. The variables used and the ranges over which they were considered are shown in Table 7.1.

Table 7.1 Variables Investigated in Study of Theoretical Strength and Ductility of Concrete Tubular Columns

Variable		Description	Range Investigated
1	$P_e / f_c' A_g$	External Axial Load Level	0. → 0.7 Compression
2	f_l / f_c'	Transverse Confining Stress Ratio	0.05 → 0.15
3	$\rho f_y / f_c'$	Longitudinal Reinforcement Index	0.02 → 0.3
4	f_y	Longitudinal Reinforcement Yield Stress	250 MPa → 450 MPa
5	f_c'	Concrete Compressive Cylinder Strength	30 MPa → 70 MPa
6	c /t	Cover to Wall Thickness Ratio	0.02 → 0.10
7	$P_{ps} / f_c' A_g$	Axial Prestress Stress	0. → 0.3

Axial load level was expected to have a major effect on moment-curvature behaviour and available ultimate curvature. The study considered axial load levels between zero and $0.7 f_c' A_g$ compression, where f_c' is the unconfined concrete compressive cylinder strength and A_g is the gross area of the cross-section. The upper limit is approximately the maximum axial load level allowed by design codes. Axial tension loads were not investigated as the computer program could not cope with that case in its present form. It was expected that moment-curvature response of members subject to axial tensions would be dominated by the behaviour of the longitudinal reinforcement and large ultimate curvatures could normally be sustained.

The amount of transverse confining reinforcement was also expected to be very important. Quantities of transverse confining reinforcement were not specified directly in this study. The variable chosen was f_l/f_c', the ratio of the transverse confining stress f_l to the unconfined compressive cylinder strength of the concrete f_c'. Confining stress ratios between 0.02 and 0.15 were considered.

Strain energy capacity of transverse hoop reinforcement was directly proportional to the transverse confining stress ratio. In accordance with findings by Mander et al [7.1], it was assumed that the strain energy at fracture was approximately 105 MJ/m^3, which is appropriate for typical New Zealand reinforcing steels. No variation of this value was considered.

A longitudinal reinforcement index was specified by the variable $\rho f_y/f_c'$ where ρ = volumetric content of longitudinal reinforcement and f_y = longitudinal reinforcement yield stress. This parameter was expected to be more appropriate than simply using the volumetric steel content. A range of values of the variable $\rho f_y/f_c'$ between 0.02 and 0.3 was considered.

Longitudinal reinforcement yield stresses between 250 MPa and 450 MPa and concrete compressive cylinder strengths between 30 MPa and 70 MPa were considered.

For sections containing relatively few large diameter longitudinal bars the critical hoop leg receives a somewhat higher proportion of the strain energy absorbed by the longitudinal reinforcement. For this reason sections with different numbers of longitudinal bars were considered. In the large members used in offshore concrete platform structures this effect is unlikely to be significant as there would normally be a very large number of longitudinal bars present.

Ratios of concrete cover thickness to member wall thickness (c/t) between 0.02 and 0.15 were considered. Typical offshore platform members would have wall thicknesses (t) of about 1 m and concrete cover thicknesses (c) of about 75 mm thus giving a ratio $c/t = 0.075$.

The available ultimate curvature results presented in this chapter are based on cyclic moment-curvature analyses of sections undergoing four complete loading cycles to equal positive and negative curvatures. This is consistent with performance criteria suggested by the New Zealand Loadings Code NZS 4203 [7.4]. The results are compared for a limited number of cases with those where only two complete cycles or one half cycle (monotonic loading) were required to be sustained.

Information regarding the stress-strain behaviour of concrete and longitudinal reinforcement assumed in the analyses is discussed in more detail in Section 7.7 and the control parameters required as input are given in Tables 7.2 to 7.4.

This study also investigated the moment-curvature behaviour of partially prestressed concrete tubular members. Levels of axial prestress stress were considered between zero (reinforced concrete) and $0.3\ f_c'$.

Most of the analyses carried out in this work were for hollow circular concrete members with outside diameter to wall thickness ratios (D/t) equal to 20. It was expected that the diameter to wall thickness ratio would have only a small influence on both yield curvature and available ultimate curvature. A small number of analyses were carried out for sections with D/t ratios equal to 5.0 to confirm that the results were not significantly changed.

7.5 ULTIMATE CURVATURE CRITERIA

Three criteria were chosen to determine the available ultimate curvature, marking the end of useful load-carrying capacity. The first criterion was based on the important result found from the experimental study, reported in Chapter 6, that sudden failures of these thin walled members occurred if the peak of the moment-curvature curve was exceeded at the critical section. In the analyses it was deemed that the ultimate curvature had been reached if the moment of resistance of the section started reducing on any of the cycles of loading. Previous studies [7.6] have assumed that useful capacity can be obtained from the falling branch of the moment-curvature response curve but the experimental results of Chapter 6 indicate that this is not appropriate for thin-walled members. The second criterion for ultimate curvature used

was the prediction of transverse hoop fracture and the third criterion was elongation capacity of the longitudinal reinforcement being exceeded.

Mander's computer program was modified to automatically calculate the proportion of internal work done on each concrete strip and area of longitudinal reinforcement which would contribute strain energy to the critical hoop leg. The analysis was terminated if the strain energy capacity of the tie leg was exceeded.

The energy balance theory developed by Mander was based on uniaxial compression tests of short circular, square and rectangular concrete column members. The theory predicted the occurrence of hoop fractures in these test specimens quite accurately. The method has also been used to predict hoop fractures in solid reinforced concrete members tested under axial load and flexure. For these members the method predicts hoop fractures much earlier than was observed in the tests. Other researchers [7.6] have found it necessary to artificially increase the strain energy capacity of the hoops by a factor of approximately 2.0 to get reasonable predictions. It has been suggested by Zahn [7.6] that the presence of a strain gradient across the section due to flexure results in more favourable confinement conditions in the concrete core of the section and less strain energy input to the critical transverse hoop leg.

For the hollow circular tube sections of interest in this study the critical transverse hoop leg was the one through the thickness of the tube wall at the extreme compression side of the section. The strain gradient effect was not expected to be as important in these sections as the longitudinal compression strains would be more nearly uniform over the thickness of the tube wall. The strain energy capacity was not increased as had been found necessary for solid members. It should be noted that if there is a strain gradient effect in these members, the results obtained by not increasing the strain energy capacity, are conservative.

The third criterion for available ultimate curvature was the exceedance of elongation capacity of the longitudinal reinforcement. For most non-prestressed reinforcement fracture strains would be considerably in excess of 10 percent. For prestressing tendons fracture strains of between 5 percent and 10 percent would be usual. For circular tube sections containing a large number of longitudinal bars distributed around the circumference, fracture of the extreme tension reinforcement does not result in drastic loss of moment resistance from the section. This was observed in the experimental tests reported in Chapter 6. However, fracture of the longitudinal reinforcement represents the onset of failure and is a reasonable criterion for available ultimate curvature. Ultimate curvatures corresponding to a range of elongations in the longitudinal reinforcement were noted.

7.6 IDEAL MOMENT CAPACITY AND YIELD CURVATURE

The ACI flexural strength method [7.2], also incorporated in the New Zealand Concrete Design Code NZS 3101 [7.3], is based on an assumed extreme fibre compression strain of 0.003 and ACI stress-block parameters. Results of experimental testing and theoretical moment-curvature analyses have indicated that this is reasonable for members with low levels of applied axial load but quite conservative for members with moderate to high levels of axial load. Moment-curvature analyses have shown that moments of resistance of up to twice that given by the ACI method could be mobilized by members with high levels of axial load.

The effect is due to the enhanced strength of the concrete above the confined value in the compression zone of the section. Moment-curvature analyses using realistic stress-strain models for confined concrete can closely predict the experimentally observed strength gains.

For members carrying moderate to high levels of axial load a larger proportion of the flexural strength is contributed by the internal concrete forces than for members with only light axial loads. It follows that the enhanced concrete strength due to the confining action of any transverse reinforcement which is present will have a more significant effect on the overall moment of resistance of the section. Substantial economies are available if flexural strength estimates are based on the likely confined stress-strain behaviour of the concrete, rather than on the assumption that only unconfined strength is available.

In order to quantify the useful increase in moment of resistance it was necessary to choose suitable criteria for defining the ideal moment capacity. Experimental studies have shown [7.7] that extreme fibre strains considerably higher than the 0.003 assumed by the ACI strength method can be sustained before crushing or spalling of the unconfined cover concrete occurs. Much higher strains can be sustained by the confined concrete in the core of the section. A more realistic estimate of the maximum sustainable compression strain in the cover concrete would be 0.005. However, it was found that for sections with low axial load levels substantial curvatures were required to induce extreme fibre strains of this magnitude. It was found that for high axial load levels extreme fibre strains of 0.005 corresponded to curvatures of approximately 5 times the yield curvature.

Care must be exercised in interpreting what is meant by the term "yield curvature". In some cases it is taken to mean the curvature at first yield of reinforcement in a section. Mander et al [7.1] proposed that first-yield curvature in a section be calculated as the curvature at which either any longitudinal reinforcement reached yield strain or the extreme compression fibre concrete reached a strain of 0.002, the expected peak in the unconfined stress-strain curve. The moment of resistance corresponding to this curvature was called the "first-yield moment". Yield curvature was then defined as the first-yield curvature scaled by the ratio of the ideal moment of resistance using the ACI method to the first-yield moment.

A recent study of the strength and ductility of solid members by Zahn [7.6] suggested new definitions for the yield curvature and ideal moment capacity to allow for the expected enhancement of flexural strength above the ACI method predictions. Although this definition was arbitrary it has been used for consistency in this study also. The definitions are illustrated for a typical moment-curvature curve expected for a hollow circular member in Fig. 7.1. The actual moment-curvature behaviour is idealised as elasto-plastic with the initial elastic portion passing through the point where first-yield occurs. The first-yield moment M_y and curvature ϕ_y' are defined exactly as by Mander above. The ideal moment capacity M_i is taken as the maximum moment of resistance attained before the curvature exceeds five times the yield curvature. The yield curvature ϕ_y is found by scaling the first-yield curvature ϕ_y' by the ratio of the ideal moment capacity M_i to the first-yield moment M_y as shown in Fig. 7.1. While this definition may seem rather circular, with both of the unknown quantities being mutually dependent, it is a simple matter to find both from the calculated moment-curvature response.

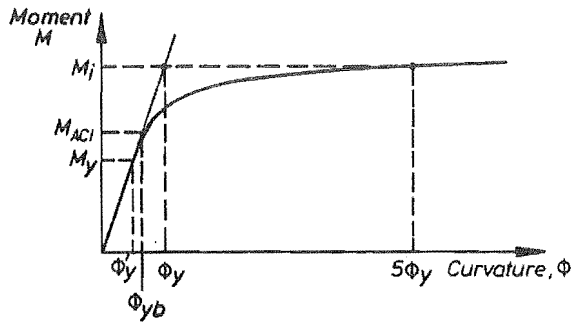

Fig. 7.1 Typical Moment-Curvature Behaviour

7.7 STRESS - STRAIN MODELS FOR CONCRETE AND REINFORCING STEELS

The stress-strain models for confined concrete and non-prestressed reinforcement used in this study were developed by Mander et al [7.1] and incorporated in the moment-curvature analysis computer program. The models are used to predict the stresses resulting from an arbitrary applied strain history, and allow for effects of reversed cyclic loading. The monotonic loading curves for tension and compression envelope the behaviour predicted for

cyclic loading. The models have been found [7.1] to give good agreement with experimentally measured uniaxial stress-strain response.

7.7.1 Stress - Strain Model for Confined Concrete

7.7.1.1 Control Parameters

Fig. 7.2 shows the monotonic stress-strain behaviour for unconfined and confined concrete. It was necessary to input the following parameters to the computer program to control the stress-strain behaviour.

For unconfined concrete:

f_c' = unconfined compressive cylinder strength
f_t' = concrete tensile strength
E_c = initial tangent modulus of elasticity = $5000\sqrt{f_c'}$ in MPa units
ε_{co} = strain at unconfined strength f_c'
ε_{spall} = strain at which unconfined cover concrete spalls

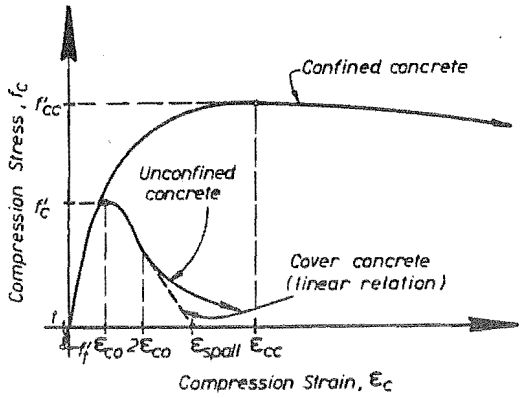

Fig. 7.2 Monotonic Stress-Strain Behaviour of Concrete

For confined concrete:

f_{cc}' = peak strength of confined concrete
ε_{cc} = strain at confined strength f_{cc}'
ε_{cu} = ultimate strain sustainable

The standard values of these parameters assumed in the analyses are given in Table 7.2.

7.7.1.2 Monotonic Loading Behaviour

Monotonic Compression Loading:

The monotonic envelope stress-strain relation in compression for confined concrete is given by Eqn 7.1.

$$f_c = f_{cc}' x\, r / (r - 1 + x^r) \qquad (7.1)$$

where f_c = concrete stress
$x = \varepsilon / \varepsilon_{cc}$

Table 7.2 Concrete Stress-Strain Behaviour - Analysis Input Data

Parameter	Description	Value
Unconfined Concrete Parameters		
f_c'	= Compressive cylinder strength	50 MPa
ε_{co}	= Strain at peak stress	0.002
E_c	= Initial Young's modulus	$5000\sqrt{f_c'}$
f_t'	= Tensile strength	$0.6\sqrt{f_c'}$
ε_{spall}	= Strain at which unconfined cover spalls	0.004
Confined Concrete Parameters		
f_{cc}'	= Confined peak stress	Variable
ε_{cc}	= Strain at peak stress	ε_{co} $[(1+5(f_{cc}'/f_c'-1)]$
ε_{cu}	= Ultimate strain capacity	Large

ε = concrete compression strain
r = $E_c / (E_c - E_{sec})$
E_{sec} = secant modulus = f_{cc}'/ε_{cc}

For unconfined concrete the same equation is used but the parameters f_{cc}' and ε_{cc} are replaced by f_c' and ε_{co}. The falling branch of the stress-strain curve for the unconfined cover concrete for strains ε greater than $2\varepsilon_{co}$ is taken as a straight line reducing to zero stress at the spalling strain ε_{spall}.

Monotonic Tension Loading:

The tension strength f_t' was input by the user. The New Zealand Concrete Design Code NZS 3101 [7.3] suggests that f_t' can be determined from the unconfined cylinder compressive strength f_c' by the expression in Eqn. 7.2.

$$f_t' = 0.6\sqrt{f_c'} \qquad (f_t' \text{ and } f_c' \text{ in MPa units}) \qquad (7.2)$$

The stress-strain behaviour in tension is assumed to be elastic until the tensile strength f_t' is exceeded, as given by Eqns. 7.3 and 7.4.

$$f_c = E_c \varepsilon \qquad \text{for} \quad f_c < f_t' \qquad (7.3)$$

$$f_c = \text{zero} \qquad f_c \geq f_t' \qquad (7.4)$$

Determination of Confined Strength f_{cc}':

The peak strength f_{cc}' of confined concrete which can be mobilized in the longitudinal direction is dependent on the confining stresses f_{l1} and f_{l2} provided by transverse

reinforcement in the two transverse directions . The confining stress ratios f_{l1}/f_c' and f_{l2}/f_c' are calculated and the confined strength ratio f_{cc}'/f_c' can be found from Fig. 7.3.

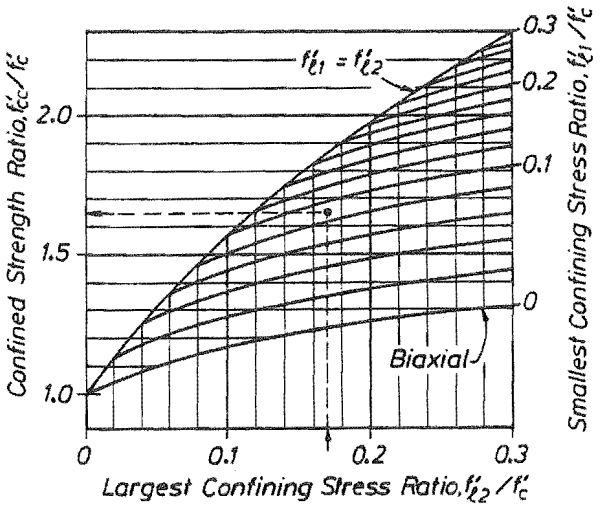

Fig. 7.3 Determination of Confined Strength Ratio f_{cc}'/f_c'

Determination of Strain ε_{cc} at Confined Strength:

The strain ε_{cc} at the confined strength f_{cc}' can be found using the expression in Eqn. 7.5.

$$\varepsilon_{cc} = \varepsilon_{co}\,[\,1 + R(\,f_{cc}'/f_c' - 1\,)\,] \qquad (7.5)$$

The parameter R has been found to be approximately constant by previous researchers but values between about 3. and 10. have been suggested. In line with Mander's recommendations a constant value of R = 5. was used in this study. The strain ε_{co} corresponding to the unconfined strength f_c' was assumed to be equal to 0.002 for all concrete strengths considered. This value of ε_{co} is commonly used for normal strength concretes but recent Norwegian data [7.8] suggests that this is appropriate for high strength concretes also.

7.7.1.3 Cyclic Loading Behaviour

Initial loading is assumed to traverse along the envelope stress-strain curves. Different behaviour is assumed for unloading from either the compression or tension envelope curves.

Compression Unloading:

Behaviour on unloading from the compression envelope curve is shown diagrammatically in Fig. 7.4. Unloading is assumed to take place from a strain, stress coordinate $(\varepsilon_{un}, f_{un})$. The tangent modulus at the start of unloading E_u is assumed to be given by Eqn. 7.6.

$$E_u = b\,c\,E_c \qquad (7.6)$$

where $b = f_{un}/f_c'$ but $b \geq 1$ (7.7)

$c = (\varepsilon_{cc}/\varepsilon_{un})^{0.5}$ but $c \leq 1$ (7.8)

E_c = initial tangent modulus

The stress-strain relation is given by Eqn. 7.9.

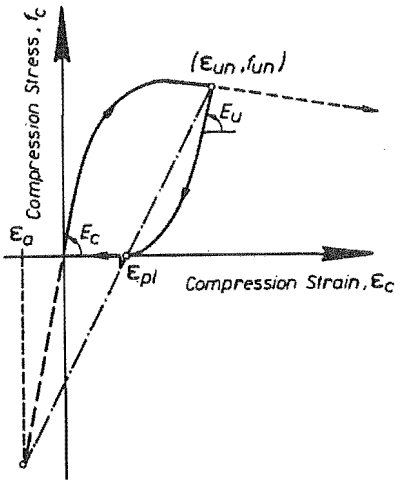

Fig. 7.4 Behaviour on Unloading from Compression Envelope

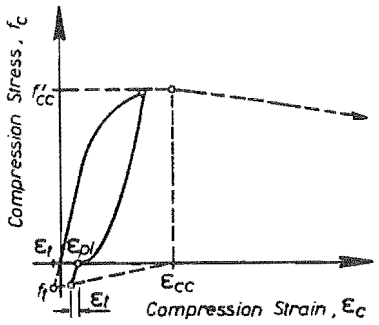

Fig. 7.5 Assumed Deterioration of Tensile Strength Due to Previous Compressive Straining

$$f_c = f_{un} - f_{un} \times r / (r - 1 + x^r) \quad (7.9)$$

where $r = E_c / (E_c - E_{sec})$ (7.10)

$E_{sec} = f_{un} / (\varepsilon_{un} - \varepsilon_{pl})$ (7.11)

$\varepsilon_{pl} = \varepsilon_{un} - (\varepsilon_{un} + \varepsilon_a) / (1 + E_c \varepsilon_a / f_{un})$ = plastic strain (7.12)

$\varepsilon_a = a (\varepsilon_{un} \varepsilon_{cc})^{0.5}$ = common strain (7.13)

$a = \varepsilon_{cc} / (\varepsilon_{cc} + \varepsilon_{un})$ or $0.09 \varepsilon_{un} / \varepsilon_{cc}$ whichever is greater (7.14)

$x = (\varepsilon - \varepsilon_{un}) / (\varepsilon_{pl} - \varepsilon_{un})$ (7.15)

Tensile Unloading:

Tensile strength is assumed to deteriorate depending on the magnitude of previous compressive straining, as shown in Fig. 7.5. On unloading from compression the tensile strength is assumed to be given by the expression in Eqn. 7.16.

$$f_t = f_t' (1 - \varepsilon_{pl} / \varepsilon_{cc}) \quad \text{for } \varepsilon_{cc} > \varepsilon_{pl}$$

$$= \text{zero} \quad \text{for } \varepsilon_{cc} < \varepsilon_{pl} \quad (7.16)$$

The stress-strain relation is given by Eqn. 7.17.

$$f_c = E_t (\varepsilon - \varepsilon_{pl}) \quad (7.17)$$

where $E_t = f_t / \varepsilon_t$ (7.18)

$\varepsilon_t = f_t' / E_t$ (7.19)

After the cracking strain has been exceeded, $\varepsilon > (\varepsilon_t - \varepsilon_{pl})$, the tensile strength is assumed to be zero.

Reloading Behaviour:

Fig. 7.6 illustrates situations where reloading may occur from either the compression unloading curve or the tension unloading curve after cracking. Reloading is assumed to occur from a strain, stress coordinate (ε_{ro} , f_{ro}) and the stress-strain relation is assumed to be linear as the previous compression loading curve is approached. The stress at the previous unloading strain ε_{un} is reduced from f_{un} to f_{new} , as given by Eqn. 7.20 to allow for degradation effects due to load cycling.

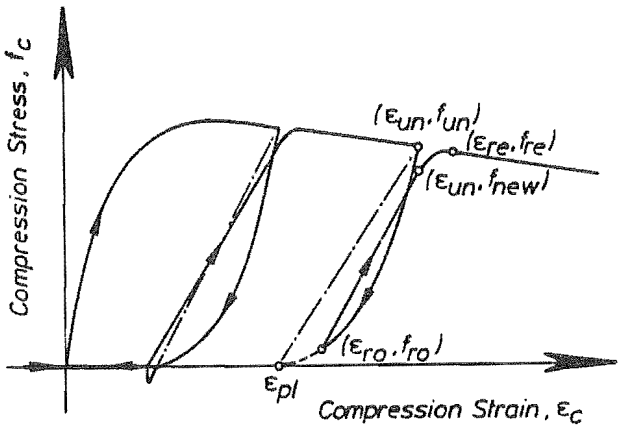

Fig. 7.6 Reloading Behaviour

$$f_{new} = 0.92\, f_{un} + 0.08\, f_{ro} \tag{7.20}$$

The linear stress-strain relation relation is given by Eqn. 7.21.

$$f_c = f_{ro} + E_r\,(\varepsilon - \varepsilon_{ro}) \tag{7.21}$$

where $$E_r = (f_{new} - f_{ro}) / (\varepsilon_{un} - \varepsilon_{ro}) \tag{7.22}$$

A parabolic transition is then used to intersect the monotonic compression curve at a return coordinate (ε_{re} , f_{re}) where ε_{re} is given by Eqn. 7.23 and f_{re} is given by the expression for the monotonic compression curve in Eqn. 7.1.

$$\varepsilon_{re} = \varepsilon_{un} + (f_{un} - f_{new}) / [E_r\,(2 + f_{cc}'/f_c')] \tag{7.23}$$

The parabolic stress-strain relation is given by Eqn. 7.24.

$$f_c = f_{re} + E_{re}\,x + Ax^2 \tag{7.24}$$

where $$x = \varepsilon - \varepsilon_{re} \tag{7.25}$$

$$A = (E_{re} - E_r) / 4\,[(f_{new} - f_{re}) - E_r\,(\varepsilon_{un} - \varepsilon_{re})] \tag{7.26}$$

E_{re} is the tangent modulus at the return coordinate determined from the monotonic equation (Eqn. 7.1).

7.7.2 Stress - Strain Model for Reinforcing Steel

7.7.2.1 Monotonic stress-strain Behaviour

The assumed monotonic stress-strain behaviour for reinforcing steel is illustrated in Fig. 7.7. The application of the model in the computer analysis program requires the following parameters governing the monotonic stress-strain behaviour to be input by the user for both tension and compression loading cases: -

f_y = yield stress
f_{su} = ultimate steel stress
ε_{sh} = strain at commencement of strain hardening
ε_{su} = strain at ultimate stress
E_s = elastic Young's modulus
E_{sh} = modulus at beginning of strain hardened branch of curve

The standard values of these parameters assumed in the analyses are given in Table 7.3. The stress-strain relations are then given by Eqns. 7.27, 7.28 and 7.29 for loading on the initial elastic line, yield plateau, and on the strain hardened curve respectively.

$$f_s = E_s \varepsilon_s \qquad \text{where} \quad 0 < \varepsilon_s < \varepsilon_y \qquad (7.27)$$

$$f_s = f_y \qquad \text{where} \quad \varepsilon_y < \varepsilon_s < \varepsilon_{sh} \qquad (7.28)$$

$$f_s = f_{su} + (f_y - f_{su}) \left| (\varepsilon_{su} - \varepsilon_s)/(\varepsilon_{su} - \varepsilon_{sh}) \right|^P \qquad \text{where} \quad \varepsilon_{sh} < \varepsilon_s < \varepsilon_{su} \qquad (7.29)$$

where f_s = steel stress
ε_s = steel strain
ε_y = yield strain = f_y / E_s
$|\ |$ = absolute value of enclosed term

and P = strain hardening exponent = $E_{sh} (\varepsilon_{su} - \varepsilon_{sh}) / (f_{su} - f_y)$ (7.30)

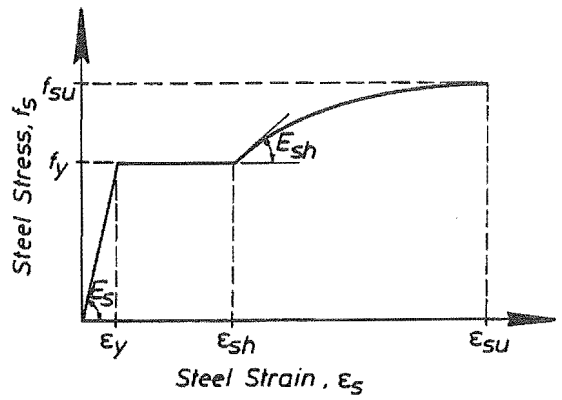

Fig. 7.7 Monotonic Stress-Strain Behaviour of Reinforcing Steel

Table 7.3 Non-Prestressed Longitudinal Reinforcement Stress-Strain Behaviour - Analysis Input Data

Parameter	Description	Value
Tension and compression behaviour identical		
f_y	= Yield stress	350 MPa
f_u	= Ultimate stress	500 MPa
E_s	= Young's modulus	200 000 MPa
E_{sh}	= Initial modulus of strain hardened branch	5000 MPa
ε_{sh}	= Strain at start of strain hardening	0.015
ε_{su}	= Strain at ultimate stress	0.10

7.7.2.2 Cyclic Loading Behaviour

On load reversal from coordinate (ε_o , f_o) on the monotonic curve a softened curve is followed due to Bauschinger effects as illustrated in Fig. 7.8. The monotonic or "skeleton" curve is shifted to a new coordinate origin at $(\varepsilon_{mo} , 0)$ where ε_{mo} is a function of the plastic deformation history as given by Eqn. 7.31.

$$\varepsilon_{mo} = \varepsilon_o - f_o / E_s + \varepsilon_{shift} \tag{7.31}$$

where ε_{shift} = zero for $|\varepsilon_s| < |\varepsilon_{sh}|$ (7.32)

or $\varepsilon_{shift} = \varepsilon_{ss} |\varepsilon_{ss} / \varepsilon_{su}| + 2.0 f_y / E_s$ for $|\varepsilon_s| \geq |\varepsilon_{sh}|$ (7.33)

ε_{ss} is the skeleton strain from the previous cycle, as shown in Fig. 7.8.

The softened branch of the reversed curve merges with the shifted monotonic curve from the previous cycle at coordinates (ε_b , f_b). When reversal is from the yield plateau, as shown by the coordinates $(\varepsilon_o^- , f_o^-)$ in Fig. 7.8 (negative superscripts indicating compression say), then ε_b and f_b are given by Eqns. 7.34 and 7.35.

$$\varepsilon_b = \varepsilon_{mo}^+ - \varepsilon_{ss}^- \tag{7.34}$$

$$f_b = f_y \tag{7.35}$$

When reversal takes place from the strain hardened skeleton curve then ε_b and f_b are given by Eqns. 7.36 and 7.37.

$$\varepsilon_b^+ = \varepsilon_{mo}^+ - \varepsilon_{ss}^- \tag{7.36}$$

$$f_b^+ = f_{su}^+ + (f_y^+ - f_{su}^+) \left| (\varepsilon_{su}^+ + \varepsilon_{ss}^-)/(\varepsilon_{su}^+ - \varepsilon_{sh}^+) \right|^P \tag{7.37}$$

The superscript positive and negative signs would be interchanged for either tension (+) or compression (-) reversals.

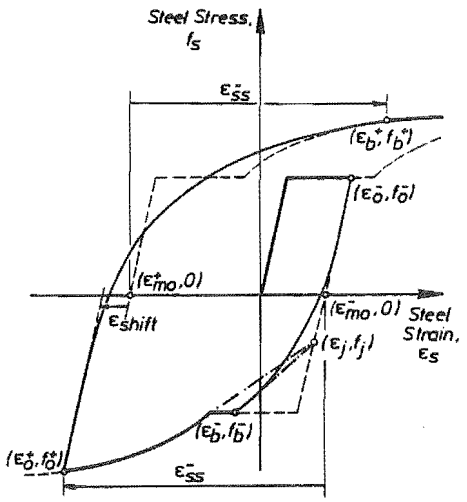

Fig. 7.8 Behaviour on Load Reversal from Skeleton Branch

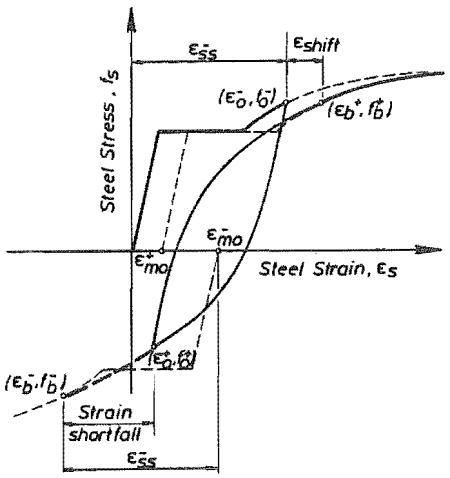

Fig. 7.9 Behaviour on Reversal from a Softened Branch

Reversal may occur from a softened branch before merging with the skeleton curve has occurred, as illustrated in Fig. 7.9. The junction coordinates (ε_b , f_b) are then determined from Eqns. 7.38 and 7.39.

$$\varepsilon_b = \varepsilon_{max} + \varepsilon_{shift} \tag{7.38}$$

$$f_b = f_{max} \tag{7.39}$$

where $(\varepsilon_{max} , f_{max})$ is the previous maximum stress coordinate and f_{max} is the greater of the maximum previous reversal point stress f_o^- and the last junction point stress f_b.

For reversal from the yield plateau ε_{shift} is given by Eqn. 7.40 or 7. 41.

$$\varepsilon_{shift}^+ = \varepsilon_{su}^+ (\varepsilon_o^+ - \varepsilon_b^-) \tag{7.40}$$

$$\varepsilon_{shift}^- = \varepsilon_{su}^- (\varepsilon_o^- - \varepsilon_b^+) \tag{7.41}$$

And for reversal from the strain hardened branch ε_{shift} is given by Eqn. 7.42 or 7. 43.

$$\varepsilon_{shift}^+ = \varepsilon_{su}^+ (\varepsilon_o^+ - \varepsilon_b^-) - 0.5 f_y^+ / E_s^+ \tag{7.42}$$

$$\varepsilon_{shift}^- = \varepsilon_{su}^- (\varepsilon_o^- - \varepsilon_b^+) - 0.5 f_y^- / E_s^- \tag{7.43}$$

The stress-strain relation on the softened branch between the reversal coordinates (ε_o , f_o) and the junction coordinates (ε_b , f_b) is given by Eqn. 7.44.

$$f_s = f_o + (\varepsilon_s - \varepsilon_o) E_m [Q + (1 - Q) / (1 + | E_m (\varepsilon_s - \varepsilon_o) / (f_{ch} - f_o) |)^{1/R}] \tag{7.44}$$

where E_m = a modified initial modulus of elasticity chosen so that the stress-strain curve passes through a fictitious yield coordinate $(\varepsilon_o + \varepsilon_y , f_o + f_y)$

f_{ch} = a characteristic stress (usually $f_y < f_{ch} < f_b$)

Q = ratio of final tangent slope to initial tangent slope
R = a Ramberg-Osgood parameter governing the curvature between the initial tangent slope and the final tangent slope. For R large the curve approaches bilinear and for R small (R=1) the curve is hyperbolic.

The parameters Q, R, f_{ch} and E_m are determined iteratively in the model, as discussed by Mander et al [7.1].

7.7.3 Stress-Strain Model for Prestressing Tendons

The stress-strain model used for high tensile prestressing tendons was that proposed by Thompson [7.9]. The computer program developed by Mander for reinforced concrete columns was extended to include the possibility of prestressing tendons being present in the section. A subroutine written originally by Thompson was adapted for tracking the stress-strain behaviour of the tendons.

7.7.3.1 Monotonic Stress-Strain Behaviour

A monotonic stress-strain relation is assumed to form an envelope for repeated loadings of the same sign and is illustrated in Fig. 7.10. The curve is defined piece-wise as an initial linear portion, a hyperbolic curved portion, and an upper linear branch. The following input data is required to describe the monotonic stress-strain behaviour of the tendons: -

ε_{pa} = strain at limit of proportionality
ε_{pb} = strain at beginning of upper linear branch
ε_{pu} = ultimate strain
f_{pa} = stress corresponding to ε_{pa}
f_{pb} = stress corresponding to ε_{pb}
f_{pu} = ultimate stress at strain ε_{pu}
f_{pi} = initial tendon stress after losses

The standard values of these parameters assumed in the analyses are given in Table 7.4. The stress-strain relations corresponding to the monotonic loading curve in Fig. 7.10 are defined piece-wise by Eqns. 7. 45 to 7.47.

$$f_p = \varepsilon_p E_p \qquad \text{for } \varepsilon_p \le \varepsilon_{pa} \qquad (7.45)$$

$$f_p = (f_{pb}\varepsilon_{pb} - f_{pa}\varepsilon_{pa})/(\varepsilon_{pb} - \varepsilon_{pa}) + \varepsilon_{pa}\varepsilon_{pb}\,(f_{pa} - f_{pb})/\varepsilon_p(\varepsilon_{pb} - \varepsilon_{pa})$$

$$\text{for } \varepsilon_{pa} < \varepsilon_p \le \varepsilon_{pb} \qquad (7.46)$$

$$f_p = f_{pb} + (f_{pu} - f_{pb})\,(\varepsilon_p - \varepsilon_{pb})/(\varepsilon_{pu} - \varepsilon_{pb}) \qquad \text{for } \varepsilon_{pb} < \varepsilon_p \le \varepsilon_{pu} \qquad (7.47)$$

where ε_p = tendon strain
f_p = tendon stress
E_p = initial Young's modulus = f_{pa}/ε_{pa}

7.7.3.2 Cyclic Loading Behaviour

Load reversal in the elastic range will be governed by Eqn. 7.45. For load reversal in the inelastic range the stress-strain behaviour is illustrated in Fig. 7.11. (ε_o , f_o) are the coordinates of the reversal point. Unloading will occur along a curve with initial slope $\text{ø}\, E_p$, where ø is a modification factor to allow for softening effects which occur with increasing levels of strain. The stress-strain relationship is obtained from Eqn. 7.48.

Table 7.4 Prestressed Longitudinal Reinforcement
Stress-Strain Behaviour - Analysis Input Data

Parameter	Description	Value
Tension and compression behaviour identical		
f_{pa}	= Stress at limit of proportionality	1200 MPa
f_{pb}	= Stress at start of upper straight branch	1600 MPa
f_{pu}	= Ultimate stress	1800 MPa
ε_{pa}	= Strain at limit of proportionality	0.006
ε_{pb}	= Strain at start of upper straight branch	0.014
ε_{pu}	= Ultimate strain	0.06
f_{pi}	= Initial tendon stress after losses	1200 MPa

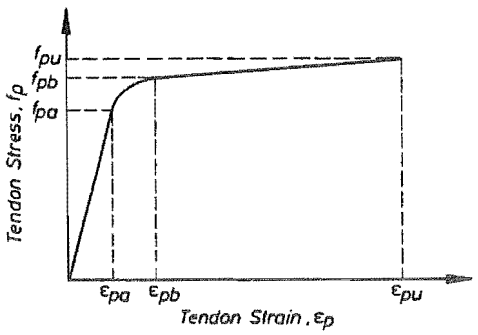

Fig. 7.10 Monotonic Stress-Strain Behaviour of Prestressing Tendon

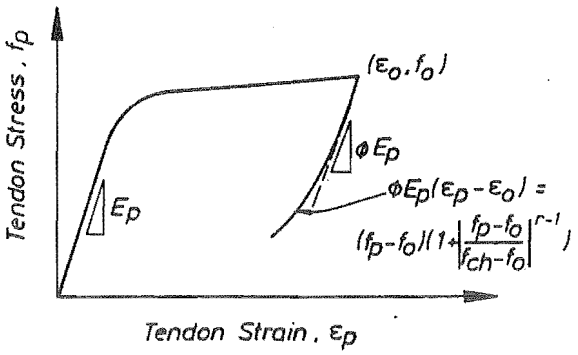

Fig. 7.11 Load Reversal in the Inelastic Range

$$(\varepsilon_p - \varepsilon_o)\, \text{ø}\, E_p = (f_p - f_o)\,[\,1 + \{\,(f_p - f_o)/(f_{ch} - f_o)\,\}^{r-1}\,] \qquad (7.48)$$

where $\text{ø} = 58.27\,\varepsilon_m^2 - 7.506\,\varepsilon_m + 1.043$ but $\text{ø} < 1.0$ (7.49)

ε_m = current value of maximum imposed strain

The stress-strain envelope for reversed loading is taken as the original monotonic envelope shifted along the strain axis as is shown in Fig. 7.12. The origin of the envelope is taken at coordinates (ε_{zmx} , 0) for tensile loading and (ε_{zmn} , 0) for compressive loading. ε_{zmx} is the maximum tensile value of the residual strain ε_{zero} which would be the strain at zero stress if the tendon unloaded with modulus equal to the initial Young's modulus. Similarly ε_{zmn} is the maximum compressive value of ε_{zero} .

The parameter f_{ch}, given by Eqn. 7. 50, is a characteristic stress and r, given by Eqn. 7.51, is a Ramberg-Osgood exponent.

$$f_{ch} = \text{ø}\, E_p\, U\,(\varepsilon_{pb} + \varepsilon_o - \varepsilon_{zmx} - f_{pb}/U - 2f_o/\text{ø}E_p)\,/\,(\text{ø}E_p - U) \qquad (7.50)$$

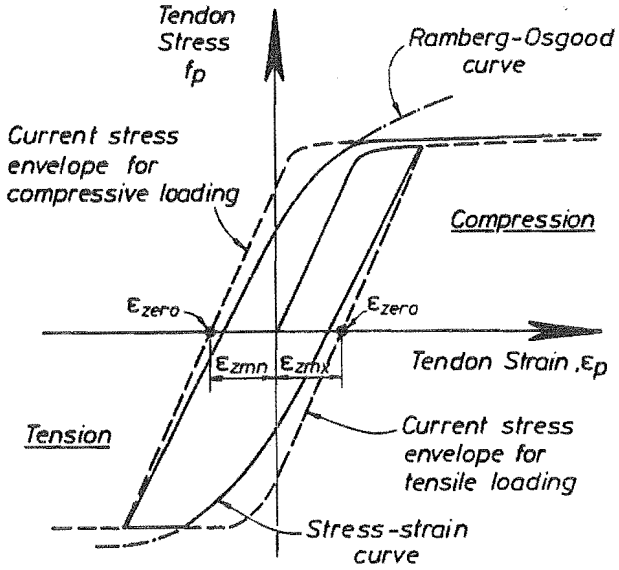

Fig. 7.12 Shifted Envelope for Load Reversal Behaviour

$$r = 57.883 - 59116\,\varepsilon_{pl} \qquad \text{but} \qquad r > 20 \tag{7.51}$$

For compressive unloading these parameters are found using Eqns. 7.52 and 7.53.

$$f_{ch} = \varnothing E_p\, U\,(-\varepsilon_{pb} + \varepsilon_o - \varepsilon_{zmn} + f_{pb}/U - 2f_o/\varnothing E_p)\,/\,(\varnothing E_p - U) \tag{7.52}$$

$$r = 5.003 - 194.5\,\varepsilon_{pl} \tag{7.53}$$

where ε_{pl} = plastic strain on the previous cycle

$$U = (f_{pu} - f_{pb})\,/\,(\varepsilon_{pu} - \varepsilon_{pb}) \tag{7.54}$$

Where the plastic strain in the previous cycle ε_{pl} is less than 0.001 for tensile loading or 0.0003 for compressive loading, the previous loading curve in that direction is followed once it is reached. Also, the tendon stress f_p cannot exceed the monotonic curve value (refer Fig. 7.10).

A typical example of stress-strain response for prestressing tendons obtained from the model is shown in Fig. 7.13.

7.8 RESULTS OF MOMENT - CURVATURE ANALYSES

7.8.1 General Results

Approximately 150 separate moment-curvature analyses were carried out to provide the results which are presented in this chapter. Although this did not allow every possible combination of variables to be considered, it did enable the important trends to be identified. The most influential variables were found to be the axial load level and the transverse confining stress ratio. The results are generally based on average values of the other variables, which were found to have less effect on the moment-curvature response. The effects of varying these less important variables were adequately dealt with by examining the trends observed from the results.

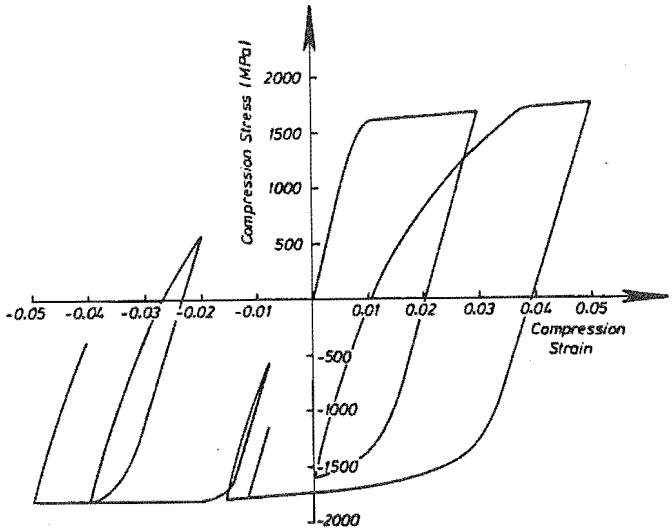

Fig. 7.13 Typical Stress-Strain Response of 7 mm Solid Wire Prestressing Tendon

From each section analysis the predicted moment versus curvature behaviour was plotted. Typical shapes of the hysteresis loops obtained for various combinations of axial load and transverse confining stress are shown in Figs. 7.14 to 7.17.

In Fig. 7.14 typical moment-curvature hysteresis loops are shown for a section with low axial load and low transverse confining stress. On the vertical axis the parameter M/M_{ACI} represents the ratio of the moment of resistance to the ideal flexural strength calculated using the ACI section analysis method. On the horizontal axis is shown the curvature ductility factor imposed on the section. In the initial loading cycle the section attains the ACI ideal flexural strength at a curvature ductility of about 2.0 after which the moment of resistance stays approximately constant until a curvature ductility of approximately 7.0 is reached. Some additional strength is mobilized as larger curvatures are imposed due to the effects of concrete confinement and strain hardening of the longitudinal reinforcement. When the loading is reversed very similar behaviour is predicted. For the second and subsequent cycles of loading the flexural stiffness of the section is very much lower than for the first cycle of loading. As the maximum previously imposed curvature is reached in each successive cycle the moment of resistance almost regains its former level, although some degradation of strength is predicted as cycling continues. The characteristic pinching of the hysteresis loops is typical of behaviour observed for members with low axial load. The analysis predicts that the flexural stiffness suddenly increases as the cracks close. In real members this regain of stiffness is more gradual because of the imperfect closure of cracks and inevitable mismatches which occur between the two crack surfaces.

In this case the ultimate curvature would be governed by either fracture of the longitudinal reinforcement or the strain energy capacity of the transverse hoops being exceeded. The available curvature ductility factor of 30, indicated in the figure, is typical of what could be expected from the critical section of a beam, or a column member with a low axial load level.

In Fig. 7.15 typical moment-curvature hysteresis loops are shown for a section with low axial load and high transverse confining stress. The predicted behaviour is very similar to that for the section with low axial load level and low transverse confining stress except that slightly larger moments of resistance are mobilized and the degradation of strength and stiffness is not as severe. In this case the ultimate curvature would probably be governed by fracture of the longitudinal reinforcement.

In Fig. 7.16 typical moment-curvature hysteresis loops are shown for a section with high axial load and low transverse confining stress. Maximum moments of resistance more than 50 percent in excess of the ACI ideal flexural capacity are predicted, which is expected for members with a high applied axial load level. Stiffness degradation is only very slight and

this is mainly due to the fact that cracks do not spread over as much of the section depth and close much more quickly on reversal of the lateral load in members with substantial axial load. Strength degradation is more significant in sections with high axial load.

The available curvature ductility from this section is very much smaller than from sections with low applied axial load levels. For the case shown, a curvature ductility factor of only about 2.0 was available. The ultimate curvature was normally governed in these cases by reaching a peak in the moment-curvature response during one of the loading cycles. In the example shown it can be seen that moment-curvature curves did reach peaks and the moments of resistance reduced quite quickly for curvatures greater than the value at the peak.

In Fig. 7.17 typical moment-curvature hysteresis loops are shown for a section with high axial load and high transverse confining stress. Maximum moments of resistance of up to twice the ACI ideal flexural strength are predicted. Although there is little stiffness degradation, the high axial load level causes significant strength degradation to occur with cycling of the lateral load. Ultimate curvature was normally governed in this case by reaching a peak in the moment-curvature response on one of the loading cycles.

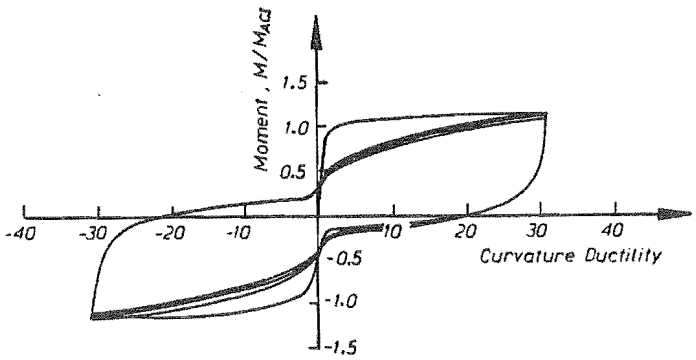

Fig. 7.14 Typical M-Ø Response with Low Axial Load Level and Low Confining Stress

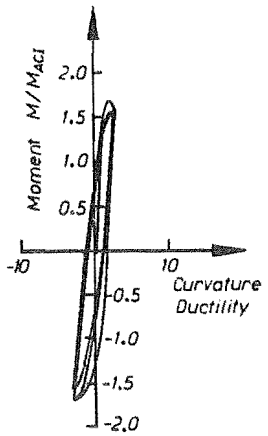

Fig. 7.16 Typical M-Ø Response with High Axial Load Level and Low Confining Stress

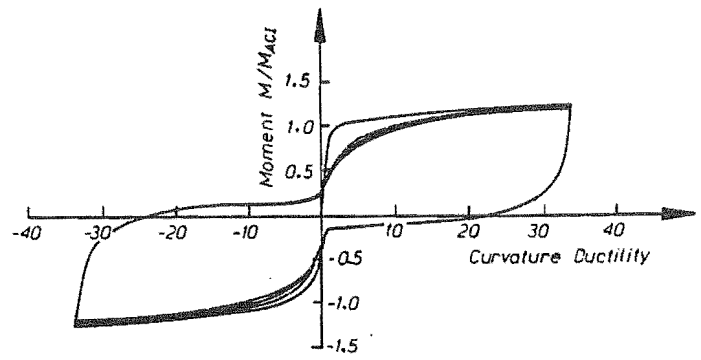

Fig. 7.15 Typical M-Ø Response with Low Axial Load Level and High Confining Stress

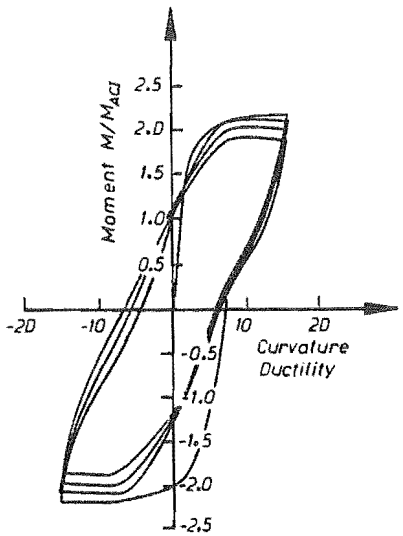

Fig. 7.17 Typical M-Ø Response with High Axial Load Level and High Confining Stress

The information of most interest from the section analyses was the ideal flexural strength M_i (and the amount of enhancement above ACI predictions), the yield curvature ϕ_y and the available ultimate curvature ϕ_u from the section.

7.8.2 Yield Curvature and Ideal Moment Capacity

Previous studies have defined the yield curvature to be the first-yield curvature scaled by the ratio of the moment capacity based on the ACI strength method M_{ACI} to the first-yield moment M_y. This quantity is independent of the strength enhancement provided by concrete confinement and is termed here the "basic yield curvature" ϕ_{yb}. The yield curvature ϕ_y as defined in this study (refer Section 7.6) is greater than the basic yield curvature by the same ratio that the ideal moment capacity exceeds the ACI flexural strength. Fig. 7.18 shows the influence of axial load level and longitudinal reinforcement index $\rho f_y/f_c'$ on the basic yield curvature ϕ_{yb}. The basic yield curvature has been made dimensionless by multiplying by the outside diameter of the tubular member D. The yield curvature ϕ_y is found from the basic yield curvature ϕ_{yb} by multiplying by a series of adjustment factors as in Eqn. 7.55. Similarly, the ideal moment capacity M_i can be found from the ACI moment capacity using the same adjustment factors, as in Eqn. 7.56.

$$\phi_y = \phi_{yb} K_{tc} K_{ri} K_{fc'} K_{cr} \tag{7.55}$$

$$M_i = M_{ACI} K_{tc} K_{ri} K_{fc'} K_{cr} \tag{7.56}$$

The adjustment factor K_{tc} is to allow for variation in the transverse confining stress ratio f_l/f_c'. This is the most significant adjustment factor and is dependent on axial load level as shown in Fig. 7.19. For a high axial load level and high transverse confining stress ratio the ideal moment capacity can be more than twice the ACI value.

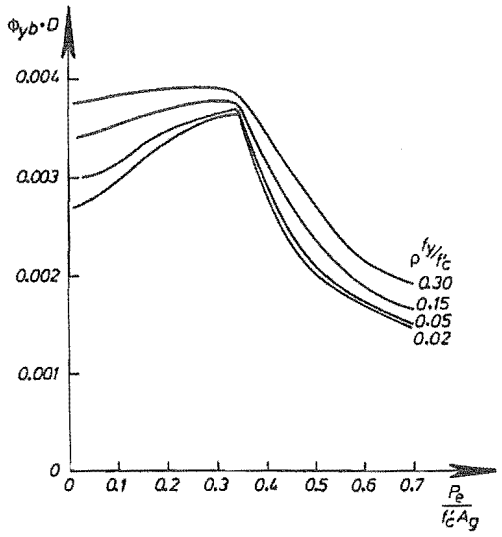

Fig. 7.18 Determination of Basic Yield Curvature

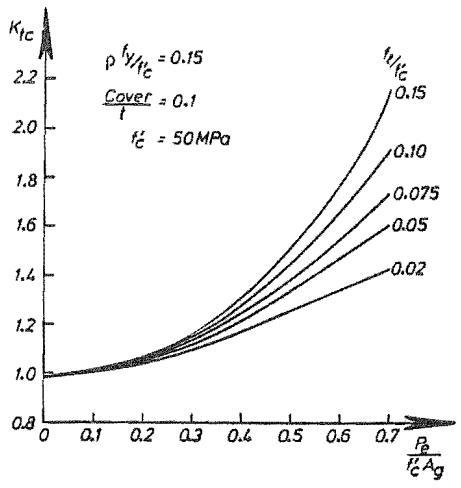

Fig. 7.19 Adjustment Factor K_{tc} for Ideal Moment Capacity and Yield Curvature

The adjustment factors K_{ri}, $K_{fc'}$ and K_{cr} are to allow for variation in longitudinal reinforcement index $\rho f_y/f_c'$, unconfined concrete compressive cylinder strength f_c', and the cover to wall thickness ratio c/t, and are shown in Fig. 7.20.

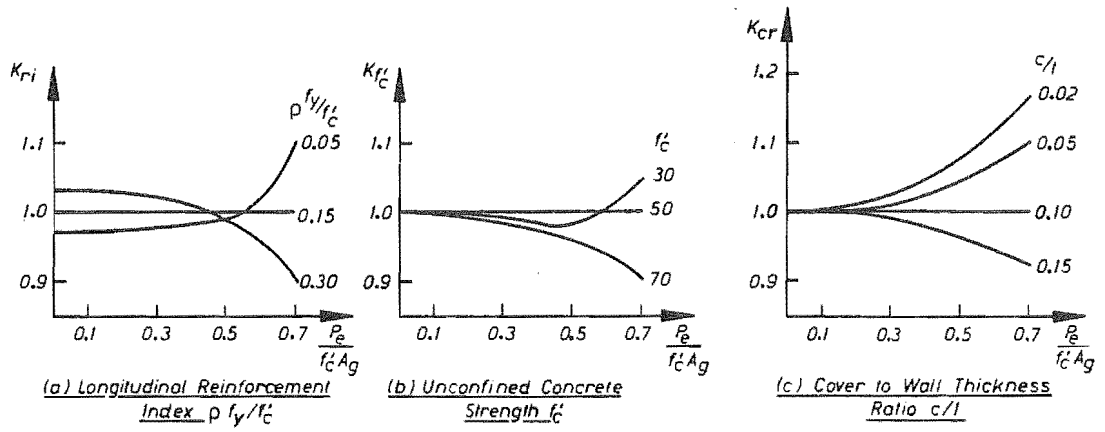

Fig. 7.20 Adjustment Factors K_{ri} $K_{fc'}$ and K_{cr} for Ideal Moment Capacity and Yield Curvature

It should be noted that the adjustment factors K_{tc}, K_{ri}, $K_{fc'}$ and K_{cr} are not perfectly independent, as changes in one variable have some influence on the effect of others. However, it is clear that the most influential parameters are the axial load level and the transverse confining stress ratio. Variations in the other parameters have less effect. Although not all combinations of parameters were used in deriving these charts, the major effects seem to be predicted quite well by the series of multiplicative adjustment factors. Additional check analyses on a few extreme combinations of parameters showed reasonable agreement with behaviour predicted using the charts and adjustment factors presented.

Variation of the longitudinal reinforcement yield strength between 250 MPa and 450 MPa was found to have insignificant effect on the yield curvature and ideal moment capacity. The yield stress value was already incorporated into the longitudinal reinforcement index.

Although most of the hollow circular sections analysed had outside diameter to wall thickness ratios of 20, examples were also considered with this ratio reduced to 5, but the results were almost unchanged.

Fig. 7.21 shows the axial load versus ACI moment capacity interaction behaviour for hollow tubular reinforced concrete sections. The ACI (or NZS 3101) flexural strength is not dependent on the transverse confining stress ratio. The main influences are due to the longitudinal reinforcement index $\rho f_y/f_c'$ and axial load level $P_e/f_c'A_g$. Other parameters such as the longitudinal reinforcement yield stress f_y, the concrete strength f_c', and the cover to wall thickness ratio c/t, have very little effect within the ranges considered.

Similar interaction diagrams have been prepared for obtaining the enhanced ideal flexural capacity M_i which takes into account the level of transverse confining stress. Figs. 7.22 to 7.24 show the axial load versus ideal moment capacity behaviour for reinforced concrete hollow circular sections with transverse confining stress levels f_l/f_c' of 0.05 , 0.10 and 0.15 respectively. The influence of cover thickness ratio c/t can be included by multiplying by the adjustment factor K_{cr} from Fig. 7.20.

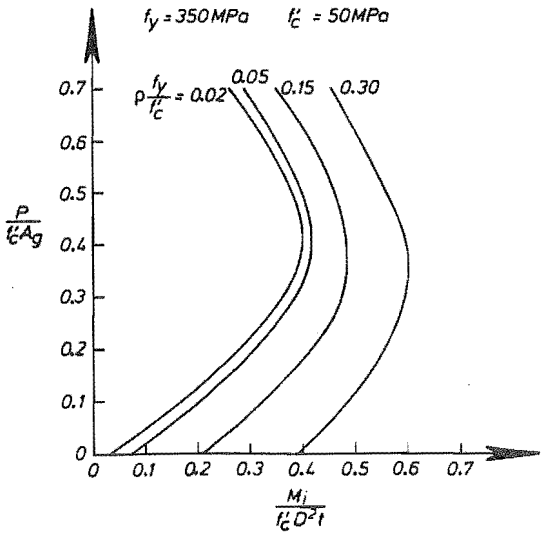

Fig. 7.21 ACI Moment Capacity versus Axial Load Interaction

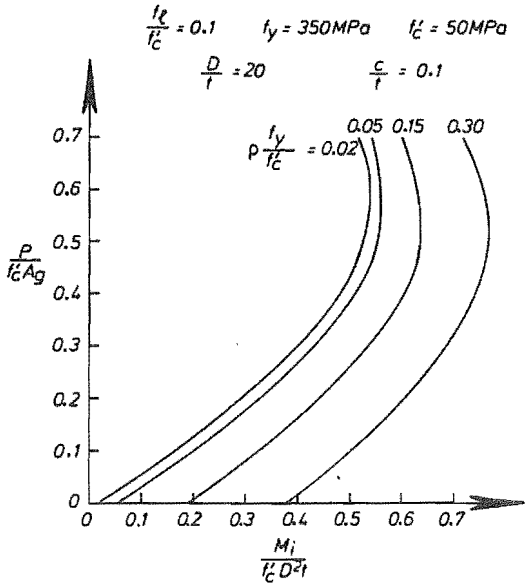

Fig. 7.23 Ideal Moment versus Axial Load Interaction - Moderate Transverse Confinement

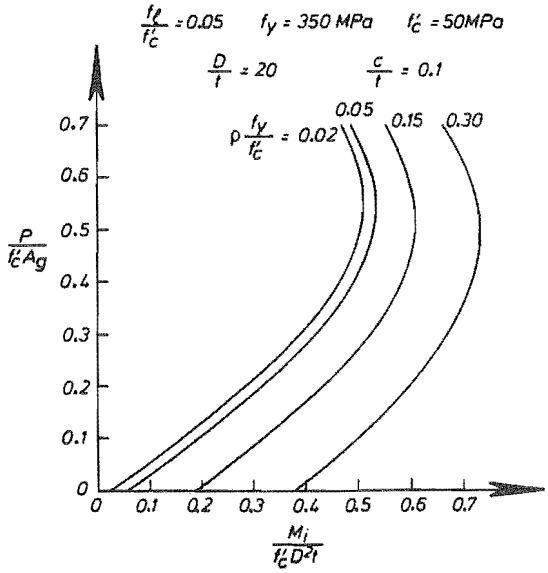

Fig. 7.22 Ideal Moment versus Axial Load Interaction - Low Transverse Confinement

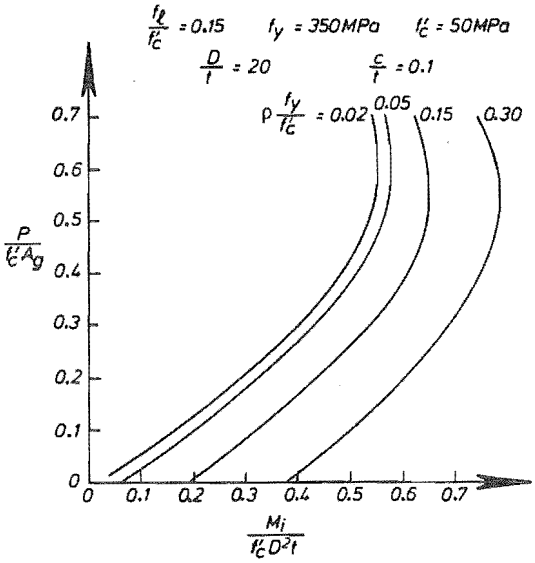

Fig. 7.24 Ideal Moment versus Axial Load Interaction - High Transverse Confinement

7.8.3 Effective Flexural Stiffness

It is often necessary to estimate the stiffness of concrete members after cracking. Such estimates may be required for deflection calculations or for input to dynamic analysis models. If useful predictions of actions induced by earthquake shaking are to be obtained it is necessary to use realistic values of the effective member stiffnesses.

From the results presented in the previous section it is possible to idealize the moment-curvature behaviour of these concrete sections as elasto-plastic, as was shown in Fig. 7.1. It should be noted that the uncracked behaviour was not shown in that figure and the initial

uncracked flexural stiffness would be larger than indicated. The initial behaviour is assumed to be linear and pass through the "first-yield" point on the actual moment-curvature response curve. The equivalent plastic moment is assumed to be equal to the ideal moment capacity. The effective cracked flexural stiffness can be calculated by dividing the ideal moment by the yield curvature. The ratio of the effective second moment of area to the gross concrete section second moment of area can be calculated by dividing this by the gross section flexural rigidity, as indicated by Eqn. 7.57.

$$I_{cr} / I_g = M_i / \phi_y I_g E_c \qquad (7.57)$$

Effective second moments of area calculated in this way are presented in Fig. 7.25 for a number of the sections analysed in this study. The values of I_{cr} / I_g are plotted against axial load level for different values of the longitudinal reinforcing index $\rho f_y / f_c'$. For members with low axial load levels the effective second moment of area is predicted to be only about 30 percent of the gross value. For members with a high level of axial load and having a large longitudinal reinforcing index the effective second moment of area can be larger than the gross concrete value.

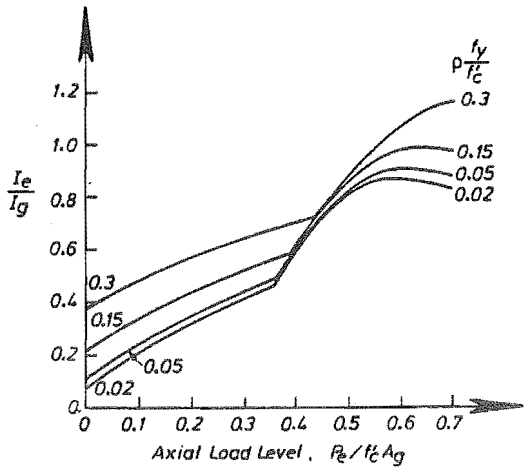

Fig. 7.25 Reduction Factor for Second Moment of Area

The effective second moment of area results presented in Fig. 7.25 strictly only apply to the critical section. In real members the bending moments vary along the member and some parts may even remain uncracked. Flexural cracking only occurs at discrete points and between cracks the flexural rigidity is larger than the cracked section value (the so-called tension stiffening effect). However, consideration of the likely distribution of curvature in a simple cantilever member undergoing large inelastic deformations shows that most of the deflection at the free end is contributed by the large curvatures which occur near the critical section. Satisfactory estimates of deflection can often be made by assuming that the cracked second moment of area applies along the entire length of the member. The predicted effective second moment of area results were found to give reasonable agreement with the measured values from the experimental tests conducted as part of this study, which were presented in Chapter 6. However, on average the experimental ratios of effective second moment of area to gross second moment of area were about 10 percent larger then the theoretical values. It is suggested that the theoretical values could be increased by 10 percent to allow for likely tension stiffening effects.

7.8.4 Available Ultimate Curvature and Curvature Ductility Factor

The most significant variables affecting the available ultimate curvature ϕ_u were axial load level $P_e/f_c'A_g$ and transverse confining stress ratio f_l/f_c'. Fig. 7.26 shows the influence of

these variables on the available ultimate curvature. Average values of the other parameters were assumed and the curvature values were made dimensionless by multiplying by the outside diameter of the tubular member, D. The available ultimate curvature increases as the transverse confining stress ratio f_l/f_c' increases and as the axial load level $P_e/f_c'A_g$ decreases. The available curvature curves (solid lines) are intercepted by several dashed curves corresponding to various values of the ultimate tensile strain ε_{su} in the longitudinal reinforcement. For curvatures above each of the dashed curves the tensile strains in the reinforcement would exceed the stated values.

The longitudinal reinforcement index $\rho f_y/f_c'$ did not have a significant effect on the available ultimate curvature. Although some variations were apparent, these were generally small and trends were unclear. Good estimates of the available ultimate curvature for sections with longitudinal reinforcement indices over the whole range considered can be obtained from the values presented in Fig. 7.26 for $\rho f_y/f_c' = 0.15$.

The results in Fig. 7.26 are presented again in terms of curvature ductility factors μ_ϕ in Fig. 7.27. Curvature ductility factors were obtained by dividing the available ultimate curvature ϕ_u by the yield curvature ϕ_y. It is likely that designers will have more familiarity with curvature ductility factors than with absolute values of curvature. However, it should be noted that the curvature ductility factor values are dependent on the method of determining the yield curvature.

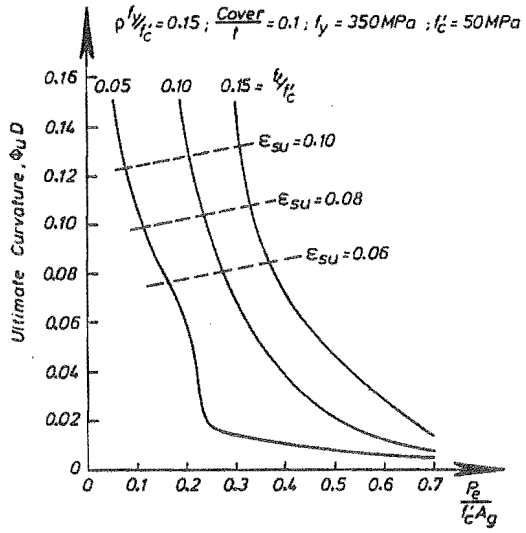

Fig. 7.26 Available Ultimate Curvature

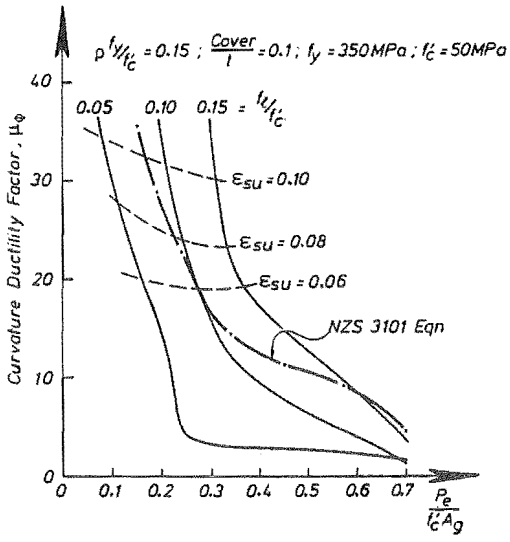

Fig. 7.27 Available Curvature Ductility Factor

The influence of cover thickness ratio c/t on available ultimate curvature was found to be very similar to the effect on ideal moment capacity or yield curvature. The moment of resistance of a section tends to reduce when the cover concrete spalls and so degrades more significantly when the cover thickness is a greater proportion of the member wall thickness. The effect is more significant in members with high levels of applied axial load. It is suggested that the adjustment factor K_{cr} shown in Fig. 7.20c should be applied to the available ultimate curvature to allow for variations of the cover thickness ratio. However, for determining the available curvature ductility factor the results in Fig. 7.27 should be used without adjustment for cover thickness ratio. This is because the adjustment factor applies to both the available ultimate curvature and the yield curvature, and so cancels.

The influence of variations in yield strength of the longitudinal reinforcement f_y, unconfined concrete compressive strength f_c' and the outside diameter to wall thickness ratio D/t were found to be insignificant to within a few percent over the ranges considered.

For most of the analyses the ultimate curvature was governed by the requirement that the peak of the moment-curvature curve should not be exceeded. For sections carrying only low levels of applied axial load, strain hardening of the longitudinal reinforcement, and the relatively small contribution of the concrete, resulted in the moment of resistance continuing to rise even at large curvatures. In this case transverse hoop fracture tended to govern the available ultimate curvature.

7.8.5 Flexural Overcapacity

The maximum moments of resistance obtained from sections during the moment-curvature analyses were in most cases very similar to the the ideal moment capacities, as in most cases there were no significant gains in the moment of resistance after curvatures of $5\phi_y$ were exceeded. In general the maximum moment mobilized was only greater than the assumed ideal flexural capacity for sections with low levels of axial load. In that case the ideal moment capacity M_i was exceeded at curvatures large enough to cause strain hardening of the longitudinal reinforcement. Fig. 7.28 shows the influence of axial load level and transverse confining stress ratio on the flexural overstrength, shown as the ratio of the maximum moment M_{max} to the ACI moment capacity M_{ACI}. Also shown in that figure, as a shaded region, is a range of values reported by Ang [7.10] giving the experimentally observed overstrength factors from about 30 tests on solid reinforced concrete members tested at the University of Canterbury in recent years. The majority of these test results fell within the 15 percent limits of the curve representing the average behaviour. These limits are also shown. The theoretically predicted and experimentally observed results appear to be in very good agreement, particularly for levels of transverse confining stress corresponding to quantities of confining reinforcement required by the New Zealand Concrete Design Code NZS 3101. Design of transverse reinforcement used in many of the University of Canterbury test units was based around the requirements of NZS 3101.

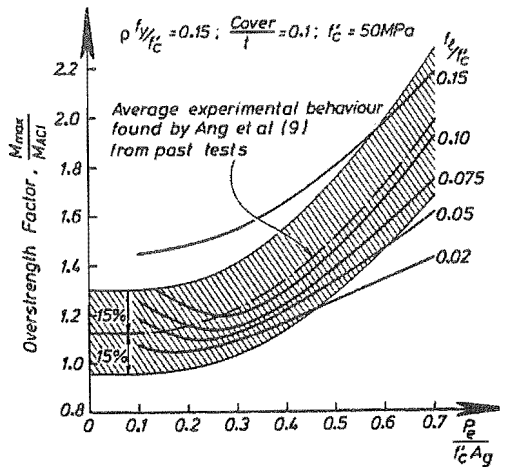

Fig. 7.28 Comparison of Theoretical and Experimental Flexural Overstrength

7.8.6 Influence of Load-Cycling on Available Ultimate Curvature

The results for available ultimate curvature presented in Fig. 7.26 were based on cyclic loading analyses where four complete reversed loading cycles were imposed to equal positive and negative curvatures. This loading programme was consistent with the requirements of the New Zealand Loadings Code for Buildings NZS 4203 [7.4]. It was important to consider cyclic loading histories as significant strength and stiffness degradation can occur during successive cycles.

Analyses were carried out for a limited number of cases to investigate how the available ultimate curvature would change if the number of loading cycles required to be sustained by

the section was reduced to two complete reversed load cycles or only one monotonic half-cycle. For members with high levels of axial load ($P_e/f_c'A_g > 0.5$) the available ultimate curvature was increased by approximately 50 percent where only two reversed loading cycles were required and by more than 100 percent for the monotonic loading case. The effect was less marked at lower levels of axial load with almost no difference in available ultimate curvature for low axial load levels ($P_e/f_c'A_g < 0.1$).

It is clear that estimates of available ultimate curvature based on monotonic moment-curvature analyses can be misleading and unconservative.

7.8.7 Influence of Unequal Transverse Confining Stresses

The results for available ultimate curvature presented in Fig. 7.26 were based on the assumption that equal confining stresses were effective in each of the transverse directions. In real sections it is most likely that practical reinforcement layouts will result in different quantities of transverse reinforcement, and hence different confining stress ratios being provided in each of the transverse directions. A limited number of additional analyses were carried out to assess the influence of having different transverse confining stress ratios f_l/f_c'.

The main effect of having unequal confining stresses in each of the transverse directions is to change the confined concrete stress-strain behaviour. This can be quantified with reference to Fig. 7.3 which gives the confined strength ratio f_{cc}'/f_c' as a function of the confining stress ratios in the two transverse directions. An equivalent level of equal confining stress ratio f_l/f_c' can be found such that the same confined strength ratio f_{cc}'/f_c' is achieved and $f_l = f_{l1} = f_{l2}$. The equivalent equal confining stress f_l will be between the two unequal confining stresses f_{l1} and f_{l2}.

It should be noted that the analytical method for determining the available ultimate curvature from the critical sections assumed that half of the internal work done was stored in the hoops in each of the transverse directions. Where the transverse confining stress ratios are different in each direction, because different quantities of transverse reinforcement are provided, then it would be expected that hoop fracture would theoretically occur first in the direction with lower confinement. In most cases available ultimate curvature was governed by a peak in the moment-curvature curve being reached rather than by fracture of the critical transverse hoop leg. Reduction in moment of resistance of the section is related directly to the falling branch of the confined concrete stress-strain curve. It is thus reasonable to expect that for such sections the available ultimate curvature depends on the equivalent equal confining stress ratio.

However, for sections with low levels of axial load the ultimate curvature was generally governed by the prediction of transverse hoop fracture. In this case there is no advantage in having the confining stress in one transverse direction higher than in the other transverse direction. In this case the ultimate curvature should be determined based on the smallest transverse confining stress ratio. It was found from the analyses carried out that a reasonable level of axial load to distinguish between the two cases was $P_e/f_c'A_g = 0.2$.

In summary, for estimating the strength and ductility behaviour of sections with unequal confining stress ratios in the walls, the equivalent equal confining stress ratio may be used. This should be determined from Fig. 7.3 so that the confined strength ratio f_{cc}'/f_c' is the same as obtained from the actual transverse confining stress ratios. For sections with axial load levels $P_e/f_c'A_g < 0.2$ the available ultimate curvature should be determined based on the smaller of the transverse confining stress ratios.

7.8.8 Partially Prestressed Hollow Circular Sections

Offshore concrete platform members are normally prestressed to enhance fatigue life and crack control. A limited number of examples of tubular sections with various amounts of prestressed and non-prestressed longitudinal reinforcement were examined as part of this

study. The cyclic stress-strain model for prestressing tendons proposed by Thompson (refer Section 7.7.3) was incorporated in the moment-curvature analysis program.

The moment-curvature behaviour of partially prestressed hollow circular column sections is very similar to that of of sections containing only non-prestressed reinforcement. The major difference is in the shape of the moment-curvature hysteresis loops. Where prestressed reinforcement is present the area enclosed by the loops tends to be smaller. The case where only prestressed longitudinal reinforcement was present in the section was not considered to be of practical use in offshore concrete platform members and was not investigated. However, it is well known that load-deformation hysteresis curves of prestressed concrete members can become quite "pinched" and result in significant reduction in the energy dissipation capability of those members. Because of this it is generally expected that the displacement response of prestressed concrete structures may be somewhat higher than for equivalent partially prestressed or reinforced concrete structures. This feature should also be considered when choosing load-deformation relations for modelling the critical regions of prestressed concrete structures in inelastic dynamic analyses.

Partially prestressed hollow circular concrete sections were considered with levels of axial prestress stress varying from zero (reinforced concrete) to $0.3f_c'$ where f_c' = unconfined concrete compressive cylinder strength. The required number of prestressing tendon areas were distributed evenly around the circumference of the section at the middle of the wall thickness. The assumed control parameters for the stress-strain curve of the prestressing steel were given in Table 7.4 and are typical of the properties of the high strength tendon steels used in New Zealand.

The analyses of partially prestressed concrete members indicate that results such as the ideal moment capacity, section yield curvature, cracked section flexural stiffness and available ultimate curvature can be obtained from the charts already presented for reinforced concrete members. Some additional considerations are necessary to determine the effective axial load level and the longitudinal reinforcement index.

7.8.8.1 Yield Curvature and Ideal Moment Capacity

The moment-curvature analysis program developed by Mander et al for reinforced concrete sections was modified to analyse prestressed concrete members. The method for determining yield curvature in the program was adapted to account for the presence of prestressing tendons. First-yield curvature was chosen as that curvature at which either the concrete reached the strain corresponding to the unconfined strength (generally $\varepsilon_{co} = 0.002$), or the non-prestressed reinforcement reached yield strain, or the prestressing tendons reached the strain ε_{pb} at the beginning of the upper straight branch of the stress-strain curve. Yield curvature was then obtained by scaling the first-yield curvature by the ratio of the ideal moment capacity to the first-yield moment.

As curvatures are imposed on a partially prestressed concrete section, tendons on the tension side of the member are subject to increased tensile strains and tendons on the compression side of the section have their tensile strains due to initial prestress reduced. For imposed curvatures up to about the yield curvature the sum of the tendon forces across the section does not change significantly from the initial axial prestress force.

Yield curvature ϕ_y and ideal moment capacity M_i can be obtained from Eqns. 7.55 and 7.56 and Figs. 7.18 to 7.21. The axial load level $P_e/f_c'A_g$ should be calculated based on the sum of the externally applied axial load and the internally applied axial prestress force. Transverse confining stress ratios f_l/f_c' can be calculated as for members without prestress. Calculation of the longitudinal reinforcement index should take account of both the prestressed and non-prestressed longitudinal reinforcement. It was found appropriate to calculate this index using the expression in Eqn. 7.58.

$$\rho f_y/f_c' = (\rho + \rho_p) f_y/f_c' \qquad (7.58)$$

where $\rho_p = A_{ps}/A_g$ = the volumetric content of prestressed reinforcement

and f_y = yield stress of longitudinal reinforcement

This is reasonable as the prestressing steel will undergo similar changes in strain to those in the non-prestressed reinforcement. Also, the yield curvature and first-yield curvature will generally be governed by the non-prestressed reinforcement reaching the yield strain before the prestressing tendons reach the strain ε_{pb}.

7.8.8.2 Available Ultimate Curvature

Where large curvatures are imposed on a prestressed concrete section large strains will be induced in the tendons. On the tension side of the section the stress-strain behaviour will proceed along the upper branch of the tensile stress-strain curve. On the compression side of the section the tendons will be subject to nett compression strains when the flexural compression strains exceed the initial prestress tension strain of approximately 0.006. It is likely that when the section reaches its ultimate curvature the tendons on the compression side will be subject to compression strains well in excess of the elastic limit. The stress-strain behaviour of prestressing tendons in compression is difficult to determine in practice. In this study it was assumed that buckling of the tendons would not occur as they were located in the middle of the confined concrete wall and would be continuously restrained.

If the neutral axis is located close to the centroid of the section then approximately equal numbers of tendons would be subject to nett tension or compression strains and the overall effect would be no resultant axial force on the section. Under ultimate curvature conditions the flexural strains would generally be so large that the initial strain due to prestress would be of little consequence. Thus it is expected that as ultimate curvature is approached the initial prestress force would tend to disappear and the section would behave more like a reinforced concrete section.

The available ultimate curvature or curvature ductility factor of partially prestressed concrete members with hollow circular cross-section can be determined from Figs. 7.26 or 7.27. The axial load level should correspond to the externally applied axial load only. The longitudinal reinforcement index should be calculated from Eqn. 7.59.

$$\rho f_y/f_c' = (\rho f_y + \rho_p f_{pb})/f_c' \qquad (7.59)$$

where $\rho = A_s/A_g$ = the volumetric content of non-prestressed reinforcement
$\rho_p = A_{ps}/A_g$ = the volumetric content of prestressed reinforcement
f_y = yield stress of non-prestressed reinforcement
f_{pb} = stress at beginning of upper branch of tendon stress-strain curve
f_c' = unconfined concrete compressive cylinder strength

The ultimate curvature of the critical section may be limited by the tensile strain capacity of the prestressing tendons or non-prestressed longitudinal reinforcement, whichever is expected to have the lower elongation capacity. Normally the fracture strain of high strength prestressing steel would be lower than that of non-prestressed reinforcing steel. A cut-off curve appropriate to the maximum elongation capacity should be chosen in determining the available ultimate curvature values $\phi_u D$ from Fig. 7.26 or the available curvature ductility factor from Fig. 7.27.

7.8.9 Comparison of Available Ultimate Curvature Results with New Zealand Concrete Design Code NZS 3101 Recommendations

The New Zealand Concrete Design Code NZS 3101 [7.3] specifies the following minimum quantities of transverse reinforcement to be provided by rectangular hoops, with or without supplementary cross-ties.

$$A_{sh} = 0.3\, s_h\, h''\, [A_g / A_c - 1]\, f_c'/f_{yh}\, [0.5 + 1.25\, P_e / \phi\, f_c' A_g] \qquad (7.60)$$

but not less than

$$A_{sh} = 0.12\, s_h\, h''\, f_c'/f_{yh}\, [0.5 + 1.25\, P_e / \phi\, f_c' A_g] \qquad (7.61)$$

where A_{sh} = total area of transverse hoops in direction considered
s_h = spacing of transverse reinforcement hoop sets
h'' = width of concrete core (at right angles to direction being considered) to outside of hoops
A_g = gross area of concrete section
A_c = core area of section to outside of hoops
f_c' = unconfined concrete compressive cylinder strength
f_{yh} = yield stress of transverse hoops
P_e = external axial load carried by member
ϕ = strength reduction factor

For hollow circular members with inside and outside cover thickness of less than 20 percent of the the gross wall thickness Eqn. 7.61 will govern. This would apply for all members likely to be used in offshore concrete platform structures. By rearranging this equation the expression in Eqn. 7.62 can be obtained, giving the transverse confining stress ratio f_l/f_c', assuming 100 percent effectiveness of the transverse hoops.

$$f_l / f_c' = A_{sh}\, f_{yh} / s_h\, h''\, f_c' = 0.12\, [0.5 + 1.25\, P_e / \phi\, f_c' A_g] \qquad (7.62)$$

This gives the dependence of the transverse confining stress ratio on axial load, implied by the code equation. The dashed line shown in Fig. 7.27 shows the curvature ductility factors which could be expected from sections detailed according to the code, based on the results of this theoretical study. It is evident that for very high levels of axial load ($P_e = 0.7 f_c' A_g$) the code requirements would ensure an available curvature ductility factor of only about 5. It can be seen that at lower levels of axial load higher curvature ductilities would be available. These results suggest that if the code aim of providing available curvature ductilities of approximately 20 was to be met then the quantities of transverse confining reinforcement could be reduced for members with axial load levels less than about $P_e = 0.3 f_c' A_g$. However, for members with axial load levels greater than about $P_e = 0.3 f_c' A_g$ the quantities of transverse confining reinforcement would have to be increased.

It should be noted that the yield curvature used in deriving the curvature ductility factors was up to twice that used in previous studies and therefore the available curvature ductility factors are apparently halved at very high axial load levels.

7.9 CONCLUSIONS

1. A cyclic moment-curvature computer analysis program has been used to predict the theoretical strength and ductility characteristics of reinforced and partially prestressed hollow circular concrete members. This incorporated refined stress-strain models for confined concrete, reinforcing steel and prestressing tendons. A range of variables has been considered which is appropriate to the members which would be used in offshore concrete platform structures. Moment-curvature analyses of a large number of possible sections have been carried out to determine the ideal flexural strength, yield curvature and available ultimate curvature of such members. Actual

moment-curvature response was idealised as elasto-plastic. Results were presented in non-dimensionalised chart form which could be used directly by structural designers.

2. With regard to flexural strength the results show that the conventionally used ACI flexural strength theory is reasonable for members with low levels of axial load but significantly underestimates the flexural strength at moderate to high levels of axial load. The charts presented for estimating flexural strength of these sections give more realistic estimates of available strength at all levels of axial load. This could enable significant economies to be made in designing hollow circular column members with moderate to high levels of axial load.

3. Yield curvatures can also be estimated using charts provided. These results were combined with the results for ideal moment capacity to estimate the effective second moments of area of cracked hollow circular concrete members. These can be used for input to analytical models for estimating behaviour of cracked structures.

4. Charts are provided for estimating the ultimate curvatures available from these sections. These results are also presented in terms of curvature ductility factors. Criteria for determining ultimate curvature were chosen to correspond to the expected limit of useful load carrying capacity. The important finding from the experimental study that curvatures should not be allowed to exceed the peak of the moment-curvature response curve was included as one of the criteria and governed many of the results obtained.

5. The design charts can be used to estimate the quantities of transverse confining reinforcement required to enable the critical sections of hollow circular concrete members to sustain particular ductility demands.

6. Comparison of the theoretical results with the recommendations of the New Zealand Concrete Design Code NZS 3101 indicated the curvature ductility factors which would be available from members designed according to those requirements. For members with low levels of axial load the results predicted that curvature ductility factors in excess of 30 would be available. For members with very high levels of axial load it was predicted that curvature ductility factors of only 5 to 10 would be available.

7.10 REFERENCES - CHAPTER 7

7.1 Mander, J. B. , Priestley, M. J. N. and Park, R. , "Seismic Design of Bridge Piers", Research Report 84-2, Department of Civil Engineering, University of Canterbury, February 1984.

7.2 ACI 318, "Building Code Requirements for Reinforced Concrete", American Concrete Institute, Detroit, 1983.

7.3 NZS 3101, "Code of Practice for the Design of Concrete Structures", Parts 1 and 2, Code and Commentary, Standards Association of New Zealand, Wellington, 1982.

7.4 NZS 4203, "Code of Practice for General Structural Design and Design Loadings for Buildings", Standards Association of New Zealand, Wellington, 1976.

7.5 CDP 701/D, "Highway Bridge Design Brief", New Zealand Ministry of Works and Development, September 1978 (including 1978 addendum).

7.6 Zahn, F. A. , "The Ductility of Bridges", Ph.D. Thesis, University of Canterbury, 1985.

7.7 Priestley, M. J. N. and Park R. , "Strength and Ductility of Bridge Substructures", RRU Bulletin 71, National Roads Board, Wellington, 1984.

7.8 Thorenfeldt, E. , "Design Properties for High Strength Concrete", Nordisk Betong, Journal of the Nordic Concrete Federation, Vol. 1-2: 1986 , pp 71-73.

7.9 Thompson K. J. , "Ductility of Concrete Frames Under Seismic Loading", Ph.D. Thesis, University of Canterbury, 1975.

7.10 Ang Beng Ghee, "Dynamic Shear Strength of Concrete Piers", Ph.D. Thesis, University of Canterbury, 1985.

Chapter 8

DESIGN AND ANALYSIS OF POSSIBLE OFFSHORE CONCRETE PLATFORM STRUCTURES FOR USE IN NEW ZEALAND

8.1 INTRODUCTION

Although almost twenty offshore concrete gravity platforms have now been designed or already installed in the North Sea, no platforms have yet been placed in seismically active areas. In this chapter two different types of concrete gravity platform are investigated in order to assess their likely seismic performance. The platforms are considered to be located near the known Maui gas field, off the west coast of the North Island, New Zealand. Platform configurations considered were a North Sea type cantilever structure, and a hybrid concrete and steel structure which has been developed for use in the China Sea. Possible philosophies for the seismic design of these structures are discussed and two different approaches are chosen for determining the design lateral loading for each of the platforms. Some assumptions were necessary regarding deck masses and foundation material properties.

Design of these platforms for seismic loading used a two-tier approach in which both design levels and extreme levels of earthquake shaking were considered. A design level of loading was chosen to proportion the strength of the structures. Checks were then made on the effects of the extreme level of earthquake shaking to see if any parts of the structure or foundation became inelastic and what levels of ductility were implied. Inelastic time history analyses were performed to determine the dynamic response to earthquake loading. Artificial earthquake records were used which matched the response spectra of the recently proposed revisions to the New Zealand loadings code for buildings, NZS 4203.

Platform layouts satisfying the various design criteria are presented. Comparisons are made in each case between wave loading, design level earthquake and extreme level earthquake effects. The expected performance of these structures is also discussed.

8.2 PREVIOUS USE OF OFFSHORE CONCRETE GRAVITY PLATFORMS

Concrete has been used as a building material in the sea for more than a thousand years in harbour constructions and the like. Boats have been built from concrete for about a hundred years. With the discovery of the extensive reserves of oil and gas in the North Sea in the 1960's, very large fixed concrete platforms were considered as an economic alternative to the steel jacket platform structures which had been widely used in other offshore developments. Since that time about twenty have been constructed.

Details of fifteen of the North Sea platforms already installed are summarised in Table 8.1 [8.1, 8.2]. The layout of a typical platform is shown diagrammatically in Fig. 8.1. A large cellular base sits on the sea bed, sometimes with an arrangement of bottom penetrating steel or concrete skirts to help key the base to the seabed. Water depths for these structures have been between 70 m and 150 m and the horizontal dimension of the base has varied from about 70 m to about 130 m. The number of legs supporting the deck has varied from one to four, with leg diameters ranging from about 10 m up to 35 m on mono-tower platforms, and wall thicknesses between 0.5 m and 1 m. Topside masses have typically ranged from about 10 000 tonnes to about 50 000 tonnes. Further platforms are currently being built for water depths up to about 200 m and designs are being considered for depths of up to 300 m [8.3]. Concrete strengths used in the first platform structures were around 40 MPa but strengths have steadily increased in more recent designs up to 60 MPa or more. The storm conditions which these structures must withstand are severe. North Sea platforms have been designed for waves up to about 31 m in height.

Table 8.1 Concrete Gravity Platforms in the North Sea

	Platform	Design	Water Depth (m)	Base Dimension (m)	Concrete Volume (cu. m)	Design Wave Height (m)
1	Ekofisk I	Doris	70	92	90 000	24.0
2	Beryl A	Condeep	120	100	55 000	29.5
3	Brent B	Condeep	142	100	65 000	30.5
4	Frigg CDP1	Doris	96	101	60 000	29.0
5	Brent C	Sea Tank	142	100	105 000	30.5
6	Frigg TP1	Sea Tank	104	72	70 000	29.0
7	Cormorant A	Sea Tank	152	100	115 000	30.5
8	Brent D	Condeep	142	100	65 000	30.5
9	Dunlin A	Andoc	152	104	90 000	30.5
10	Statfjord A	Condeep	145	110	70 000	30.5
11	Frigg TCP2	Condeep	104	100	50 000	29.0
12	Frigg MP2	Doris	94	101	60 000	29.0
13	Ninian	Doris	139	140	170 000	31.2
14	Statfjord B	Condeep	146	171	140 000	30.0
15	Statfjord C	Condeep	146	170	130 000	30.0

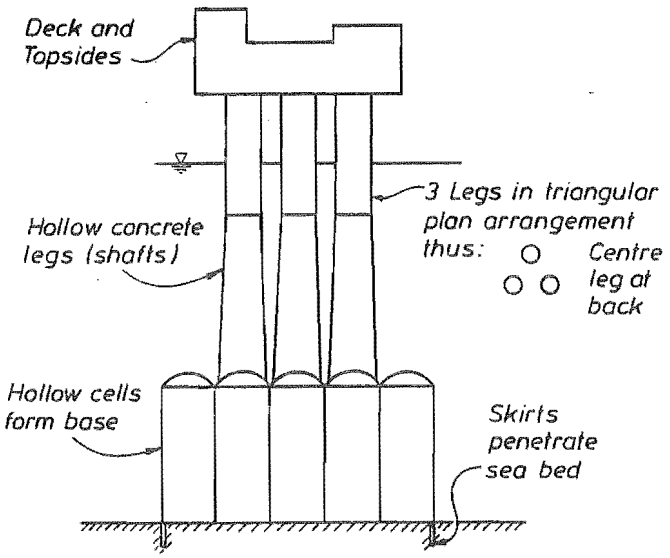

Fig. 8.1 Layout of Typical North Sea Type Offshore Concrete Gravity Platform

A typical construction sequence for one of the North Sea concrete platforms is shown in Fig. 8.2. A dry dock (a) is formed in a suitably sheltered bay which is accessible to construction forces and materials supply. Further excavation is sometimes necessary to form the skirts attached to the bottom of the base. The base or "caisson" is then started (b) either with a large concrete slab or from a number of inverted dome shapes, sometimes called the "lower domes". The cell walls forming the base are built up by slip-forming, and when the base is sufficiently complete to float, the dock is flooded and the platform base is floated out (c) and moored. As construction continues the structure sinks lower in the water, and sufficient water depth is required to float the complete concrete structure without the deck. The tops of the base cells are enclosed by the "upper domes". In some of the platforms gravel ballast has been placed inside the base also. The cells in the base are arranged so that some of them can be continued up to form the legs, or "shafts" (d). Slipforming of the legs is complicated by the tapers in diameter and variations in wall thickness over the height, but the technology for achieving this is now well established [8.3].

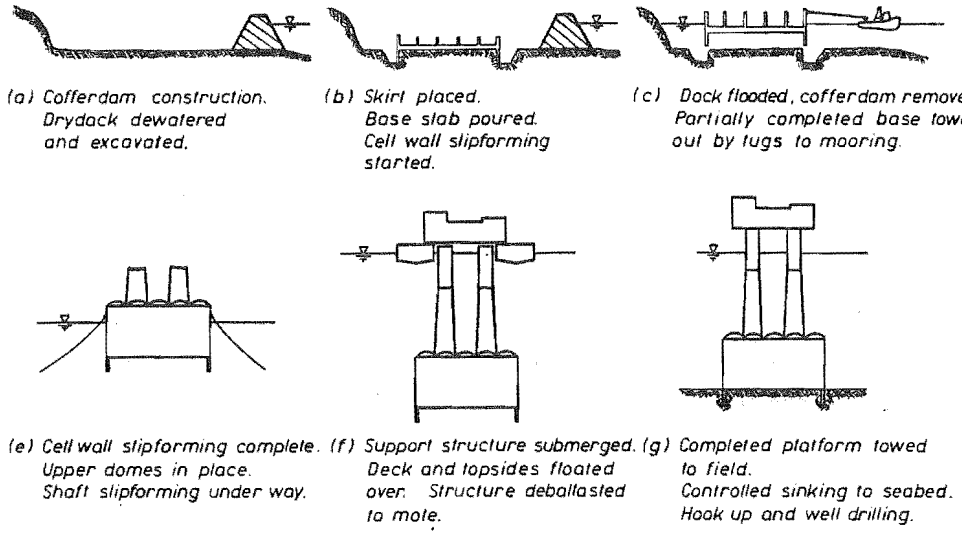

Fig. 8.2 Construction Sequence for North Sea Type Platform

While the concrete support structure is being constructed the deck and topside facilities can also be assembled with many of the mechanical services already connected. The concrete tower and the deck, both floating on barges, are towed to a sheltered deep-water site for the mating operation. The tower is ballasted down by controlled flooding of the internal chambers until it is almost completely submerged and the deck is floated over the top (Fig. 8.2 f). The tower is then slowly deballasted and lifts the deck off the barges. The whole platform can then be towed to the offshore site and ballasted down into the required position (Fig. 8.2 g). Where skirts are present under the platform these are normally able to penetrate the sea bed under the weight of the platform alone. Once in place production wells can be drilled from the platform and final hook-up of the topside facilities completed.

8.3 PHILOSOPHY FOR LATERAL - LOAD DESIGN OF OFFSHORE PLATFORM STRUCTURES

Design for wave loading has governed the lateral load design of the existing North Sea concrete platforms. Storm waves with an expected return period of 100 years have been considered, and design wave heights have ranged from about 22 m to 31 m. Platform structures are designed to remain elastic under design wave loading and axial prestress is provided in the members to prevent tensile stresses being induced in the concrete. During large storms a platform could be subjected to hundreds of cycles of loading, and the aim of not allowing tensile stresses is to reduce the risk of fatigue problems in the members. Dynamic magnification effects, due to very large waves, are generally small because the wave periods (typically around 15 seconds) are much longer than the periods of vibration of platforms.

Earthquake loading effects have not been a major consideration in the North Sea platforms, although it appears that earthquake effects have been considered in those designs. Seismicity levels in the North Sea are quite low [8.1] compared with other parts of the world. Currently available design recommendations for offshore platform structures contain guidance on design for earthquakes, though often in rather general terms [8.4 - 8.7]. In such guide-lines design level loadings for environmental loadings such as wind, wave or earthquake are normally associated with return periods of about 100 years. Extreme events are often associated with return periods of up to 10 000 years. It is possible for large earthquakes to occur anywhere in the world, not just at the boundaries of the known tectonic plates. Large intra-plate earthquakes can occur within tectonic plates even though the probability of occurrence may be extremely small.

With the development of offshore fields in new areas there has been a need to investigate new factors affecting platform design. At present much exploration is going on in polar regions where ice presents a problem. Considerable research effort has been directed toward understanding ice loading effects and in finding suitable platform types to withstand ice floes. Platforms are also being considered for use in seismically active areas. Previous studies investigated the feasibility of using concrete platforms in the Gulf of Alaska [8.8, 8.9]. Prospects for future development of offshore oil and gas fields in New Zealand have been largely responsible for the present research being undertaken. There is little information published regarding the seismic performance of concrete offshore platforms.

Suitable design criteria for the seismic design of offshore concrete platforms have not been developed in detail. It seems reasonable that a similar philosophy to that already used for the seismic design of major onshore structures should also be applied to these structures.

A philosophy for the seismic design of structures has evolved in New Zealand and other countries over the past fifty years or so. It is recognised that it is generally uneconomic to design structures to resist very large, infrequent earthquakes without damage. Instead, structures are provided with sufficient strength to resist small, frequent earthquakes without damage. Also, it is attempted to build in a degree of ductility to structures to enable them to deform inelastically during larger, less frequent disturbances. It is anticipated that sufficient ductility is available to allow structures to survive even very large rare earthquakes without collapse. It is accepted that structures will be damaged by large earthquakes, sometimes beyond repair. Capacity design procedures have been developed with the aim of suppressing undesirable modes of failure in favour of those which can sustain substantial inelastic deformations.

Prior to about 1930 there were no requirements in New Zealand to design structures for lateral loading caused by earthquakes. After the large, damaging Napier earthquake in 1931 simple building code regulations were introduced in New Zealand requiring buildings to be designed for minimum levels of lateral load. All structures were designed considering lateral loads at each floor level equal to about 8 percent of the floor weight. Later, these levels were increased and it was also recognised that flexible, long period structures experienced lower response accelerations than stiff, short period structures. Design response spectra were introduced in which the base shear depended on the fundamental period of vibration of the structure. Methods of distributing the base shear were also introduced to recognise that response accelerations near the top of a structure were higher than in areas close to the ground. It was clear that the response accelerations for which structures were designed were still much less than could be expected during some of the large earthquakes that had been felt around the world. Requirements for ductile detailing were introduced to give structures protection against collapse in the event that the relatively modest lateral load resistance was exceeded.

Currently, earthquake design loads for buildings in New Zealand are specified by NZS 4203, the Code of Practice for General Structural Design and Design Loadings for Buildings [8.10]. Simple design acceleration response spectra are specified and base shear forces are derived by multiplying by the seismic weight by a series of modifying factors allowing for the type of structure, material used and importance of usage. For ductile design the factors do not differ greatly from unity, but for elastic design the loading is increased by a factor of at least four. The basic seismic coefficients have a maximum value of about 15 percent of the acceleration of gravity for short period structures and about 7.5 percent for longer period structures. For elastically designed structures the resulting seismic coefficients have a maximum value of at least 60 percent of the acceleration of gravity. Although there are relatively few very intense earthquake records available at present, maximum ground accelerations of more than the acceleration of gravity have been measured, and maximum structural response accelerations of at least two times gravity could be expected from earthquakes of this intensity. It is clear that during a very large earthquake structures designed using even the most recent recommendations for determining earthquake loadings could have to sustain substantial ductilities.

Because of the considerable importance of offshore platform structures and the severe consequences of loss of production, it is reasonable that a suitably cautious approach should be used in setting earthquake performance criteria and in choosing levels of earthquake loading for design. It is appropriate that a rational and detailed approach should be used to design such large structures. Probabilistic methods are now being used more widely for estimating levels of earthquake shaking and their expected frequency of occurrence. It is possible to estimate response spectra appropriate for various return periods. A detailed account of the seismic hazard analysis method, and results obtained, was given in Chapter 3.

The design acceleration response spectra given by the NZS 4203 code correspond to earthquakes with return periods of the order of a hundred years or so, scaled down by the implied ductility factor of about four. Thus structures designed to that code could be expected to have their lateral load capacity exceeded about once every twenty years on average.

Since the existing platform structures in the North Sea have been designed for no damage from environmental loads with return periods of 100 years, it could be argued that a similar criterion should be applied with respect to earthquake induced loads. However, it is felt that this is probably too severe. Because of the large number of cycles of wave loading possible in a single storm with a return period of 100 years, the elastic response with no tensile stresses in the concrete is a reasonable requirement in order to avoid fatigue problems. By contrast, during a 100 year return period earthquake there would only be a few large amplitude cycles of ground motion, say ten at most. Allowable stress limits for low cycle fatigue loadings can be substantially higher than for large cycle fatigue loadings. Elastic response to earthquakes with return periods of 100 years is thus considered to be rather more conservative than criteria used for wave loading.

At the other extreme it could be considered that substantial lateral strength is already provided in platforms for resisting wave loading. It may be found that this strength is sufficient to prevent damage from small or moderate sized earthquakes and that the ductility demands from an extreme earthquake are not severe. Of course, the distribution of strength required for earthquake and wave loading may be somewhat different. In order to ensure satisfactory post-elastic behaviour during severe earthquakes it is desirable to direct inelastic deformations into selected areas, such as at the bottom of legs, where careful detailing could promote ductile flexural yielding.

It is possible that a realistic choice of design lateral load levels may be somewhere between the two levels discussed briefly above. These two approaches to proportioning strength to resist earthquake loadings probably represent rather extreme choices. In the following section two alternative platform types are considered and the implications of these approaches are examined. In the "conservative approach" elastic response to the 100 year return period earthquake is required. In the "less conservative approach" no additional strength is provided at the critical sections above the nominal amount required by design for wave loading. The performance is then checked during a very severe earthquake chosen to have a return period of 2000 years.

8.4 DETAILS OF DESIGN STUDIES

In order to determine the feasibility of designing offshore concrete gravity platforms for seismic effects, preliminary design studies of two different gravity platform configurations were carried out. Aspects of particular interest were the required layout and distribution of strength, and also the ductility demands at critical sections in the structures during severe earthquake shaking. It was beyond the scope of this research to determine optimum platform layouts or economic feasibility. Therefore the platform configurations chosen were based on existing designs.

The platforms designed in this study were intended to be sited at the Maui gas field, which is located off the west coast of New Zealand in a water depth of approximately 105 m. It is understood that further offshore developments will be required there in the near future to supplement the existing Maui A steel jacket structure. It was assumed that approximately

12000 tonnes of topside equipment would be required on the proposed platform. This mass is similar to that present on the existing Maui A platform structure. It was also expected that pipelines would be used to take gas and condensate ashore so that no substantial storage would be required on the platform. The 100 year return period design wave is currently estimated to be 22 m in height [8.11]. Both platform types were assumed to use high strength concrete with a compressive cylinder strength of 60 MPa.

The first platform type considered was based on the North Sea cantilever type platforms. The existing Frigg TP1 gas production platform was used in almost the same water depth as at the Maui field and would appear to have had similar functional requirements. The overall layout of the platform assumed for this study is shown in Fig. 8.1. A 10 m deep foundation penetrating skirt was assumed around the perimeter of the base. Previous studies [8.9] have highlighted the problem of providing sufficient lateral resistance to sliding. This problem should be eased by providing skirts to help key the platform in place. Because of the larger overturning effects expected on the foundation due to earthquake loading, the horizontal dimension of the Frigg platform base was increased from 72 m to 80 m. Only two legs were used to support the deck of the Frigg platform. It was considered that this could be undesirable for earthquake resistance as this configuration offers little resistance to rotational inertia effects about an axis between the tops of the two legs. The three leg proposal avoids this problem. It would allow the connection between the legs and deck to be pinned if required, thus avoiding the need to detail the top regions of the legs for possible plastic hinging. The use of three legs provides a torsionally stronger system, the symmetry being a desirable feature for earthquake resistance. The actual dimensions of the legs were varied, depending on the design level of earthquake loading chosen.

The second platform type considered was a hybrid steel and concrete structure developed for use in the China Sea in almost the same water depth existing at the Maui field [8.12, 8.13]. The layout of this framed platform is shown in Fig. 8.3. Torus shaped concrete footings are located at the base of each of the four concrete legs. These footings are sunk down into the seabed (depending on conditions) to achieve required founding. Three horizontal concrete beams span across each of the four sides of the platform. The concrete beams and columns are 10 m in diameter, and are hollow. The upper part of the structure is made from hollow steel tubular members, forming a truss on top of which the steel deck is placed.

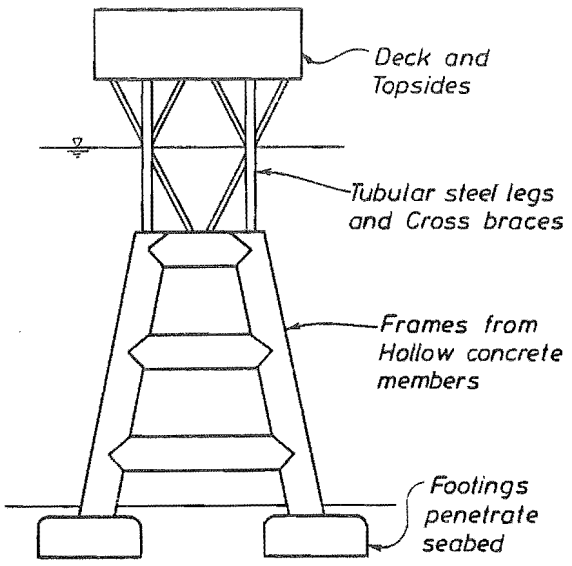

Fig. 8.3 Layout of Hybrid Frame Platform

The technology for constructing the hollow concrete members has been developed for building submerged concrete tunnels which are formed in sections and prestressed together. The upper steel sections would be fabricated as for other steel jacket structures. An interesting

construction sequence is suggested by the designers as shown in Fig. 8.4. The concrete substructure is built up in two halves in a dry dock (a). The dock is then flooded and the halves are floated out (b) and fitted with steelwork and footings (c). The two halves are located next to each other, joined by a central hinge (d) and rotated around to be joined together (e). The completed concrete support structure would then be towed out and put in place at the field (f,g). The footings would be jetted down into the seabed (h) and the deck would be floated over the top (i).

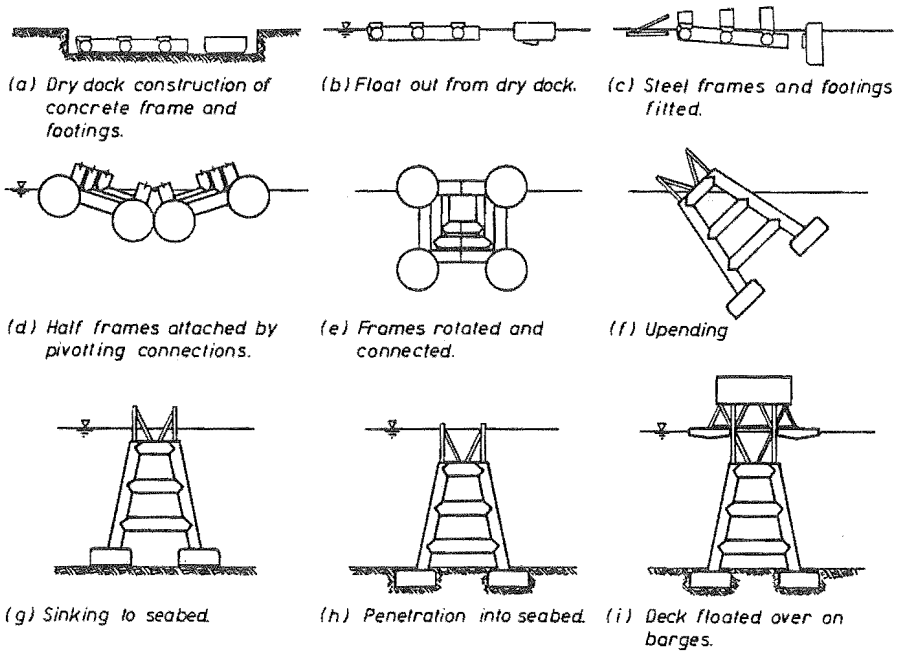

Fig. 8.4 Construction Sequence for Hybrid Platform

The hybrid platform would appear to have some advantages over the conventional North Sea type. The main advantage is that less material is used. By not having the massive base which is used on the North Sea structures the large added and contained water mass contributions to the seismic inertia are avoided. Although wave loading may not be critical for structures such as these used at the Maui field, the wave effects are lessened considerably by the use of the relatively small steel members in the vicinity of the water surface, where wave loading is most severe. The concrete frames may offer an efficient system for resisting lateral loading induced by waves and earthquakes.

8.5 DYNAMIC ANALYSIS OF RESPONSE TO EARTHQUAKE EXCITATION

A brief feasibility study of both the three leg North Sea and the hybrid platform types was carried out to assess the suitability of each for use at the Maui offshore field with regard to earthquake resistance. The two alternative levels of earthquake design load discussed in Section 8.3 were considered for each. The various platform designs were checked using dynamic time history analyses with artificially generated earthquake records. A trial and error procedure was required to determine suitable member geometries which could sustain the actions predicted by the dynamic analyses.

The dynamic analysis program used was RUAUMOKO [8.14], a two dimensional inelastic frame time history analysis program. This was discussed more fully in Chapter 2.

The acceleration response spectra used for the design of these structures were those recommended by the draft revisions to New Zealand Standard NZS 4203 which were discussed in Chapter 3. These represent an up to date estimate of design spectra appropriate

for New Zealand, based on recent seismic hazard analysis research. A suite of artificial earthquake records matching the proposed elastic spectra for soft ground were generated and presented in Chapter 5. These were used as ground acceleration histories for the dynamic analyses. The levels of earthquake intensity used in these analyses corresponded to 100 year and 2000 year return period events. The draft revision proposals for NZS 4203 enable the acceleration response spectra to be scaled according to the return period required.

Results of most interest from the analyses were the envelopes of nodal displacements and member actions. Where elastic design criteria were applied, the distribution of maximum bending moments and axial forces induced in the members were found, and checks were made for maximum bending stresses and required levels of axial prestress. In analyses of platforms responding to very severe 2000 year return period earthquakes, checks were made to determine where the strength of the structure was exceeded. Levels of inelastic deformation imposed during the response were also found. Also of interest was the magnitude of the shear stresses in the members during this level of excitation. Simple checks were made on likely foundation performance including the calculation of factors of safety against sliding and bearing failure.

8.6 DYNAMIC ANALYSIS MODELS

The two-dimensional dynamic analysis model used for the North Sea type platform is shown in Fig. 8.5. It should be noted that the three legs are in a triangular plan arrangement. Although the three legs in the actual platform are not intended to be in the same plane, as is assumed in the model, three dimensional effects were not expected to be overly important as the tops of the legs were assumed to be perfectly pinned. The dynamic analysis model used for the hybrid steel and concrete platform is shown in Fig. 8.6. This two-dimensional model represented only a half of the total structure. Rigid end blocks were considered to be present in the junction regions of members in the hybrid platform.

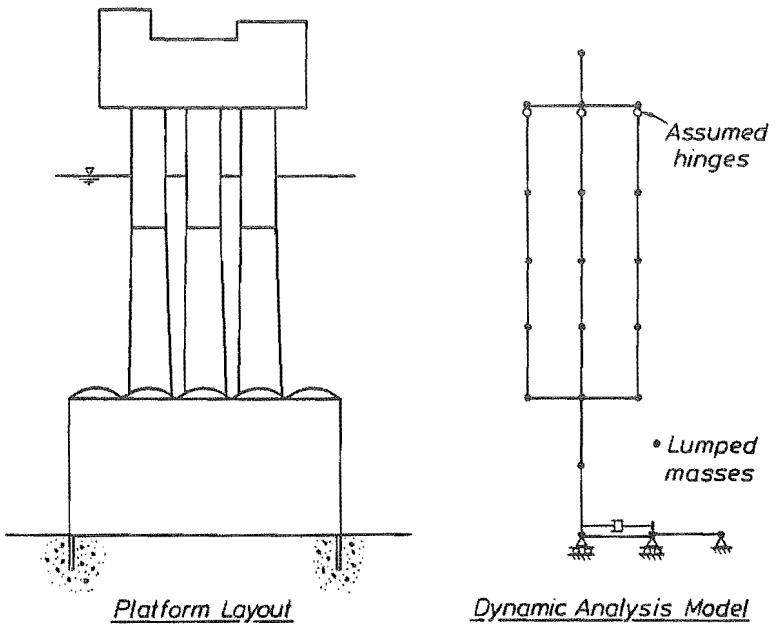

Fig. 8.5 Layout and Dynamic Analysis Model of North Sea Type Platform

The assemblage of members used at the base of the North Sea type platform, and the bottom of each leg in the hybrid structure, were included to model the soil-structure interaction effects. One flexural beam member, one truss member and one dashpot member was used. The flexural beam was given appropriate axial and flexural stiffness to model the soil flexibility, and the parallel dashpot member was included to model the expected soil damping. The inelastic truss member was connected in series with the beam and dashpot members to model

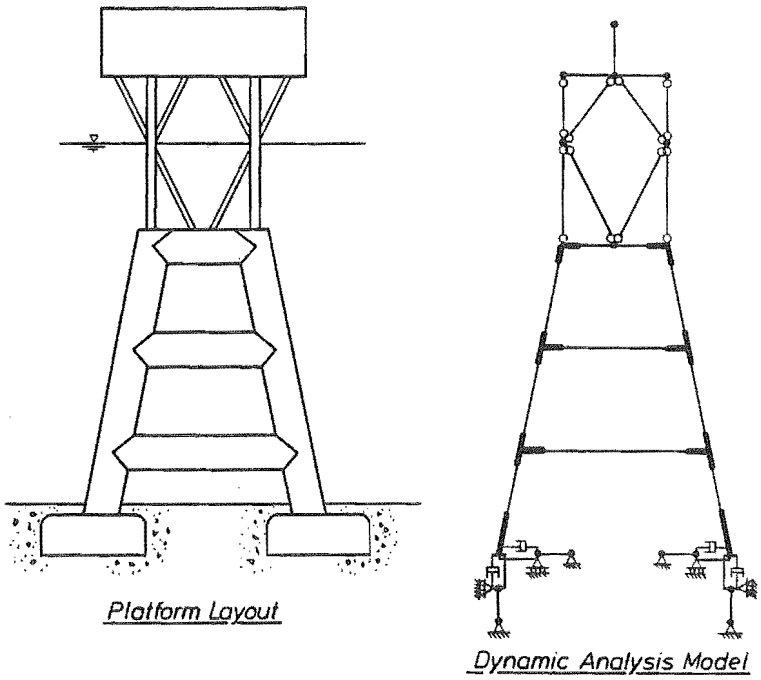

Fig. 8.6 Layout and Dynamic Analysis Model of Hybrid Platform

possible sliding of the platform base or leg footing over the seabed. The axial stiffness in the member was made large and the yield force was set equal to the calculated sliding resistance which could be mobilized.

For the conservative design approach the concrete members in each platform were required to remain uncracked during the 100 year earthquake so the uncracked member properties were assumed in the model. For the analysis of response to the 2000 year earthquake the cracked member stiffnesses were calculated based on the theoretical results presented in Chapter 7, in which the cracked flexural stiffness depended on the level of axial load and the longitudinal reinforcement index. Cracked stiffnesses were used in the less conservative design analyses for both the 100 year and 2000 year responses. Where the members were tapered, such as in the legs of the North Sea type platform, appropriate average properties were assumed in the model.

Lumped masses were used at the nodes. All hollow submerged members were assumed to be flooded and the full mass of contained water was divided between the end nodes for each member. Added water mass was calculated for most members assuming an added mass coefficient of 1.0. However for very large members, such as for those representing the massive base on the North Sea type platform, added mass coefficients of less than 1.0 were appropriate. The method of determining added mass coefficients by Liaw and Chopra [8.15], presented in Chapter 2, was used.

For the inelastic analyses, flexural strengths of the hollow circular members were estimated using the charts of ideal flexural capacity presented in Chapter 7. It was assumed that an area of nonprestressed reinforcement equal to 1 percent of the gross section area would be present in the members in addition to any prestressed reinforcement required to control cracking at the design loading level. In the North Sea type platform the variation of axial load in the leg members was quite small and a constant yield moment, independent of axial load, was used. In the hybrid structure substantial variations of axial load were induced in the members and interaction behaviour between flexural strength and axial load was assumed. The program RUAUMOKO has several different options available for specifying interaction behaviour for concrete members and Fig. 8.7 shows the form of the interaction chosen for these members. P_{yc} and P_{yt} are the ultimate axial forces in compression and tension respectively. M_o is the flexural capacity with zero axial load. M_b and P_b are the so-called balanced moment capacity and axial load but need not correspond to the actual balanced

failure conditions in the member. Between the ultimate compression capacity and the balanced point a linear variation is assumed. A linear variation is also assumed between the ultimate tension capacity and the pure flexure point. Over the axial load range between zero and the assumed balanced axial force a cubic dependence of moment capacity on axial load is assumed. Two additional moment capacities M_{1b} and M_{2b} are specified which determine the coordinates of the interaction curve at axial loads of $2P_b/3$ and $P_b/3$, respectively. The four points are used to determine the unique cubic variation. The interaction behaviour is assumed to be symmetrical about the axial load axis.

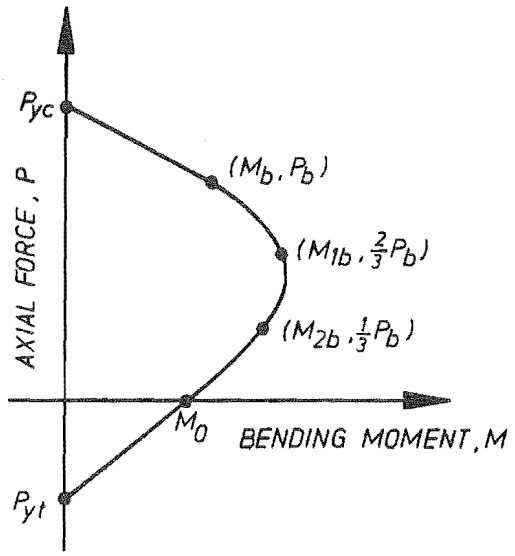

Fig. 8.7 Axial Force versus Yield Moment Interaction

The program RUAUMOKO incorporates flexural members which form concentrated plastic hinges at the member ends. Many different hysteresis rules are available but simple elasto-plastic behaviour was used in this study.

8.6 SOIL-STRUCTURE INTERACTION MODELLING

The interaction of the platforms with the seabed was modelled in the dynamic analyses using the simple rotational and translational spring and dashpot models discussed in Chapter 2. A number of assumptions were necessary in making use of the idealised soil compliance functions. In Chapter 2 the frequency dependent nature of the compliance functions was investigated and it was concluded that this could be adequately taken account of by using constant values of spring and dashpot properties, based on the dominant frequency of the rotational response of the platform base.

In the theoretical development of the compliance functions by Veletsos and Verbic [8.16] the idealised soil is assumed to be a linearly-elastic homogeneous half-space. During earthquake shaking with the intensity of interest most soil deposits will be responding in a highly non-linear manner. Normally foundation materials are far from being a homogeneous half-space. Even the assumption of a layered site of infinite horizontal extent would be an over simplification for most onshore sites, but it may be reasonable for many offshore sites. Also, for sites with fairly uniform material over considerable depth, it would be expected that the shear wave velocity and shear modulus would increase with depth. The effective (secant) shear modulus also varies with the level of shear strain. Thus it becomes necessary to estimate an appropriate depth at which the small strain shear modulus should be estimated. An allowance must then be made for the reduction in shear modulus which would occur due to the level of shear strain which would be imposed on the soil.

Little information is published on the actual foundation conditions which exist at the site of the proposed Maui Field platform, although a broad soil description is available for the Maui A site [8.17]. In these studies the simple assumption was made that the foundation material would be a dense sand. For these preliminary feasibility checks it was considered that this simplification was adequate. Many of the North Sea cantilever structures have been installed on dense sand foundations. From the indications of this study it is likely that soils any less competent than dense sand would be inadequate for founding this type of platform in seismically active areas. The other important consideration for this study was the general lack of information on the dynamic properties of soils. The publication of soil moduli and damping factors by Seed et al [8.18] is a useful source of information, mainly for cohesionless materials (sands and gravels). The average soil parameters suggested for dense sands with relative density of about 90 percent were used in this study.

The soil compliance functions given by Veletsos and Verbic [8.16]] are dependent on the shear modulus of the soil. The appropriate shear modulus was calculated at a depth equal to half the base dimension of the platform. For the hybrid structure, a depth of half of one footing diameter below the underside of each footing was used. The variation of shear modulus with depth given by Seed et al [8.18] was used. The metric version of this expression was given by Eqn. 4.4. The parameter K_2 gives the influence of the soil shear strain amplitude which is varied from the small strain value of 10^{-4} percent up to a large strain value of 1 percent. From the results of the site response studies presented in Chapter 4 a soil shear strain of 0.1 percent was chosen which resulted in the shear modulus being about 24 percent of the small strain value. In calculating the mean effective stress in Eqn. 4.4 a coefficient of lateral earth pressure of 0.6 (slightly over-consolidated) was assumed which resulted in a mean effective soil stress equal to approximately 75 percent of the effective overburden stress.

The unit weight of the saturated dense sand was taken as approximately 16 kN/m^3 and the Poisson's ratio was assumed to be 0.3.

The loading rates associated with earthquake response are quite fast and it is possible that undrained behaviour would occur even in sands. In finer grained cohesive soils it is most likely that only undrained response could occur. The soils beneath offshore platforms are fully saturated and it is possible that any modes of deformation in the soil associated with dilatational strains could not occur. Deformations which involve pure distortion, such as in simple shearing, can occur by dislocation of the soil grains relative to each other with no overall volume change. However, dilatational deformations, such as in simple extension, involve volume changes which require a migration of pore water through the soil matrix. As there is probably insufficient time for this drainage to occur, the soil response will be governed by the incompressible pore water. The critical factor is whether the soil is sufficiently permeable to allow drainage to occur. It may be that some drainage can occur in sands. It is likely that this depends on the actual strain rate, the permeability of the soil and the length of drainage path. It is somewhat beyond the scope of this study to investigate this problem. Instead, the extreme behaviour was assumed with either full drainage or no drainage.

The implications of this behaviour are extremely important with regard to the dynamic response of platform structures subject to earthquake shaking and it is noteworthy that this phenomenon does not seem to be widely discussed in the literature. If the foundation material is effectively undrained then dilatational deformations could not occur. Rigid body rotations and vertical deformations of platform footings both involve dilatational strains in the soil. Horizontal translation of the base and soil requires only distortional strains. Thus horizontal translational compliance could still develop but rotational and vertical compliance could not. For the platform designs checked as part of this study, analyses were carried out both with and without rotational and vertical compliance. Vertical earthquake effects were not investigated in these feasibility studies, so for the North Sea type platform, with only a single base, modelling of vertical soil compliance was not required. However, in modelling the hybrid frame structure, which had isolated footings, vertical compliance was considered.

8.8 FOUNDATION CAPACITY ASSESSMENT

Although this study was principally concerned with the effects of earthquake shaking on the concrete platforms, it was necessary to check the feasibility of the possible designs with respect to foundation capacity. This was done in only a cursory manner. It would be necessary for a much more detailed check of foundations to be carried out in a complete design.

Probably the two main requirements with regard to the foundation design of a platform are that adequate factors of safety should be available against bearing failure and horizontal sliding. Results from this and other studies [8.9] indicate that it may not be possible to prevent platforms from undergoing small sliding displacements during very severe earthquakes. However, it is reasonable that no sliding should take place in a moderate level of shaking such as for the design level earthquake. It is desirable that a bearing failure should not occur, even in the most extreme earthquake.

Most methods for estimating soil bearing capacity are based on Terzaghi's classical work on shallow foundations. Terzaghi's formula for the bearing capacity of an infinitely long strip foundation placed on the soil surface is based on analysis of an assumed rupture mechanism in which soil wedges are pushed out from each side of the footing and is given by Eqn. 8.1.

$$Q/B = 0.5\,\gamma B N_\gamma + qN_q + cN_c \qquad (8.1)$$

where Q is the ultimate bearing capacity per unit length, B is the width of the footing, γ is the effective unit weight of the soil, c is the soil cohesion and q is the surcharge per unit length. N_γ, N_q and N_c are the bearing capacity coefficients and depend on ϕ, the angle of internal friction of the soil.

N_γ is the gravity coefficient and is determined from consideration of a rough foundation on cohesionless, frictional soil with non-zero weight. N_q is the surcharge coefficient and is determined from consideration of a rough foundation on weightless, cohesionless, frictional soil with a log-spiral failure surface. N_c is the cohesion coefficient and is determined from consideration of a rough foundation on frictionless, cohesive soil in which the logarithmic spiral failure surface degenerates into a circle. The surcharge and cohesion coefficients were derived by Prandtl for a weightless soil and are related by the expression in Eqn. 8.2.

$$N_c = (N_q - 1)\cot\phi \qquad (8.2)$$

The three terms in Eqn. 8.1 are considered to be independent and can be added to give a conservative estimate of the actual bearing strength. It should be noted that the ultimate bearing capacity applies to the soil at the point of failure and that safe bearing loads can be derived by dividing by a factor of safety. Factors of safety for soils are normally taken in range of 2 to 3, depending on the type of loading being considered. The value of the angle of internal friction must be appropriate to the conditions of loading. For a drained analysis effective stress strength parameters would be used. For an undrained analysis immediate stability is usually critical and total stress strength parameters would be used.

The Terzaghi bearing capacity formula has been adapted by various researchers for use on isolated footings with inclined and eccentrically applied loads. Failure of an isolated footing involves some form of rupture zone around the ends of the foundation. The bearing capacity formula has been modified to include empirical shape factors for various simple footing shapes [8.19] and to allow for the effects of depth of footing embedment and inclination of load from vertical [8.20]. Eccentric loadings on footings can be treated as concentric loadings on an equivalent "effective area" A_e so that the geometric centre of the effective area coincides with the centre of the applied load. The effective width B_e of the footing with a vertical load applied at an eccentricity e is found using Eqn. 8.3.

$$B_e = B - 2e \qquad (8.3)$$

Hansen [8.21] introduced a more general form of the bearing capacity formula which, in the special case of a footing on a horizontal ground surface reduces to Eqn. 8.4.

$$Q/A_e = 0.5\, B_e N_\gamma s_\gamma d_\gamma i_\gamma + (q+c\cot\phi)N_q s_q d_q i_q - c\cot\phi \qquad (8.4)$$

Q is now the ultimate bearing capacity and $A_e = B_e L$ is the effective area of the footing which has effective width B_e and actual length L. The s, d and i factors account for the footing shape, embedment depth and load inclination. The subscripts γ and q refer to the gravity and surcharge terms.

Considerable reduction of bearing capacity can result where the applied load is inclined to the vertical. For friction angles ϕ between 30° and 45° approximate expressions for the load inclination factors have been derived by various researchers. The relationships given by Eqns. 8.5 and 8.6 were proposed by Hansen [8.21].

$$i_q = [1 - 0.5H/(V + A_e c \cot\phi)]^5 \qquad (8.5)$$

$$i_\gamma = [1 - 0.7H/(V + A_e c \cot\phi)]^5 \qquad (8.6)$$

where H and V are the horizontal and vertical components of the applied load. The term in the square brackets should not be taken as less than zero. In reality the bearing capacity does not reduce to zero when the lateral component of applied load becomes large, but will retain some small value.

The shape factors and depth of embedment factors do not differ greatly from unity.

The lateral resistance of a simple footing to sliding can be estimated using a number of methods. It is normally considered to be a combination of frictional resistance on the underneath and sides of the footing together with active/passive effects on the ends. For the base of a concrete gravity platform such as those used in the North Sea there are often foundation penetrating skirts which will increase the resistance to lateral sliding. There are many modes of failure which can occur in this case [8.22] depending on the particular geometry and soil properties. Local passive failure can occur at each skirt, or a sliding plane could develop through the skirt tips, or there could be a deep-seated failure.

A paper by Hansen [8.23] gives a convenient simplified method for determining bearing capacity for drained, undrained or partially drained soils. Implicit in the method is an estimate of the lateral sliding resistance and the residual bearing capacity after sliding has occurred. The method was used in this study for checking the factors of safety against bearing capacity and horizontal sliding failures.

The Hansen method for partially drained failure in sands involves carrying out a stress analysis using total stresses and loads on the assumed critical plane beneath the footing. In simple terms, an equivalent cohesion is calculated in the sand and the bearing capacity for a cohesive soil is calculated. The method as applied in this study is summarised below.

The critical plane is assumed to be just beneath the platform base or, if skirts are present, a horizontal plane through the skirt tips. It is expected that the soil within the skirts will have an enhanced strength due to the confining action of the skirts and would not fail first.

The mean effective normal stress σ_m on the critical plane is calculated as in Eqn. 8.7. which assumes that the mean effective normal stress is equal to 65 percent of the effective vertical stress σ_1. It is also assumed that the soil is completely consolidated under the excess overburden due to the buoyant weight of the platform. For a sand this would have occurred very soon after installation.

$$\sigma_m = 0.65\, \sigma_1 \qquad (8.7)$$

The equivalent cohesion c_u is calculated using the expression in Eqn. 8.8.

$$c_u = K\sigma_m \tag{8.8}$$

where $K = \sin\phi$ (8.9)

or $K = \tan\phi$ (8.10)

or $K = \sin\phi/(1-\sin\phi)$ (8.11)

Any of the above values of K can be used with Eqn. 8.9 being the most conservative and Eqn. 8.11 being the least conservative, implying some strength gain due to a decrease in pore pressure in a dilatant (dense) sand. Eqn. 8.11 was used in this work.

The bearing capacity formula for an undrained clay is then used which takes the form of Eqn. 8.12 in which N_c is the Prandtl bearing capacity factor given by Eqn. 8.13 and i_c is the load inclination factor.

$$Q/B_e = c_u N_c i_c + q \tag{8.12}$$

$$N_c = \pi + 2 \tag{8.13}$$

For a centrally loaded footing an angle v is defined by Eqn. 8.14 and the value of $N_c i_c$ becomes equal to the expression in Eqn. 8.15 and is shown in Fig. 8.8 as the full line.

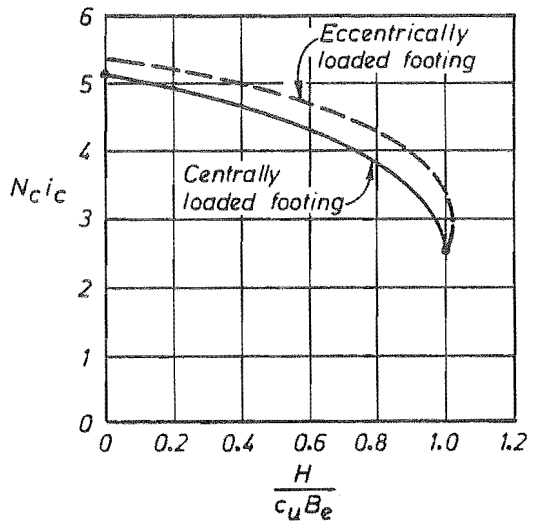

Fig. 8.8 Bearing Capacity Coefficients $N_c i_c$ for Undrained Clay (from Hansen)

$$\sin v = H/B_e c_u \tag{8.14}$$

$$N_c i_c = \pi + 1 - v + \cos v \tag{8.15}$$

For eccentrically loaded footings where the ratio of the load eccentricity to the actual footing width e/B is greater than about 0.05 the rupture mechanism takes an unsymmetrical form and the dashed line in Fig. 8.8 is found to be more appropriate. It should be noted that when the angle v reaches $\pi/2$ then fully developed sliding occurs. Thus the maximum implied sliding resistance H_{max} is given by Eqn. 8.16.

$$H_{max} = B_e L c_u \quad (8.16)$$

It can be seen from Fig. 8.8 that considerable reserve bearing capacity is predicted even after sliding has commenced.

In calculating the factor of safety against failure it is appropriate to consider only the transient loads. The permanent, constant loads, such as those due to overburden can be ignored. For example, in calculating the factor of safety (FOS) against bearing failure, the formula in Eqn. 8.17 was used, in which Q_u was the ultimate bearing capacity on the potential failure plane, Q_o was the total overburden load on the potential failure plane without the platform present and Q_a was the total load on the potential failure plane with the platform in place.

$$FOS = (Q_u - Q_o)/(Q_a - Q_o) \quad (8.17)$$

8.9 WAVE LOADING ANALYSIS

Lateral load design of the existing North Sea platforms has been governed by wave loading considerations and much previous research has been directed at providing information about wave characteristics and the forces induced on submerged bodies by waves. As it was expected that wave loading would not govern the lateral load design of platforms used off the coast of New Zealand, or other earthquake prone areas, only a simple approach was used for the wave loading analysis of these proposed designs.

Fully developed sea states which would be encountered during storms are probably best described using probabilistic methods. Although there is a well established trend between wave height and wave length which is supported by theoretical analysis, real storm seas tend to be very confused, irregular combinations of many different wave sizes, shapes and directions of propagation. Techniques are now available for the probabilistic determination of wave effects on structures. Starting from observed wave statistics power spectra can be derived, and with the use of transfer functions and analysis in the frequency domain, probabilistic estimates of forces, stresses and deflections in the platform structures can be made [8.24].

The simplest wave theory available is linear (Airy) wave theory. Although more complex, higher order theories have been shown to give better agreement with real sea waves, the difference in effect on platform structures is not great. It appears that the earlier North Sea structures were designed using simple linear wave theory approximations to storm waves. Most sea states will be dominated by large waves from a particular direction with a reasonably distinct wave height and period. In the North Sea wave heights between about 20 m and 31 m (trough to crest) have been considered as representative of the 100 year storm wave. For the existing Maui A platform a 22 m design wave was used.

The dispersion relation arising from the linear wave theory is given in Eqn. 8.18. This relates the circular frequency ω to the gravitational acceleration g, the wave number k and the undisturbed water depth d.

$$\omega^2 = gk \tanh(kd) \quad (8.18)$$

or $$\omega^2 \approx gk \quad (8.19)$$

where $$k = 2\pi/\lambda \quad (8.20)$$

In many cases the hyperbolic tangent function is very close to unity and the approximate "deep water" expression given in Eqn. 8.19 is applicable. λ is the wavelength and is normally about fifteen times the trough to crest wave height H, but in steep waves, which usually

induce the most severe loading on the legs of typical gravity platforms, λ/H can be as low as ten.

Linear water waves cause water particles to undergo elliptic orbits with amplitudes which decay with an inverse exponential dependence on depth. The horizontal water particle displacement x, velocity v and acceleration a, which are functions of depth z and time t, are given by Eqns. 8.21 to 8.23. The depth is measured positive upwards from the still water level.

$$x(z,t) = 0.5\,H\,\{\cosh[k(d+z)] / \sinh kd\}\,\sin\omega t \tag{8.21}$$

$$v(z,t) = 0.5\,\omega\,H\,\{\cosh[k(d+z)] / \sinh kd\}\,\cos\omega t \tag{8.22}$$

$$a(z,t) = -0.5\omega^2 H\,\{\cosh[k(d+z)] / \sinh kd\}\,\sin\omega t \tag{8.23}$$

Vertical motion is also produced which induces forces on submerged structures but generally the horizontal motion which generates transverse loading to platform structures which is more important.

The force per unit length F exerted on a stationary submerged cylindrical body with cross-sectional area A and diameter D by a fluid with mass density ρ is calculated using the well known Morison equation [8.25], which is given in Eqn. 8.24. The quantities a and v are the instantaneous fluid acceleration and velocity.

$$F = C_i \rho A a + 0.5\,C_d \rho D v^2 \tag{8.24}$$

The first term is the so-called the inertia force and C_i is the inertia coefficient. The inertia force can be thought of as having two components. The quantity $C_i\rho A$ represents the virtual or effective mass of fluid displaced by the cylinder and can be divided into the displaced fluid mass and an added fluid mass as indicated by Eqn. 8.25.

$$\begin{aligned} C_i \rho A &= \rho A + c_m \rho A \\ &= (1+c_m)\,\rho A \end{aligned} \tag{8.25}$$

The added mass represents the fluid mass which is entrained to the stationary cylinder and c_m is the added mass coefficient which is the ratio of the added mass to the displaced mass.

The second term in the Morison equation is the drag force. It should be noted that this is a function of the fluid velocity, and so reaches a maximum when the fluid velocity is a maximum. The inertia term reaches a maximum when the fluid acceleration is maximum. Because the fluid velocity and acceleration are out of phase with each other, the inertia and drag force maxima are also out of phase.

Inertia and drag coefficients have been obtained from experimental and theoretical research. The values have varied considerably but it appears that they may conservatively be taken as the values given in Eqns. 8.26 and 8.27 [8.24].

$$C_i = 2.0 \tag{8.26}$$

$$C_d = 1.0 \tag{8.27}$$

For large members, such as those used in concrete offshore platforms, the inertia forces dominate and it has been found reasonable to ignore the drag terms [8.24].

In members where the diameter is greater than about 20 percent of the wavelength then the inertia coefficient of 2.0 is overly conservative because the fluid accelerations can vary considerably over distance occupied by the member. This is the case with the large bases used

in the North Sea gravity platforms. Diffraction theory is normally used in this case to determine an appropriate inertia coefficient. In this study the results presented by Hogben and Standing [8.26] were used. They considered a large cylindrical submerged body with height h and radius r, as shown in Fig. 8.9. The equivalent horizontal inertia coefficient for loading by a wave with wave number k is given by Eqn. 8.28.

$$C_i = 1 + 0.75\,(h/2r)^{1/3}\,(1 - 0.3\,k^2\,r^2) \qquad (8.28)$$

where $h/d < 0.6$ and $0.3 < h/2r < 2.3$

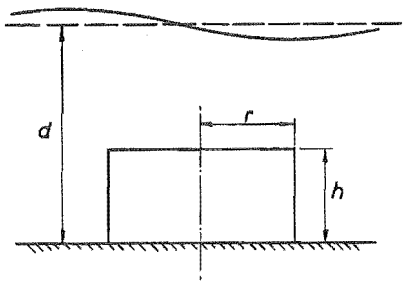

Fig. 8.9 A large Submerged Cylindrical Body

Assuming the deep water approximation in Eqn. 8.19 to be valid and ignoring the drag terms the expression which can be used to determine the maximum force per unit length induced on a cylindrical member with radius r reduces to Eqn. 8.29.

$$F(x) = 0.5\,C_i\,e^{-kx}\,\pi\,H\,r^2\,\omega^2 \qquad (8.29)$$

If the equivalent member diameter is greater than about 20 percent of the wavelength the expression for C_i in Eqn. 8.28 should be used, otherwise a value of 2.0 is appropriate. The variable x is now the distance measured vertically downward from the undisturbed water level. The expression can also be used for non-cylindrical members in which the diameter varies, by expressing the equivalent radius "r" as a function of the depth x also. This method was followed in calculating the wave loadings on the platform designs considered in this study.

It was assumed that a wind of 60 m/s would be blowing on an effective topside projected area of 1500 m^2 simultaneous with the wave loading. This represented about 10 percent additional lateral load.

8.10 FEASIBILITY STUDY RESULTS: NORTH SEA TYPE CANTILEVER PLATFORM

In this section the feasibility of a North Sea type concrete gravity platform is considered for the Maui offshore gas field. The first design is based on what is considered to be a "conservative design" method in which the platform is required to remain elastic during the 100 year return period earthquake. The second design assumes that only wave loading requirements would be satisfied and no significant additional strength would be provided in the structure. This is referred to as the "less conservative design". The layout of this platform was based on some of the existing North Sea platforms, particularly the Frigg TP1 platform, as this would seem to have had similar functional requirements to those assumed for the proposed Maui field platform.

8.10.1 Conservative Platform Design

The conservative design approach required that allowable stresses should not be exceeded in the structure during the 100 year return period earthquake. The final sizes of the platform members which were found to satisfy the conservative design approach are shown in Fig. 8.10. Also shown in that figure are the levels of axial prestress which were found necessary to prevent cracking of the concrete legs. The outside diameter of the legs varied from 15 m at the bottom to 12 m at a height of 50 m above the platform base, above which it was constant. The wall thickness varied linearly from 1.5 m at the base to 1.0 m at the deck.

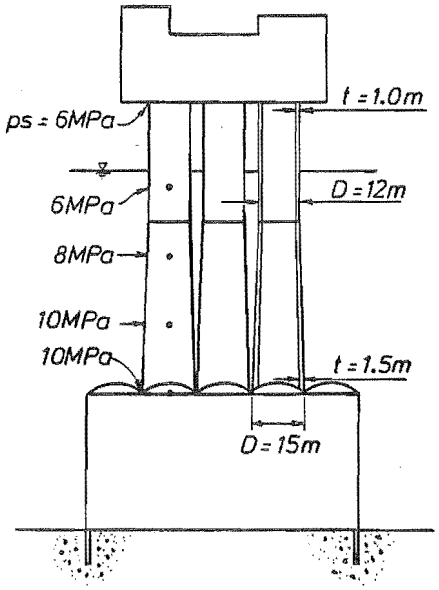

Fig. 8.10 North Sea Type Platform for Maui Site - "Conservative Design" Member Dimensions and Axial Prestress Levels

Fig. 8.11 shows the effects of the wind and wave loading on the the assumed platform layout. Overall bending moments induced in the structure and the lateral displacement profile are shown for both normal ($\lambda/H=15$) and steep ($\lambda/H=10$) 22 m high design waves. As can be seen from the figure, deck displacements of about 80 mm are expected. The flexural stresses induced in the legs at the connection to the base were approximately 6 MPa. The maximum induced soil stress just beneath the edge of the base due to the foundation overturning moment was approximately 110 kPa.

The envelope of moment demands caused by the 100 year return period earthquake on the uncracked structure is shown in Fig. 8.12. The fundamental natural period of vibration was 2.29 seconds. Three artificial earthquake records were used to give a reasonable match to the desired design acceleration response spectrum. Full foundation compliance (drained soil behaviour allowing rotational compliance) was assumed in these analyses based on a soil shear strain of 0.1 percent. The shape of the bending moment envelopes is similar to the envelope for wind and wave loading but the magnitudes are substantially larger. The maximum bending moment induced at the base of each leg was about 2.7 times the maximum moment caused by wave loading, and the maximum induced bending stress (moment divided by section modulus) was almost 15 MPa. Assuming the concrete had a compressive cylinder strength of $f_c' = 60$ MPa and that the tensile strength could be estimated using the NZS 3101 [8.27] suggestion of $f_t' = 0.6\sqrt{f_c'}$, then 10 MPa of axial prestress was required to prevent cracking due to tensile stresses. The maximum compressive stress induced in the concrete, due to gravity load, prestress and earthquake induced axial load and flexure, was about 29 MPa ($0.49f_c'$). Using the Hansen [8.23] approach the available factor of safety against sliding was 2.2, and the factor of safety against bearing failure was 3.9. The maximum deck displacement relative

to the seabed was approximately 380 mm and the maximum deck acceleration was about 0.42 g.

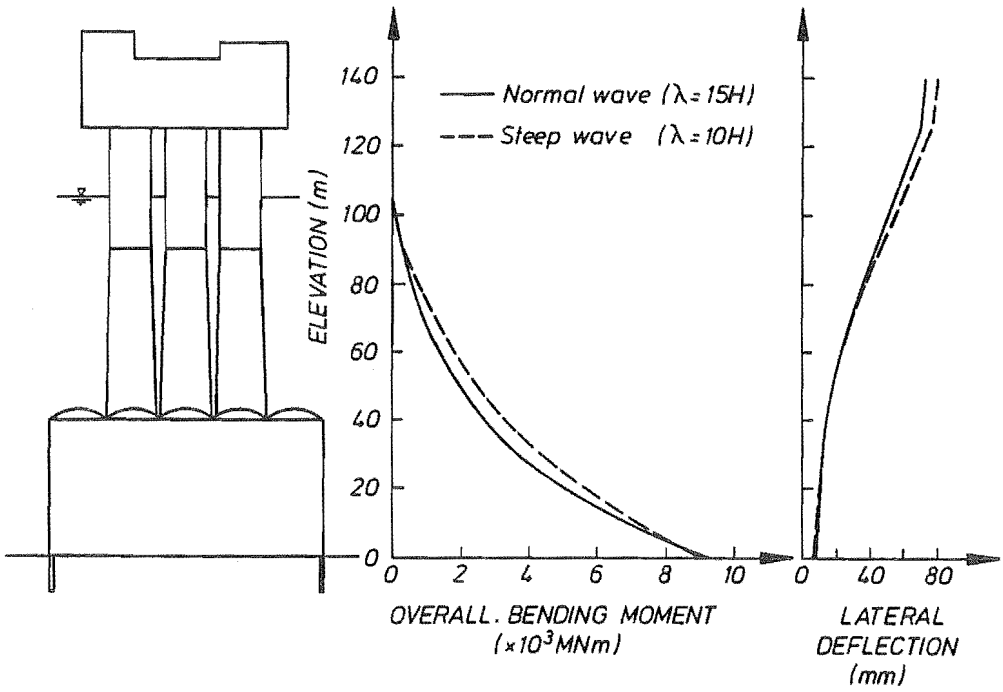

Fig. 8.11 North Sea Type Platform for Maui Site - "Conservative Design" Wind and Wave Effects

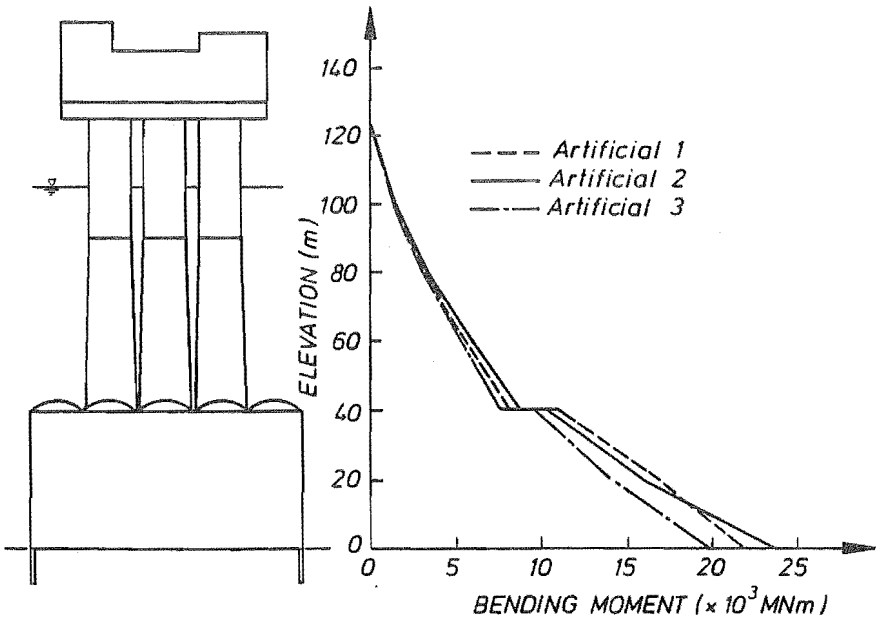

Fig. 8.12 North Sea Type Platform for Maui Site - "Conservative Design" 100 Year Earthquake Moment Demand - Full Soil Compliance ($\gamma = 0.1$ percent)

The flexural strength of the members was calculated based on the assumed member properties and reinforcement contents. An inelastic analysis was carried out using a factored up earthquake to give a record corresponding to a 2000 year return period. The leg members were assumed to be initially cracked in this case. Two analyses were carried out with soil

compliance based on different values of maximum soil shear strain. From site response analyses reported in Chapter 4 it was estimated that soil shear strains of about 0.1 percent were appropriate for the 100 year earthquake. However, for the 2000 year earthquake, with an intensity about three times greater, it was estimated that a maximum soil shear strain of about 1 percent was appropriate. An analysis of response to the 2000 year earthquake was performed assuming soil interaction based on maximum soil shear strains of both 0.1 percent and 1.0 percent. These analyses used both translational and rotational soil compliance. The resulting distributions of bending moments induced in the platform are shown in Fig. 8.13. Clearly, the lower soil compliance based on the lower soil shear strain results in significantly larger loads being induced in the platform structure. In the analysis based on 1 percent soil shear strain no members reached their flexural strength, whereas in the analysis based on 0.1 percent soil shear strain, the moments were about twice as large and a curvature ductility factor of 3.0 was imposed in the plastic hinges which formed at the bases of the legs. Also shown in Fig. 8.13 is the envelope of moment demand on one of the legs and the distribution of strength provided. Plastic hinging occurred only at the bottom of the leg. It was apparent from other analyses carried out that if the legs were tapered too quickly then hinging could occur at other locations. This may be undesirable as confining reinforcement would have to be provided at locations other than just in the bottom region of the leg.

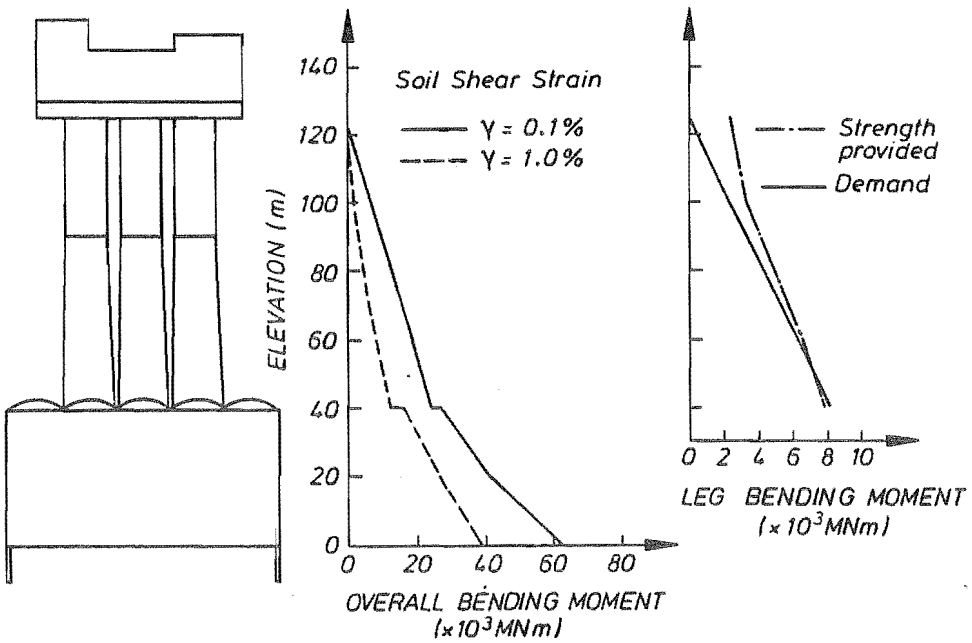

Fig. 8.13 North Sea Type Platform for Maui Site - "Conservative Design" 2000 Year Earthquake Moment Demand

The analysis showed that the platform base would slide over the seabed several times during the earthquake. A maximum sliding displacement of approximately 120 mm was predicted. The foundation bearing capacity at the level of the skirt tips was checked assuming that the maximum overturning moment coincided with maximum base shear (and sliding). The overturning moment at seabed level was extrapolated to the level at the skirt tips. For the analysis with soil interaction based on maximum soil shear strain of 0.1 percent the factor of safety against bearing failure was only 0.93 implying that a failure would occur. However, if the larger soil shear strain was used the overturning moments were reduced considerably and the factor of safety against bearing failure increased to about 1.3.

For the analysis based on soil shear strains of 0.1 percent the fundamental natural period of vibration of the cracked structure was 2.57 seconds, the maximum deck displacement relative to the seabed was 1500 mm and the maximum deck acceleration was about 1.78 g. For the analysis based on soil shear strains of 1.0 percent the fundamental period was 5.3 seconds, the

maximum relative deck displacement was 2700 mm and the maximum deck acceleration was 0.6 g. The very large relative displacement occurred because of the large soil flexibility. Of the 2700 mm displacement at the deck about 2000 mm was contributed by rotation of the platform base, 200 mm from translation of the base and 500 mm from flexure in the legs.

The envelopes of bending moment and shear in the platform legs for the 100 and 2000 year earthquakes are compared in Fig. 8.14. Both sets of results are from analyses based on soil shear strains of 0.1 percent, and thus it is thought that the 2000 year results are conservatively large predictions. The maximum shear force induced in one platform leg was about 150 MN. Assuming an area of 64 percent of the gross section area as being effective at resisting shear (refer Chapter 6) the imposed shear stress on the leg was about 3.7 MPa, which was large but could be designed for.

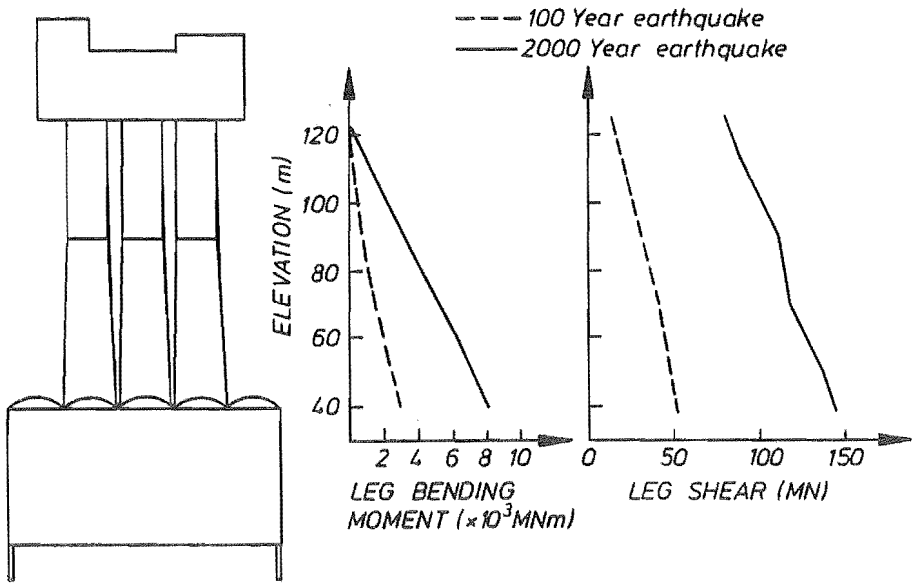

Fig. 8.14 North Sea Type Platform for Maui Site - "Conservative Design" Comparison of 100 and 2000 Year Earthquake Induced Leg Actions

As discussed in Section 8.6 it is possible that rotational soil compliance would not develop if the soil behaviour was effectively undrained. The influence of rotational compliance was investigated for the 100 year earthquake by carrying out a further analysis with the platform base node at seabed level restrained against rotation. The overall bending moment envelope obtained for the analysis with and without rotational compliance is shown in Fig. 8.15. For the case with no rotational compliance the maximum leg moments are slightly larger but there is very little difference between the two envelopes for the 100 year earthquake so rotational compliance appeared to have little influence. Also shown is the bending moment envelope for the 2000 year earthquake.

8.10.2 Less Conservative Design

The less conservative design philosophy assumed that no significant increase in strength would be given to the platform members above that which would have been provided for design of the structure for wave loading at the chosen New Zealand site. The final sizes of the members and levels of axial prestress which were found to satisfy the design requirements are shown in Fig. 8.16. The outside diameter of the legs was 12 m at the bottom and tapered to 10 m at a level 50 m above the base, above which it was kept constant. The wall thickness was 0.8 m and the axial prestress was 6 MPa over the entire height of the leg. The 6 MPa (0.1 f_c') prestress stress was considered to be a reasonable minimum, and although this level of

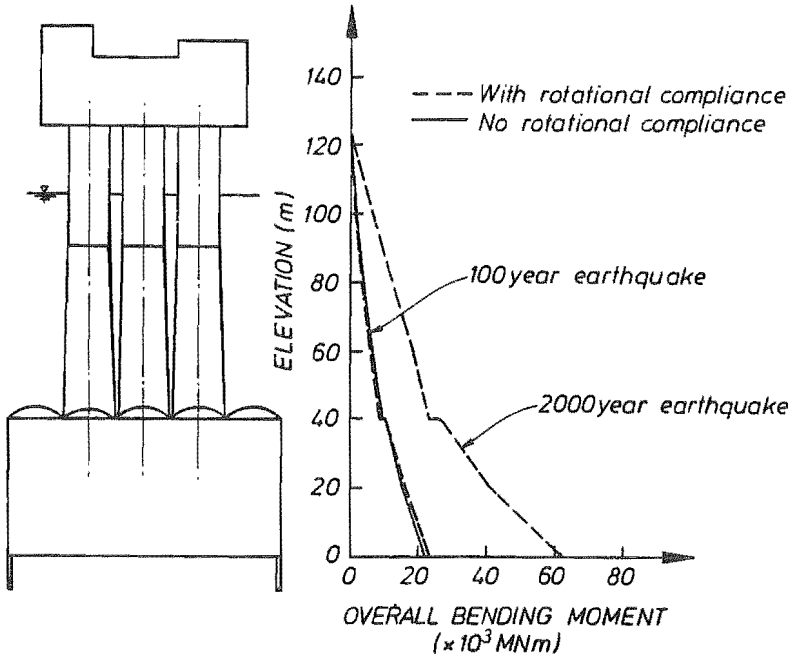

Fig. 8.15 North Sea Type Platform for Maui Site - "Conservative Design"
Influence of Rotational Foundation Compliance on Bending Moment Envelopes

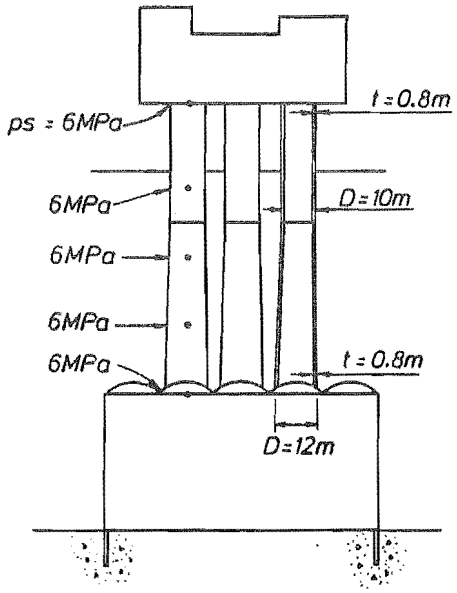

Fig. 8.16 North Sea Type Platform for Maui Site - "Less Conservative Design"
Member Dimensions and Axial Prestress Levels

prestress was not required by design above the critical section at the base, it was continued over the whole height. Prestressing is normally included in these members to enhance the fatigue resistance, crack control, water tightness and durability.

Fig. 8.17 shows the effects of the 100 year wind and wave loading on the platform. The members were assumed to be elastic and uncracked in this analysis. Overall bending moments induced in the structure and the profile of lateral displacements are shown for both normal and steep 22 m design waves. As can be seen from the figure, deck displacements of

approximately 140 mm are expected. The flexural stresses induced in the legs at the connection to the base were approximately 11 MPa. The maximum induced soil stress just beneath the edge of the base due to the foundation overturning moment was approximately 90 kPa.

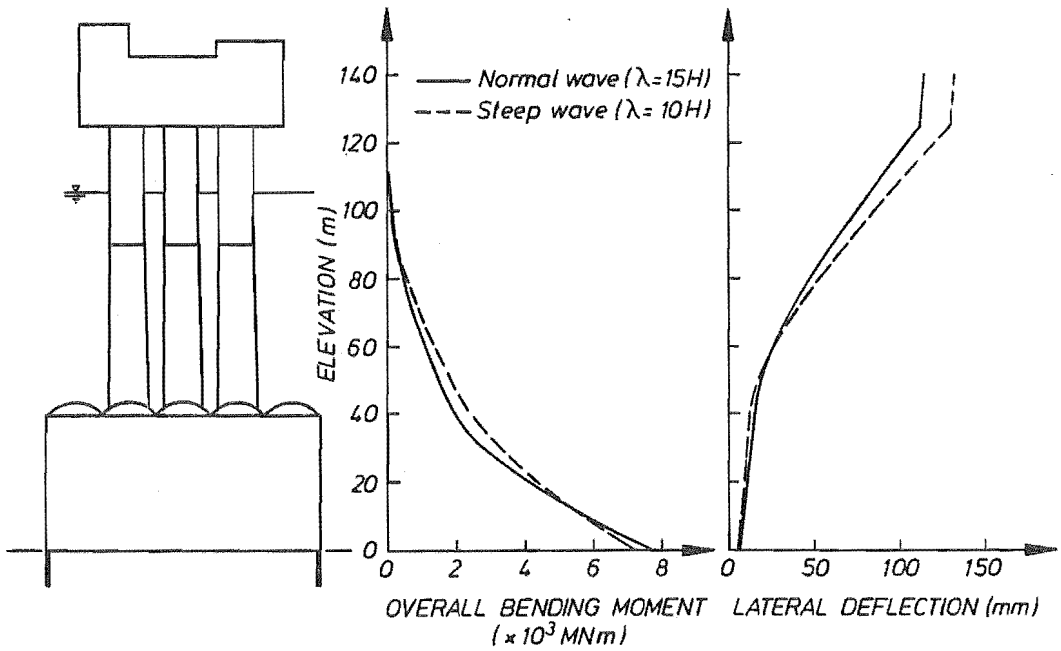

Fig. 8.17 North Sea Type Platform for Maui Site - "Less Conservative Design" Wind and Wave Effects

Earthquake response analyses were carried out for both the 100 and 2000 year earthquake levels and it was assumed that the legs would be cracked by both of these levels of excitation. Soil interaction based on maximum soil shear strains of 0.1 percent was assumed for both analyses. Results from the 100 year earthquake analysis confirmed that the legs would crack but no ductility was induced in any of the members as only about 65 percent of the flexural strength was mobilized. Two analyses were carried out to check the influence of rotational soil compliance. The overall bending moment envelopes on the platform are shown in Fig. 8.18. The moment demands for the 100 year earthquake were about twice as large as for wave loading and there appeared to be a more substantial difference between the results with and without rotational soil compliance.

For the 100 year earthquake analysis with full soil compliance the fundamental natural period of the cracked structure was 3.59 seconds, the maximum displacement of the deck relative to the seabed was 650 mm and the maximum deck acceleration was about 0.28 g. For the analysis assuming only horizontal compliance the fundamental period was 3.39 seconds, the maximum relative deck displacement was 450 mm and the maximum deck acceleration was 0.25 g.

For the 2000 year earthquake the analysis was only carried out using soil interaction based on soil shear strains of 0.1 percent as it was expected this would result in the most severe effects. This analysis used only translational (no rotational) soil compliance. The resulting envelope of overall bending moment induced in the platform are also shown in Fig. 8.18. Flexural yielding occurred at the base of the legs and a maximum curvature ductility factor of 2.4 was imposed in the plastic hinges. Fig. 8.19 shows the envelope of moment demand on one of the legs for the 100 and 2000 year earthquakes and the distribution of strength provided. Plastic hinging occurred only at the bottom of the leg. As in the conservative design it was apparent from other analyses carried out that if the leg was tapered too quickly then hinging could

occur at other locations. For example, instead of tapering to 10 m at the transition point the platform leg was tried with a taper to only 9 m. In this case the strength of the leg was insufficient to avoid plastic hinging at the transition point and substantially more flexural reinforcement would have been required in this region.

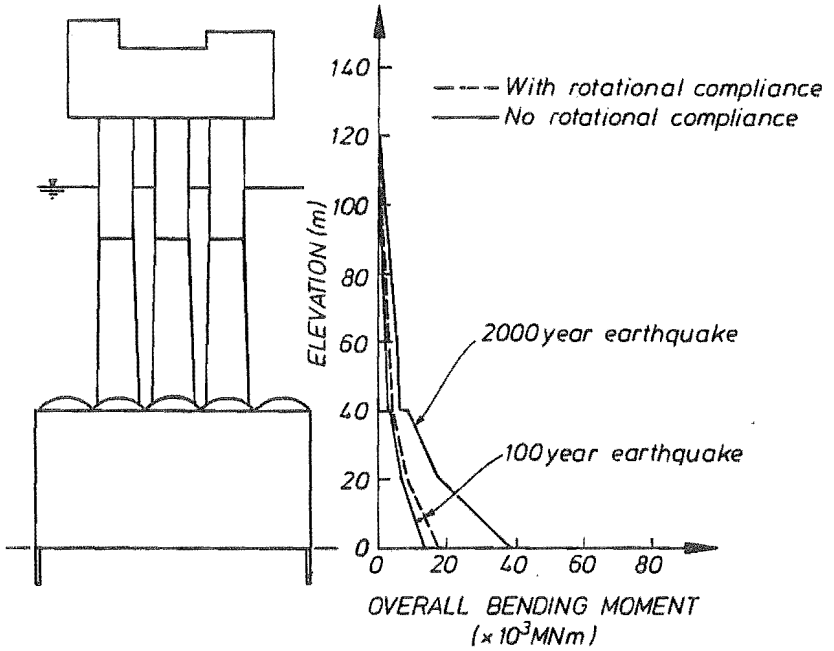

Fig. 8.18 North Sea Type Platform for Maui Site - "Less Conservative Design"
Bending Moment Envelopes for 100 and 2000 Year Earthquakes

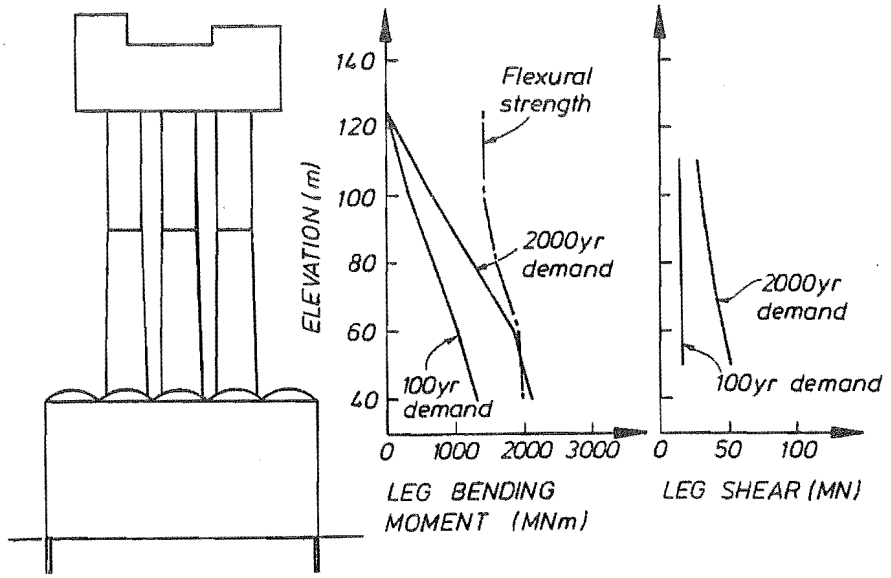

Fig. 8.19 North Sea Type Platform for Maui Site - "Less Conservative Design"
2000 Year Earthquake Bending Moment and Shear Force Envelopes in Legs
No Rotational Foundation Compliance

The analyses showed that during the 2000 year earthquake the maximum deck displacement relative to the seabed would be about 1100 mm and the maximum deck acceleration would be about 0.55 g. The platform base would slide over the seabed several times and a maximum sliding displacement of approximately 75 mm was predicted.

The foundation bearing capacity at the level of the skirt tips was checked assuming that the maximum overturning moment coincided with maximum base shear (and sliding for the 2000 year earthquake). The overturning moment at seabed level was extrapolated to the level at the skirt tips. For the 100 year earthquake the factor of safety against sliding was approximately 2.0 and the factor of safety against bearing failure was 3.8. For the 2000 year earthquake analysis with soil interaction based on maximum soil shear strain of 0.1 percent sliding occurred and the factor of safety against bearing failure was about 1.3.

The envelopes of shear in the platform legs for the 100 and 2000 year earthquakes are also compared in Fig. 8.19. Both sets of results are from analyses based on soil shear strains of 0.1 percent, and thus it is thought that the 2000 year results are conservatively large predictions. The maximum shear force induced in one platform leg was about 50 MN. Assuming an area of 64 percent of the gross section area as being effective at resisting shear the imposed shear stress on the leg was about 2.8 MPa and could be adequately designed for.

8.10.3 Comparison of Alternative Design Approaches

A summary of the results obtained from the dynamic analyses of the North Sea type platforms is given in Table 8.2.

Substantially more material is required in the legs of the platform designed using the conservative design approach. Although the level of protection against the onset of damage is higher in this structure than in the less conservatively designed platform the damage expected during the very severe 2000 year earthquake is about the same. The ductility demands in the structure with smaller legs are actually slightly less. The main reason for this is that the platform with the larger legs is stiffer, giving it a shorter fundamental period of vibration, and undergos a more vigorous seismic response in accordance with the design acceleration response spectrum. It was noticed when attempting to design the platform using the more conservative approach that increasing the size of members to satisfy allowable stress limits was often rather ineffective as the stiffness increased, the period reduced and the response increased, resulting in little,if any, reduction in maximum member stresses. An increase in member sizes to satisfy earthquake design requirements also leads to significant increases in wave loading although that was not expected to affect the design of these platforms. Flexible structures tend to respond less severely to earthquakes than stiff structures. Long period structures generally have lower response accelerations but the displacements tend to be larger. Provided that other design criteria, such as serviceability limit states, can be satisfied it would seem desirable to make a platform structure as flexible as possible.

A dominant feature of the North Sea type of platform is the very large base. Allowing for the water contained inside the base and the added water mass, the base contributes about 95 percent of the total seismic inertia of the structure. As this is rather rigidly attached to the seabed, and the lateral resistance to sliding relies mostly on the platforms own self weight, it is apparent that lateral sliding would be difficult to prevent in very severe earthquake shaking. For both of the platforms designed a minimum factor of safety against sliding of about 2.0 was available during the 100 year earthquake but sliding would occur during the 2000 year earthquake. This is considered quite satisfactory and, in fact, sliding acts as a base isolation mechanism and should limit the actions induced in the platform itself.

Another major factor affecting the response of these platforms was the stiffness of the underlying soil. Earthquake effects are propagated through the ground and into any structures which may be present. Studies such as those carried out in Chapter 4 indicate that substantial shear strains may be induced in soil deposits by earthquake shaking. It seems likely that during very large earthquakes soil may soften enough to effectively limit the magnitude of the ground accelerations and the level of motion input to structures. Levels of soil shear strain were estimated to evaluate soil structure interaction parameters but there was considerable uncertainty involved. For the 2000 year earthquake it was thought that the assumed soil shear strain level of 0.1 percent, used in most cases, was conservatively low.

The ductility demands in the members of these platform structures were very low, even in the extremely long return period earthquake events. Platforms designed to resist the quite severe loadings imposed by waves in excess of 20 m in height have considerable strength reserves and response even to extreme levels of earthquake shaking results in only modest ductility demands at the critical sections. This should enable a considerable relaxation of the requirements for quantities of transverse confining reinforcement given by design codes such as the New Zealand Concrete Design Code NZS 3101.

In summary, it appears that the less conservative design approach, in which the strength of the platform members was chosen to satisfy wave loading requirements only, resulted in a structure with adequate earthquake resistance. The alternative structure designed to a higher level of earthquake loading gave no significant advantage with respect to protection from very severe earthquakes. In practice it would be desirable to check the return period of earthquakes which would begin to cause damage in proposed platform designs.

Table 8.2 Summary of Results - North Sea Type Platform

Case	Item	Conservative Design	Less Conservative Design
Member Sizing	Bottom of leg OD / Thick.	15 m / 1.5 m	12 m / 0.8 m
	Transition OD / Thick.	12 m / 1.2 m	10 m / 0.8m
	Top of Leg OD / Thick.	12 m / 1.0 m	10 m / 0.8 m
Prestress	Maximum leg prestress	10 MPa	6 MPa
100 Year Wave	Deck displacement	80 mm	140 mm
	Leg bending stress	6 MPa	11 MPa
	Soil bearing stress	110 kPa	90 kPa
Fundamental Period	Uncracked (soil strain = .1%)	2.29 sec	3.10 sec
	Cracked (soil strain = .1%)	2.57 sec	3.39 sec
100 Year Earthquake	Member bending stress	15 MPa	18 MPa
	Deck displacement	380 mm	450 mm
	Deck acceleration	0.42 g	0.25 g
	FOS sliding	2.2	2.0
	FOS bearing failure	3.9	3.8
2000 Year Earthquake	Leg curvature Ductility	3.0	2.4
	Leg shear stress	3.7 MPa	2.8 MPa
	Deck displacement	1500 mm	1100 mm
	Deck acceleration	1.78 g	0.55 g
	Sliding displacement	120 mm	75 mm
	FOS bearing failure	0.93	1.3

8.10.4 Critical Section Detailing Requirements

As a further check on the feasibility of the design of a North Sea type platform for use in New Zealand conditions, the detailing requirements of the critical sections at the base of each leg were examined and a suitable layout of longitudinal and transverse reinforcement was determined. The example sections considered were appropriate to the less conservative platform design.

The outside diameter of the section was 12 m and the wall thickness was 0.8 m. 75 mm cover concrete was assumed on the inner and outer faces. A total area of nonprestressed longitudinal

reinforcement equal to 1 percent of the gross section area was assumed and sufficient prestressed reinforcement was provided to give 6 MPa of axial prestress.

Transverse reinforcement was designed to satisfy requirements for shear and confinement. From the dynamic analyses reported in this chapter it was found that the curvature ductility demands were very low compared with what might be expected in typical building or bridge structures. For design purposes it was conservatively estimated that the maximum curvature ductility demand in the potential plastic hinges at the leg bases would be 5. Confining reinforcement was proportioned according to the results of the theoretical study reported in Chapter 7. The effective axial load level was conservatively taken as the sum of the gravity and prestress forces at the section. Design for shear was carried out according to the recommendations made in Chapter 6. The design shear force was taken as the maximum shear predicted by the 2000 year earthquake analysis.

The final layout of reinforcement found to be suitable is shown in Fig. 8.20. The non-prestressed reinforcement could be provided by deformed 24 mm diameter (D24) bars spaced at approximately 150 mm centres around the inside and outside faces together with two inner layers of D20 bars at approximately 300 mm spacings. Transverse reinforcement could be provided by a system of 16 mm diameter plain round (R16) rectangular ties, circular spirals around the outside and cross ties through the wall. Some of the reinforcement could be prefabricated in cages about 1 m long and placed in the wall. Two cages are shown in Fig. 8.20 within the wall thickness as this allows for a greater area of transverse reinforcement to be provided in the circumferential direction. The prestressed longitudinal reinforcement could be provided by groups of solid or braided wire tendons positioned near the middle of the reinforcing cages as indicated.

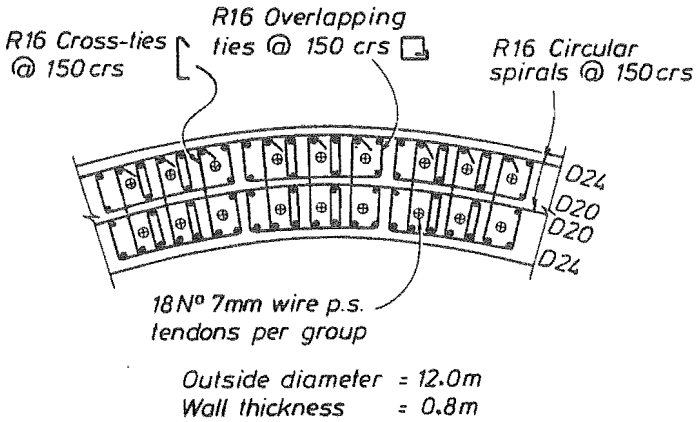

Fig. 8.20 North Sea Type Platform Reinforcement Layout at Leg Base Section - "Less Conservative Design"

8.11 FEASIBILITY STUDY RESULTS: HYBRID PLATFORM

The feasibility of a hybrid steel and concrete gravity platform is considered for the Maui offshore gas field. The first design is based on what is considered to be a conservative design method in which the platform is required to remain elastic during the 100 year earthquake. The second design assumes that only wave loading requirements would be satisfied and no significant additional strength would be provided in the structure. This is referred to as the "less conservative design". The layout of this platform was based on information published about this proposed design [8.12, 8.13].

8.11.1 Conservative Platform Design

As for the North Sea type platform, the "conservative design" philosophy required that allowable stresses should not be exceeded during the 100 year earthquake. The final sizes of the platform members which were found to satisfy the conservative design approach are shown in Fig. 8.21. Also shown in that figure are the levels of axial prestress which were necessary to prevent cracking of the concrete legs. It is likely that other layouts of wall thicknesses and levels of axial prestress would also satisfy the design requirements, but no others were investigated. The outside diameter of all of the hollow concrete frame members was 10 m. It was found necessary to make the wall thickness 1.25 m in the lower portion of the legs and 1.0 m in the lower beam members. A wall thickness of 750 mm was adequate in all other members. The maximum axial prestress required was 12 MPa in the lower beam members. 8 MPa prestress was required in the middle and lower portions of the legs and also in the middle level beam. Secondary effects due to the axial prestress forces in the members were included in the analysis but these effects were quite small.

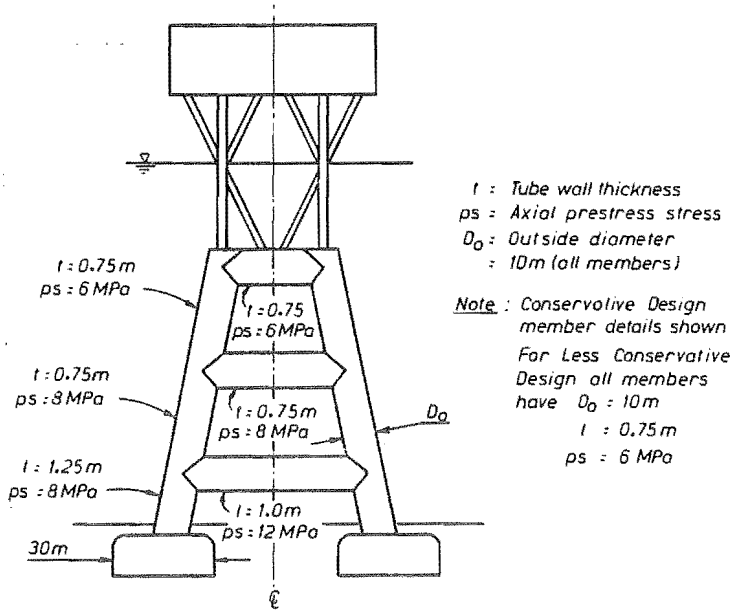

Fig. 8.21 Hybrid Platform - Concrete Member Sizes and Axial Prestress Levels

Bending moments, shears and axial forces are induced in the frames due to gravity loading. Relatively small moments arise from the self-weight of the beams. Because the beams were assumed to be flooded with water and had quite thick walls, it was found that buoyancy was not sufficient to overcome their own weight. Quite large moments could be induced in the lower legs depending on what rotational restraint was assumed on the footings.

The platform design incorporates an ingenious method for the controlled sinking of footings into the seabed [8.13]. A system of jets is incorporated to remove material from beneath the footings and allow the platform to settle. It is not clear what the final distribution of bearing pressures would be, or how much rotation of the footing could have taken place when the sinking operation was complete. Two cases were considered for this study. Firstly, it was assumed that no rotation of the footing would occur, which corresponded to the footing being fully fixed. Secondly, it was assumed that no moment restraint would be offered by the soil with the footing free to rotate. The bending moment and axial force distributions for these two cases, including axial prestress effects, are shown in Fig. 8.22. Fig. 8.23 shows the envelope of gravity load effects from the two analyses. In the dynamic analyses it was assumed that the footings would be restrained by the appropriate soil compliance effects.
Fig. 8.24 shows the combined effects of gravity, wind and 100 year wave loading on the assumed platform layout. Overall bending moments and axial forces induced in the structure

are shown for the 22 m high design wave. Only a steep wave was considered as this was expected to be more severe. Assuming uncracked behaviour maximum deck displacements of about 30 mm were predicted. The maximum flexural stresses induced in the legs were approximately 6 MPa. The maximum increase in induced soil stress just beneath the edge of a footing due to the foundation overturning moment was approximately 140 kPa.

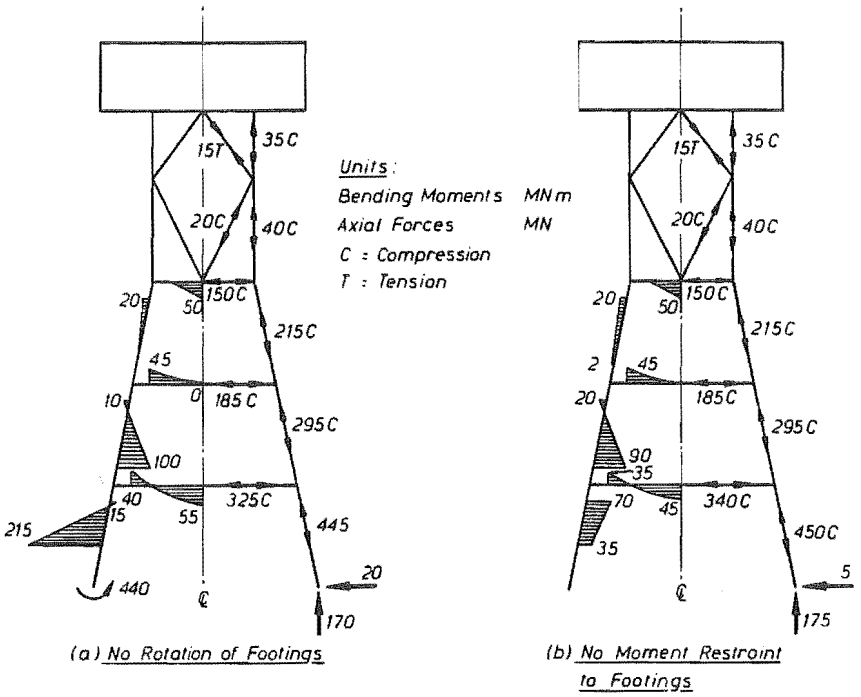

Fig. 8.22 Hybrid Platform - "Conservative Design" Gravity Load and Prestress Effects

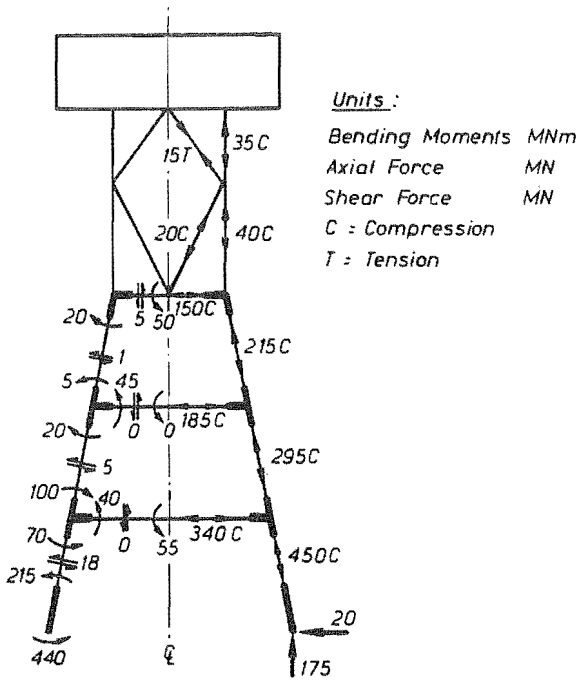

Fig. 8.23 Hybrid Platform - "Conservative Design" Envelope of Static Load Member Actions

Fig. 8.25a shows the envelope of actions from the 100 year earthquake loading assuming full soil compliance including horizontal, vertical and rotational components. The fundamental natural period assuming uncracked behaviour was 1.87 seconds. Fig. 8.25b shows the envelope

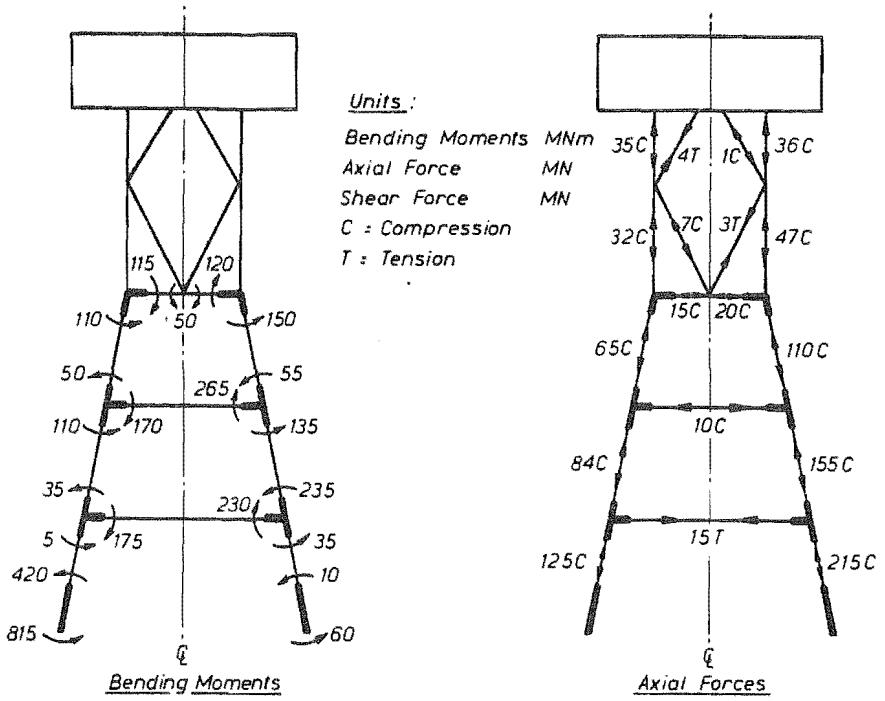

Fig. 8.24 Hybrid Platform - "Conservative Design" Gravity Load and 100 Year Wave Effects

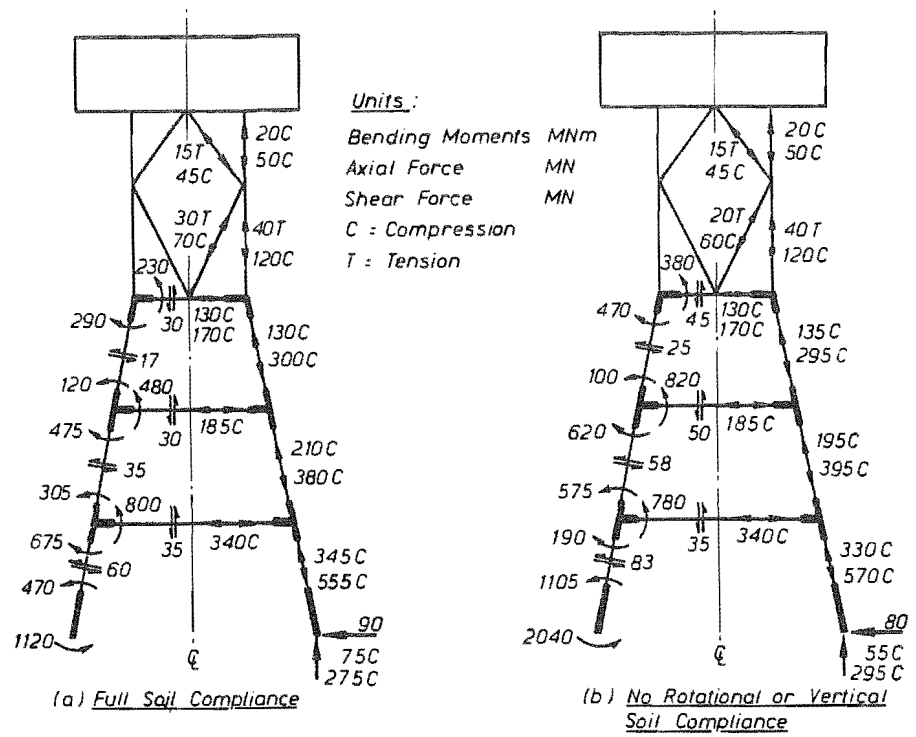

Fig. 8.25 Hybrid Platform - "Conservative Design" Envelopes of Actions - 100 Year Earthquake Including Gravity Loads and Prestress

of actions assuming that no soil drainage would occur and only horizontal compliance would be operative. In this case the fundamental period had reduced to 1.26 seconds. Member design was carried out for the worst combination of gravity and 100 year earthquake effects. At the critical sections the 100 year earthquake induced maximum tensile stresses of about 3 MPa and maximum compressive stresses of about 29 MPa ($0.48f_c'$) in the concrete. The available factor of safety against sliding was 2.7 and the factor of safety against bearing failure was 2.5. The maximum deck displacement relative to the seabed was about 280 mm and the maximum deck acceleration was about 0.58 g.

For the 2000 year earthquake response analysis the members were assumed to be cracked and the flexural strengths were estimated from the member sizes which satisfied the elastic stress limits for the 100 year earthquake. Two analyses were carried out, the first assuming full soil compliance and the second assuming only horizontal compliance.

The envelopes of bending moment, shear and axial force obtained from the analysis assuming full compliance are shown in Fig. 8.26a. The fundamental natural period of the cracked platform structure was 2.02 seconds. Although the actions are considerably larger than for the 100 year earthquake response, no ductility was required in the structure. The calculated sliding resistance of approximately 180 MN per footing was reached during the analysis but sliding displacements of less than 1 mm were predicted. The factor of safety against bearing failure was only 0.59 and thus a bearing failure was predicted. The maximum deck displacement was about 990 mm relative to the seabed and the maximum deck acceleration was about 1.6 g.

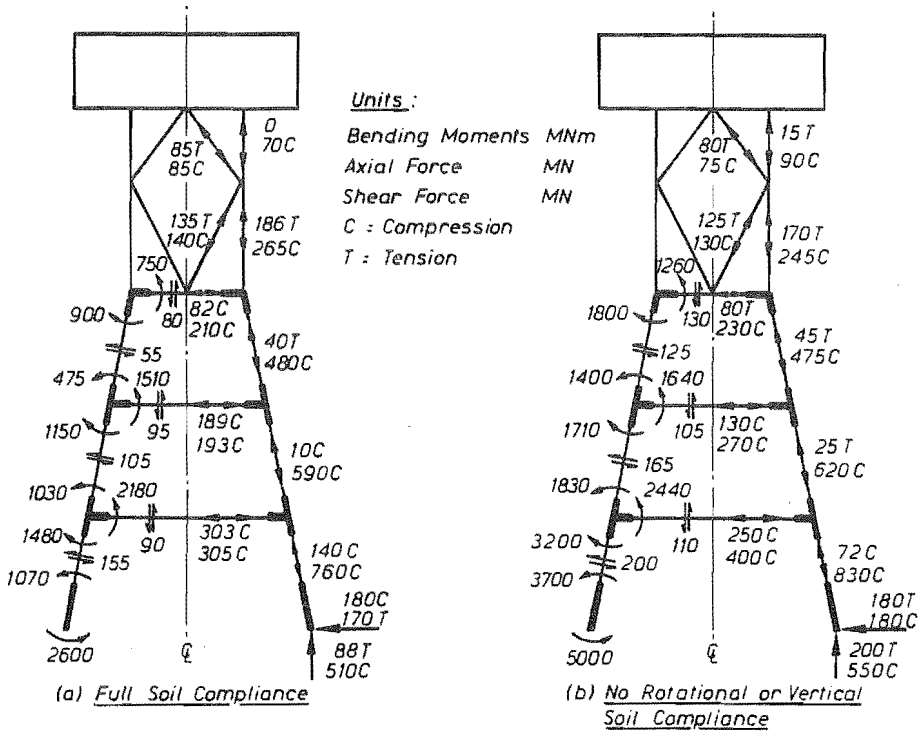

Fig. 8.26 Hybrid Platform - "Conservative Design" Envelopes of Actions - 2000 Year Earthquake Including Gravity Load and Prestress

The envelopes of bending moment, shear and axial force obtained from the analysis assuming undrained soil response and only horizontal soil compliance are shown in Fig. 8.26b. The fundamental period of this structure-soil system was 1.45 seconds. The maximum inelastic deformations predicted during the analysis, including curvature ductility factors and sliding displacements at the footings, are shown in Fig. 8.27. Maximum curvature ductilities of about 5.0 were imposed in the plastic hinge which formed in the middle portion of each leg just above the lower beam. The sliding resistance was exceeded at both footings and a maximum

sliding displacement of about 6 mm was predicted. Bearing failure was also predicted from this analysis with a factor of safety of only 0.42. The maximum deck displacement was about 630 mm and the maximum deck acceleration was about 1.5 g.

No attempts were made to restrict plastic hinging to either beam or column members. If it was thought desirable to encourage a beam sidesway mechanism to develop then capacity design methods could easily be used to avoid column hinging. However, the ductility demands are very modest and the axial load levels in the beams and columns are very similar due to the levels of axial prestress used. Such a requirement would also result in more strength being provided at critical column sections, which would seem to be unnecessary.

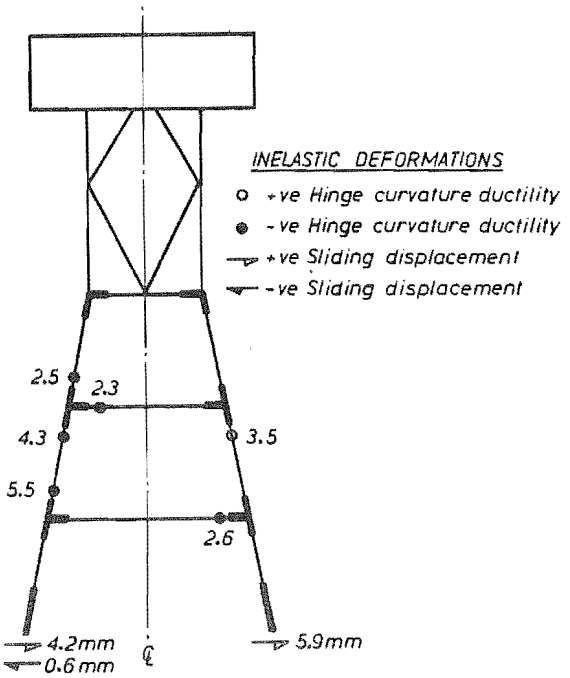

Fig. 8.27 Hybrid Platform - "Conservative Design" 2000 Year Earthquake Imposed Curvature Ductilities and Sliding Displacements (Horizontal Compliance Only)

The shear forces induced in the members were very large, particularly in the legs, where a maximum shear of 165 MN was predicted in the middle leg portion. This resulted in a maximum nominal shear stress of approximately 12 MPa which would be impossible to design for. This rather alarming result is due to the very short shear span relative to the member diameter. The clear span between beams of 20 m is only twice the member diameter.

8.11.2 Less Conservative Platform Design

The less conservative design philosophy assumed that no significant increase in strength would be given to the platform members above that which would have been provided for design of the structure for wave loading at the chosen New Zealand site. The final sizes of the members and levels of axial prestress which were found to satisfy the design requirements were shown in Fig. 8.21. All concrete members were assumed to to have outside diameter of 10 m, wall thickness 750 mm and axial prestress of 6 MPa.

Fig. 8.28 shows the combined effects of gravity, wind and 100 year wave loading on the assumed platform layout. Overall bending moments and axial forces induced in the structure are shown for the 22 m high steep design wave. Assuming uncracked behaviour maximum deck displacements of about 50 mm were predicted. The maximum flexural stresses induced in the

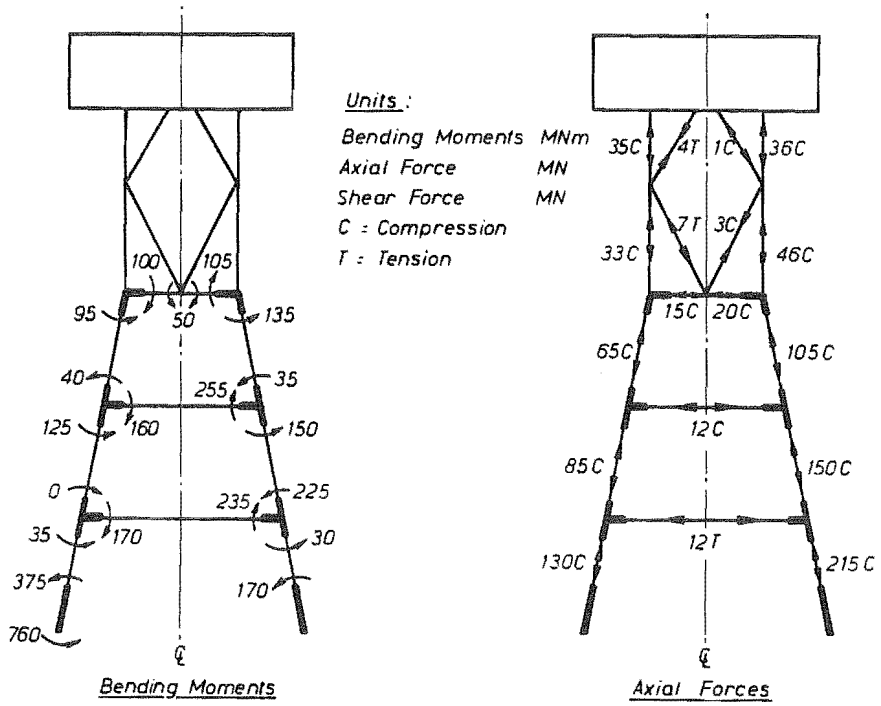

Fig. 8.28 Hybrid Platform - "Less Conservative Design" Gravity Load and 100 Year Wave Effects

legs were approximately 8 MPa. The maximum increase in induced soil stress just beneath the edge of a footing due to the foundation overturning moment and increased footing reaction was approximately 175 kPa.

Earthquake response analyses were carried out for both the 100 and 2000 year earthquake levels and it was assumed that the legs would be cracked by both of these levels of excitation. Soil interaction based on maximum soil shear strains of 0.1 percent was assumed for both analyses. It was also assumed that no drainage would occur in the soil and only horizontal compliance would be effective. The fundamental natural period of the structure was 1.53 seconds. Results from the 100 year earthquake analysis, shown in Fig. 8.29, confirmed that the legs would crack but no ductility was induced in any of the members as only about 65 percent of the flexural strength would be mobilized. The moment demands are about three times as large as for wave loading. The maximum deck displacement predicted was approximately 260 mm and the maximum deck acceleration was about 0.54 g. The maximum horizontal shear under a single footing was approximately 100 MN which gave a factor of safety against sliding of about 1.8 and the factor of safety against bearing failure was calculated as being 2.1.

The envelopes of bending moment, shear and axial force obtained from the 2000 year earthquake analysis are shown in Fig. 8.30a. The maximum inelastic deformations predicted during the analysis, including curvature ductility factors and sliding displacements at the footings, are shown in Fig. 8.30b. Maximum curvature ductility factors of about 9.5 were predicted in the lower beam plastic hinges. The sliding resistance was exceeded at both footings and a maximum sliding displacement of about 4 mm was predicted. A bearing failure under the footings was predicted with the available factor of safety being only 0.39. The maximum deck displacement was about 620 mm and the maximum deck acceleration was about 1.3 g.

As for the more conservatively designed hybrid frame platform, the shear forces induced in the members were very large. A maximum shear of 210 MN was induced in the lower leg portion. This resulted in a maximum nominal shear stress of approximately 15 MPa which, again, would be impossible to design for in conventional reinforced concrete members.

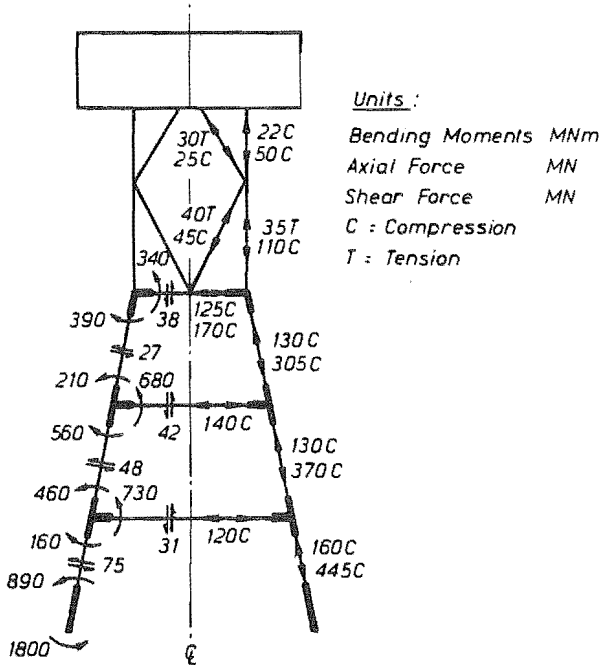

Fig. 8.29 Hybrid Platform - "Less Conservative Design" Horizontal Soil Compliance Only Envelopes of Actions - 100 Year Earthquake Including Gravity Loads and Prestress

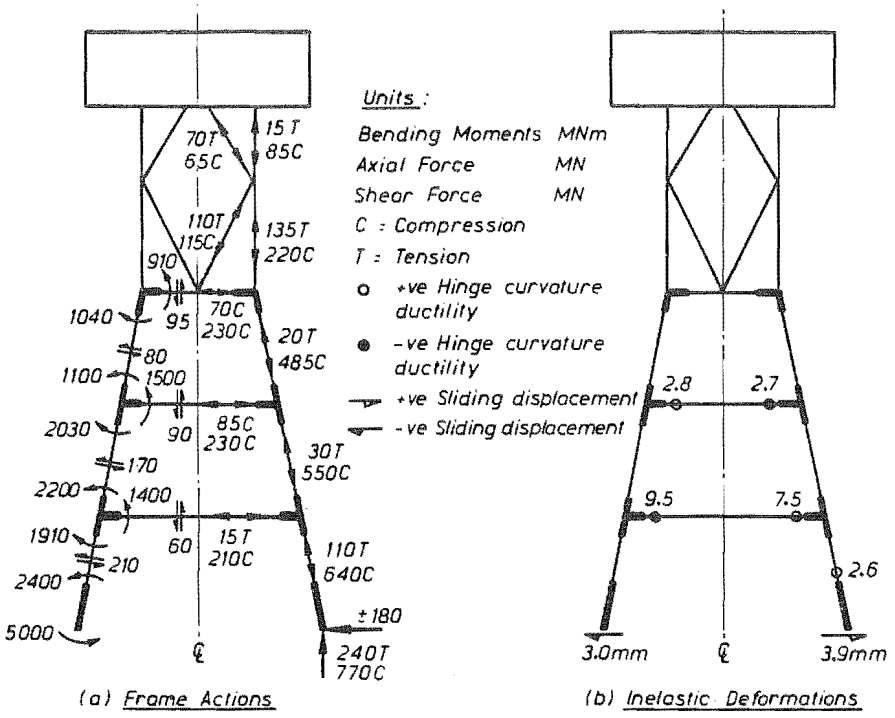

Fig. 8.30 Hybrid Platform - "Less Conservative Design" Horizontal Soil Compliance Only Envelopes of Actions - 2000 Year Earthquake

8.11.3 Comparison of Alternative Approaches to Hybrid Platform Design

A summary of the results obtained from the dynamic analyses of the hybrid type platforms is given in Table 8.3.

As in the alternative design approaches to the North Sea type platform, there are clear penalties arising from the conservative design approach in which the structure is required to remain elastic and uncracked during response to the 100 year earthquake. The member sizes in the critical areas increase substantially, as do the levels of axial prestress required. Balancing this, there are of course benefits in the form of increased protection against damage in the conservatively designed structure.

Platforms designed to both the conservative and less conservative approaches had adequate factors of safety against foundation failures for the 100 year earthquake loading. Sliding of the footings occurred in both cases for the 2000 year earthquake although the magnitude of sliding displacements was quite small in each case. Bearing failures were predicted beneath the footings of both platforms. To provide additional protection against this the footing sizes would have to be increased or the soil bearing capacity improved.

Curvature ductility demands from the 2000 year earthquake were only quite moderate and although about twice as large in the less conservatively designed platform the maximum curvature ductility of about 10 could be adequately detailed for.

Table 8.3 Summary of Results - Hybrid Type Platform

Case	Item	Conservative Design	Less Conservative Design
Member Sizing	Lower leg OD / Thick.	10 m / 1.25 m	10 m / 0.75 m
	Lower beam OD / Thick.	10 m / 1.0 m	10 m / 0.75 m
	Other members OD / Thick.	10 m / 0.75 m	10 m / 0.75 m
Prestress	Maximum leg prestress	12 MPa	6 MPa
100 Year Wave	Deck displacement	30 mm	50 mm
	Leg bending stress	6 MPa	8 MPa
	Soil bearing stress	140 kPa	120 kPa
Fundamental Period	Uncracked (soil strain = .1%)	1.26 sec	1.35 sec
	Cracked (soil strain = .1%)	1.45 sec	1.53 sec
100 Year Earthquake	Member bending stress	14 MPa	19 MPa
	Deck displacement	280 mm	260 mm
	Deck acceleration	0.58 g	0.54 g
	FOS sliding	2.7	1.8
	FOS bearing failure	2.5	2.1
2000 Year Earthquake	Leg curvature Ductility	5.0	9.5
	Leg shear stress	12 MPa	15 MPa
	Deck displacement	630 mm	620 mm
	Deck acceleration	1.5 g	1.3 g
	Sliding displacement	6 mm	4 mm
	FOS bearing failure	0.42	0.39

The critical factor affecting feasibility of this type of platform is the shear design of the members. It would be necessary to provide shear resistance in the members to match the maximum shear forces induced by very large earthquakes. The normal capacity design approach for determining design shear forces in concrete members involves considering

simultaneous plastic hinges at each end of the member. The ideal shear strength is made equal to at least the shear force corresponding to flexural overstrength in the hinges. As these structures did not undergo very large inelastic deformations, simultaneous hinging did not occur and the maximum shear forces were slightly less than the maximum possible. The maximum levels of shear induced by the 2000 year return period earthquake in both of the alternative designs were excessive and could not be designed for. This rather alarming result was due to the very short shear span relative to the member diameter. The 20 m clear span between beams was only twice the member diameter.

8.12 COMPARISON OF NORTH SEA AND HYBRID PLATFORM TYPES

The major advantage of the hybrid steel and concrete platform over the North Sea type platform is in the amount of material used. Comparing the platform layouts based on the less conservative design approach for each, the North Sea type platform used approximately 120 000 tonnes of prestressed concrete whereas the hybrid structure required only about 54 000 tonnes of prestressed concrete and an estimated 3000 tonnes of structural steel. These figures are for the support structures only with no deck or topside mass included. The frame action used in the hybrid structure provides an efficient method of resisting lateral loads and allows the same earthquake levels to be resisted using less material. The hybrid frame avoids the large added water masses attracted to the massive base structure in the North Sea type platform.

While the flexural strength and section ductility demands could be provided in both structures without major difficulty, foundation design and member shear capacity appeared to be inadequate in the hybrid structure. Sliding of the both structures over the foundation was predicted during very severe earthquake shaking. Bearing capacity was only just adequate beneath the North Sea type platform but inadequate for the hybrid structure. More detailed foundation analysis methods may show the foundations to be adequate. No consideration was given to problems associated with liquefaction of the soil beneath the platform structures.

The shear strength of the concrete members in the hybrid structure was quite inadequate to resist the shear forces imposed by the very severe earthquake level. As discussed in section 8.11.3 this was because the members were relatively short in comparison with their span. The maximum shear forces predicted in the North Sea type platform during the 2000 year earthquake could be designed for.

The members in the North Sea type platform were considerably longer and more flexible than the members in the hybrid structure, which resulted in longer natural periods of vibration. This gave reduced levels of acceleration response together with increased maximum displacements relative to the seabed. If the larger relative displacements can be tolerated in these structures it would seem desirable to aim at quite flexible platforms for use in highly seismic areas. This is expected, as longer period structures tend to be isolated from ground motion. The absolute response accelerations become small and the maximum displacements approach the maximum ground displacement as the period of vibration becomes very long. An extreme example of such a structure would be the so-called tension leg platform in which the buoyant deck floats at the sea surface and is anchored down to the sea bed by tensioned vertical legs or cables which are laterally flexible.

8.13 CONCLUSIONS OF FEASIBILITY STUDIES

1. The North Sea type platform could be adequately designed using either the conservative or the less conservative design approach. Although the conservative design approach resulted in greater protection of the structure from the onset of damage, there was a considerable penalty in the amount of material and the levels of axial prestress required in the leg members. For response to the severe 2000 year return period earthquake shaking, the ductility demands were quite modest for both platforms with maximum curvature ductility factors of not more than 5 required at the critical sections

at the base of each leg. Design of the leg members for shear was also found to be feasible. Adequate factors of safety against overall platform sliding and bearing failure were available.

2. The hybrid steel and concrete platform structure used much less material than the North Sea type platform while satisfying the same general design requirements. Flexural strength and adequate ductility could be provided in the framed structure but shear design of the legs would not be possible in the platform layouts examined. Such a framed structure may be feasible for resisting earthquake effects in other configurations or where the seismicity levels were lower.

3. Earthquake loading effects rather than wave loading would govern the design of offshore concrete platforms of the type considered for use in the area off the west coast of the North Island of New Zealand, or other seismically active areas with similar water depths. For the site considered the 100 year return period earthquake loading was two to three times greater than the 100 year return period wave loading. The extreme level earthquake imposed deformations on the platforms which were a further factor of two to three times greater and generally caused the platforms yield at the critical sections and also slide over the seabed.

4. Soil-structure interaction was found to have a very significant effect on the levels of dynamic response experienced by platform structures during earthquake excitation. It was also highlighted in this study that, due to the rapid loading rates which occur during earthquakes and the saturated nature of the foundation, drainage of even relatively permeable granular soils may not have time to take place. If not, then deformation modes in the soil involving dilatational strains, such as rocking and vertical movements of a platform base, would be restrained. Soil compliance may thus only occur for horizontal translational motions of the platform base but not for rotational or vertical motions. Analyses both with and without vertical and rotational soil compliance were carried out. In general it seems conservative to ignore the possible compliance but this is not always the case. Further investigation of this phenomenon is required.

8.14 REFERENCES - CHAPTER 8

8.1 Dowrick, D. J., "Modes of Failure of Concrete Platforms", Concrete in the Oceans, Technical Report No. 2, CIRIA/UEG, Cement and Concrete Association, Department of Energy, United Kingdom.

8.2 "Statfjord 'B' Technical Briefing Booklet", Mobil Exploration Norway Incorporated, April 1983, 23 pp.

8.3 Moksnes, J., "Inclined Slipforming - Slipforming of Large Freestanding Inclined Towers of Varying Diameter and Wall Thickness", Nordisk Betong, Journal of the Nordic Concrete Federation, Vol. 1-2: 1986, pp 46-50.

8.4 "Rules for the Design, Construction and Inspection of Offshore Structures", Det norske Veritas, Norway, 1977, 67 pp. and Appendices.

8.5 API RP 2A, "API Recommended Practice for Planning, Designing and Constructing Fixed Offshore Platforms", American Petroleum Institute, Washington D.C., Thirteenth Edition, Jan. 1982, 96 pp.

8.6 "Design and Construction of Concrete Sea Structures", FIP Recommendations, 4th Edition, 1985.

8.7 BS 6235 : 1982, Code of Practice for Fixed Offshore Structures", British Standards Institution.

8.8 Watt, B. J., Boaz, I. B. and Dowrick, D. J., "Response of Concrete Gravity Platforms to Earthquake Excitations", Journal of Petroleum Technology, March 1978, pp 318-324.

8.9 Watt, B. J., Boaz, I. B., Ruhl, J. A., Shipley, S. A., and Dowrick, D. J., "Earthquake Survivability of Concrete Platforms", Paper 3159, Offshore Technology Conference, Houston, Texas, 1978, pp 957-973.

8.10 NZS 4203 : 1984, "Code of Practice for General Structural Design and Design Loadings for Buildings", Standards Association of New Zealand, Wellington, 100 pp.

8.11 Fried, P., Handy, F. and Seccombe, P., "The Story of Maui", Maui Development Limited, Wellington, 1979, 255pp.

8.12 Hansen, F. J., Inoue, T. and Henrichsen, J. P., "A New Concept for Offshore Platform Construction", Proceedings of the 22nd Technical Conference, New Zealand Concrete Society, Christchurch, Sept. 1986, pp 2-3.

8.13 "Offshore Platform of Hybrid Structure", Kumagai-Kampsax Brochure, 1985, 6 pp.

8.14 Carr, A. J., "RUAUMOKO", Computer Program Library, Department of Civil Engineering, University of Canterbury, 1986.

8.15 Liaw, C.-Y. and Chopra, A. K., "Earthquake Response of Axisymmetric Towers Structures Surrounded by Water", Earthquake Engineering Research Center, Report No. UBC/EERC-80/13, University of California Berkeley, May 1973, 161 pp.

8.16 Veletsos, A. S. and Verbic, B., "Basic Response Functions for Elastic Foundations", Journal of the Engineering Mechanics Division, ASCE, Vol. 100, No. EM2, April 1974, pp 189-202.

8.17 "Maui Development Environmental Impact Report", Vols I and II, Shell BP and Todd Oil Services Limited, New Plymouth, New Zealand, June 1974.

8.18 Seed, H. B. and Idriss, I. M., "Soil Moduli and Damping Factors for Dynamic Response Analyses", Earthquake Engineering Research Center, Report No. EERC 70-10, University of California Berkeley, Dec. 1970, 39 pp.

8.19 Myerhof, G. G., "The Ultimate Bearing Capacity of Foundations", Geotechnique, II, 4, 301, London, 1951.

8.20 Hansen, J. Brinch, "Foundation of Structures - General Report", Proc. 4th International Conf. on Soil Mechanics and Foundation Engineering, II, London, 1957, pp 441-447.

8.21 Hansen, J. Brinch, "A revised and Extended Formula for Bearing Capacity", Bulletin No. 28, Danish Geotechnical Institute, 1970, pp 5-11.

8.22 Young, A. G., Kraft, L. M. and Focht, J. A., "Geotechnical Considerations in Foundation Design of Offshore Gravity Structures", Journal of Petroleum Technology, Vol. 28, August 1976.

8.23 Hansen, J. Brinch, "Modes of Failure Under Inclined Eccentric Loads", Vol. One, Intnl. Conf. on the Behaviour of Offshore Structures, Norwegian Institute of Technology, Trondheim, 1976, pp 488-500.

8.24 Brebbia, C. A. and Walker, S., " Dynamic Analysis of Offshore Structures", Newnes-Butterworths, 1979, 323 pp.

8.25 Morison, J. R., O'Brien, M. P., Johnson, J. W. and Schaaf, S. A., "The Force Exerted by Surface Waves on Piles", Petroleum Transactions, AIME, Vol. 189, 1950, pp 149-154.

8.26 Hogben, N. and Standing, R. G., "Experience in Computing Wave Loads on Large Bodies", Paper 2189, Proc. Offshore Technology Conference, Houston Texas, 1975.

8.27 NZS 3101: 1982, "Code of Practice for the Design of Concrete Structures", Standards Association of New Zealand, Wellington.

Chapter 9

SUMMARY OF CONCLUSIONS AND RECOMMENDATIONS FOR FUTURE RESEARCH

9.1 SUMMARY OF CONCLUSIONS

Conclusions drawn from each section of work were generally stated at the end of each chapter. A summary of the most important findings is given in the following.

1. For the purposes of seismic analysis of large offshore concrete gravity platforms, water-structure interaction effects can be adequately allowed for using added mass concepts. Inertia effects dominate the interaction and viscous drag terms can normally be ignored as being small. Added water masses can be estimated from the analytically derived curves for cylindrical members which depend on the member radius to water depth. For non-prismatic members the added mass can be adequately estimated from the curve appropriate for the radius to water depth at each point over the member length. For slender members the added water mass will be equal to the displaced mass of water. For members with radii greater than about 10 percent of the water depth the added mass can be substantially less than the displaced mass of water.

2. Soil-structure interaction remains a major source of uncertainty in the analysis of offshore platform structures, as with onshore structures. The effects of this interaction on platform structures of the type installed in the North Sea were briefly studied. A method of allowing for foundation interaction on an elastic half-space using translational and rotational spring and dashpot members, with frequency dependent properties suggested by previous researchers, was adopted. For the North Sea type structure soil-structure did not seem to have a major influence on the strength or ductility demands in the leg members but did have a major influence on foundation loadings. The frequency dependence of the rotational interaction behaviour could be reasonably allowed for by choosing constant valued properties based on the dominant frequency of rotational response of the platform base.

3. Principles of seismic hazard analysis were reviewed and seismic hazard analysis predictions of uniform risk response spectral accelerations were presented for structures in New Zealand. Presentation of the results paid particular attention to the predictions for structures with long periods of vibration as interest had not been focussed on these in the past. Predicted acceleration response spectra were compared with spectra from some of the extreme strong-motion seismological records available at present. It was emphasised that some account should be taken of these in determining appropriate design spectra corresponding to long return periods. A suitable compromise between the hazard analysis results and spectra from existing strong-motion records is embodied in the proposed amendment to the New Zealand Loadings Code NZS 4203. It is suggested that design response spectra for fixed offshore platform structures in New Zealand should be based on those recommendations.

4. The site response effects of some simple example sites was investigated using dynamic time-history computer analyses to examine the influence of flexible nonlinear soil deposits on seabed surface motions. Response of the dense sand deposits was strongly nonlinear and influenced by the level of shear strain induced in the soil. Shear strains of up to 1 percent could be expected from moderate to high intensity earthquake shaking. A number of analyses were carried out to investigate the likely distributions of maximum soil shear strains and response spectra derived from seabed surface motions. The study briefly examined the effects of intensity of input motion, depth of soil over bedrock, refinement of finite element mesh and type of nonlinear hysteresis rule. Studies were not extensive enough to make detailed conclusions about the influence of flexible non-linear material on the response spectra which should be used for design

purposes. It is suggested that the design spectra for soft ground presented in Chapter 3 should be used in lieu of comprehensive site response studies.

Site-platform interaction was also investigated using simple two-dimensional dynamic analysis models with nonlinear soil members. These studies showed qualitatively the considerable difference between effects which could be expected to occur locally around a gravity platform base and in the so-called free-field at a distance from the platform. Much more detailed analysis techniques are required to obtain quantitative conclusions about the interaction between platform structures and nonlinear soil materials. At present interaction effects are based on elastic half-space theories, such as those discussed in Chapter 2. It appears reasonable in estimating foundation compliance characteristics using such methods, to take account of the likely levels of shear strain which could be expected from the intensity of earthquake shaking.

5. The need for generating artificial earthquake records was discussed and methods by which such records can be obtained were presented. A suite of artificial accelerograms was obtained to match the soft ground design acceleration response spectra by the recently proposed amendment to the New Zealand Loadings Code NZS 4203.

6. An experimental study was carried out to investigate the strength and ductility characteristics of hollow circular concrete members. Many tests had been conducted on solid members in the past but very few had looked at the performance of thin-walled hollow members. Six partially prestressed or reinforced concrete columns were tested which represented scale models of members which could be used in offshore platform structures. Results showed that such members could display ductile behaviour if a sufficient quantity of well detailed transverse confining reinforcement was present in the plastic hinge regions. Final failure was characterised by sudden losses of strength and severe concentrations of compression zone damage. Thin-walled members appear to be less capable of spreading compression zone damage along the plastic hinge region. It was reasoned that satisfactory behaviour could be expected until the critical section reached the peak of the governing moment-curvature relationship. As in previous tests of solid members, flexural strength calculations based on the ACI 318 flexural strength analysis gave quite conservative estimates of the actual strength mobilized by the test units. The method adopted for shear design of these members was found to be conservative.

7. Cyclic moment-curvature analyses incorporating refined stress-strain models for concrete and reinforcing steels were used to predict the theoretical strength and ductility available from hollow circular concrete sections. A range of variables appropriate to the members which could be used in offshore concrete platforms was considered. Charts were presented to enable ideal flexural strength, effective flexural stiffness, yield curvature and available ultimate curvature to be estimated for such sections. The charts were presented in nondimensional form and could be used directly by designers for members of any size. The design charts could also be used to estimate quantities of transverse confining reinforcement required in plastic hinge regions of members to enable them to sustain particular ductility demands.

8. Feasibility studies were carried out to estimate the seismic performance of two different concrete gravity platforms at a site off the New Zealand coast. A three legged North Sea type platform, and a hybrid concrete and steel frame were considered. Two different levels of design earthquake loading were applied to each to assess the influence on the size and design of critical members and their inelastic performance during very large earthquakes. The hybrid structure used much less material but very high levels of shear were predicted in the hollow concrete members during severe earthquake excitation. Simple checks indicated that effects on the foundation would also be more severe in this structure using the assumed footing configuration. Performance of the North Sea type cantilever structure was adequate. Flexural ductility demands in both structures were quite modest, as considerable levels of strength were provided to resist wave loadings and moderate earthquake shaking without damage.

9.2 RECOMMENDATIONS FOR FUTURE RESEARCH

This research looked briefly at many aspects of the seismic performance of offshore concrete gravity platform structures. As a result the scope in each area was limited but a number of important issues have been highlighted and it is possible to identify needs for future research.

1. Probably the most important problem identified by this research is that of soil-structure interaction. This problem faces designers of all structures, not just offshore platforms. For the case where the foundation material can be assumed elastic there are techniques available to allow for the interaction effects. However, it is clear that materials likely to be found at offshore sites could become nonlinear at quite low levels of earthquake induced ground shaking. Interaction of structures with nonlinear foundation materials needs extensive research. For offshore sites the additional complication of the foundation material being saturated, and possibly not allowing compliance, arises. This also requires investigation.

2. Determination of appropriate acceleration response spectra remains a problem for the design of all structures. Seismic hazard analysis predictions should improve as more strong-motion records are obtained from the epicentral region of large earthquakes. Continuing investigations of seismic hazard should be carried out as further data is obtained.

3. Further investigation is necessary to determine a conservative method for allowing for local site response effects. These may be very important at offshore sites where relatively flexible materials are often encountered. The influence of the nonlinear material behaviour on the character of the seabed surface motions could be studied in much more detail than has been attempted in this research.

4. Experimental research should be continued to determine the likely behaviour of high strength concrete with transverse confinement. Concretes with compressive cylinder strengths of 50 MPa are being used routinely in large structures such as offshore platforms. There is a current trend toward the use of very high strength concretes with cylinder strengths up to 100 MPa. Little is known about the behaviour of members or the effectiveness of confinement in members constructed from those very high strength concretes.

5. No sign of buckling was observed in the walls of the column units tested in this study. Members with substantially larger diameter to wall thickness ratios may be contemplated for use in offshore concrete platforms. Theoretical and/or experimental research could be undertaken to assess the likelihood of wall buckling in the plastic hinge regions of thin walled members during severe inelastic loading.

6. Further research could identify types of offshore concrete platform that are particularly well suited for seismic resistance. Compliant platforms or structures isolated from the seabed would appear to be sensible alternatives.

Classn:

SEISMIC PERFORMANCE OF OFFSHORE CONCRETE GRAVITY PLATFORMS

D. Whittaker

ABSTRACT: Dynamic analysis procedures are discussed with particular reference to water-structure and soil-structure interaction. Results of seismic hazard analysis for New Zealand are presented and design spectra are suggested. Experimental and companion theoretical studies investigated the strength and ductility of circular hollow members. Preliminary design studies of possible platforms are presented.

Department of Civil Engineering, University of Canterbury,
Doctor of Philosophy Thesis, 1987.